2010

Modeling discharge and surface processes in capacitively coupled reactors

Yang Yang
Iowa State University

Modeling discharge and surface processes in capacitively coupled reactors

by

Yang Yang

A dissertation submitted to the graduate faculty

in partial fulfillment of the requirements for the degree of

DOCTOR OF PHILOSOPHY

Major: Electrical Engineering

Program of Study Committee:
Mark J. Kushner, Major Professor
Gary L. Tuttle
Jiming Song
Steve W. Martin
Vikram L. Dalal

Iowa State University

Ames, Iowa

2010

TABLE OF CONTENTS

ACKNOWLEDGMENTS

Five years ago, in 136 Everitt Lab, Urbana, IL.

"So you agree to advise me?" I asked.

"Yes." Mark answered.

Five years later, I still feel excited when I recall this short conversation. I thank Prof. Mark J. Kushner for teaching me plasma physics; for showing me his commitment to our society; for enlightening me through conversations; for stimulating me with his own hard-working; for introducing me to all kinds of engineering-and-technology educational magazines; for numerous chances to interact with the world's leading plasma engineers and scientists; and most important, for helping me understand what lies behind U. S.'s world leading science and technology: the spirit of invention and fine engineering. I feel very lucky to have been advised by Prof. Mark J. Kushner.

I am also grateful to the members of my committee – Prof. Jiming Song, Prof. Steve Martin, Prof. Vikram Dalal, and Prof. Garry Tuttle for their valuable advice and helpful discussions.

I am thankful to Prof. George H. Miley at University of Illinois at Urbana-Champaign, for introducing me to the world of plasma.

I am thankful to the past and present members of the Optical and Discharge Physics Group for their friendship and support – Dr. Shahid Rauf, Dr. Peter Ventzek, Dr. Wenli Z. Collison, Dr. Phillip Stout, Dr. Ronald L. Kinder, Dr. Junqing Lu, Dr. Kapil Rajaraman, Dr. Vivek Vyas, Dr. Ananth Bhoj, Dr. Ramesh Arakoni, Dr. Ankur Agarwal, Dr. Natalia Babaeva, Mingmei Wang, Juline Shoeb, Dr. Zhongmin Xiong, Jun-chieh Wang and Sang-heon Song.

I'd like to thank Pamela J. Myers in Electrical and Computer Engineering at Iowa State University for helping with paper work through my doctorate. Special thanks to Nancy Knight for helping me make an easy transition to Iowa State University. Special thanks to Paul Jewell (ISU) and Jonathan Plumber (UMICH) for arranging the videoconferencing. Thanks are also due to Becky Meline at University of Illinois at Urbana-Champaign for her great help and valuable advices.

I'd like to acknowledge all my friends in China and U. S., for all the comfort, warmth and smiling faces from you.

My parents, grandparents and other relatives have always been extremely supportive thorough the many years of my education. Without your support and love, I cannot go this far. I'm also grateful to the faculty at the Department of Nuclear Engineering at Shanghai Jiaotong University, especially to Miss Lianying Zhou, Prof. Wenjuan Zhou, Prof. Jijun Xu, Prof. Yanhua Yang, Prof. Bo Kuang, for educating me and giving me a solid base for Ph. D. study, and also to my graduate student fellows, Dr. Wei Yao, Dr. Ronghua Zhang and Nanhai Zou, from whom I learned a lot.

Finally, I would like to thank my wife, Ying Yi and my son, Adam Yuheng Yang − because of you my life is full of joy.

ABSTRACT

Plasmas are ideal for producing reactive species (radicals, ions) for modifying surface properties to achieve desired mechanical or chemical functionality. Two of the most technologically (and commercially) important applications of plasmas are etching/deposition for microelectronic fabrication and functionalization of polymers. Among these applications, capacitively coupled plasma (CCP) sources are widely used.

In this work, different types of capacitively coupled plasma sources and fluorination of polypropylene in a large-area CCP source are modeled using a 2-d hybrid plasma equipment model. As improvements to the model, algorithms such as a full-wave Maxwell solver, fully implicit electron drift-diffusion transport, and fully implicit electron momentum transport were developed and integrated into the model. In this thesis, we looked at the following problems:

Magnetically enhanced, capacitively coupled radio frequency plasma sources are finding continued use for etching of materials for microelectronics fabrication. MERIE (magnetically enhanced reactive ion etching) sources typically use magnetic fields of tens to hundreds of Gauss parallel to the substrate. Multi-frequency sources are used to separately control the magnitude of the ion and radical fluxes (typically with a high frequency source) and the ion energy distributions (typically with a low frequency) to the substrate. The properties of a dual frequency MERIE reactor are discussed using results from a computational investigation. There is a gradual convergence of the ion flux to the wafer from being nearly uniform to center peaked with increasing strength of radial magnetic field from 0 G to 200 G. There are peaks in electron temperature at both electrodes and a local minimum in the bulk plasma for a radial magnetic field of 150 G due to local sheathing heating from decreased cross field mobility.

Dual frequency, capacitively coupled plasma (DF-CCP) tools for etching and deposition for microelectronics fabrication typically use a high frequency (*HF*, tens to hundreds of MHz) to sustain the plasma and a low frequency (*LF*, a few to 10 MHz) for ion acceleration into the wafer. With an increase in both the high frequency and wafer size, electromagnetic wave effects (i.e., propagation, constructive and destructive interference) can affect the spatial distribution of power deposition and reactive fluxes to the wafer. Results from a two-dimensional computational investigation of a DF-CCP reactor, incorporating a full-wave solution of Maxwell's equations, are discussed. As in single frequency CCPs, the electron density transitions from edge

high to center high with increasing *HF*. This transition is analyzed by correlating the spatial variation of the phase, magnitude and wavelength of the *HF* electric field to the spatial variation of the electron energy distributions (EEDs) and ionization sources. This transition is sensitive to the gas mixture, particularly those containing electronegative gases due to the accompany change in conductivity. Process parameters, such as pressure, gas mixture, and *LF* and *HF* power deposition are important to determining the uniformity of the plasma and properties of ions incident on the wafer. The consequences of process parameters, *i. e.*, pressure, gas mixture and *LF* and *HF* power on uniformity and ion energy distributions to the wafer are also investigated. Due to the coupling of finite wavelength, electromagnetic skin, electrostatic edge and electronegative effects, there are no simple scaling laws for plasma uniformity. The plasma uniformity is ultimately a function of conductivity and energy relaxation distance of electrons accelerated by electric fields in and near the sheath. There is a strong second-order effect on uniformity due to feedback from the electron energy distributions (EEDs) to ionization sources. The trends are correlated to the spatial variation of the *HF* electric field, to the total power deposition and to the spatial variation of EEDs and ionization sources.

Another application of CCP sources is polymer surface modification. The surface energy and adhesion properties of commodity polymers such as polypropylene (PP) can be controlled by functionalization of the surface layers in plasmas. We developed a surface reaction mechanism for fluorination of PP in fluorine containing CCP plasmas which includes a hierarchy of reactions beginning with H abstraction by F atoms and followed by passivation by F and F_2, and cross-linking, ion (sputtering, scission) and photon (H_2 abstraction, scission) activated processes. Predicted surface compositions show good agreement with experiment results. The lack of total fluorination with long plasma exposure is found to be likely caused by cross-linking, which creates Carbon–Carbon (C-C) bonds that might otherwise be passivated by F atoms. Increasing steric hindrances as fluorination proceeds also contribute to lower F/C ratios.

1. INTRODUCTION

1.1 Plasmas: An Introduction

Plasma is often referred to as the fourth state of matter and is the most common form of matter in the universe. It is estimated that 99 percent of the known universe, not including dark matter, is made of plasma. As a comparison, a gas is a collection of atoms and molecules and is neutral on a "local" and global basis, but a plasma contains a substantial number of both positively and negatively charged particles. Therefore, the physical properties of the plasma medium are affected by electromagnetic interactions.

A gaseous plasma is obtained by ionizing atoms or molecules in the gas, thereby creating a fluid containing ions, electrons and neutral particles. When an electric field is applied to a gas, free electrons are accelerated by the field. Because the mass of an electron is much smaller than that of a neutral species, electrons lose almost no energy during electron-neutral momentum transfer collisions. As a result, the free electrons are accelerated to very high energies, typically several electron volts (eVs). When electron energies exceed the threshold energies of inelastic collisions (ionization or excitation), electron impact neutral species produces electron-ion pairs and neutral radicals.

Although some degree of ionization will occur in any gas under most circumstances, the term "plasma" technically refers to the state where charge density in the gas is large enough for 1) the gas to remain almost electrically neutral and 2) electric field generated by the ionized gas to shield out the influence of external electric fields. Technological plasmas or low temperature non-equilibrium plasmas refer to partially ionized gases with electrons at highly elevated temperatures (few to 10s of eV) that are larger than the ion and neutral gas temperatures, which

remain close to room temperature. Technological plasmas are a power transfer media. Electrons transfer power from the "wall plug" to internal modes of atoms / molecules, a process illustrated in Fig.1. Partially ionized plasmas contain neutral atoms and molecules, electrons, positive ions and negative ions and are not neutral on a microscopic scale, but are neutral on a global scale.

Parameters such as the degree of ionization (ratio of electrons to neutral particles density, n_e / N), density of electrons, n_e, and the electron temperature, T_e can be used to characterize a plasma in a broad sense. Regardless of the large variation of the methods to generate technological plasmas (inductive coupling, capacitive coupling, microwave, electron beam, helicon, *et al*.) and wide operating conditions, technological low pressure plasmas have following common characteristics:

a) Ionization fraction (n_e/N): in the range of 10^{-2}-10^{-6}.

b) Electron temperature: a few electron volts (eV, 1 eV ≈ 11,600 K).

c) Electron density: 10^{9}-10^{11} cm^{-3}

Technological plasmas are called “collisional” because electrons impart energy to neutrals by physical impact. In these plasmas, electron impact on otherwise unreactive gases produces neutral radicals and ions which drift or diffuse to surfaces where they add, remove or modify materials. As such, partially ionized plasmas are ideal for modifying surface properties to achieve desired mechanical or chemical functionality. Two of the most technologically (and commercially) important uses of plasmas are functionalization of polymers and etching/deposition for microelectronic fabrication.[1-10]

1.2 Plasma Processing Tools in Microelectronics Fabrication

Moore's law has characterized the microelectronics industry since 1980, when Gordon Moore observed that the number of transistors in microprocessors doubles every 18 months. The doubling cycle was later extended to 24 months, to compensate for expected increases in the complexity of semiconductors. The industry has obeyed Moore's law for over 20 generations. This has lead to smaller devices and features and improved capabilities over the years. The process of fabricating these devices involves hundreds of steps while critical dimensions have shrunk to 10's of Å (a few atomic monolayers).

Plasma processing of materials is an essential technology for microelectronics fabrication. The prevalence of plasma processing equipment in microelectronics fabrication will continue through future technology nodes. For applications such as dielectric etching and thin film deposition, capacitively driven radio frequency (rf) discharges are commonly used. An idealized discharge in plane parallel geometry, shown in Fig. 2, consists of a vacuum chamber containing two planar electrodes separated by a spacing *l* and driven by an rf power source.[11] The substrates are placed on one electrode, feedstock gases are injected through the shower head, which also serves as the grounded electrode, and effluent gases are removed by the vacuum pump. When operated at low pressure, with the wafer mounted on the powered electrode, and used to remove substrate material, such reactors are commonly called reactive ion etchers (RIEs). A schematic diagram of a commercial RIE and typical etch rates for photoresist are shown in Fig.3.[12]

One method of improving the performance of capacitively coupled plasma (CCP) sources is applying multi-frequency radio frequency (rf) sources with the goal of separately controlling ion and radical fluxes, and ion energy distributions to the substrate.[13-18] Typically in a dual frequency CCP reactor (DF-CCP), power is applied at a lower frequency to the bottom electrode

(a few MHz to 10 MHz) holding the wafer; and higher frequency power is applied to the upper electrode (tens of MHz to hundreds of MHz) often serving as the shower head. Power at the lower frequency (*LF*) is intended to control the shape of the ion energy and angular distributions (IEADs) to the wafer. Power at the higher frequency (*HF*) is intended to control the production of ions and radicals. (In some variants of DF-CCP, both frequencies are applied to the lower electrode.[19]) Decoupling the two rf sources is therefore desirable to achieving these separate controls. With the lower frequency kept at a few MHz, increasing the higher frequency to tens and hundreds of MHz is necessary to functionally separate the two rf sources. The use of very-high-frequency rf (> 100 MHz) also provides a plasma environment, presumably a low electron temperature, that is conducive to producing a favorable distribution of radicals by electron impact dissociation. The low electron temperature is also preferred to minimize plasma damage and photoresist erosion. An example of a DF-CCP reactor used for dielectric etching is shown in Fig. 4.

DF-CCP reactors were first developed at a time when the wafer size was transitioning from 200 mm to 300 mm. With shrinking geometries, large wafers and new materials, it is more important and more difficult to deliver uniform fluxes of radicals and ions to the substrate. However, as the excitation frequency increases, the effective wavelengths of the electromagnetic power could be commensurate with the radius of the electrode and the rf power deposition transitions from a electrostatic manner to a electromagnetic manner. Thus, finite wavelength effects and skin effects can limit processing uniformity.[19] For example, the electromagnetic wave launched by rf sources can not penetrate the metal electrode and must propagate around it and into the plasma. As the electromagnetic wave propagates inward along the electrode surface, the constructive interference in the center of the reactor enhances the local power deposition

thereby increasing the plasma density at the center of the reactor. This effect is usually referred to as standing wave effect or finite wavelength effect in the literature.[19-22] For example, Hebner *et al.* performed diagnostics of single frequency operating in argon and driven at frequencies between 10 and 190 MHz.[22] They found that with grounded lower electrode the spatial distribution of argon ions transitioned from uniform to center peaked as the excitation frequency was increased on the upper electrode, as shown in Fig. 5. As the excitation frequency increases, the plasma skin depth also decreases, which leads to skin effect. Skin effects usually develop with increasing power deposition or pressure and tends to enhance the power deposition near the electrode edges.[19-22]

Another method of improving the performance of CCP sources is applying a transverse static magnetic field (tens to hundreds of Gauss) approximately parallel to the electrodes with the goal of either increasing the plasma density for a given pressure or lowering the operating pressure. In this configuration the devices are often called magnetically enhanced reactive ion etching (MERIE) reactors.[23-26] MERIE reactors are also finding continued use for etching of materials for microelectronics fabrication at a time when DF-CCP sources are also being developed.[27] An example of MERIE reactor is shown in Fig. 6, where the static magnetic field is provided by two pairs of electromagnets located on opposite sides of the reactor.[28]

A typical MERIE reactor is a parallel plate device operating at tens to hundreds mTorr of gas pressure and few to tens MHz excitation frequency. A static magnetic field is usually applied parallel to the electrodes with the goal of increasing the plasma density for a given power deposition by reducing the rate of loss of charged particles. Due to the difficulty of obtaining tailored magnetic fields across large wafers, MERIE reactors often use rotating static magnetic fields to average out nonuniformities resulting from $\vec{v} \times \vec{B}$ forces.[23] MERIE reactors have been

used for microelectronics fabrication for many years with there being few quantitative experimental or modeling studies reported in the open literature. For single frequency reactors, it has been found that the spatial distribution of the plasma is sensitive to the magnitude of the magnetic field and may transition from edge high to center high to uniform with increasing magnetic field.[29] As the magnetic field increases and electron mobility decreases the proportion of the rf cycle during which the sheath potential is at its minimum value increases, and in some cases the sheath field reverses during the anodic portion of the rf cycle.[29-30]

1.3 Plasma Polymer Processing

Plasma treatment is a potentially attractive method for modifying the surface characteristics of a polymer without affecting the bulk properties of the material.[31-34] Plasma treatment also has the advantages of short treatment times and room temperature operation. Surface functionalization using plasmas involves the reactive species including ions, electrons, radicals and photons generated in the plasmas. These species are transported to the surface and where they react to alter surface composition and bring about marked changes in surface properties. The process is dry that eliminates the need for subsequent cleaning and waste disposal when using liquids.

In the industry, a class of technological plasmas that operate around atmospheric pressure has been widely used for surface functionalization of polymers for many years. The primary advantage of using atmospheric pressure plasma treatment is the absence of expensive vacuum equipment required for low pressure operation. Typical examples of such devices are the dielectric barrier discharge (DBD), shown in Fig. 7, also called the 'corona discharge'.[35-36] The device is about 1 m wide and uses roller drums rotating at controlled speeds to move

polymer sheets across the device to enable continuous treatment in a web arrangement. In industry, these systems tend to be used for functionalization of low-value added, commodity materials, such as polypropylene used in packaging. Functionalization improves the surface energy and consequently the wettability and adhesion properties of these polymer surfaces.

A schematic for the web treatment of polymer films is in Fig. 8. The apparatus consists of a powered electrode embedded within dielectric structure that is exposed to the processing gas at its tip. There is a gas gap of a few mm between the powered electrode and the polymer which is placed on the grounded surface. The discharge is generated by the application of few to 10s of kVs voltage pulses at a few to 10s of kHz to breakdown the gas gap. Discharges generated at atmospheric pressure may be either diffuse or filamentary; a condition which depends on the gas composition and other factors such as the frequency of pulsing.[37-39] Typically, the gas is simply room air or O_2 containing mixtures, but other gases and mixtures including Ar, He, N_2, and NH_3 plasmas have also been used for polymer surface functionalization.[40-46] A range of polymers such as polypropylene [47], polyethylene [48], polyetheretherketone [49] used in packaging, polyamide fibers [50], polymethylmethacrylate [51], polystyrene [52], polyethylene terephthalate [53], polytetrafluoroethylene [54] and polyvinyl chloride [55] have been functionalized using plasmas.

The fluorination of organic polymers is of interest to modify their wetting properties by increasing their hydrophobicity.[56-59] The conventional approach to fluorinating polyolefin surfaces is to simply expose the polymer to fluorine gas. However, this method suffers from several disadvantages. Uncontrolled direct fluorination can cause degradation or deformation of the polymer substrate. Even with mild, nondisruptive direct fluorination, undesirably long reaction times are often necessary to achieve perfluorination of polyolefin substrates.[59-60]

The desire to produce fluorine containing radicals at low temperatures makes the use of low pressure, non-equilibrium plasmas an attractive option for this surface treatment. In low pressure fluorine containing plasmas, electrons impact on feedstock gases (mainly by dissociative excitation or attachment) produces fluorine containing radicals. These radicals both abstract hydrogen from the polymer surface layers, producing a dangling bond, and passivate that bond with a fluorine atom, a process know as fluorination. Also, in these plasmas, the PP sheets are subject to both energetic ion and photon fluxes which can sputter and initiate cross-linking. The modeling of the fluorination process is therefore challenging due to vast number of reactions from the interaction of different processes and lack of fundamental data for reaction rates.

Typical low pressure plasma sources for fluorination are capacitively coupled discharges in a parallel plate configuration operating at a few MHz with electrode separations of a few cm. Such discharges are used to inexpensively (a few cents per m^2) functionalize the surfaces of large areas of commodity polymer films (e.g. polypropylene) in a web configuration using an apparatus analogous to a printing press. In web processing, the film is continuously moved through the discharge at speeds of up to many centimeters per second with residence times of tens of seconds to a few seconds in the discharge. In high volume industrial processing, the polymer sheets may be moved through multiple stages of treatment, one or more of which may involve plasma treatment.

1.4 Challenges in Modeling of Plasma Processes

The use of modeling and simulation for the development of plasma equipment and etch processes has made significant progress over the past decade. Reactor scale modeling tools linked to profile simulators are now in daily use in the design of physical vapor deposition,

plasma deposition, plasma etching and ion implantation tools.[61-62] These modeling efforts have had quantifiable improvements in the development cycle of these tools as well as providing more qualitative improvements in our fundamental understanding of the plasma transport and chemistry occurring in the tools. Although these successes are encouraging, there are still significant challenges that face modeling and simulation to continue to provide added value to the industry. The origins of these challenges include the introduction of new materials (e.g., high-k dielectrics) for which knowledge bases are limited, increasing the dynamic range of operating conditions (e.g., very high frequency plasma sources) that extend beyond the realm of established modeling techniques, and accurately addressing manufacturing issues that require extreme spatial resolution. Addressing these challenges will require, as a highest priority, an improvement in the knowledge base of material properties for plasma transport (e.g., cross sections and transport coefficients) but, more importantly, for the plasma surface interactions that result in feature evolution. Beyond those improvements in knowledge bases are challenges in creating more robust modeling platforms that are able to predict new operating regimes, as opposed to simply analyzing those regimes that are initially empirically established.

The use of very high excitation frequencies highlights at least two issues. First, at frequencies exceeding 10s MHz, the electrons swarm is no longer in equilibrium with the electric field. As such, the traditional drift-diffusion approach for electron transport is not accurate. To address these conditions a kinetic approach is required (such as Monte Carlo) or the electron momentum equation must explicitly be solved. The second issue is the finite wavelength effect. As the plasma reduced wavelength of the rf power applied to the reactor approaches the size of the reactor, finite wavelength effects become increasingly more important. This in turn becomes increasingly more challenging for modeling due to the need for including a full solution of the

electromagnetic Maxwell's equations, as opposed to only the electrostatic Poisson's equation. These approaches should simultaneously resolve capacitive and inductive coupling.

1.5 Issues to Be Discussed

The goals of this thesis are to develop improved fundamental understanding and improve computational tools of reactor and plasma processing over a broad range of tools, chemistries and applications. In this thesis, I will discuss the following issues.

- A case study of the use of plasma equipment modeling for the development of a dual frequency magnetically enhanced reactive ion etching plasma source. In this work, the properties of a dual frequency MERIE reactor scaling to high frequency and low frequency power, and the strength of the applied magnetic field will be discussed.
- Computationally investigate the surface kinetics, plasma chemistry and scaling of low pressure plasma fluorination of polypropylene. In this work, a surface reaction mechanism for fluorination of polypropylene by neutral species, ion and photon bombardment produced in fluorine containing plasmas were developed and validated with surface diagnostics performed by 3M collaborators.
- Develop the computational capability to address DF-CCP plasma tools using very high frequencies (> 100s MHz). Use this capability to investigate scaling laws for etching and deposition systems to determine the mechanisms for “preferred” operation in these high frequency regimes; and means to design plasma tools which maximize uniformity. In this work, algorithms to solve the full set of Maxwell’s equations and the electron momentum equation were developed and added to the Hybird Plasma Equipment Model.

1.6 Summary

The organization of this thesis is as follows. The algorithms developed in this work were incorporated into the 2-dimensional (2d) Hybrid Plasma Equipment Model (HPEM) which is discussed in detail in Chapter 2. The Hybrid Plasma Equipment Model is a 2-dimensional hybrid simulator in which the densities, fluxes and temperatures of all charged and neutral species are solved for on a rectilinear mesh. Solutions of Maxwell's and Poisson's equations are included, as are kinetic simulations of electron and ion transport.

In Chapter 3, the properties of a 2-frequency MERIE reactor are discussed using results from a computational investigation. As in single frequency sources, the reduction in transverse electron mobility as the magnetic field increases can produce a reversal of the electric field in the sheath and an increase in voltage drop across the bulk plasma. These trends decrease ion energies and increase the angular spread of ions. Similar trends are found here, including a field reversal in the sheath at the high frequency electrode. These effects produce a coupling between the high and low frequency sources that compromise the independence of ion production and ion acceleration by the two sources.

In Chapter 4, results from a two-dimensional computational investigation of a DF-CCP reactor, incorporating a full-wave solution of Maxwell's equations, are discussed. As in single frequency CCPs, the electron density transitions from edge high to center high with increasing *HF*. This transition is analyzed by correlating the spatial variation of the phase, magnitude and wavelength of the *HF* electric field to the spatial variation of the electron energy distributions (EEDs) and ionization sources. This transition is sensitive to the gas mixture, particularly those containing electronegative gases due to the accompany change in conductivity. The consequences of these wave effects on the ion energy distributions incident onto the wafer are

also discussed. The consequences of operating pressure, *LF* and *HF* power deposition, and gas mixture on plasma uniformity are also examined by a parametric study. For example, the plasma uniformity is improved with CF_4 fractions larger than 0.2, mostly due to the decreasing finite wavelength effect from the decreasing plasma conductivity. The trends from our parametric study are analyzed by correlating the spatial variation of the *HF* electric field; to the total power deposition and to the spatial variation of the electron energy distributions (EEDs) and ionization sources. The consequences of these operating parameters on the ion energy distributions incident onto the wafer are also discussed.

In Chapter 5, the low-pressure plasma fluorination of PP in an industrially relevant CCP sustained in Ar/F_2 mixtures is discussed with results from a computational investigation. The surface reaction mechanism includes a hierarchy of processes beginning with H abstraction by F atoms followed by passivation by F and F_2. The mechanism also includes cross-linking, and ion (sputtering, scission) and photon-activated processes (H_2 abstraction, scission). Predictions for surface composition were compared to experiments for validation. It is found that the lack of total fluorination with long plasma exposure is likely caused by cross-linking, which creates C–C bonds that might otherwise be passivated by F atoms. Increasing steric hindrances as fluorination proceeds also contribute to lower F/C ratios. Sputtering of previously fluorinated sites followed by slow re-fluorination of underlying sites limits the total fluorination for long exposure times. The consequences of UV illumination from the plasma are generally only significant for long exposure times as photon fluxes are several orders of magnitude lower than those for neutral fluxes.

1.7 Figures

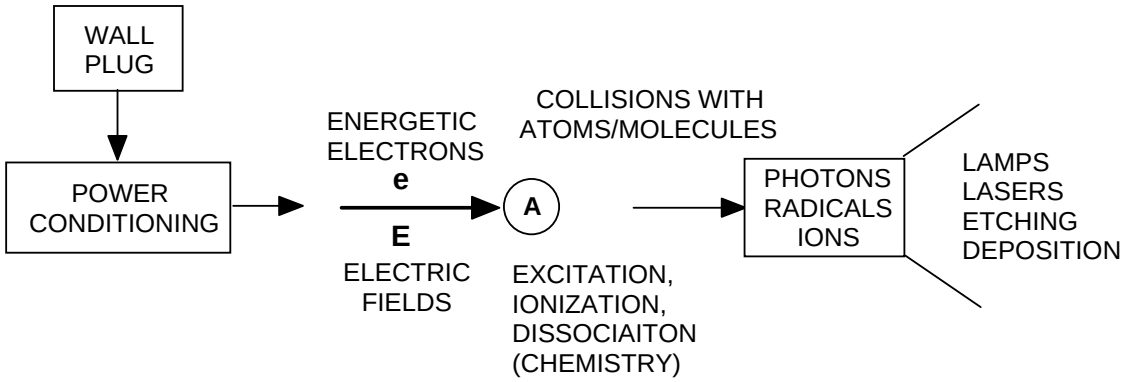

Fig. 1 Technological plasmas are a power transfer media.

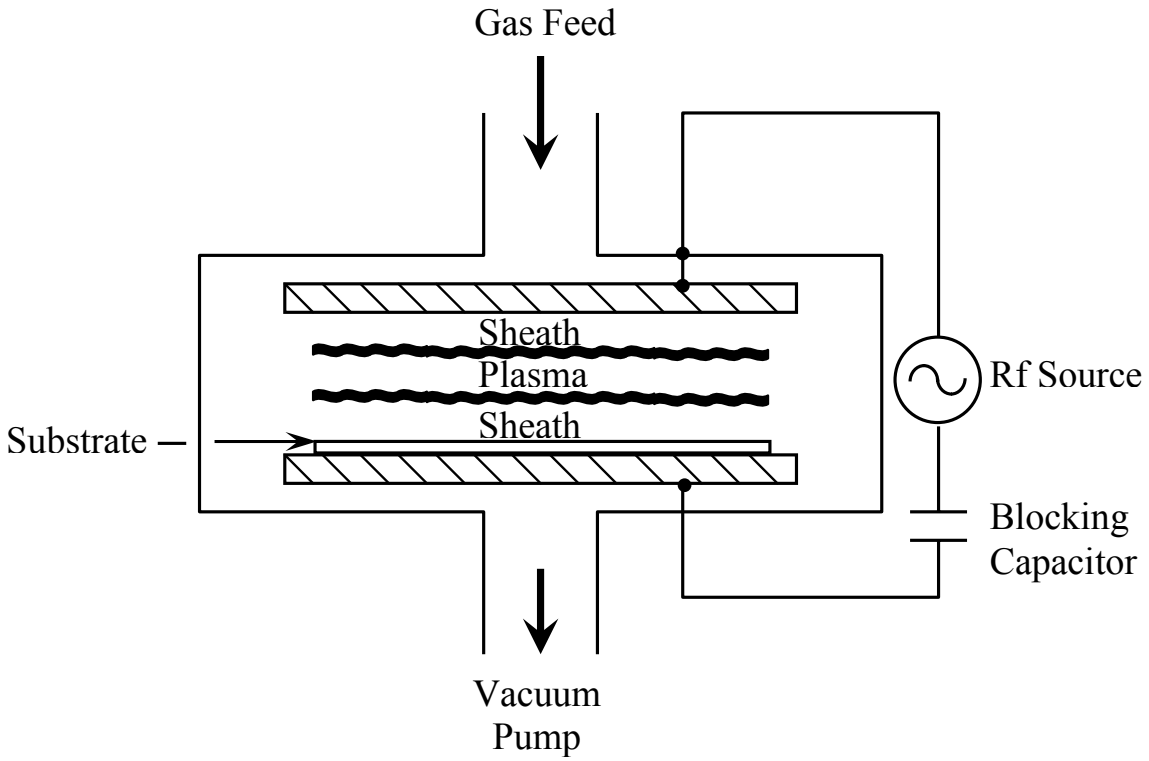

Fig. 2 Capacitive rf discharge in plane parallel geometry. [11]

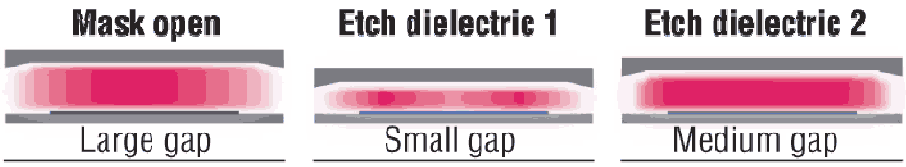

(a)

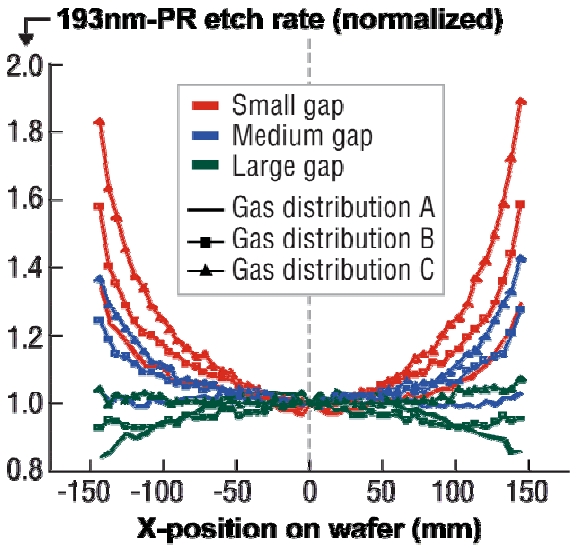

(b)

Fig. 3 A schematic diagram of a RIE and etch rate. (a) The RIE. The wafer sits on the bottom electrode. The electrode gap is adjusted for etching of different materials (mask, dielectric 1 and 2). (b) Control for etch rate with adjustable gap capability and multi-zone gas distribution.[12]

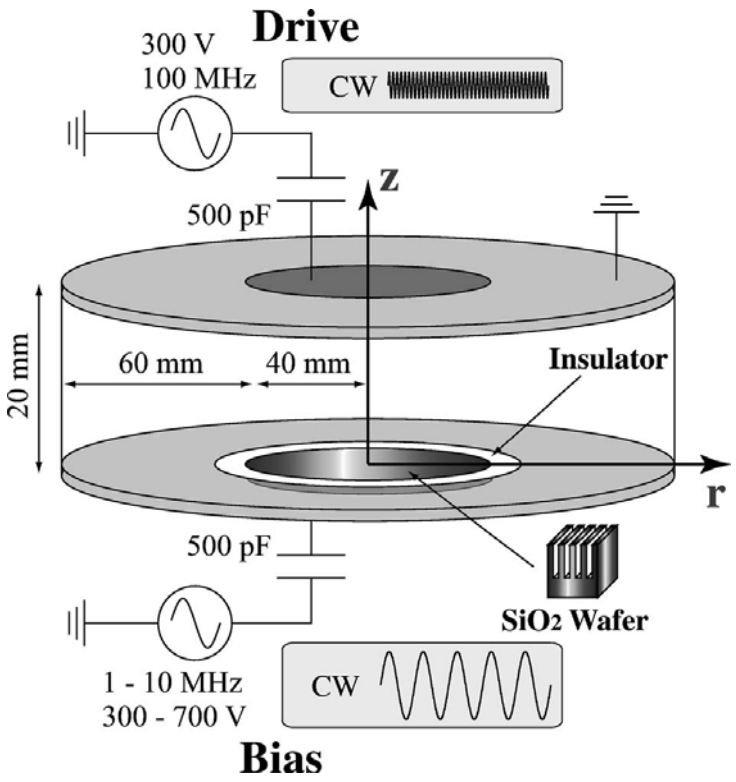

Fig. 4 Schematic diagram of a DF-CCP reactor. The top electrode is driven at 100 MHz and the bottom electrode is driven from 1 to 10 MHz. The wafer sits on the bottom electrode and is surrounded by a dielectric focus ring.[6]

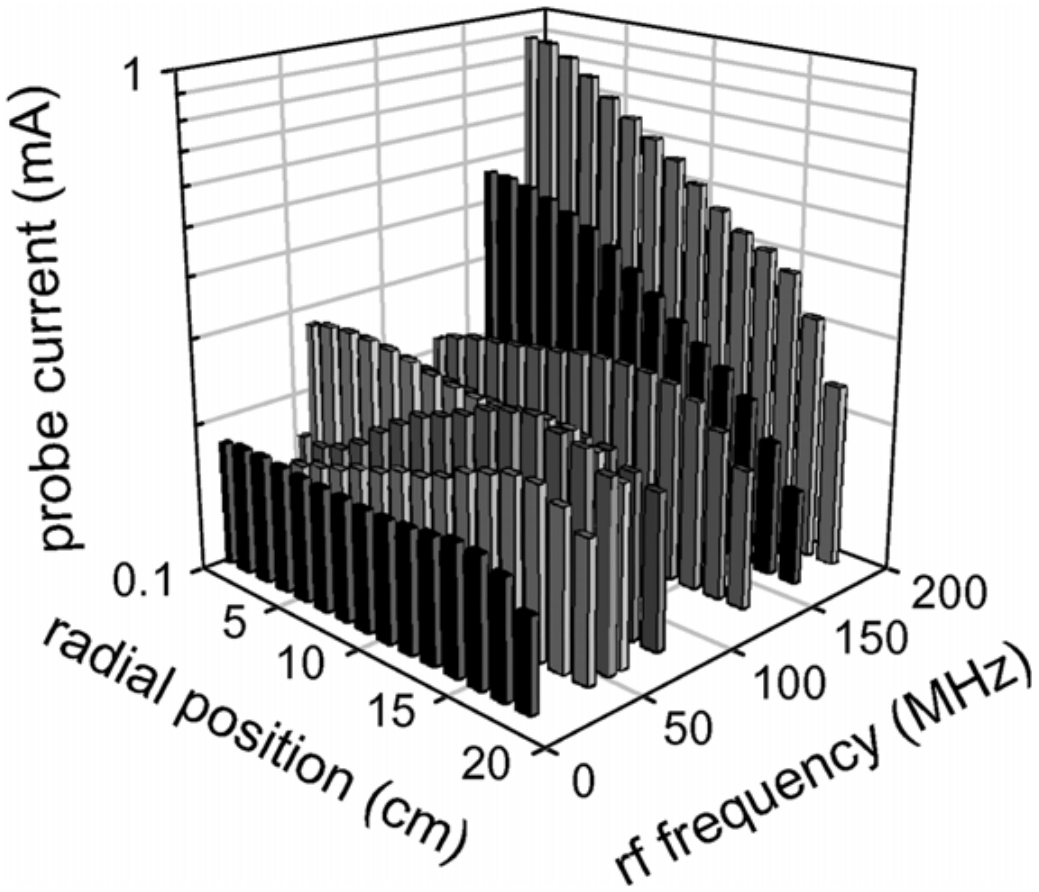

Fig. 5 Measurement of ion saturation current in a single frequency CCP reactor for rf drive frequencies between 13 and 189 MHz. The plasma transitioned from flat at 13 MHz, to edge high at intermediate frequencies, and to center high for frequencies exceeding 163 MHz.[22]

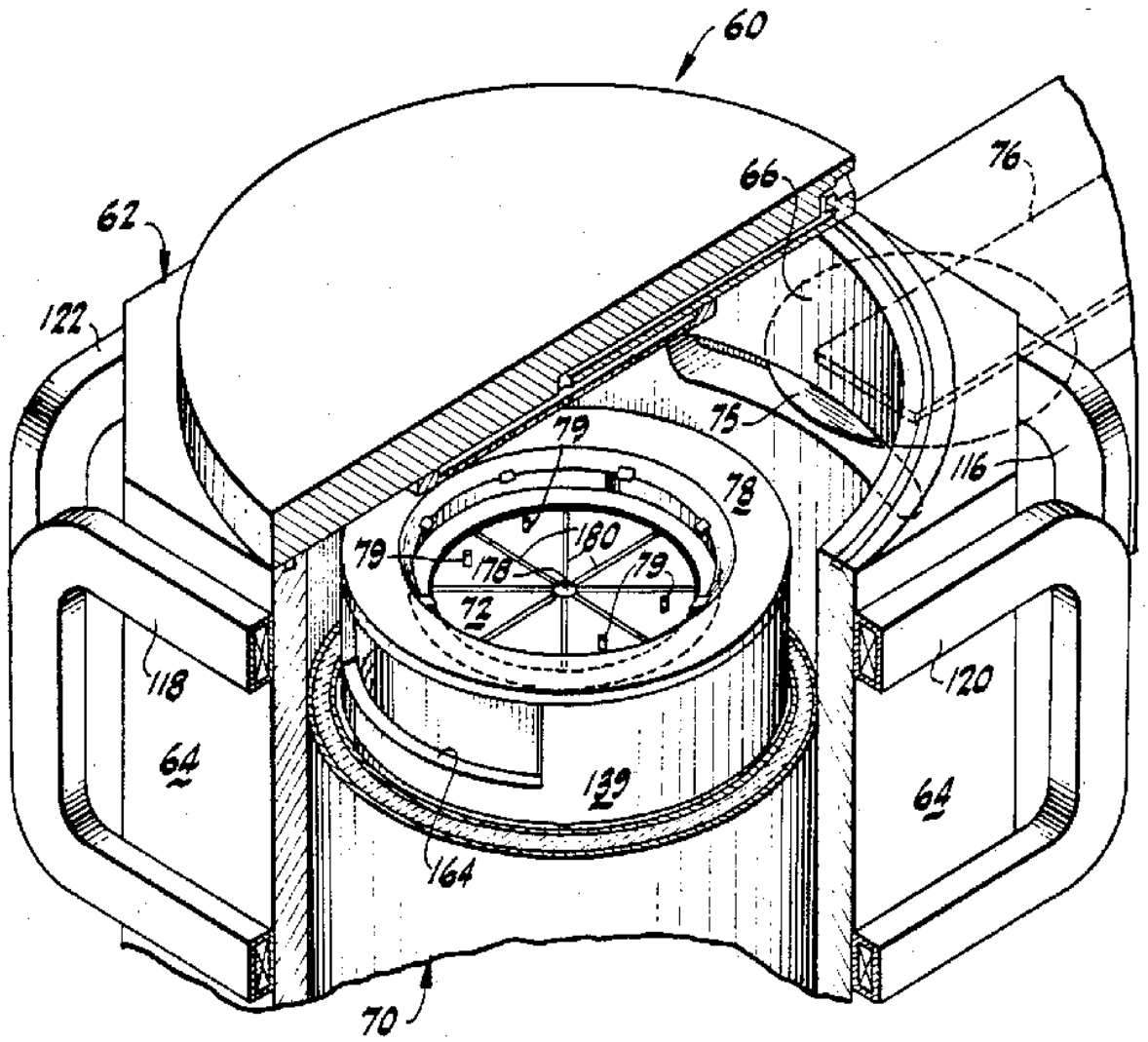

Fig. 6 Schematic diagram of a MERIE reactor. An electrically-controlled D.C. magnetic field parallel to the wafer surface is applied to provide high rate uniform etching at high pressures. The magnetic field is provided by two pairs of electromagnets located on opposite sides of the reactor.[28]

(a)

(b)

Fig. 7 Typical atmospheric pressure plasma treatment devices used to functionalize the surfaces of polymers (a) above, courtesy Tantec Inc. (b) below, courtesy Sigma Inc.

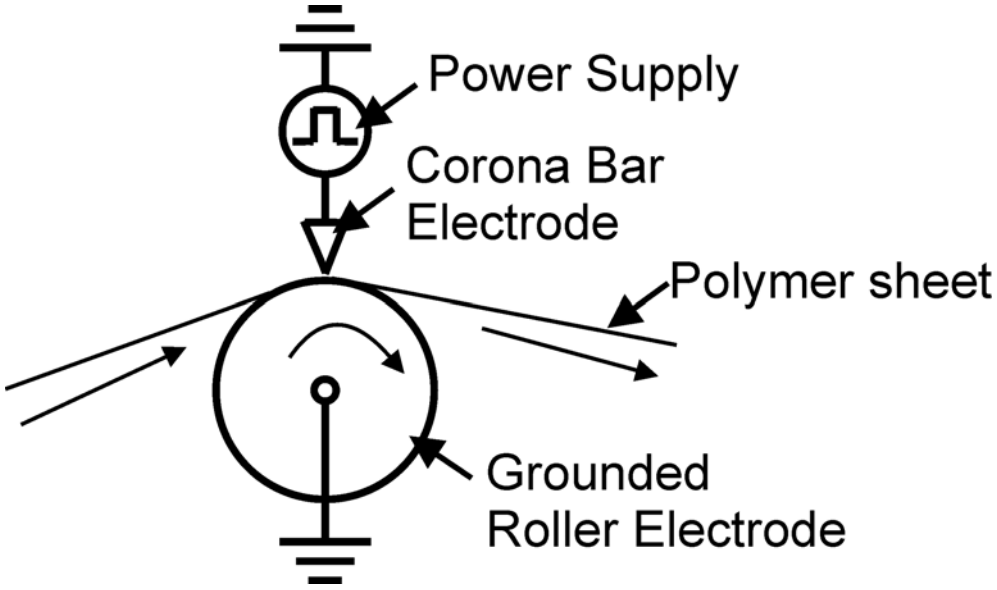

Fig. 8 Schematic of the web treatment arrangement used for the continuous plasma treatment of polymer sheets.

1.8 References

1. G.S. Oehrlein and J.F. Rembetski, IBM J. Res. Develop. **36**, 140 (1992).
2. D. M. Manos and D. L. Flamm, Plasma Etching: An Introduction., Academic Press, San Diego, 1989.
3. H. R. Koenig and L. I. Maissel, IBM J. Res. Develop. **14**, 106 (2000).
4. S. Matsumoto, J. Mat. Sci. Lett. **4**, 600 (1985).
5. R. A. Gottscho, C. W. Jurgensen and D. J. Vitkavage, J. Vac. Sci. Technol. B **10**, 2133 (1992).
6. T. Yagisawa, T. Shimada and T. Makabe, J. Vac. Sci. Technol. B **23**, 2212 (2005).
7. J. Schmitt, M. Elyaakoubi and L. Sansonnens, Plasma Sources Sci. Technol. **11**, A206 (2002).
8. W. Schwarzenbach, J. Derouard and N. Sadeghi, J. Appl. Phys. **90**, 5491 (2001).
9. H. Biederman, Vacuum **59**, 594 (2000).
10. D. T. Clark and A. Dilks, J. Plolymer Sci.: Polymer Chem. Edition **16**, 911 (1978).
11. M.A. Lieberman and A.J. Lichtenberg, Principles of Plasma Discharges and Materials Processing, Wiley, 1994.
12. V. Vahedi, M. Srinivasan and A. Bailey, Solid State Technology, 51, November, 2008.
13. P. C. Boyle, A. R. Ellingboe, M. M. Turner, J. Phys. D: Appl. Phys. **37**, 697 (2004).
14. T. Kitajima, Y. Takeo and T. Makabe, J. Vac. Sci. Technol. A **17**, 2510 (1999).
15. S. Rauf and M. J. Kushner, IEEE Trac. Plasma Sci. **27**, 1329 (1999).
16. T. Kitajima, Y. Takeo, N. Nakano and T. Makabe, J. Appl. Phys. **84**, 5928 (1998).
17. V. Georgieva V, A. Bogaerts, R. Gijbels, J. Appl. Phys. **94**, 3748 (2003)
18. J. Schulze, T. Gans, D. O'Connell, U. Czarnetzki, A. R. Ellingboe and M. M. Turner, J.

Phys. D: Appl. Phys. **40**, 7008 (2007).

19. P. Chabert, J. Phys. D: Appl. Phys. **40**, R63 (2007).

20. M. A. Lieberman, J. P. Booth, P. Chabert, J. M. Rax and M. M. Turner, Plasma Sources Sci. Technol. **11**, 283 (2002).

21. A. Perret, P. Chabert, J. P. Booth, J. Jolly, J. Guillon and Ph. Auvray, Appl. Phys. Lett. **83**, 243 (2003).

22. G. A. Hebner, E. V. Barnat, P. A. Miller, A. M. Paterson and J. P. Holland, Plasma Sources Sci. Technol. 15, 879 (2006).

23. R. A. Lindley, C. H. Bjorkman, H. Shan, K.-H. Ke, K. Doan, R. R. Mett and M. Welch, J. Vac. Sci. Technol. A **16**, 1600 (1998).

24. K. E. Davies, M. Gross and C. M. Horwitz, J. Vac. Sci. Technol. A **11**, 2752 (1993).

25. M. J. Buie, J. T. P. Pender and P. L. G. Ventzek, Jpn. J. Appl. Phys. **36**, 4838 (1997).

26. P. Berruyer, F. Vinet, H. Feldis, R. Blanc, M. Lerme, Y. Morand and T. Poiroux, J. Vac. Sci. Technol. A **16**, 1604 (1998).

27. S. Rauf, IEEE Trans. Plasma Sci. 31, 471 (2003).

28. D. Cheng, D. Maydan, S. Somekh, K. R. Stalder,, D. L. Andrews, M. Chang, J. M. White, Y. K. Wong, V. J. Zeitlin, D. N. Wang, U. S. Patent 4, 842, 683.

29. M. J. Kushner, J. Appl. Phys. **94**, 1436 (2003).

30. G. Y. Yeom, J. A. Thornton, and M. J. Kushner, J. Appl. Phys. **65**, 3825 (1989).

31. T. Yagi, A. E. Pavlath and A. G. Pittman, J. Appl. Polym. Sci. **27**, 4019 (1982).

32. J. P. Manion and D. J. Davies, U.S. Patent No. 3674667 (1982).

33. M. Strobel, S. Corn, C. S. Lyons and G. A. Korba, J. Polym. Sci. A: Polym. Chem. **25**, 1295 (1987).

34. N. Inagaki, S. Tasaka and M. Imai, J. Appl. Polym. Sci. **48**, 1963 (1993).

35. U. Kogelschatz, Plasma Chemistry and Plasma Processing, 23, 1 (2003).

36. H.-E. Wagner, R. Brandenburg, K.V. Kozlov, A. Sonnenfeld, P. Michel and J.F. Behnk, Vacuum, 71, 417, (2003).

37. F. Massines and G. Gouda, Journal of Physics D: Applied Physics, 31, 3411 (1998).

38. U. Kogelschatz, IEEE Transactions on Plasma Science, 30, 1400 (2002).

39. J. Rahel and D. M. Sherman, Journal of Physics D: Applied Physics, 38, 547 (2005).

40. G. Borcia, C. A. Anderson, N. M. D. Brown, Applied Surface Science 221, 203 (2004).

41. J. B. Lynch, P. D. Spence, D. E. Baker and T. A. Postlethwaite, Journal of Applied Polymer Science, 71, 319 (1999).

42. Yu. S. Akishev, M. E. Grushin, A. E. Monich, A. P. Napartovich, and N. I. Trushkin, High Energy Chemistry, 37, 286 (2003).

43. S. De, R. Sharma, N. Ali, and M. K. Mazumder, IEEE IAS, 39, 932 (2004).

44. S. Guimond, I. Radu, G. Czeremuszkin, D. J. Carlsson, and M. R. Wertheimer, Plasmas and Polymers, 7, 71 (2002)

45. G. Borcia, C. A. Anderson and N. M. D. Brown, Plasma Sources Science and Technology, 14, 259 (2005).

46. M. Sira, D. Trunec, P. Stahel, V. Bursikova, Z. Navratil and J. Bursik., Journal of Physics D: Applied Physics, 38, 621 (2005)

47. N. Sellin and J. S-C. Campos, Materials Research, 6, 163 (2003).

48. G. Borcia, N. M. D. Brown, D. Dixon and R. McIlhagger, Surface and Coatings Technology, 179, 70 (2004).

49. J. Comyn, L. Mascia, G. Xiao and B.M. Parker, Int. J. Adhesion and Adhesives, 16, 301

(1996) .

50. G. Borcia, N. Dumitrascu and G. Popa, Surface & Coatings Technology, 197, 316 (2005).

51. U. Schulz, P. Munzert and N. Kaiser, Surface and Coatings Technology, 142-144, 507 (2001).

52. K. Schroder, G. Babucke and A. Ohl, Surface and Interface Analysis, 36, 702 (2004).

53. L-A. O'Hare, J. A. Smith, S. R. Leadley, B. Parbhoo, A. J. Goodwin and J. F. Watts, Surface and Interface Analysis, 33, 617 (2002).

54. S. Ishikawa, K. Yukimura, K. Matsunaga and T. Maruyama, Surface and Coatings Technology, 130, 52, (2000).

55. N. Dumitrascu, G. Borcia and G. Popa, Journal of Applied Polymer Science, 81, 2419 (2001).

56. M. Anand, R. E. Cohen and R. F. Baddour, Polymer **22**, 361 (1981).

57. C.-M. Chan, Polymer Surface Modification and Characterization, Hanser-Gardner, Cincinnati, 1994.

58. G. A. Corbin, R. E. Cohen and R. F. Baddour, Polymer **23**, 1546 (1982).

59. R. J. Lagow and J. L. Margrave, Progress in Inorganic Chemistry **26**, 161 (1979).

60. D. T. Clark, W. J. Feast, W. K. R. Musgrave and I. Ritchie, J. Polym. Sci. Polym. Chem. Ed. **13**, 857 (1975).

61. P. L. G. Ventzek, S. Rauf, P. J. Stout, D. Zhang, W. Dauksher and E. Hall, Appl. Surf. Sci. **192**, 201 (2002).

62. S. Rauf, L. A. Gochberg, P. L. G. Ventzek and E. J. McInerney, Semiconductor International, Nov. 2005.

2. HYBRID PLASMA EQUIPMENT MODEL

2.1 Hybrid Plasma Equipment Model

The HPEM is a plasma equipment model developed to numerically investigate plasma processing reactors in two and three dimensions.[1-13] The HPEM has the capability of modeling complex reactor geometries and a wide variety of operating conditions. All the algorithms developed in this work have been integrated into the HPEM.

The HPEM addresses plasma physics and plasma chemistry in a modular fashion. The main body of the two dimensional (2D) HPEM consists of an electromagnetic module (EMM), an electron energy transport module (EETM), and a fluid kinetics module (FKM). The EMM calculates inductively coupled electric (from rf coils) and magnetic fields as well as static magnetic fields produced by dc magnetic coils or permanent magnets. The EETM solves for electron impact source functions and transport coefficients based on phase-resolved electromagnetic fields from the FKM and inductive and magnetic fields from the EMM. Results from the EETM are passed to the FKM, which solves the continuity, momentum, and energy equations coupled with Maxwell's equations to determine the spatially dependent density of charged and neutral species as well as electromagnetic fields generated by the plasma itself and electrodes (capacitive coupled fields). The outputs from the FKM are then fed back to the EMM or the EETM (in the absence of inductively coupled fields), a sequence that constitutes an iteration. Additional iterations are computed until a cycle-averaged steady state is achieved. Acceleration techniques are used to speed the cycle-averaged convergence of plasma properties.

Note that the HPEM is a comprehensive modeling platform developed for low pressure (< 10's Torr) plasma processing reactors. The HPEM is capable of addressing a variety of plasma processing tools, such as inductively coupled plasma (ICP) tools, reactive ion etchers (RIE), electron cyclotron resonance (ECR) sources, magnetron sputter and ionized metal physical vapor deposition (IMPVD), remote plasma activated chemical vapor deposition (RPACVD) and dust particle transport in plasma tools. For a specific application, not all modules in the HPEM will necessarily be called. For example, for capacitively coupled plasma RIE tools, the EMM module may not be called as there are no inductively coupled fields. (In this application, the EMM will be called only if there is static magnetic field from dc coils or permanent magnets.)

Several in-line modules of the HPEM have been developed for other specific purposes. Following every iteration, the converged electric fields and source functions for ions and neutrals may be recorded as a function of position and phase in the rf cycle. With these values, the energy and angular distributions of ions and neutrals incident on the substrate can be obtained using the Plasma Chemistry Monte Carlo Module (PCMCM).[10] Surface reactions in the HPEM are addressed by the Surface Chemistry Module (SCM) which not only provides the boundary conditions for the HPEM but also computes rates of material addition and removal on all surfaces in the reactor which, for the wafer, yields an etch rate.[8] The Monte Carlo radiation transport module (MCRTM) addresses the coupling of radiation transport with plasma kinetics.[11] The MCRTM directly interfaces with the FKM following its execution during each iteration through the HPEM. The MCRTM receives species densities, gas temperatures, and rate constants from the FKM. With these parameters the frequencies for perturbing and quenching collisions affecting the species participating in radiative transfer reactions are calculated.

Radiation trapping factors that modify the lifetime of radiating specie (which are then used in formulating rate equations during the next execution of the FKM) are also produced.

2.2 The Electromagnetics Module

The EMM calculates the coil generated electric and magnetic fields in the reactor as a function of position and phase ϕ during the rf cycle. The solution for the electromagnetic fields requires knowledge of the plasma conductivity, which is obtained from the FKM. The EMM also calculates the static magnetic fields generated by the permanent magnets or by equivalent dc loops, that is, currents that change on time scales which are long compared to the time in which the plasma reaches quasi-equilibrium.

The amplitude of electromagnetic field $\vec{E}$ in the frequency domain, is obtained by solving the following form of the wave equation:

$$\nabla\left(\frac{1}{\mu}\nabla\cdot\vec{E}\right)-\nabla\cdot\left(\frac{1}{\mu}\nabla\vec{E}\right)-\omega^2\varepsilon\vec{E}=-i\omega(\vec{J}+\overline{\overline{\sigma}}\cdot\vec{E}) \qquad (2.1)$$

where μ is the permeability, $\vec{E}$ is the electric field, ω is the frequency of the source current, ε is the permittivity, and $\vec{J}$ is the external antenna current density. $\overline{\overline{\sigma}}$ is the tensor conductivity and $\overline{\overline{\sigma}}\cdot\vec{E}$ is the conduction current. The ion current in solution of Eq. (2.1) is ignored due to the low mobility of ions. The tensor form of the conductivity is derived from its isotropic value, σ_0 by

$$\overline{\overline{\sigma}}=\frac{\sigma_0}{(\alpha^2+|B|^2)}\times\begin{pmatrix}\alpha^2B_r^2 & \alpha B_z+B_rB_\theta & -\alpha B_\theta+B_rB_z\\ -\alpha B_z+B_rB_\theta & \alpha^2+B_\theta^2 & \alpha B_r+B_\theta B_z\\ +\alpha B_\theta+B_rB_z & -\alpha B_r+B_\theta B_z & \alpha^2+B_z^2\end{pmatrix}$$

$$\alpha = \frac{(i\omega + \nu_m)}{q/m_e} \tag{2.2}$$

$$\sigma_0 = \frac{q_e^2 n_e}{m_e} \frac{1}{\nu_m + i\omega}$$

where B is the static applied magnetic field, q_e is the unit electron charge, n_e represents electron density, m_e denotes electron mass, ν_m is the electron momentum transfer collision.

The leading divergence term in Eq. (2.1) can be included by using a perturbation form of Poisson's equation. For a quasineutral plasma, neglecting ion mobility over the rf cycle, the divergence of the electric field is equal to the perturbation in the electron density from neutrality, defined as,

$$\nabla \cdot \vec{E} = \frac{\rho}{\varepsilon} = \frac{\sum_i q n_i}{\varepsilon} = \frac{q_+ N_+ + q_- N_- + q_e n_e + q_e \Delta n_e}{\varepsilon} = \frac{q_e \Delta n_e}{\varepsilon} \tag{2.3}$$

where ρ, n_i, N_+, N_-, Δn_e are the charge density, density of the i^{th} charge species, total positive ion density, total negative ion density and perturbation to the electron density, respectively. On the time scale of the electromagnetic period, the total electron density, $n_e(t)$, is the sum of the steady state electron density n_e, and the perturbed electron density $\Delta n_e \exp(i\omega t)$,

$$\frac{\partial n_e(t)}{\partial t} = \frac{\partial}{\partial t}\left[n_e + \Delta n_e \exp(i\omega t)\right] = i\omega \Delta n_e \exp(i\omega t) \tag{2.4}$$

The magnitude of the perturbed electron density is obtained by solving the continuity equation for the electron density, with an appropriate damping term,

$$\Delta n_e = \frac{-\nabla \cdot \left(\frac{\bar{\bar{\sigma}} \cdot \vec{E}}{q} \right)}{\left(\frac{1}{\tau} + i\omega \right)} \tag{2.5}$$

The damping factor τ takes into account the average time it takes a perturbed electron to return to the steady state.

The static magnetic fields are solved in cylindrical geometry in the the radial and axial directions assuming azimuthal symmetry. Under these conditions, the magnetic field can be represented as a vector potential which has only a single component in the azimuthal direction. The current loops, which provide source terms when solving for vector potential $\vec{A}$, by differentiation, yields the static magnetic fields

$$\begin{aligned} &\nabla \times \vec{A} = \vec{B}; \\ &\nabla \times \frac{1}{\mu} \nabla \times \vec{A} = \vec{J} \end{aligned} \tag{2.6}$$

where μ is the permeability, and $\vec{J}$ is the current density of the source current loops. The vector potential is solved as a boundary value problem using successive-over-relaxation (SOR), with the same convergence criteria as the electric field.[14]

2.3 The Electron Energy Transport Module

In the Electron Energy Transport Module, the power deposition into the electrons, as well as the electron impact sources, are modeled and the electron transport properties are computed. These can be solved in two different ways. The first method is to solve the 2d electron energy equation. Electron transport properties as a function of temperature are obtained by solving the 0d Boltzmann equation. The second method is to utilize a Monte Carlo simulation, in which electron pseudo-particles are moved in the computed fields and have collisions with other plasma species. The trajectories are integrated over a period of time and the statistics are collected to generate the electron energy distribution functions (EEDs), which are then used to calculate the rate coefficients.

2.3.1 The Electron Energy Equation Method

When solving the electron energy equation the 0d Boltzmann equation is solved for a range of values of electric field divided by total gas density (E/N) in order to create a lookup table correlating average energy with a transport coefficient. The Boltzmann equation is expressed as

$$\frac{\partial f_e}{\partial t} + \mathbf{v} \cdot \nabla_{\mathbf{r}} f_e - \frac{e(\vec{E} + \vec{v} \times \vec{B})}{m_e} \cdot \nabla_{\mathbf{v}} f_e = \left(\frac{\delta f_e}{\delta t} \right)_{collision} \tag{2.7}$$

where $f_e = f_e(t, \boldsymbol{r}, \boldsymbol{v})$ is the electron distribution function, ∇_r is the spatial gradient, $\nabla_{\mathbf{v}}$ is the velocity gradient, m_e is the electron mass, and $\left(\frac{\delta f_e}{\delta t} \right)_{collision}$ represents the effect of collisions. The solution of Eq. (2.7) is obtained using a two-term spherical harmonic expansion approximation.[15] The resulting values are then used as a lookup table, which yields electron

mobility, thermal conductivity, and energy-loss rate due to collisions and electron impact rate coefficients as a function of electron temperature. T_e is defined as $\frac{2}{3}<\varepsilon>$, where $<\varepsilon>$ is the average energy computed from the EEDs.

With the EEDs known as a function of temperature, the electron energy equation is solved as follows

$$\frac{\partial\left(\frac{3}{2}n_e kT_e(\vec{r})\right)}{\partial t} = P(\vec{r}) - L(T_e) - \nabla\cdot\left(\frac{5}{2}\vec{\phi}_e kT_e - \overline{\overline{\kappa}}(T_e)\cdot\nabla T_e\right) + P_{EB}(\vec{r}) \qquad (2.8)$$

where $\overline{\overline{\kappa}}$ is the tensor thermal conductivity, T_e is the electron temperature, $\vec{\phi}_e$ is the electron flux provided by the Fluid Kinetics Module, P is the electron heating due to deposition, and P_{EB} is the power transferred from slowing beam electrons (and their progeny) to bulk distribution, and L is the power loss due to collisions. The electron heating is given by collisional Joule heating $P(\vec{r}) = q_e\vec{\phi}_e\cdot\vec{E}$ and so ignores the stochastic component. The Eq. (2.8) is discritized using the central-differencing scheme and solved by the method of SOR.[14]

2.3.2 The Electron Monte Carlo Method

The second method for determining electron transport properties is the Electron Monte Carlo Simulation (EMCS). The EMCS simulates electron trajectories according to local electric and magnetic fields and collision processes. Initially, the electrons are given a Maxwellian

distribution and randomly distributed in the reactor weighted by the current electron density. Particle trajectories are computed using the Lorentz equation,

$$\frac{d\vec{v}}{dt} = \frac{q_e}{m_e}(\vec{E} + \vec{v} \times \vec{B}) \tag{2.9}$$

and

$$\frac{d\vec{r}}{dt} = \vec{v} \tag{2.10}$$

where $\vec{v}$, $\vec{E}$ and $\vec{B}$ are the electron velocity, local electric field, and magnetic field respectively. Eq. (2.9) and (2.10) are updated using a second-order predictor corrector scheme. Electric fields are both the inductive fields computed in the EMM and the time-dependent electrostatic fields computed in the FKM. Time steps are chosen to be less than both 1% of the rf period and 1% of the cyclotron frequency, and small enough that the particles do not cross more than one-half computational cell in one time step. Several hundred to a few thousand particles are integrated in time for many rf cycles, typically greater than 100 rf cycles.

The Monte Carlo method is a fully kinetic treatment, which resolves the transport of electrons in electric and magnetic fields using a semi-implicit technique. Noncollisional heating can be kinetically resolved by producing electron currents, which are used to correct the assumption of collisional power deposition in the EMM.

The electron energy range is divided into discritized energy bins for collision determination and this binning also helps in collecting statistics. The collision frequency, ν_i, within any energy bin is computed by summing all possible collision within the energy range

$$\nu_i = \left(\frac{2\varepsilon_i}{m_e}\right)^{\frac{1}{2}} \sum_{j,k} \sigma_{ijk} N_j \tag{2.11}$$

where ε_i is the average energy within the bin, σ_{ijk} is the cross section at energy *i,* for species *j* and collision process *k*, and N_j is the number density of species *j*. The time between the collisions is randomly determined using the maximum collision frequency for all energy bins, $\Delta t = -\frac{1}{\upsilon}\ln(r)$, r = (0,1). At the time of a collision, the reaction that occurs is chosen randomly from all the possible reactions for that energy bin. A null collision cross section makes up the difference between the actual collision frequency and the maximum collision frequency at any given spatial location. The velocity of the electrons is adjusted based on the type of collision it undergoes. If the collision is null then the electron's trajectory is unaltered.

The statistics for computing the electron energy distributions are updated every time an electron is moved in the mesh, that is, at every time step using finite particle techniques. These statistics are collected into an array for energy *i* and location *l*.

$$F_{il} = \sum_j w_j \delta[(\varepsilon_i \pm \frac{1}{2}\Delta\varepsilon_i) - \varepsilon_j]\delta[(\vec{r}_l \pm \Delta\vec{r}) - \vec{r}_j] \tag{2.12}$$

where the summation is over particles, w_j is the weighting of the particle, ε_i is the energy and r_k is the bin location. The weighting w_j is a product of three factors; the relative number of electrons each pseudo-particle represents, the time step used to advance the trajectory, and a spatial weighting obtained using the method of finite-sized particles (FSP). At the end of the EMCS, the electron temperature, collision frequency and electron-impact rate coefficients are computed as a function of position from the EEDs. The EEDs, f_{ik}, are obtained from the raw statistics, F_{ik}, by requiring normalization of each spatial location.

$$\sum_i F_{ik}\Delta\varepsilon_i = \sum_i f_{ik}\varepsilon_i^{\frac{1}{2}}\Delta\varepsilon_i = 1 \tag{2.13}$$

The electron temperature is defined by convention to be $\frac{2}{3}<\varepsilon>$. The electron impact rate coefficient (k_m) for electron impact process *m* and location *l* is computed as

$$k_{ml} = \int_0^\infty \left(\frac{2\varepsilon}{m_e}\right)^{\frac{1}{2}} \sigma_m(\varepsilon) f_l(\varepsilon)\varepsilon^{\frac{1}{2}}\, d\varepsilon = \sum_i \left(\frac{2\varepsilon_i}{m_e}\right)^{\frac{1}{2}} \sigma_{mi} f_{il}(\varepsilon)\varepsilon_i^{\frac{1}{2}}\Delta\varepsilon \tag{2.14}$$

2.4 The Fluid Kinetics Module

In the FKM, the continuum transport equations for the gas species are solved simultaneously with the electromagnetic fields to determine the spatial distribution of species densities as well as the momentum flux fields within the reactor. The equations solved for neutral and ion transport (continuity, momentum and energy) are

$$\frac{\partial N_i}{\partial t} = -\nabla \cdot \vec{\phi}_i + S_i - \left[\sum_j \gamma_{ij} (\nabla \cdot \vec{\phi}_j) \right]_S \tag{2.15}$$

$$\begin{aligned} \frac{\partial \phi_i}{\partial t} = \frac{\partial (N_i \vec{v}_i)}{\partial t} = & -\frac{1}{m_i} \nabla (k N_i T_i) - \nabla \cdot (N_i \vec{v}_i \vec{v}_i) + \frac{q_i N_i}{m_i} (\vec{E} + \vec{v}_i \times \vec{B}) \\ & - \nabla \cdot \overline{\overline{\mu}}_i - \sum_j \frac{m_j}{m_i + m_j} N_i N_j (\vec{v}_i - \vec{v}_j) \nu_{ij} + S_{mi} \end{aligned} \tag{2.16}$$

$$\begin{aligned} \frac{\partial N_i \varepsilon_i}{\partial t} = & -\nabla \cdot \overline{\overline{\kappa}} \nabla T_i - P_i \nabla \cdot \vec{v}_i - \nabla \cdot (N_i \vec{v}_i \varepsilon_i) + q_i \vec{\phi}_i \vec{E} \\ & - (\overline{\overline{\mu}}_i \nabla \cdot \nabla \vec{v}_i) - \sum_{m,j} k_{mij} N_i N_j \varepsilon_i + \sum_{m,j,l} k_{mjl} N_j N_l \Delta \varepsilon_{mjl} \end{aligned} \tag{2.17}$$

where $\vec{\phi}_i$ is the flux of species *i* having density N_i, velocity $\vec{v}_i$, mass m_i, temperature T_i, viscosity $\overline{\overline{\mu}}_i$, pressure P_i, and total energy ε_i. S_i is the source for species *i* due to gas phase collision processes, ν_{ij} is the momentum transfer collision frequency between species *i* and *j*, and $\overline{\overline{\kappa}}$ is the thermal conductivity which, in the case of charged species, has tensor form as discussed before.

In Eq. (2.15), the last term accounts for the consumption and production of species on surfaces, where γ_{ij} is the coefficient for production of species *i* by reactions of species *j* on a surface. Computationally, we assume all species are consumed with unity probability on surfaces, implemented in the first term of Eq. (2.15) by having a zero density on the surface. If a species is unreactive, it is ‘‘replaced’’ at the boundary by specifying a flux returning to the plasma having the same magnitude as incident onto the surface. For example, $\gamma_{ij} = 1.0$ for species having a zero reactive sticking coefficient. S_i contains contributions from electron impact reactions resulting from secondary electrons as obtained from the EMCS. In the case of

electrons, this contribution also includes the slowing of beam electrons into the bulk distribution and so represents the injected negative charge from secondary emission.

In Eq. (2.16), S_{mi} is the rate of generation and loss of momentum for species i resulting from collisions which change the identity of the reactant. These are collisions other than elastic momentum transfer collisions which are accounted for by the term containing ν_{ij}. For example, a process progressing at rate r (1/s) which produces species i from species j (as in a charge exchange) has $S_{mi} = rN_j v_j$. Effects such as cataphoresis are captured by the term for momentum transfer between ions and neutrals. Since viscous forces are negligible for ions for our conditions, that term is not included for charged species when solving Eq. (2.16).

A separate total energy for each species is tracked based on the solution of Eq. (2.17). Here, the definition of total energy is the sum of directed and random translational energy. As such, power transfer by thermal conductivity, compressive heating, advective transport, Joule heating, and viscous dissipative heating is included for each species on an individual basis. The method for accounting for the change in enthalpy is somewhat non-conventional, and is accounted for by the last two terms of Eq. (2.17). All reactions m of species i with species j having rate coefficient k_{mij} which results in removal of species i produces a loss of total energy for species i of ε_i per event. All reactions m between species j and l which produce species i, including elastic collisions, provides for a unique contribution to the total energy of $\Delta\varepsilon_{mjl}$ per event. For example, the electron impact reaction e + Ar → Ar^+ + e + e makes a contribution of only $\varepsilon(Ar^+)$, that is the translational energy of Ar^+ and not the total change in enthalpy difference between Ar and Ar^+ because the energy of each species is separately tracked. For reactions such as e + O_2 → O + O + e, the translational and Frank–Condon heating contributions

are both included. Heavy particle chemical reactions would include the appropriate exothermicities.

Various options can be used to compute electron fluxes. The first method is using the conventional drift-diffusion approximation and electron fluxes are given by

$$\vec{\phi}_e = q_e n_e \overline{\overline{\mu}}_e \cdot \vec{E} - \overline{\overline{D}}_e \cdot \nabla n_e , \tag{2.18}$$

where n_e is density of electrons moving in the electric field $\vec{E}$ and having tensor mobility $\overline{\overline{\mu}}_e$, tensor diffusivity $\overline{\overline{D}}_e$, and charge q_e. In the presence of static magnetic field, the transport coefficients (mobility and diffusivity) for electron (or ion) transport are of tensor forms $\overline{\overline{A}}$. Tensor forms of transport coefficients, $\overline{\overline{A}}$, are derived from their isotropic values, A_0, by

$$\overline{\overline{A}} = \frac{A_0}{(\alpha^2 + |B|^2)} \times \begin{pmatrix} \alpha^2 B_r^2 & \alpha B_z + B_r B_\theta & -\alpha B_\theta + B_r B_z \\ -\alpha B_z + B_r B_\theta & \alpha^2 + B_\theta^2 & \alpha B_r + B_\theta B_z \\ -\alpha B_\theta + B_r B_z & -\alpha B_r + B_\theta B_z & \alpha^2 + B_z^2 \end{pmatrix} \tag{2.19}$$

where $\alpha = \nu_m m_e / q$.

Alternatively, the electron flux can be computed by the Scharfetter-Gummel discritization.[16] In this method the flux $\vec{\varphi}_{i+\frac{1}{2}}$ between density mesh points (i, i+1) separated by Δx is given by

$$\vec{\varphi}_{i+\frac{1}{2}} = \frac{\alpha \overline{D}(n_{i+1} - n_i \exp(\alpha \Delta x))}{1 - \exp(\alpha \Delta x)} \tag{2.20}$$

where

$$\alpha = -q\overline{\mu}\left(\frac{\Phi_{i+1} - \Phi_i}{\Delta x}\right) \tag{2.21}$$

and $\overline{D}$ and $\overline{\mu}$ are the average diffusion coefficient and mobility in the interval.

The time rate of change in charge density ρ_m on surfaces and in materials is given by

$$\frac{\partial \rho_m}{\partial t} = \left[-\sum_i q_i (\nabla \cdot \vec{\phi}_i(t)) - \sum_{i,j} q_j (\nabla \cdot \vec{\phi}_i(t)\gamma_{ij}) \right]_S + \left[\nabla \cdot \sigma \nabla \Phi\right]_m \tag{2.22}$$

where Φ is the electric potential, σ is the conductivity of a nonplasma material, and γ_{ij} is the secondary emission coefficient for species *j* by species *i*. The first term applies to only locations on surfaces in contact with the plasma while the second term applies to points in and on nonplasma materials.

$$\begin{aligned} \nabla \cdot (\varepsilon \nabla \Phi(t + \Delta t)) = -\Bigg\{ \rho_m(t) + \sum_i q_i N_i + \Delta t \cdot \Bigg[\frac{\partial \rho_m(t')}{\partial t} - q_e \nabla \cdot \vec{\phi}_e(t') \\ - \sum_j q_j \nabla \cdot \left(\vec{\phi}_j(t) + \frac{\Delta t}{2} \frac{\partial \phi_j(t)}{\partial t} \right) \Bigg] \Bigg\} \end{aligned} \tag{2.23}$$

where ε is the local permittivity. The terms in Eq. (2.23) are for the accumulation of charge on surfaces and in the bulk plasma at the present time, and prediction of such charges at the future

time. ρ_m and N_i are evaluated at t, while t' denotes that densities are evaluated at t and potentials are evaluated at $t + \Delta t$, thereby providing implicitness. The implicitness of the solution is largely achieved through the dependence of the electron flux on the electric potential. The sum over j includes only ions. The flux of ions, on any given solution of Eq. (2.23), was given by the solution of Eq. (2.16) from the previous time step and was held constant during solution of Eq. (2.23). The second term in Taylor's expansion for the ion density was included by numerically deriving the time rate of change of the ion flux.

When the Scharfetter-Gummel discritization for electron fluxes is employed, the electron flux is not a linear function of electric field and cannot be directly discritized. As such, the implicitness is achieved by numerically deriving Jacobian elements. The form of Eq. (2.23) is then

$$\begin{aligned}\nabla\cdot(\varepsilon\nabla\Phi(t+\Delta t)) = -\Bigg\{\rho_m(t) + \sum_i q_i N_i + \Delta t\cdot\Bigg[\frac{\partial\rho_m(t')}{\partial t} \\ - q_e\nabla\cdot\left(\vec{\phi}_e(t) + \frac{\partial\vec{\phi}_e}{\partial\Phi}[\Phi(t+\Delta t)-\Phi(t)]\right) \\ - \sum_j q_j\nabla\cdot\left(\vec{\phi}_j(t) + \frac{\Delta t}{2}\frac{\partial\phi_j(t)}{\partial t}\right)\Bigg]\Bigg\}\end{aligned} \tag{2.24}$$

where Jacobian elements $\frac{\partial\vec{\phi}_e}{\partial\Phi}$ are the first-order partial derivatives of the function $\vec{\phi}_e$ with respect to Φ. Here, Jacobian elements are numerically evaluated by perturbing Φ a small fraction value and computing the change in $\vec{\phi}_e$. For example, the radial electron flux ($\phi_{r\,i,\,j}$) at

location *(i, j)* are function of potentials at adjacent vertices, $\Phi_{i,j}$ and $\Phi_{i+1,j}$. Hence two Jacobian elements are related to $\phi_{r\,i,j}$

$$\frac{\partial \phi_{r\,i,j}}{\partial \Phi_{i,j}} = \frac{\phi_{r\,i,j}(\Phi_{i,j} + \Delta\Phi_{i,j}) - \phi_{r\,i,j}(\Phi_{i,j})}{\Delta\Phi_{i,j}}$$
$$\frac{\partial \phi_{r\,i,j}}{\partial \Phi_{i+1,j}} = \frac{\phi_{r\,i,j}(\Phi_{i+1,j} + \Delta\Phi_{i+1,j}) - \phi_{r\,i,j}(\Phi_{i+1,j})}{\Delta\Phi_{i+1,j}} \qquad (2.25)$$

where $\Delta\Phi_{i,j}$ and $\Delta\Phi_{i+1,j}$ are predefined perturbations. A typical perturbation is 5% of the current value, $\Delta\Phi_{i,j} = 0.05 \times \Phi_{i,j}$.

The incomplete LU biconjugate gradient sparse matrix technique or SOR is used to solve Eq. (2.23) or Eq. (2.24).

2.5 The Fully Implicit Electron Drift-Diffusion Transport Algorithm

The time step in the FKM is fundamentally limited by integrating the electron continuity equation with Poisson's equation. Before the development of the fully implicit electron drift-diffusion transport, the HPEM addresses the electron continuity equation and Poisson's equation in a semi-implicit way, as discussed in Sec 2.3. Compared to the explicit algorithm, the time step in the semi-implicit algorithm is not limited by the dielectric relaxation time (ε_0 / n_e), which could be as small as 10^{-12} s. However, the time step in the semi-implicit algorithm is limited by the Courant limit ($\Delta x / v$, where Δx is the mesh spacing and v is the speed of electrons). To overcome the Courant limit, the fully implicit electron transport algorithm needs to be employed. That is, fully implicitly and simultaneously solving the electron continuity equation and

Poisson's equation in the same matrix. This method is most computationally challenging but it provides the closest coupling between the potential and the electron density.

If we use the drift-diffusion approximation for electron fluxes, the equations to be solved are

$$\begin{cases} -\nabla\cdot(\varepsilon\nabla\Phi^{t+\Delta t}) = \sum_i q_i N_i^t - q_i\Delta t\left[\nabla\cdot\left(\bar{\phi}_i(t) + \dfrac{\Delta t}{2}\dfrac{\partial\phi_i(t)}{\partial t}\right)\right] + q_e n_e^{t+\Delta t} \\ \dfrac{\partial n_e}{\partial t} = \dfrac{n_e^{t+\Delta t} - n_e^t}{\Delta t} = -\nabla\cdot\left(-\overline{\overline{D}}_e\nabla n_e^{t+\Delta t} - q_e\overline{\overline{\mu}}_e\nabla\Phi^{t+\Delta t}\right) + S_e \end{cases} \tag{2.26}$$

where $\Phi^{t+\Delta t}$ and $n_e^{t+\Delta t}$ are the potential and electron density evaluated at $t+\Delta t$. The sum over *i* includes only ions. The flux of ions, on any given solution of Eqs. (2.26), was given by the solution of Eq. (2.16) from the previous time step and was held constant during solution of Eq. (2.26). The second term in Taylor's expansion for the ion density was included by numerically deriving the time rate of change of the ion flux. The diffusion constant and mobility of electrons, denoted by $\overline{\overline{D}}_e$ and $\overline{\overline{\mu}}_e$ respectively, are of tensor forms. S_e is the total ionization source including the contributions from secondary electrons. After normalization, Eqs. (2.26) are solved using sparse matrix techniques.

When the Scharfetter-Gummel discritization for electron fluxes is employed, the implicitness of electron fluxes upon the electron density and potential is achieved through the numerically derived Jacobian elements.

This fully implicit electron drift-diffusion algorithm has been incorporated into the HPEM. This improves the capability of the HPEM to address plasma tools operating under

harsh conditions. In addition to more accurate physics, in the proper parameter space, the use of the fully implicit electron transport enables a larger time step to be used. This enables the code to execute significantly faster.

2.6 The Full-wave Maxwell Solver

An advanced feature of RIE plasma tools currently under development and deployment is the use of very high frequency power sources (> 100 MHz). The goal of this strategy is to better control the resulting electron energy distributions in the plasma and so better control the cracking patterns of the feedstock gases by electron impact. This will produce finer control over the reactant fluxes to the substrate. As the plasma reduced wavelength of the rf power applied to the reactor approaches the size of the reactor, finite wavelength effects become increasingly more important. This in turn becomes increasingly more challenging for modeling due to the need for including a full solution of the electromagnetic Maxwell's equations, as opposed to only the electrostatic Poisson's equation. These approaches should simultaneously resolve capacitive and inductive coupling.

As an improvement to the previously described model, a solution of Maxwell's equations is integrated into the plasma hydrodynamics modules of the HPEM. This enables the simulation of the inductive effects that result from wave penetration at high frequency into plasmas and finite wavelength effects, in addition to the electrostatic effects generally accounted for when solving Poisson's equation. This solution was implemented in the time domain so that coupling between frequencies could be explicitly addressed as well as enabling intra-rf period feedback between plasma transport and the wave.

A full-wave Maxwell solver is computationally challenging due to the coupling between

electromagnetic (EM) and electrostatic (ES) fields, the latter of which is responsible for the formation of the sheath. In principle, these fields are from different sources. EM fields are generated by waves launched into the reactor from the cable attached to the power supply which for all practical purposes acts as an antenna. ES fields are produced by charges. As such, we separately solved for the EM and ES fields and summed the fields for plasma transport. In doing so, self-consistent boundary conditions can be defined (discussed later) with the capability of addressing multiple rf sources in the time domain.

2.6.1 Electromagnetic Solution ($\vec{E}_M$)

We implemented the EM solution in a cylindrical geometry though the method is more general. We assumed that rf power is fed into a DF-CCP reactor by coaxial cables which can be at arbitrary locations. In our geometry, the wave propagates in the coaxial cables in a TEM mode, which only has components of E_r (radial electric field) when the cable is connected to horizontal surfaces, E_z (axial electric field) when the cable is connected to vertical surfaces, and B_θ (azimuthal magnetic field). As such, azimuthally symmetric TM modes are excited in the reactor.[17] So in 2-dimensional cylindrical coordinates, Faraday's law and Ampere's law can be written as

$$\frac{\partial E_r}{\partial z} - \frac{\partial E_z}{\partial r} = -\frac{\partial B_\theta}{\partial t} \tag{2.27}$$

$$-\frac{\partial B_\theta}{\partial z} = \mu J_r + \varepsilon\mu \frac{\partial E_r}{\partial t} \tag{2.28}$$

$$\frac{1}{r}\frac{\partial (rB_\theta)}{\partial r} = \mu J_z + \varepsilon\mu \frac{\partial E_z}{\partial t} \tag{2.29}$$

where J_r and J_z are the radial and axial components of the conduction current, μ is the permeability, and ε is the permittivity. Eqs. (2.27-2.29) are discritized on a staggered mesh and solved using the Finite Difference Time Domain (FDTD) techniques.[17-19] Eqs. (2.27-2.29) cab be discritized as

$$\frac{1}{\Delta z}\left(\frac{E_{ri,j+1}^{t}+E_{ri,j+1}^{t+\Delta t}}{2}-\frac{E_{ri,j}^{t}+E_{ri,j}^{t+\Delta t}}{2}\right) - \frac{1}{\Delta r}\left(\frac{E_{zi+1,j}^{t}+E_{zi+1,j}^{t+\Delta t}}{2}-\frac{E_{zi+1,j}^{t}+E_{zi+1,j}^{t+\Delta t}}{2}\right)=-\frac{B_{\theta i,j}^{t+\Delta t}-B_{\theta i,j}^{t}}{\Delta t} \tag{2.30}$$

$$-\frac{1}{\Delta z}\left(\frac{B_{\theta i,j+1}^{t}+B_{\theta i,j+1}^{t+\Delta t}}{2}-\frac{B_{\theta i,j}^{t}+B_{\theta i,j}^{t+\Delta t}}{2}\right)= (\mu_0\cdot\frac{\mu_{ri,j}+\mu_{ri,j-1}}{2})\cdot\left[\sum_k q_k(J_{ri,j}^{t}+\frac{\Delta t}{2}\frac{\partial J(t)}{\partial t})_k+\frac{1}{2}(J_{ri,j}^{t}+J_{ri,j}^{t+\Delta t})_e\right] + (\mu_0\cdot\frac{\mu_{ri,j}+\mu_{ri,j-1}}{2})\cdot(\varepsilon_0\cdot\frac{\varepsilon_{ri,j}+\varepsilon_{ri,j-1}}{2})\cdot\frac{E_{ri,j}^{t+\Delta t}-E_{ri,j}^{t}}{\Delta t} \tag{2.31}$$

$$\frac{1}{\Delta r\cdot r_{i,j}}\left(r_{i+1,j}\cdot\frac{B_{\theta i+1,j}^{t}+B_{\theta i+1,j}^{t+\Delta t}}{2}-r_{i,j}\cdot\frac{B_{\theta i,j}^{t}+B_{\theta i,j}^{t+\Delta t}}{2}\right)= (\mu_0\cdot\frac{\mu_{ri,j}+\mu_{ri-1,j}}{2})\cdot\left[\sum_k q_k(J_{zi,j}^{t}+\frac{\Delta t}{2}\frac{\partial J(t)}{\partial t})_k+\frac{1}{2}(J_{zi,j}^{t}+J_{zi,j}^{t+\Delta t})_e\right] + (\mu_0\cdot\frac{\mu_{ri,j}+\mu_{ri-1,j}}{2})\cdot(\varepsilon_0\cdot\frac{\varepsilon_{ri,j}+\varepsilon_{ri-1,j}}{2})\cdot\frac{E_{zi,j}^{t+\Delta t}-E_{zi,j}^{t}}{\Delta t} \tag{2.32}$$

where Δr and Δz are the mesh spacings in the r and z directions, and Δt is the integration time step. $r_{i,j}$ is the radius at the center of the mesh cell (i,j). The superscript '$t+\Delta t$' denotes the quantities (to be solved) evaluated at the future time $t+\Delta t$ and the superscript 't' denotes the quantities (known) evaluated at the current time t. ε_0 and μ_0 are the vacuum permittivity and

vacuum permeability, respectively. ε_r and μ_r are the local dielectric constant and relative permeability, respectively. The sum over *k* includes only ions. The ion and electron currents [J_k and J_e in the Eqs. (2.31-2.32)] are evaluated at the sides of mesh cells, which could be boundaries between different materials. Hence we average the properties of materials such as dielectric constant and relative permeability between adjacent mesh cells. The spatial locations of E_r, E_z and B_θ are chosen to provide central spatial differencing, as shown in Fig. 2.1. B_θ is computed at the centers of mesh cells while electric fields are calculated at locations shifted by half a mesh cell in the radial direction for E_z (axial direction for E_r). The electrostatic potential and plasma densities are computed at the vertices of the mesh cells. Radial and axial fluxes of all species are computed at the locations of E_r and E_z, respectively. To avoid a singularity at r = 0 in cylindrical coordinates, Eq. (2.29) is solved using the integral form at r = 0.

The rf field is launched into the DF-CCP reactor where the power cable is connected. Thus, the wave is generated by a source electric field

$$E(t) = V(t)/d \tag{2.33}$$

which is used as a boundary condition (BC) in our model. *V(t)* is the time dependent voltage drop between the center conductor and the ground shield of the cable connected to the reactor, and *d* is the spacing between them. For BCs on a metal surface, the tangential component of the electric field is zero. A first order Mur's absorbing BC is applied at pump ports or dielectric windows to represent open boundaries.[20]

If we explicitly solve Eqs. (2.27-2.29), the time step is limited by the Courant condition. To allow for larger time steps, the unconditionally stable Crank-Nicholson scheme was

employed [Eqs. (2.30-2.32)].[21] The current terms in Eqs. (2.28) and (2.29) contain two contributions - current of electrons and of ions, which are products of (electron or ion) flux and charge. The electron flux is computed using a drift-diffusion approximation which contains the term $\sigma\vec{E}$, where σ is the electron conductivity. Implicitness is therefore achieved by the dependence of the electron flux on the electric field through this term. Ion fluxes are given by the solution of their respective ion momentum equations from the previous time step and were held constant during the solution of Eqs. (2.27-2.29). Since the time steps are typically small fractions of the rf cycle (for example, 0.005 for a frequency of 150 MHz) there is little change in ion fluxes during a single time step.

We found that large gradients in plasma conductivity from the sheath to the bulk plasma produce large mesh point to mesh point changes in electric fields. These changes tend to cause numerical instabilities and artificial resonances. In principle this can be addressed by using a finer mesh for the entire calculation. We found, however, that only the mesh upon which the fields quantities are solved needed to be finer. So to make the task less computationally expensive, mesh used for plasma properties was sub-divided when solving Eqs. (2.27-2.29). Before sub-dividing, our typical numerical mesh spacing was 0.1 cm in the axial direction and 0.3 cm in the radial direction. Subdividing the cells in the axial direction by a factor of 2 is enough to prevent numerical instabilities. Eqs. (2.27-2.29) are solved on the subdivided mesh using sparse matrix techniques. Fields are then interpolated back to the original mesh for use in transport equations and other modules.

2.6.2 Electrostatic Solution ($\vec{E}_S$)

The Poisson's equation is solved using the semi-implicit technique described before. The

potentials are evaluated at a future time while densities of charged particles are evaluated at the present time. The semi-implicitness is achieved through the prediction of the accumulated charges on surfaces and in the bulk plasma at the future time by numerically evaluating Jacobian elements (perturbing the potentials by a small fraction and computing the change in electron fluxes). Ion fluxes are given by the solution of their ion momentum equations from the previous time step and were held constant during the solution of the Poisson's solution. Note that boundary conditions (BCs) for solution of $\vec{E}_S$ on the powered electrode are not the applied rf voltages as they have already been accounted for in the EM solution. Here, the BCs on the powered electrodes are either the self-developed *dc* bias or any applied *dc* voltages.

The EM and ES solutions are then summed to provide the electric field for plasma transport, $\vec{E} = \vec{E}_M + \vec{E}_S$. Since the model is written in a modular fashion, the remainder of the code is unaffected by other than substituting this value for the electric field wherever they appear in transport equations for charged particles.

2.7 The Fully Implicit Electron Momentum Transport Algorithm

Drift-diffusion approximation for electron fluxes assumes that the electron swarm is in the quasi-equilibrium state with the local electric field,

$$\frac{d\vec{E}}{dt} << \frac{d\vec{V}_d}{dt} \tag{2.34}$$

where $\vec{V}_d$ is the electron drift velocity.

In state-of-the-art DF-CCP tools, excitation frequencies can be on the order of hundreds of MHz and Eq. (2.34) is no longer a good approximation for electron transport. Electron inertia needs to be accounted. This necessitates the solving of the electron momentum equation,

$$\frac{\partial \vec{\phi}_e}{\partial t} = \frac{\partial (n_e \vec{v}_e)}{\partial t} = \frac{1}{m_e}\nabla(kn_eT_e) - \nabla\cdot(n_e\vec{v}_e\vec{v}_e) + \frac{q_e n_e}{m_e}(\vec{E} + \vec{v}_e \times \vec{B}) \\ -\nabla\cdot\bar{\bar{\mu}}_e - \sum_j \frac{m_j}{m_e + m_j} n_e N_j (\vec{v}_e - \vec{v}_j)\nu_{ej} + S_{me} \tag{2.35}$$

where ϕ_e is the flux of electrons having velocity v_e , mass m_e , temperature T_e, viscosity $\bar{\bar{\mu}}_e$. k is the Boltzmann constant. $\vec{B}$ is the magnetic field (electromagnetic or static) and S_{me} is the source due to gas phase collision processes. υ_{ej} is the momentum transfer collision frequency between electrons and species j having density N_j and mass m_j .

As in the Maxwell Solver, the electromagnetic and electrostatic fields are solved separately. We solve the electron momentum equation and continuity equation together with Poisson's equation and other Maxwell's equations in a time-slicing fashion. First, Eqs. (2.27-2.29) are solved to obtain the electromagnetic fields. Then, the electron momentum equation and continuity equation are solved fully implicitly with Poisson's equation. The matrix of the equations to be solved in this step is:

$$
\begin{cases}
\dfrac{\vec{\phi}_e^{\,t+\Delta t}-\vec{\phi}_e^{\,t}}{\Delta t}=\dfrac{1}{m_e}\nabla\left(kN_e^{t+\Delta t}T_e^t\right)-\nabla\cdot\left[(\phi\vec{v})^t+\dfrac{\partial(\phi\vec{v})}{\partial\phi}(\phi^{t+\Delta t}-\phi^t)+\dfrac{\partial(\phi\vec{v})}{\partial n_e}(n_e^{t+\Delta t}-n_e^t)\right] \\
\quad+\dfrac{q_e}{m_e}\left(n_e^{t+\Delta t}\vec{E}_M^{t+\Delta t}-n_e^t\nabla\Phi^{t+\Delta t}-n_e^{t+\Delta t}\nabla\Phi^t+n_e^t\nabla\Phi^t+\vec{\phi}_e^{\,t+\Delta t}\times\vec{B}\right) \\
\quad-\sum_j\dfrac{m_j}{m_e+m_j}n_e^tN_j^t\left(\vec{v}_e^{\,t}-\vec{v}_j^{\,t}\right)\nu_{ej}^t+S_{me} \\
\dfrac{n_e^{t+\Delta t}-n_e}{\Delta t}=-\nabla\cdot\vec{\phi}_e^{\,t+\Delta t}+S_e \\
\nabla\cdot(\varepsilon\nabla\Phi^{t+\Delta t})=\sum_i\left\{q_iN_i(t)+q_i\Delta t\left[-\nabla\cdot(\vec{\phi}_i(t)+\dfrac{\Delta t}{2}\dfrac{\partial\phi_i(t)}{\partial t}+S_i(t))\right]\right\}+q_en_e^{t+\Delta t}
\end{cases}
\tag{2.36}
$$

where $\Phi^{t+\Delta t}$, $\vec{\phi}_e^{\,t+\Delta t}$ and $n_e^{t+\Delta t}$ are the potential, electron flux and density evaluated at $t+\Delta t$. $E_M^{t+\Delta t}$ denotes the electromagnetic component of the electric fields (solution of Eqs. (2.27-2.29)). The sum over *i* includes only ions. The flux of ions, on any given solution of Eqs. (2.36), was given by the solution of Eq. (2.16) from the previous time step and was held constant during the solution of Eqs. (2.36). The second term in Taylor's expansion for the ion density was included by numerically deriving the time rate of change of the ion flux. The implicitness of the convection term $\phi\vec{v}$ (the product of flux and velocity) upon electron flux and density is achieved by including numerically derived Jacobian elements. For example, the convection term $\phi\vec{v}$ at the location (*i,j*) at the future time $t+\Delta t$ can be written as

$$
(\phi v)_{i,j}^{t+\Delta t}=(\phi v)_{i,j}^t+\sum_{m,n}\frac{\partial(\phi v)^t}{\partial n_e}(n_{e\,m,n}^{t+\Delta t}-n_{e\,m,n}^t)+\sum_{k,l}\frac{\partial(\phi v)^t}{\partial\phi}(\phi_{k,l}^{t+\Delta t}-\phi_{k,l}^t) \tag{2.37}
$$

where the sum over (*m*,*n*) and (*k*, *l*) include all adjacent electron densities and fluxes, which affect $(\phi v)_{i,j}$.

After normalization, Eqs. (2.36) are solved using sparse matrix techniques.

The capability of addressing the electron momentum transport with only the electrostatic Poisson's equation is also developed for the HPEM. The equations are of similar forms as Eqs. (2.36) (with the absence of the term $\vec{E}_M^{t+\Delta t}$).

2.7 Figures

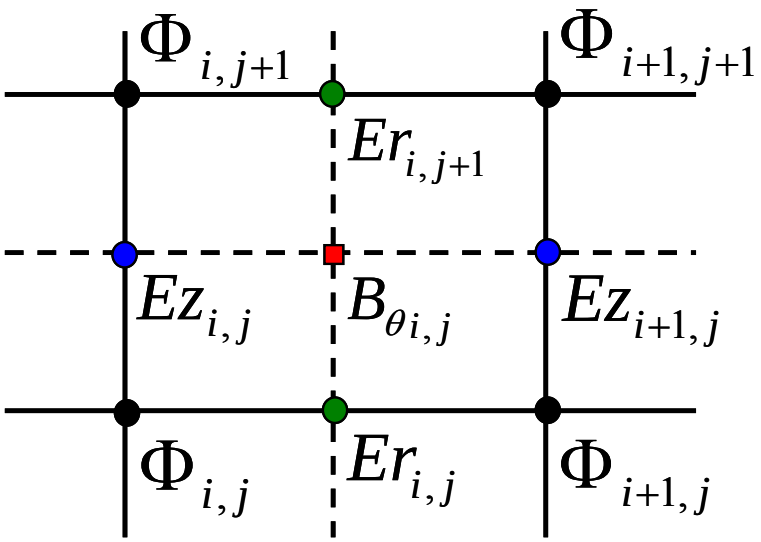

Fig. 2.1 The staggered mesh used for the discritization of Eqs. (2.27-2.29). Φ is the electrostatic potential, E_z the axial electric field and E_r the radial electric field. B_θ is the azimuthal magnetic field and is located at the center of the mesh cell (i, j). Φ is located at the vertices of the mesh cell (i, j).

2.8 References

1. P. L. G. Ventzek, R. J. Hoekstra, M. J. Kushner, J. Vac. Sci. Technol. B **12**, 461 (1994).
2. W. Z. Collison and M. J. Kushner, Appl. Phys. Lett. **68**, 903 (1996).
3. M. J. Kushner, W. Z. Collison, M. J. Grapperhaus, J. P. Holland and M. S. Barnes, J. Appl. Phys. **80**, 1337 (1996).
4. M. J. Grapperhaus and M. J. Kushner, J. Appl. Phys. **81**, 569 (1997).
5. S. Rauf and M. J. Kushner, J. Appl. Phys. **81**, 5966 (1997).
6. R. Kinder and M.J. Kushner, J. Vac. Sci. Technol. *A* **19**, 76 (2001).
7. J. Lu and M. J. Kushner, J. Appl. Phys. **87**, 7198 (2000).
8. D. Zhang, and M. J. Kushner, J. Vac. Sci. Technol. A **18**, 2661 (2000).
9. A. Sankaran and M. J. Kushner, J. Appl. Phys. **92**, 736 (2002).
10. M. J. Kushner, J. Appl. Phys. **94**, 1436 (2003).
11. K. Rajaraman, and M. J. Kushner, J. Phys. D **37**, 1780 (2004).
12. A. Agarwal and M. J. Kushner, J. Vac. Sci. Technol. A **27**, 37 (2009).
13. M. J. Kushner, J. Phys. D **42**, 194013 (2009).
14. W. H. Press, B. P. Flanney, S. A. Teukolsky and W. T. Vetterling, Numerical Recipes: The Art of Scientific Computing, Cambridge University Press, 1987.
15. S. D. Rockwood, Phys. Rev. A **8**, 2348 (1973).
16. D. L. Scharfetter and H. K. Gummel, IEEE Trans. Electronic Devices **ED-16**, 64 (1969).
17. K. S. Yee, IEEE Trans. Ant. Prop. **AP-14**, 302 (1966).
18. J. G. Maloney, G. S. Smith and W. R. Scott, IEEE Trans. Ant. Prop. **38**, 1059 (1990).
19. J. G. Maloney, K. L. Shlager and G. S. Smith, IEEE Trans. Ant. Prop. **42**, 289 (1994).
20. G. Mur, IEEE Trans. Electromag. Comp. **EMC-23**, 377 (1981).

21. Y. Yang, R. S. Chen and K. N. Yung, Microwave Opt. Technol. Lett. **48**, 1619 (2006).

3. MODELING OF MAGNETICALLY ENHANCED CAPACITIVELY COUPLED PALSMA SOURCES: 2 FREQUENCY DISCHARGES

3.1 Introduction

Parallel plate capacitively coupled plasma (CCP) sources are widely used for dry-etching and deposition of materials for microelectronics fabrication. One method of improving the performance of CCP sources is applying a transverse static magnetic field approximately parallel to the electrodes with the goal of increasing the plasma density for a given pressure. In this configuration the devices are often called magnetically enhanced reactive ion etching (MERIE) reactors.[1-4] Meanwhile, multi-frequency CCP sources have also been developed with the goal of separately controlling ion and radical fluxes, and ion energy distributions to the substrate.[5-11] Typically in a 2-frequency CCP reactor, power is applied at a lower radio frequency (rf) to the lower electrode (a few MHz to 10 MHz) holding the wafer; and higher frequency power is applied to the upper electrode (tens of MHz to hundreds of MHz). Power at the lower frequency is intended to control the shape of the ion energy distributions to the wafer. Power at the higher frequency is intended to control the production of ions and radicals. (In some variants, both frequencies are applied to the lower electrode.[12-13]) Thus, it is natural to consider what the unique characteristics are when a reactor combines magnetic enhancement, such as in a MERIE, with multi-frequency excitation.

Recently 2-frequency CCP sources have been the topic of several investigations. Hebner et al. performed diagnostics of 2-frequency CCP reactors operating in argon for frequencies between 10 and 190 MHz.[5] They found that at 50 mTorr, as the 13.56 MHz substrate power was increased from 0-1500 W, the electron density was independent of the low frequency (*LF*) power and only depended on the high frequency (*HF*) source power (60 MHz). Georgieva et al.

computationally investigated $Ar/CF_4/N_2$ discharges sustained in 2-frequency CCP reactors using a 1-dimensional particle-in-cell/Monte Carlo model.[6] They found that the average ion bombardment energy increases with both *HF* and *LF* voltage amplitudes when the other voltage amplitude is kept constant, The explanation is that the maximum sheath potential increases with the sum of the applied *HF* and *LF* voltages. They also observed that when there is only a moderate separation between the *LF* and *HF* sources (such as 2 and 27 MHz or 2 and 40 MHz) both voltage sources influenced on the plasma characteristics. Upon increasing the *HF* to 60 and 100 MHz, the plasma density and ion current density show little dependence on the *LF* source. This trend was also experimentally observed by Kitajima et al. using optical emission spectroscopy in Ar/CF_4 discharges.[7] With the *LF* kept at 700 kHz, the coupling with the *HF* source became smaller as the *HF* increased from 13.56 MHz to 100 MHz.

Goto et al. performed diagnostics of 2-frequency MERIE reactors operating in argon and H_2.[14] The magnetic field was 500 G below the upper electrode and 50 G above the wafer; and the pressure was 7 mTorr. While the 100 MHz *HF* power was held constant at 100 W, either increasing the *LF* power or decreasing the *LF* frequency decreased the dc bias (became more negative). They concluded that by treating the value of the *LF* excitation as a process parameter, the ion bombardment energy to the substrate can be effectively controlled without affecting the plasma density.

Rauf computationally investigated the influence of a radial magnetic field on the interaction of two rf sources in an Ar/C_2F_6 capacitively coupled plasma discharge using a two-dimensional continuum model.[15] He found that for constant voltage the amplitudes of rf currents at the electrodes increased with magnetic field strength over the range of 0-50 G and with source frequency over the range of 13.56-70 MHz. His results indicated that magnetic

fields in the range of 0-50 G tend to make the system less nonlinear and to separate the contributions of the rf sources.

In this chapter, results of a computational investigation of a 2-frequency MERIE reactor with plasmas sustained in argon are presented. Systematic trends for ion flux, plasma potential and ion energy and angular distribution are discussed for a reactor resembling an industrial design. Similar to the trends in a single frequency MERIE, the spatial distribution of the plasma transited from edge high to center high with increasing magnetic field.[16-17] Also, the reduction in the transverse electron mobility as the magnetic field increases can increase the voltage drop across the bulk plasma and produce reversals of the electric fields in both the high and low frequency sheaths. As such, the ion flux impinging the substrate decreases in energy and broadens in angle as the magnetic field increases. The net effect of these trends is at high magnetic fields, while keeping power of the *LF* and *HF* sources constant, the coupling between the two plasma sources increases thereby hindering the ability to separately control ion and radical fluxes and ion energy.

3.2 Description of the Model and Reaction Mechanism

Although surface wave and finite wavelength effects can be important as frequencies approach or exceed 100 MHz, or with substrate sizes greater than 20 cm, we have not addressed those effects in this work. All potentials are obtained by solving Poisson's equation assuming an electrostatic approximation. Since our frequencies are at most 40 MHz, the substrate is 20 cm, and the majority of the effects we discuss are most sensitive to transport perpendicular to the electrodes (as opposed to parallel to the electrodes, the direction most affected to finite-wavelength effects) we do not anticipate our results are terribly sensitive to surface wave and

finite wavelength effects. Their inclusion would be most evident in the radial distribution of plasma properties.

Powers are separately specified for the *LF* and *HF* electrodes, and the applied voltages are adjusted to deliver those powers. The powers are computed from $P = (1/\Delta t)\int VI \cdot \Delta t$, where *V* and *I* are the voltage and total current at the surface of the electrode, and Δt is the rf period.

The purpose of this investigation is to study the fundamentals of MERIE reactors using multiple frequencies as opposed to investigating a particular plasma chemical system. As such, the investigation was conducted using only argon as the feedstock gas whose reaction mechanism is discussed in Ref. 16. The species included in the model are Ar(3s), Ar(4s), Ar(4p), Ar^+ and electrons. The Ar(4s) is an effective state having a finite lifetime to account for the partial trapping of resonant levels in that manifold. We acknowledge that the details of our observations and conclusions may change using a more complex reaction mechanism, such as the Ar/c-C_4F_8/O_2 mixture previously investigated.[17]

3.3 Plasma Properties of 2-Frequency MERIE Reactors

The model reactor used in this study, shown schematically in Fig. 3.1, is patterned after plasma sources that are commercially available. The base case uses a metal substrate powered at the *LF* through a blocking capacitor. A conductive Si wafer (σ = 0.01/Ω-cm), 20 cm in diameter, sits in electrical contact with the substrate which is surrounded by a Si ring (focus ring 1, $\varepsilon/\varepsilon_0$ = 12.5, $\sigma = 10^{-6}$/Ω-cm) and dielectric focus ring (focus ring 2, $\varepsilon/\varepsilon_0$ = 8.0, $\sigma = 10^{-6}$/Ω-cm). Gas is injected through a shower head 24 cm in diameter that is powered at the *HF*. The *HF* electrode is surrounded by a dielectric having $\varepsilon/\varepsilon_0$ = 8.0. All other surfaces in the reactor are grounded metal including the annular pump port. A purely radial magnetic field parallel to the

wafer will have magnitudes from 0 to 200 G. The approximations that go with this form of the magnetic field are discussed in Ref. 16. The base case operating conditions are 40 mTorr of argon with a flow rate of 300 sccm, a *LF* of 5 MHz delivering a power of P_{LF} = 500 W and a *HF* of 40 MHz delivering a power of P_{HF} = 500 W.

3.3.1 Plasma Properties with a Magnetic Field

The electron temperature (T_e), ionization by bulk electrons (S_b) and ionization by beam electrons (S_{eb}) are shown in Fig. 3.2 without a magnetic field for *LF* = 5 MHz (500 W, 193 V) and *HF* = 40 MHz (500 W, 128 V). These quantities have been averaged over the longer *LF* cycle. The dc bias on the *LF* side is -22 V. The Ar^+ density is shown in Fig. 3.3. For equal powers at *LF* and *HF*, the voltage at the high frequency electrode is lower as a consequence of the more efficient power dissipation by electrons at the higher frequency. With an electron density of nearly 10^{11} cm^{-3}, the thermal conductivity is sufficiently high that T_e is nearly uniform across the plasma between the electrodes with a value of 4.4 eV, with there being a small increase at the *HF* electrode where heating is more efficient. With T_e nearly uniform between the electrodes, the rate of ionization by bulk electrons largely follows the ion density and has a maximum value of 2 x 10^{16} $cm^{-3}s^{-1}$, as shown in Fig. 3.2. With the sheath 1-2 mm thick, and the mean free path for electron collisions being longer, secondary electrons are launched into the bulk plasma from both electrodes with essentially the instantaneous sheath potential. The *LF* sheath potential has a maximum value of approximately $V_{LF} + V_{HF} - V_{dc}$ or 343 V. The mean free path for electrons in argon at 40 mTorr at this energy is 4 cm, in excess of the inter-electrode spacing of 2 cm. As a result, the secondary electrons largely pass through the plasma producing little ionization (maximum value 1 x 10^{15} $cm^{-3}s^{-1}$).

T_e, S_b and S_{eb} are shown in Fig. 3.4 for B = 150 G for *LF* = 5 MHz (500 W, 202 V, V_{dc} = -1 V) and *HF* = 40 MHz (500 W, 140 V). As with the B = 0 case, to deposit the same power, the voltage on the *HF* electrode is lower than that on the *LF* electrode. The Larmor radius for 4 eV electrons with this magnetic field is 0.03 cm. As such, the cross field mobility of ions exceeds that for the electrons. Sheath heating at both electrodes is largely local due to the inability of electrons to rapidly convect into the bulk plasma. As a result, there are peaks in T_e at both electrodes and a local minimum in T_e in the bulk plasma. The maximum value of T_e, 5.2 eV exceeds that without the magnetic field due to the more local power deposition. The parallel component of electron mobility along the magnetic field lines enables convention of electron energy into the periphery of the reactor. This creates a disc of high T_e above both electrodes. In spite of the lower voltage at the *HF* electrode, the peak in T_e there exceeds that at the *LF* electrode due to the more efficient electron heating at the higher frequency. Secondary electrons are more efficiently used as an ionization source with the magnetic field due to their being trapped on the magnetic field lines and depositing their power in the plasma. As a result, there are peaks in S_{eb} at both electrodes. Opposite to ionization by the bulk electrons, S_{eb} has a higher peak value near the *LF* electrode. This is a consequence of its larger sheath voltage which launches higher energy secondary electrons into the plasma.

The peak ion density increases by a factor of 13 to 1.3 x 10^{12} cm^{-3} with B = 150 G compared to the case without a magnetic field. The distribution of ion density is more center peaked compared to the distribution without a magnetic field. This increase results, in part, from a better utilization of secondary electrons for ionization and a decrease in diffusion losses to the upper and lower electrodes due to the decrease in the transverse value of μ_e. There is a gradual convergence of the ion flux to the wafer from being nearly uniform with B = 0 to being center

peaked with B = 200 G, as shown in Fig. 3.3. This trend is not necessarily a characteristic of two-frequency MERIEs in general but is likely a consequence of the decrease in the cross field mobility of electrons, μ_e, compared to ions, μ_I, and charging of dielectrics in this particular geometry, as discussed below. Note that in spite of a large increase in the plasma density and higher utilization of secondary electrons for ionization, the voltage required to deposit 500 W by both sources increases relative to the B = 0 case. This increase is due to the decrease in the cross field mobility of charge carriers. The increase in voltage is required to increase the bulk electric field to drive the current across the magnetic field lines.

3.3.2 Influence of Charging of Dielectrics

In an electropositive plasma, $\mu_e > \mu_I$, The transient loss of electrons prior to establishment of ambipolar fields during the creation of the plasma produces a net positive charge in the plasma. This net charge then creates the outwardly pointing ambipolar field that accelerates ions out of the plasma, while slowing the rate of electron loss, so that electron and ion losses are equal. If the walls of the discharge are dielectric, the missing electrons reside on the walls as surface charge. In MERIE discharge in the transverse direction, $\mu_e < \mu_I$, and so loss of positive charge to surfaces is more likely than the loss of negative charge. As a result, at times during the rf cycle, dielectrics may charge positively (instead of negatively) to slow the loss of the more mobile positive charge. These positively charged surfaces then affect the uniformity of the plasma.

These trends are illustrated by the electric potential at different times during the rf cycle appearing in Figs. 3.5 and 3.6 for B = 0 and B = 200 G. The frequencies are *LF* = 5 MHz and *HF* = 40 MHz. For B = 0, the electric potential has the characteristic shape of an electropositive

plasma. The potential of the bulk plasma generally sits above the potential of any surface in contact with the plasma. As both the *LF* and *HF* electrodes oscillate during their respective cycles the bulk plasma potential also oscillates in such a manner to be at a higher value than either electrode. With a magnetic field, there are significant voltage drops across the bulk plasma, as will be discussed below.

Take note of the electric potential on the surface of Focus Ring 1 and on the dielectric surrounding the *HF* electrode with and without a magnetic field. These dielectrics are functionally capacitors which charge and discharge with an RC time constant determined by their own physical capacitances and the resistance of current flow through the plasma to their surfaces. With B = 0, μ_e is large enough that the RC time constants are smaller than the rf period at either the *LF* or *HF*. As a result, the surface of, for example, the focus ring is essentially always at the local plasma potential (or displaced negative to the local plasma potential by the floating sheath potential). A voltage drop occurs through the focus ring from its surface potential to the biased substrate below it.

With B = 200 G, μ_e is smaller than μ_I. Both mobilities are small enough that the plasma resistance increases to such a large value that the RC time constant of the dielectrics exceeds the *HF* period and is commensurate to the *LF* period. Additionally, with $\mu_e < \mu_I$, the plasma acts as though it is electronegative. That is, the positive charge, being more mobile, more rapidly escapes from the plasma. Under these conditions, surfaces will naturally charge positive. As a result, during the cathodic part of the cycle of both the *HF* and *LF* electrodes when ions are accelerated into the surrounding dielectrics, the dielectrics charge positively to slow the flux of additional ions to their surfaces. The excess positive charge produces a positive potential on the top dielectric as shown in Fig. 3.6a and on Focus Ring 1 as shown in Fig. 3.6c. As the voltage

on the electrodes begins to increase towards more positive values and enters the anodic part of the cycle, electron flux is attracted to the dielectric surfaces and the excess positive charge is dissipated. This neutralization of the positive charge (and reduction in surface potential of the dielectrics) is shown in Fig. 3.6b for the *HF* electrode and Fig. 3.6d for the *LF* electrode.

As the B field increases, the length of time into the anodic part of the cycle which the dielectric surfaces remain charged positively increases. It is this peripheral positive charge with increasing B-field that contributes towards the convergence of the ion flux towards the center of the wafer shown in Fig. 3.3.

3.3.3 Secondary Electron Emission Coefficients

It is well known that the secondary electron emission coefficient, γ, is a function of both energy of the ion and the condition of the electrodes.[18] γ may increase (or decrease) by an order of magnitude or more depending on the condition of the electron emitting surface. MERIE plasma tools may be particularly sensitive to variations in γ resulting from the conditioning of surfaces due to a MERIE's higher utilization of secondary electrons as a source of ionization. This sensitivity is illustrated by the following computer experiment.

A single frequency MERIE is operated with 100 mTorr argon with a constant voltage for B = 0 G (V = 170 V) and for B = 100 G (V = 200 V) while varying γ from 0.01 to 0.45. The resulting ion density and power deposition are shown in Fig. 3.7. For B = 0, over this range of γ the ion density increases by only 5% from 1.3 x 10^{10} cm^{-3} for the smallest value of γ. The power dissipation actually decreases by about 10%. Due to the long mean free path of the secondary electrons, the majority of the electrons pass through the plasma producing little additional ionization while not dissipating their power. As a result, the plasma appears more capacitive and

so the power dissipation decreases.

With B = 150 G, the vast majority of the secondary electron energy is converted to excitation and ionization since the Larmor radius is small enough to confine the secondary electrons to the gap. With a constant voltage, an increase in γ and ionization produces a commensurate increase in ion density (increasing by a factor of 4 from 1.5 x 10^{10} cm^{-3}) and power deposition (increasing by a factor of 3).

3.3.4 Electric Potentials and Sheath Voltages

With the applied voltage oscillating at both the *LF* and *HF*, the plasma potential has both frequency components, as shown in Fig. 3.8a for B = 0 and in Fig. 3.9a for B = 150 G. The plasma potential has excursions to its maximum value at the peak of the anodic part of the *LF* cycle, reflecting both the higher value of the *LF* voltage (V_{LF} = 193 V with V_{dc} = -22 V, V_{HF} = 128 V) and contributions from the *HF*. In the absence of the *HF* the plasma potential would be pegged at near its floating potential when the *LF* cycle is in its cathodic phase. With the *HF*, the plasma potential oscillates commensurate with the oscillation with the *HF* voltage in order to keep its value positive with respect to all surfaces, including the *HF* electrode. The plasma potential for the B = 150 G case (Fig. 3.9a) has a similar time dependence (V_{LF} = 202 V with V_{dc} = -1 V, V_{HF} = 140 V), however its shape indicates a more resistive plasma commensurate with the decrease in cross field mobilities.

The spatial distributions of electric potential through the bulk plasma differ markedly for the B = 0 and B = 150 G cases. For example, the plasma potential at r = 5 cm is shown in Fig. 3.8b for B = 0 for approximately the peak of the *LF* anodic cycle (phase $\phi = \pi/2$), peak of *LF* cathodic cycle ($\phi = 3\pi/2$) and the zero crossing in the *LF* rf voltage ($\phi = 0$) displaced by V_{dc}.

These values are shown when $V_{HF} = 0$. The corresponding values are shown in Fig. 3.8c for the *HF* cycle when V_{LF} is approximately zero. At all phases, at both the *LF* and *HF* electrodes, the sheaths are electropositive. That is, the sheaths are electron repelling and ion attracting. The bulk plasma is electropositive, as indicated by the small positive potential in the center of the plasma through nearly all phases. This indicates that the diffusive electron flux to the electrodes, modulated by the sheath potential, carries the majority of the rf current.

Plasma potentials for the same phases are shown in Fig. 3.9b and 3.9c for B = 150 G. Due to the low values of μ_e and μ_I , the bulk plasma is resistive. To drive current through the plasma, a large electric field is required, approximately 30 V/cm. The voltage that is dropped across the bulk plasma to drive the current is not available to be dropped across the sheath and so is not available for ion acceleration. During the *LF* cycle, ion current is collected during the cathodic part of the cycle during which the sheaths appear electropositive. During the anodic part of the *LF* cycle electron current should be collected. μ_e is so small that the sheath must reverse (that is, become electron attracting and ion repelling) to collect enough electron current. This reversal in the direction of the electric field penetrates more than a cm into the plasma.

A similar phenomenon occurs at the *HF* electrode. During the cathodic part of the *HF* cycle, the sheath appears electropositive. During the anodic part of the cycle, insufficient electron current is collected and so the electric field in the sheath must reverse to become ion repelling and electron attracting. The reversal of the electric field in the bulk plasma begins before the zero crossing in V_{HF} and extends across the entire plasma for the majority of the anodic half of the cycle. Again, the voltage drop across the bulk plasma that is required to drive electron current to the high voltage sheath is that much less voltage available for ion acceleration across the sheath.

The reversals of the electric fields in the sheaths and the increasingly resistance of the bulk plasma with increasing B-field have important implications with respect to the ion energy and angular distributions (IEADs) that are incident onto the wafer. Neglecting floating potentials and assuming negligible voltage drop across the bulk plasma, the maximum ion energy onto the wafer is $E_m = V_{LF} + V_{HF} - V_{dc}$. This condition corresponds to when the *LF* electrode is at the minimum voltage of the cathodic cycle (offset by any additional DC bias) thereby dropping its entire voltage across the sheath; and the *HF* electrode is at the maximum voltage of its anodic cycle, thereby raising the potential of the bulk plasma by an additional V_{HF}.

In our investigation, we have specified power and adjusted the voltages on the *LF* and *HF* electrodes to deliver that power. For example, V_{LF}, V_{HF} and V_{dc} are shown in Fig. 3.10 for keeping P_{LF} = 500 W and varying P_{HF} from 100 to 1000 W. Results are shown for B = 0 and B = 100 G. With B = 0, in order to deliver a larger power, V_{HF} increases nearly linearly with P_{HF}. As the plasma density increases with increasing P_{HF}, a larger potential current source is produced for the *LF* electrode. To deliver the same power, V_{LF} can then decrease. The decrease in V_{LF} is also nearly linear with P_{HF}. For these conditions and geometry, the plasma becomes more symmetric with increasing P_{HF} and so V_{dc} decreases (becomes less negative). The end result is that E_m increases from 310 V for P_{HF} = 100 W to 350 V for P_{HF} = 1000 W. Although the goal of maintaining E_m a constant so that IEADs are unchanged when varying P_{HF} is nearly met, this goal is only fortuitously met. The constant value of E_m results from commensurate decreases in V_{LF} as V_{HF} increases.

Similar trends are obtained for B = 100 G. As P_{HF} increases, V_{HF} increases while V_{LF} decreases. Here, however, the decrease in V_{LF} is proportionately larger than the increase in V_{HF}. As a result, E_m decreases from 390 V to 345 V, opposite the trend with B = 0. Again, the goal of

maintaining E_m a constant is nearly met but only fortuitously.

Unfortunately, the maintenance of a constant E_m with B = 100 G does not translate into maintaining uniform IEADs. This trend is due to the large voltage drop across the bulk plasma resulting from the increase in plasma resistance. For example, the maximum sheath potential at the *LF* electrode, V_S, obtained with the model is shown in Fig. 3.11a as a function of P_{HF} for B = 0 and B = 100 G. When B = 0, V_S increases with increasing P_{HF} in spite of V_{LF} decreasing. This increase in V_S. results from the increase in V_{HF}, whose amplitude raises the plasma potential at the peak of its anodic cycle, which adds to V_{LF} at the minimum of its cathodic cycle. For B = 100 G, V_S decreases with increasing P_{HF} in spite of an increase in V_{HF}. The reason is that the sheath reversal at the *HF* electrode and the voltage drop across the bulk plasma remove *HF* voltage that would otherwise add to V_S at the *LF* electrode.

Plasma potentials as a function of height for B = 100 G at r = 5 cm for P_{HF} = 125 W and 1000 W are shown in Fig. 3.11b. These profiles are for when the *LF* electrode is at the minimum of the cathodic part of the cycle and the *HF* electrode is at the maximum of the anodic part of the cycle. These are conditions for which V_S should have its maximum value of $E_{m.}$. For P_{HF} = 125 W, the maximum value of E_M = 391 V whereas the actual value of V_S =289 V. The difference of 102 V is dropped roughly half across the bulk plasma and half across the sheath reversal at the *HF* electrode. Similarly for P_{HF} = 1000 W, the maximum value of E_M = 345 V whereas the actual value of V_S = 229 V. The difference of 116 V is dropped across the bulk plasma and the reversed sheath at the *HF* electrode.

3.3.5 Ion Energy Distributions: Power Applied to 1- and 2-Electrodes

These disparities in the scaling of V_S with and without a magnetic field when varying P_{HF}

produce similar disparities in the scaling of ion energy distributions (IEDs). The angularly integrated IEDs incident on the wafer for B = 0 and B = 150 G are shown in Fig. 3.12 while varying P_{HF} from 125 to 1000 W. P_{LF} is held constant at 500 W. With B = 0, as P_{HF} increases the shape of the IEDs stay nearly constant with about a 10% increase in the energy of the peak of the IED. These trends mirror the nearly constant (but slighting increasing) value of E_m. On the other hand, with B = 150 G the energy of the peak of the IED decreases from 250 eV to 125 eV as P_{HF} increases from 125 to 1000 W. The aforementioned voltage drop across the bulk plasma and reversal of the anodic sheath which removes voltage from V_S are responsible. The fact that the sheath at the *HF* electrode is reversed at the anodic maximum of the *HF* cycle means that the increase in V_{HF} with increasing P_{HF} does not fully contribute to increasing V_S. The peak of the IED then decreases because V_{LF} decreases.

IEADs as a function of magnetic field are shown in Fig. 3.13 for $P_{LF} = P_{HF} = 500$ W. With the exception of the applications of small magnetic fields (< 50 G), the IEADs generally shift to lower energies and broaden in angle. These trends are caused by the decrease in V_S with increasing B field resulting from voltage being dropped across the bulk plasma and the deceleration ions experience during the anodic part of the rf cycle when the *LF* sheath reverses. These trends are similar to those seen with single frequency MERIEs.[16,17]

IEADs for P_{LF} = 500 W, 750 W and 1000 W with and without a magnetic field are shown in Fig. 3.14. P_{HF} is held constant at 500 W. The expectation is that the peak energy and shape of the IEADs should be controlled by P_{LF} in a fairly linear fashion. In principle, holding P_{HF} constant fixes the ion current and increasing P_{LF} should only extend the IEAD to higher energies while keeping the angular spread nearly constant. This is, in fact, what is observed with B = 0 however not in a strictly linear fashion. As P_{LF} exceeds P_{HF}, increasing P_{LF} also increases the

plasma density thereby increasing the efficiency of power deposition. As a result, only a 50% increase in V_{LF} (from 193 to 289 V) is required to double the *LF* power deposition. With the limited increases in V_{LF} and a small decrease in the amplitude of V_{HF} due to the higher plasma density, the maximum energy of the IEADs does not double with a doubling of P_{LF}.

For low values of P_{LF} with B = 150 G, the sheath is reversed during a significant fraction of the rf cycle. This results in an angularly broad IEAD extending to nearly zero energy. Upon increasing P_{LF}, a smaller fraction of the rf cycle has a sheath reversal, and so the IEADs not only increase their extent in energy, but also narrow in angle. However, the extension in the energy of the IEADs with increasing P_{LF} is less compared to that for B = 0. This difference can be attributed to at least two effects; the more efficient of utilization of secondary electrons and the dependence of dc bias on magnetic field.

At B = 150 G, the secondary electrons are well confined by the magnetic field thereby providing additional ionization sources. This more efficient utilization of secondary electrons facilitates more efficient power deposition and reduces the increase in V_{LF} required to double P_{LF} (from 201 to 235 V). A second contributing cause to there being less extension of the IEADs is the behavior of the dc bias. With B = 0, the dc bias becomes more negative with increasing P_{LF}, thereby contributing to an increase in ion energy. However at B =150 G, the cross field mobility of ions is about the same as that for electrons. As a result, the proportions of the current being carried by ions and electrons are about same and the dc bias is nearly unaffected by the change in plasma density. V_{dc} therefore does not contribute to extending the IEADs with increasing P_{LF} as with B = 0.

Another method of controlling the IEAD is to adjust the frequency of the rf source. As is well known, IEADs generally narrow in energy as the frequency increases due to the finite time

required for ions to cross the sheath. For example, IEADs while varying the LF frequency, ν_{LF}, are shown in Fig. 3.15 for B = 0 and 100 G while keeping P_{LF} constant. With B = 0 and with P_{LF} constant, V_{LF} decreases with increasing ν_{LF} to reflect the more efficient electron heating at higher ν_{LF}. Correspondingly, V_{HF} increases to compensate for the decreasing stochastic heating at the *HF* sheath due to the decrease in V_{LF}. The end result is that E_m remains nearly unchanged. The final outcome is the IEADs narrow in energy as ν_{LF} increases while the angular spread remains nearly constant. With B = 100 and with P_{LF} constant, the decrease in V_{LF} with increasing ν_{LF} is proportionately larger in part because the plasma density is larger. Thus E_m decreases and the IEADs undergo more degradation in energy and more angular spreading than without a magnetic field. The low energy tails of the IEADs persist at high ν_{LF} due to the sheath reversal during the anodic phase of the *LF* cycle.

The *HF* and *LF* powers can be applied to the same electrode, and we compared such sources to the two powered electrode variant discussed thus far. In comparing these two sources, we kept the amplitudes of the applied voltages constant at V_{HF} = 150 V and V_{LF} = 250 V and forced V_{dc} to be zero. The intent was to isolate changes in plasma properties resulting from only where the *LF* and *HF* powers were applied.

The maximum plasma potential is shown in Fig. 3.16 as a function of *LF* cycles for the 2-electrode and 1-electrode sources with B = 100 G. With the applied voltage oscillating at both the *LF* and *HF*, the plasma potential has excursions to its maximum value at the simultaneous peaks of the anodic part of the *LF* and *HF* cycles. In principle, the plasma potential should have a peak value of nearly V_{LF} + V_{LF} or 400 V. In the 2-electrode case, the sheath reversal at the *HF* electrode and *HF* voltage drop across the bulk plasma removes voltage that might otherwise raise the plasma potential. As a result, the peak value of the plasma potential is only 240 V.

By also applying the *HF* source to the lower electrode, the contributions of the *HF* component to the plasma potential are fundamentally different. During the *LF* cathodic cycle, the *HF* components of the plasma potential nearly disappear. This can be attributed to V_{HF} being less than V_{LF}, and so their sum is still negative during most time of the *LF* cathodic cycle. This eliminates the *HF* modulation of the plasma potential during that part of the *LF* cycle. On the other hand, with *HF* and *LF* on the same electrode, *HF* voltage directly contributes to raising the plasma potential during the anodic peak of the *LF* cycle without loss of voltage across the bulk plasma. As a result, the peak plasma potential is 340 V.

The plasma potential as a function of height at r = 5 cm is shown in Fig. 3.17a for the 2-electrode case with B = 100 G for the peak of the *LF* anodic cycle (phase $\phi = \pi/2$), peak of *LF* cathodic cycle ($\phi = -\pi/2$) and the *LF* zero crossing voltage ($\phi = 0$). These values are shown with V_{HF} = 0. The corresponding values are shown in Fig. 3.17b for the *HF* cycle when V_{LF} is approximately zero. Similar to that shown in Fig. 3.9, the reversal of the electric field in the sheath occurs during both the *HF* and *LF* anodic cycle. The corresponding values are plotted in Fig. 3.18 for the 1-electrode case. Although there are sheath reversals during both the LF and HF cycles, the sheath is always electropositive on the upper, now grounded, electrode.

IEADs are shown in Fig. 3.19 for B = 0 and 100 G for the 1- and 2-electrode cases. In principle, applying the *HF* source to the *LF* electrode increases the effective frequency of the *LF* sheath oscillation. The multiple energy peaks in the 1-electrode IEADs reflect this high frequency modulation. The consequence is such that IEADs narrow in energy, particularly for B = 0. The lack of *HF* oscillation of the plasma potential during the cathodic part of the LF cycle emphasizes and broadens the low energy portion of the IEADs compared to the 2-electrode case. With B = 100 G, similar trends are observed. The IEADs for the 1-electrode case have a lower

peak energy and more prominent low energy tail.

3.4 Concluding Remarks

The properties of 2-frequency MERIE plasma sources sustained in argon have been computationally investigated using results from a two-dimensional plasma transport model. Similar to the single frequency MERIE, 2-frequency MERIEs show the trends of localization of plasma density near the powered electrodes and the shift of the peak ion density toward the center of the reactor as the magnetic field increases. The reduction in transverse electron mobility as the magnetic field increases causes a reversal of the electric field in both the *HF* and *LF* sheaths and produces an increase in voltage drop across the bulk plasma. The end result is a decrease in energy and broadening of angle of incidence of ions onto the substrate. The effect described here is likely a worst case as the magnetic field in this model is perfectly parallel to the substrate. In actual plasma reactors there will likely be magnetic field lines that intersect with the face of the substrate which would provide a low impedance path for electrons to the surface. Under such conditions, the magnitude of the sheath reversal would be less.

The convergence of the ion flux towards the center of the wafer with increasing magnetic field can be attributed to the peripheral positive charge collected by the dielectric surfaces during the time the sheaths are reversed at both the LF and HF electrodes. The sheath reversal and the voltage drop across the bulk plasma are responsible for the continuous downward shift in the peak in energy of IEADs as PHF increase while PLF is maintained constant. The plasma potential and IEADs obtained when applying both HF and LF to the same electrode differ from the 2-electrode variant. This results in part from the relative amplitudes of the LF and HF components; and the sheath reversal and voltage drop of the HF component across the bulk

plasma.

3.6 Figures

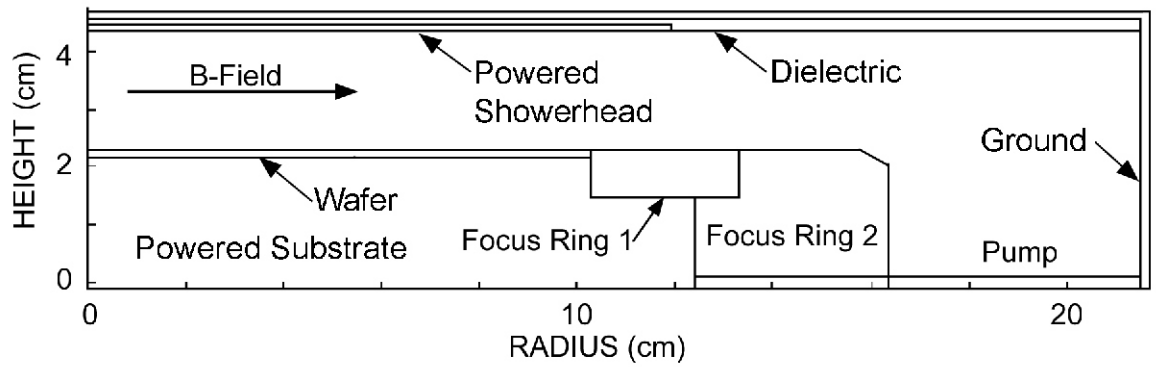

Fig. 3.1 - Geometry for the 2-frequency MERIE reactor. The wafer sits on a substrate powered at low frequency surrounded by dielectric focus rings. The showerhead is powered at high frequency and is also surrounded by dielectric. The radial magnetic field is applied parallel to the electrodes.

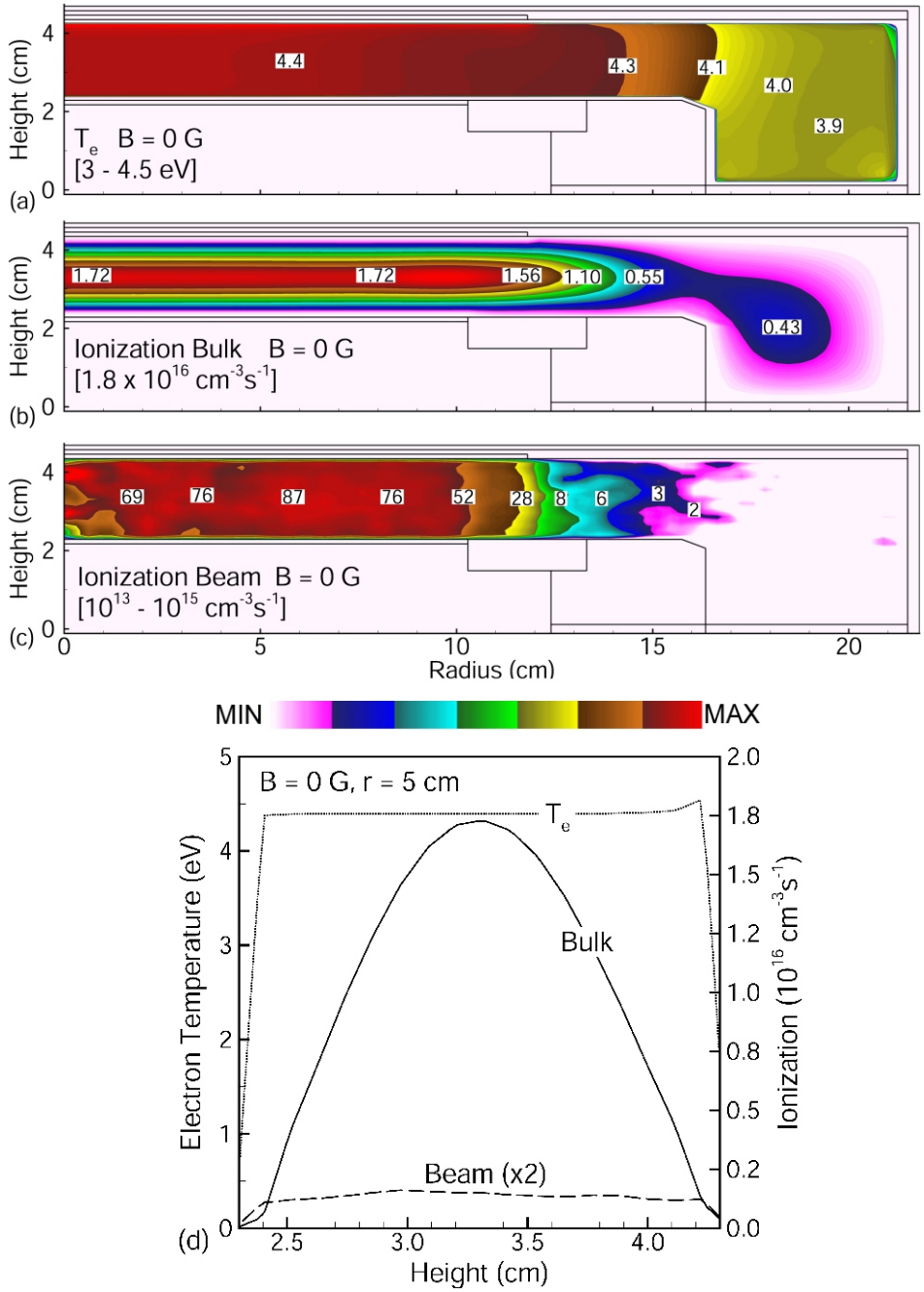

Fig. 3.2 - (Color) Plasma properties in the absence of a magnetic field for the base case (Ar, 40 mTorr, $P_{LF} = P_{HF} = 500$ W, $\nu_{LF} = 5$ MHz, $\nu_{HF} = 40$ MHz) without a magnetic field. a) Electron temperature, b) ionization by bulk electrons, c) ionization by beam electrons and d) axial values of these quantities at a radius of 5 cm. The maximum value or range of values in each frame is noted. The beam ionization is a log scale over two decades with contour labels in units of 10^{13} $cm^{-3}s^{-1}$.

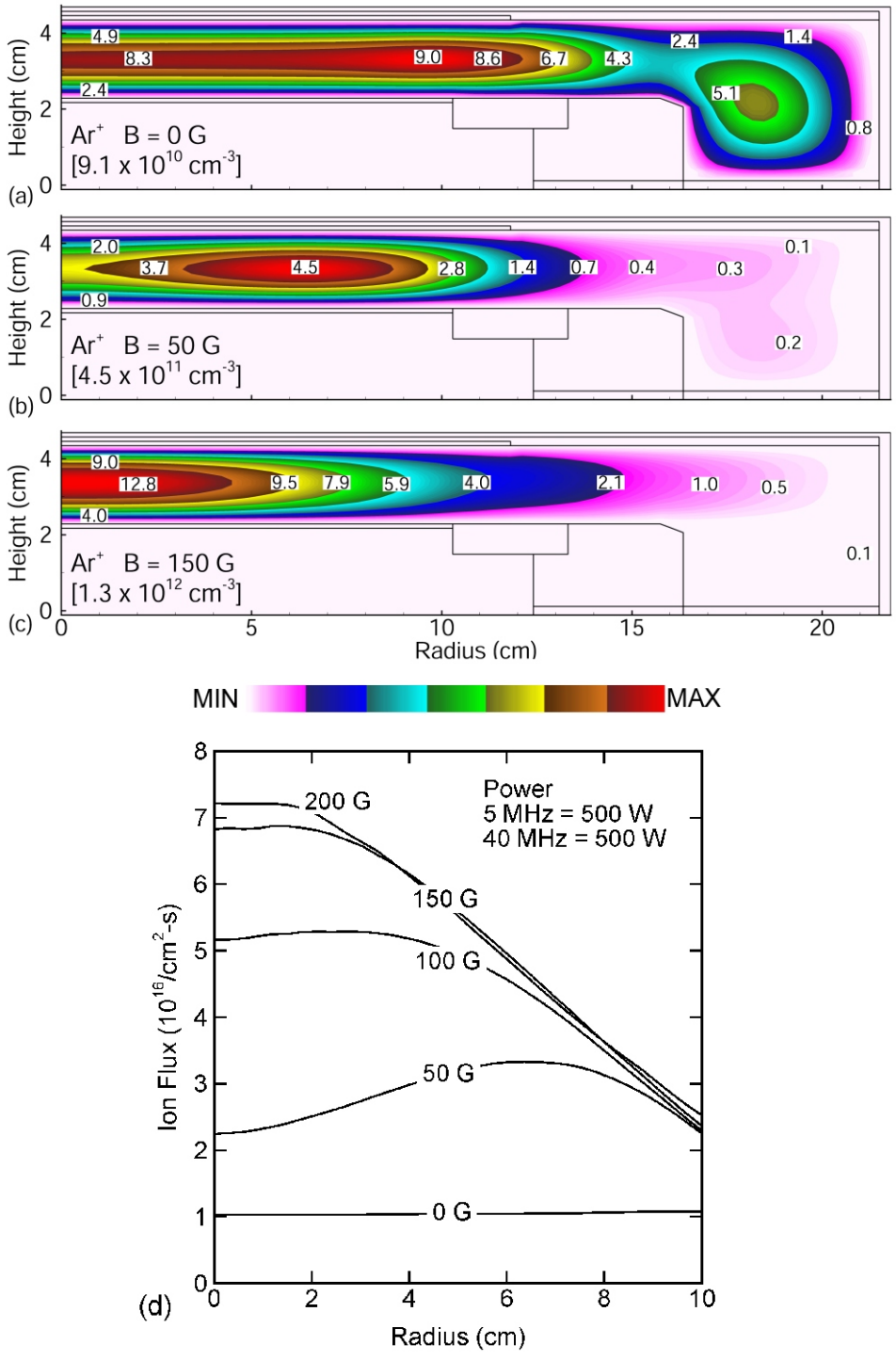

Fig. 3.3 - (Color) Time averaged ion densities and fluxes as a function of magnetic field. Ion densities for magnetic fields of (a) 0 G, (b) 50 G, (c) 150 G; and (d) ion fluxes to wafer for different magnetic fields. With increasing magnetic field the peak ion density shifts toward the center of the reactor and a gradual convergence of the ion flux occurs.

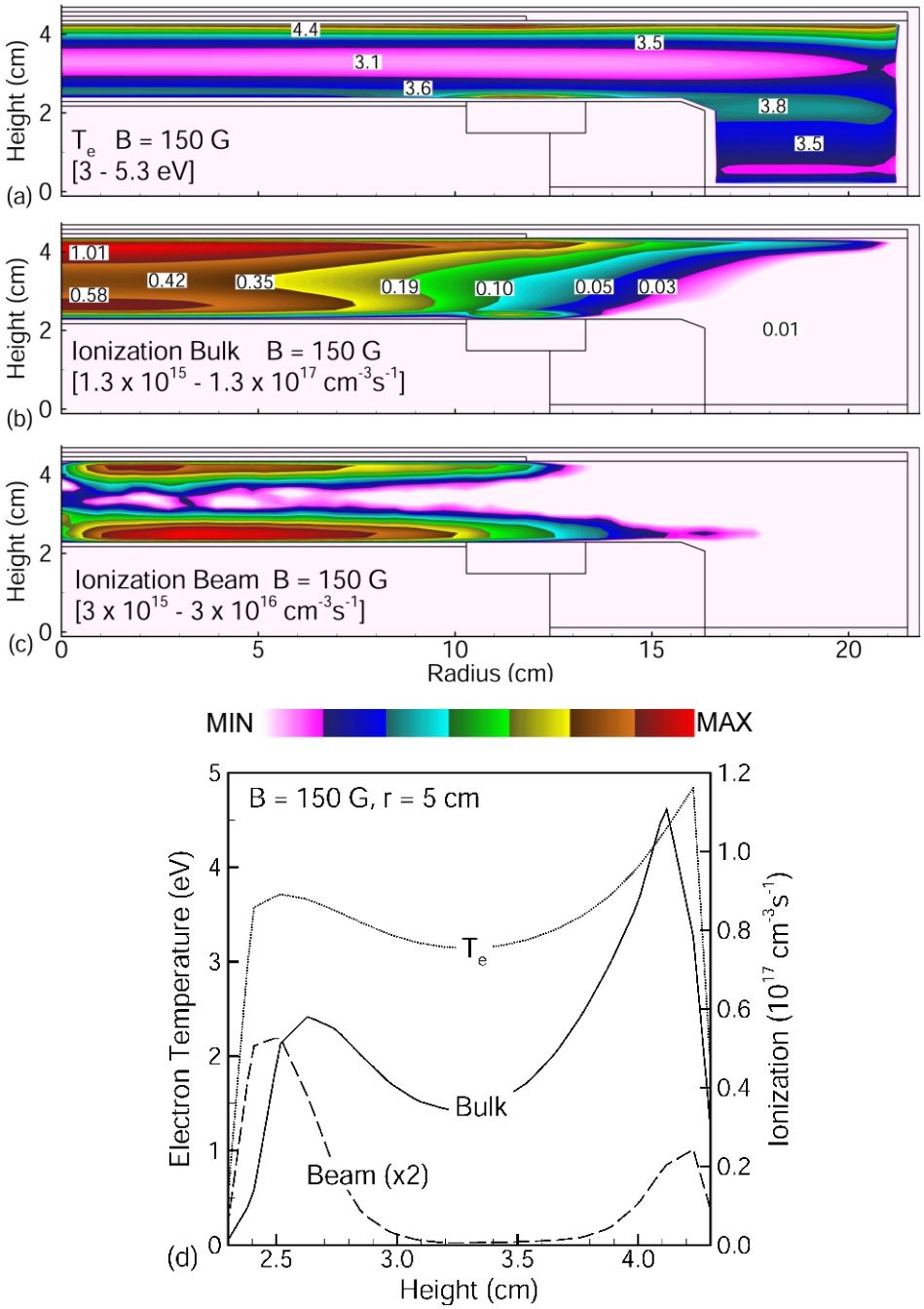

Fig. 3.4 - (Color) Plasma properties for B = 150 G for the base case (Ar, 40 mTorr, $P_{LF} = P_{HF} =$ 500 W, $\nu_{LF} = 5$ MHz, $\nu_{HF} = 40$ MHz). a) Electron temperature, b) ionization by bulk electrons, c) ionization by beam electrons and d) axial values of these quantities at a radius of 5 cm. The maximum value or range of values in each frame is noted. The bulk and beam ionization have log scales over two decades. Contour labels for bulk ionization have units of 10^{17} $cm^{-3}s^{-1}$. The bulk and beam ionization source are confined to be closer to the electrodes by the high magnetic field.

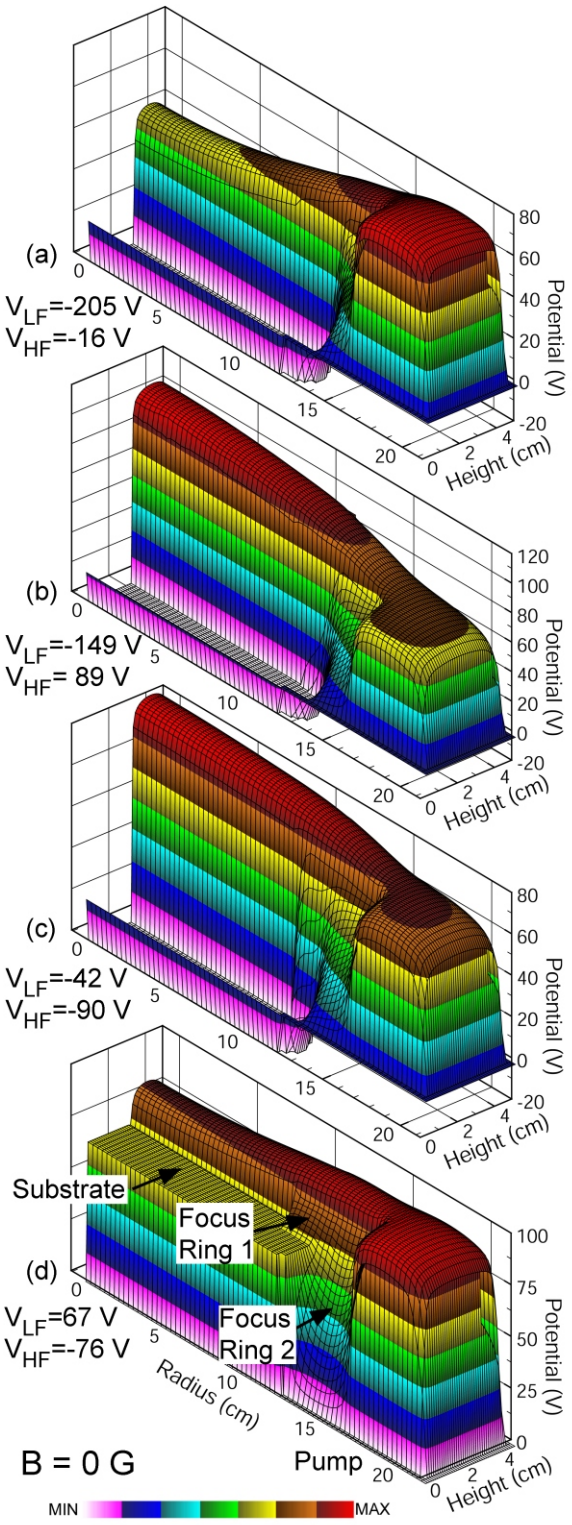

Fig. 3.5 - (Color) The electric potential for B = 0 at different times during the rf cycle. The conditions are otherwise the same as the base case (Ar, 40 mTorr, $P_{LF} = P_{HF} = 500$ W, $\nu_{LF} = 5$ MHz, $\nu_{HF} = 40$ MHz). The potential on the surface of the Focus Ring 1 is essentially always at the local plasma potential due to the large μ_e.

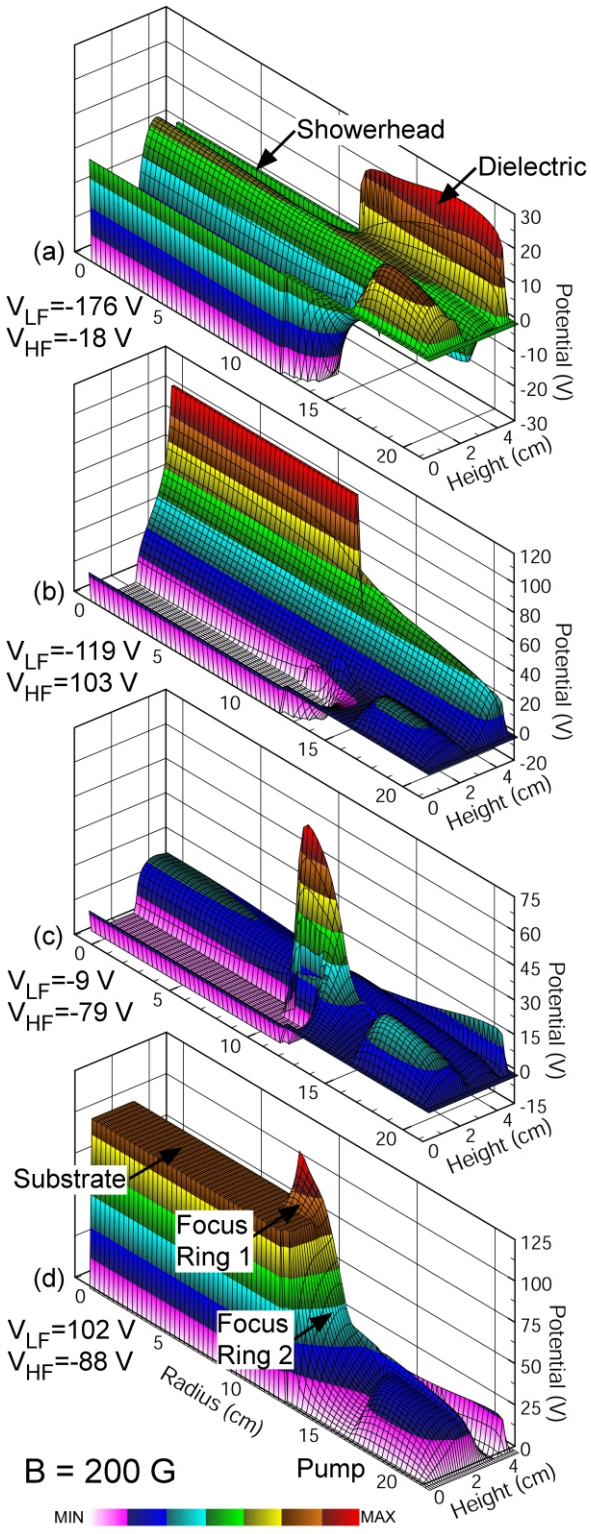

Fig. 3.6 - (Color) The electric potential for B = 200 G at different times during the rf cycle. The conditions are otherwise the same as the base case (Ar, 40 mTorr, $P_{LF} = P_{HF} = 500$ W, $\nu_{LF} = 5$ MHz, $\nu_{HF} = 40$ MHz). The positive charge collected by the dielectric surface surrounding the wafer during the *LF* and *HF* cathodic cycles charges those surfaces positive, and is neutralized by electrons during the *LF* and *HF* anodic cycles.

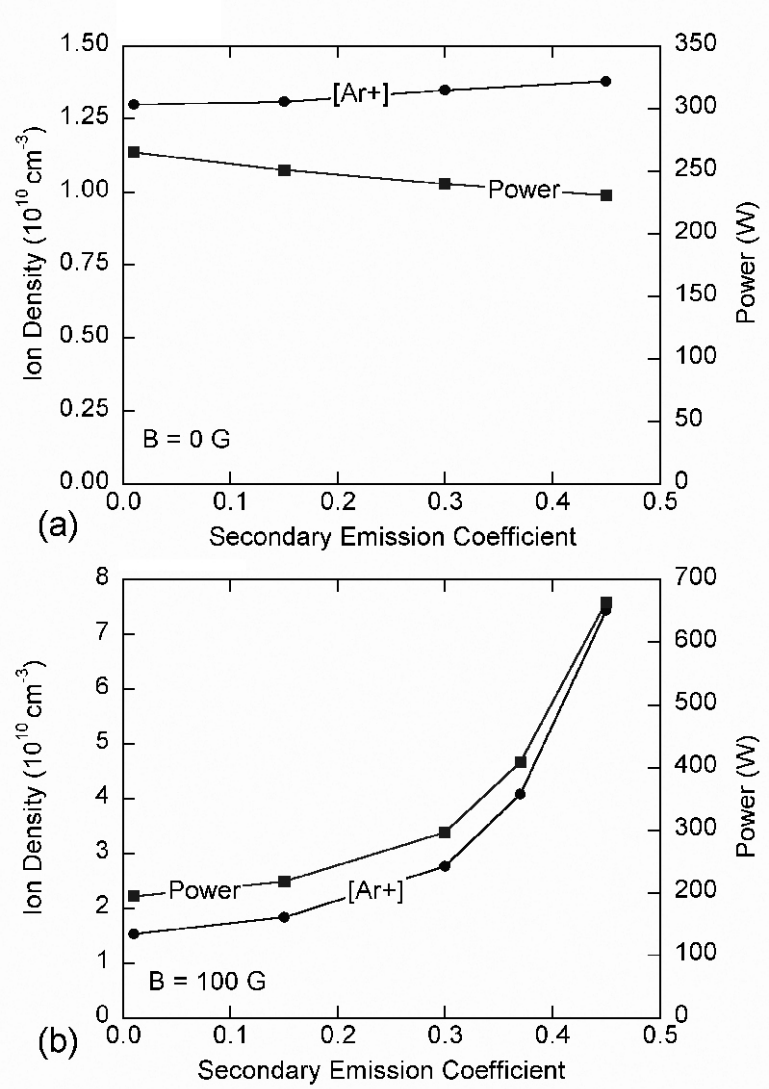

Fig. 3.7 - The argon ion density and power deposition as a function of secondary emission coefficient for different magnetic fields with constant voltage. (a) B = 0 (V = 170 V), (b) B = 150 G (V =200 V). The increase in the argon ion density with increasing γ is greater with the magnetic field as a result of more efficient utilization of beam electrons for ionization.

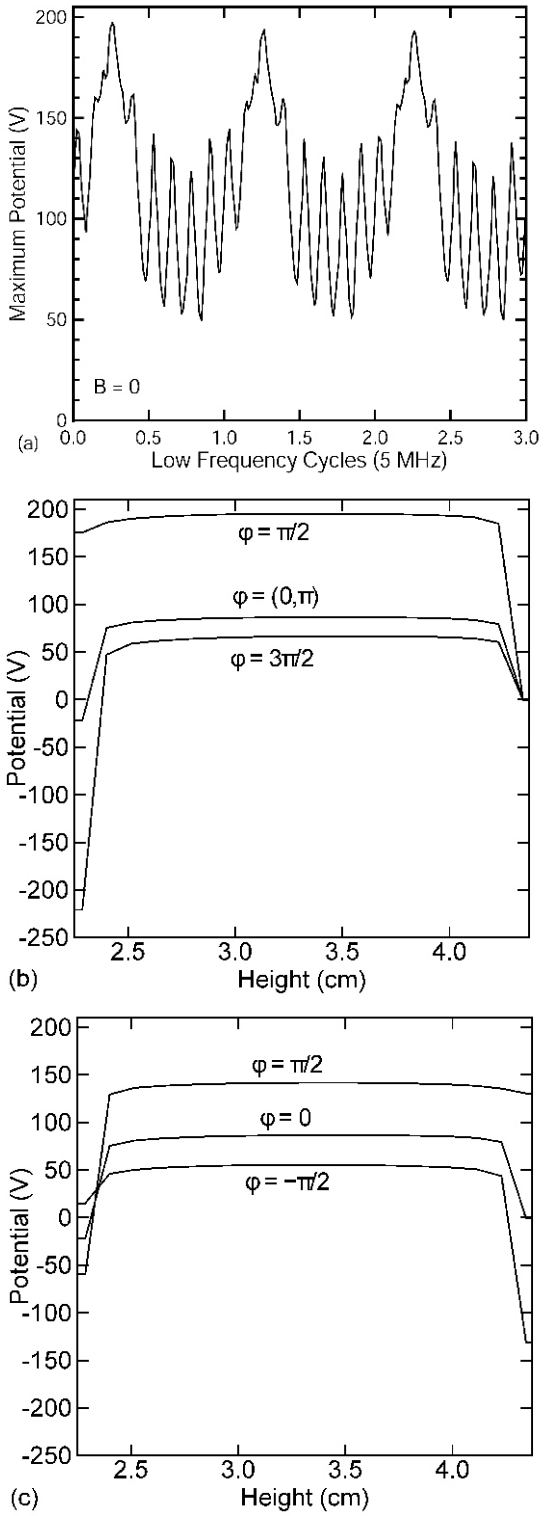

Fig. 3.8 - Plasma potential for the base case (Ar, 40 mTorr, $P_{LF} = P_{HF} = 500$ W, $\nu_{LF} = 5$ MHz, $\nu_{HF} = 40$ MHz) with B = 0. (a) maximum plasma potential as a function of *LF* cycles, (b) plasma potential as a function of height at radius r = 5 cm at different fractional phases during the *LF* cycle. (c) plasma potential as a function of height at different fractional phases during the *HF* cycle. The *HF* and *LF* sheaths are electropositive through the entire rf cycles.

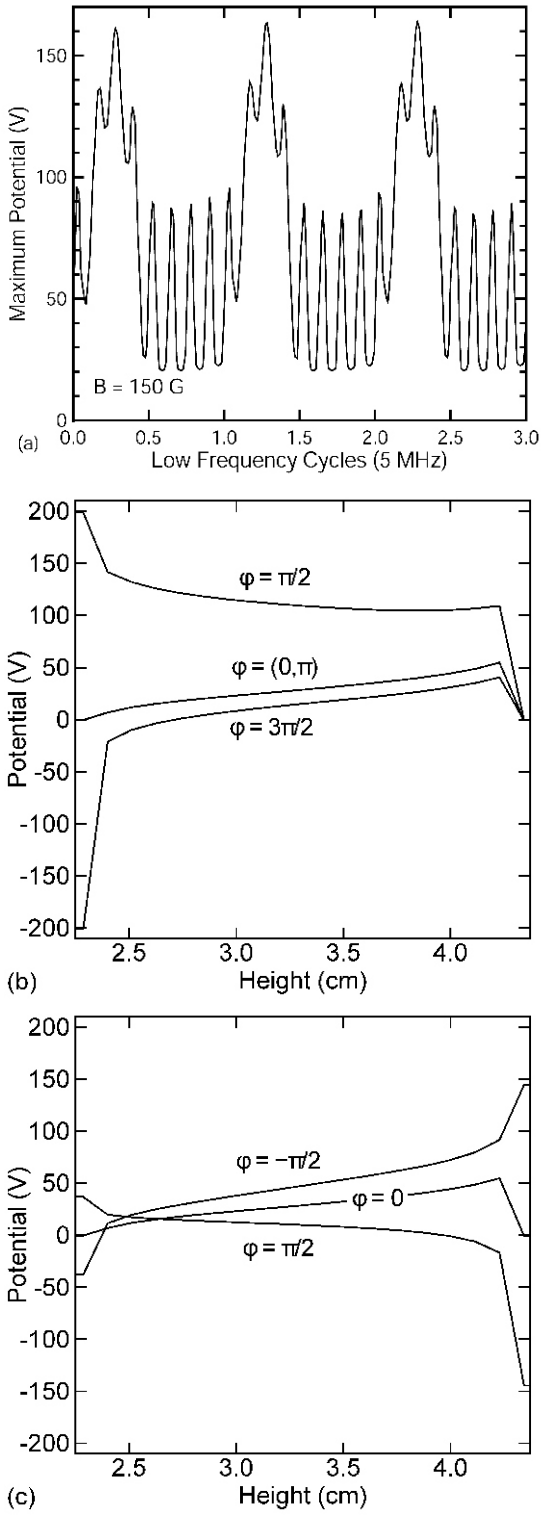

Fig. 3.9 - Plasma potential for the base case (Ar, 40 mTorr, $P_{LF} = P_{HF} = 500$ W, $\nu_{LF} = 5$ MHz, $\nu_{HF} = 40$ MHz) with B = 150 G. (a) maximum plasma potential as a function of *LF* cycles, (b) plasma potential as a function of height at radius r = 5 cm at different fractional phases during the *LF* cycle. (c) plasma potential as a function of height at different fractional phases during the *HF* cycle. Sheath reversals occur at both the *LF* and *HF* electrodes.

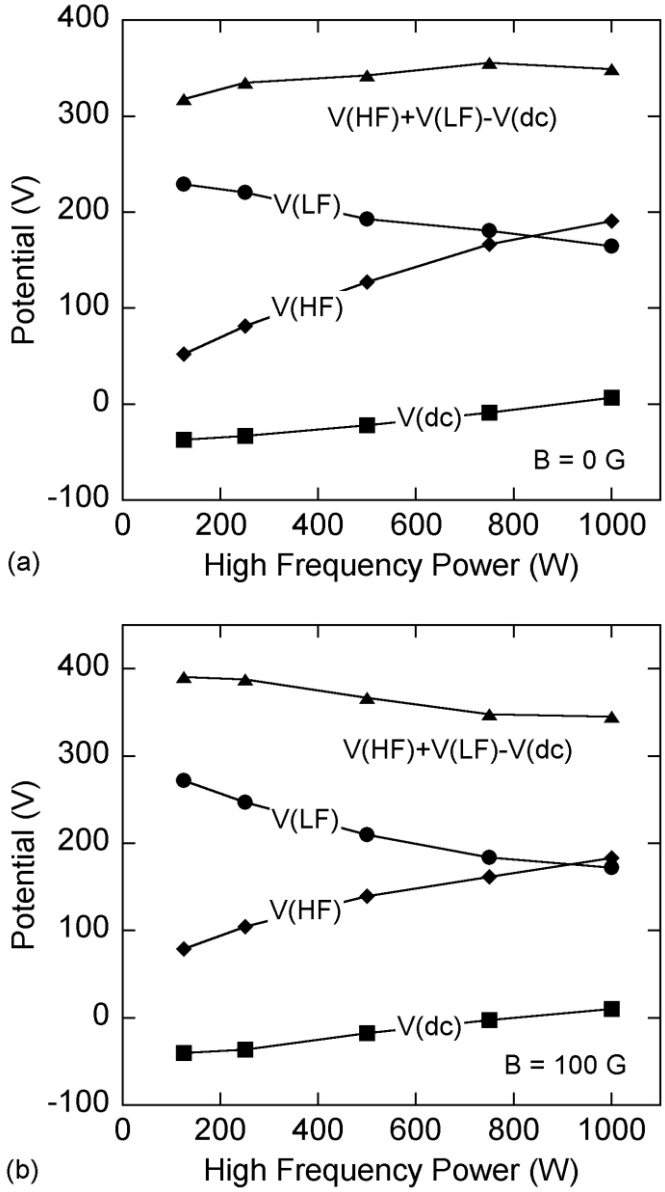

Fig. 3.10 - Electrical parameters V_{LF}, V_{HF}, V_{DC} and their sum, E_M, as a function of *HF* power. (a) B = 0, (b) B =100 G. V_{HF} increases to deliver a larger P_{HF} and V_{LF} decreases with increasing P_{HF} to maintain P_{LF} constant. The goal of keeping E_M a constant is nearly met but only fortuitously.

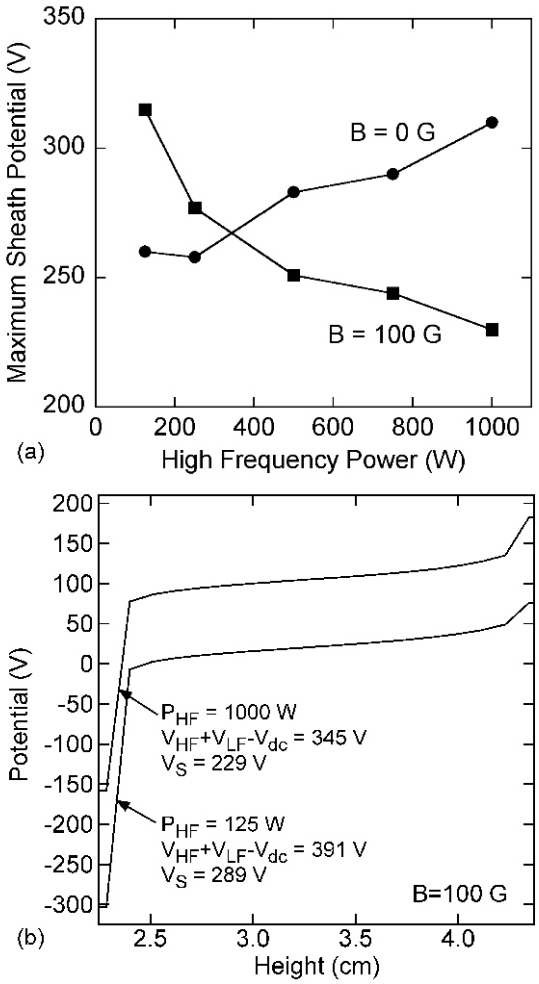

Fig. 3.11 - Potentials for different *HF* powers. (a) the maximum *LF* sheath potential as a function of *HF* power with B = 0 and B = 100 G; and (b) the plasma potential as a function of height for B = 100 G at r = 5 cm for P_{HF} = 125 W and 1000 W.

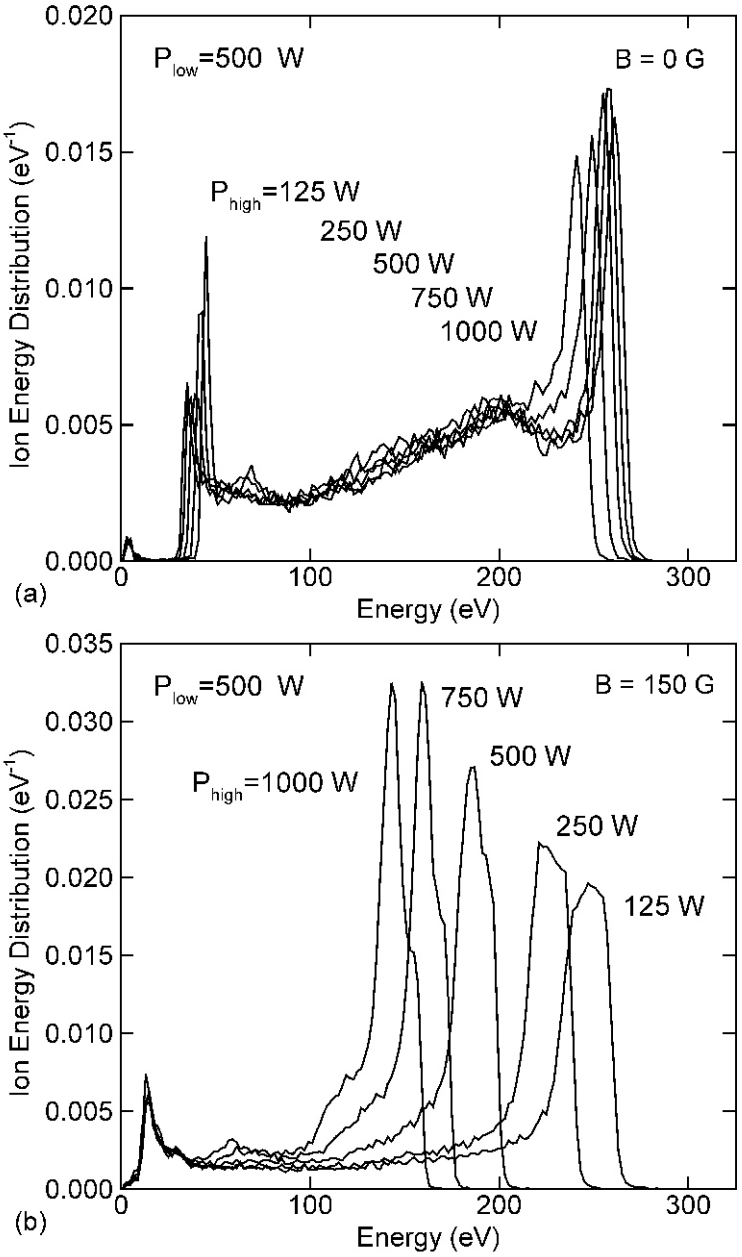

Fig. 3.12 - Ion energy distribution incident on the wafer (integrated over angle) while varying the high frequency power for (a) B = 0 and (b) B = 150 G. At B = 150 G, the voltage drop across the bulk plasma and the reversal of the *HF* sheath causes the successive shift of the energy of the peak of the IED.

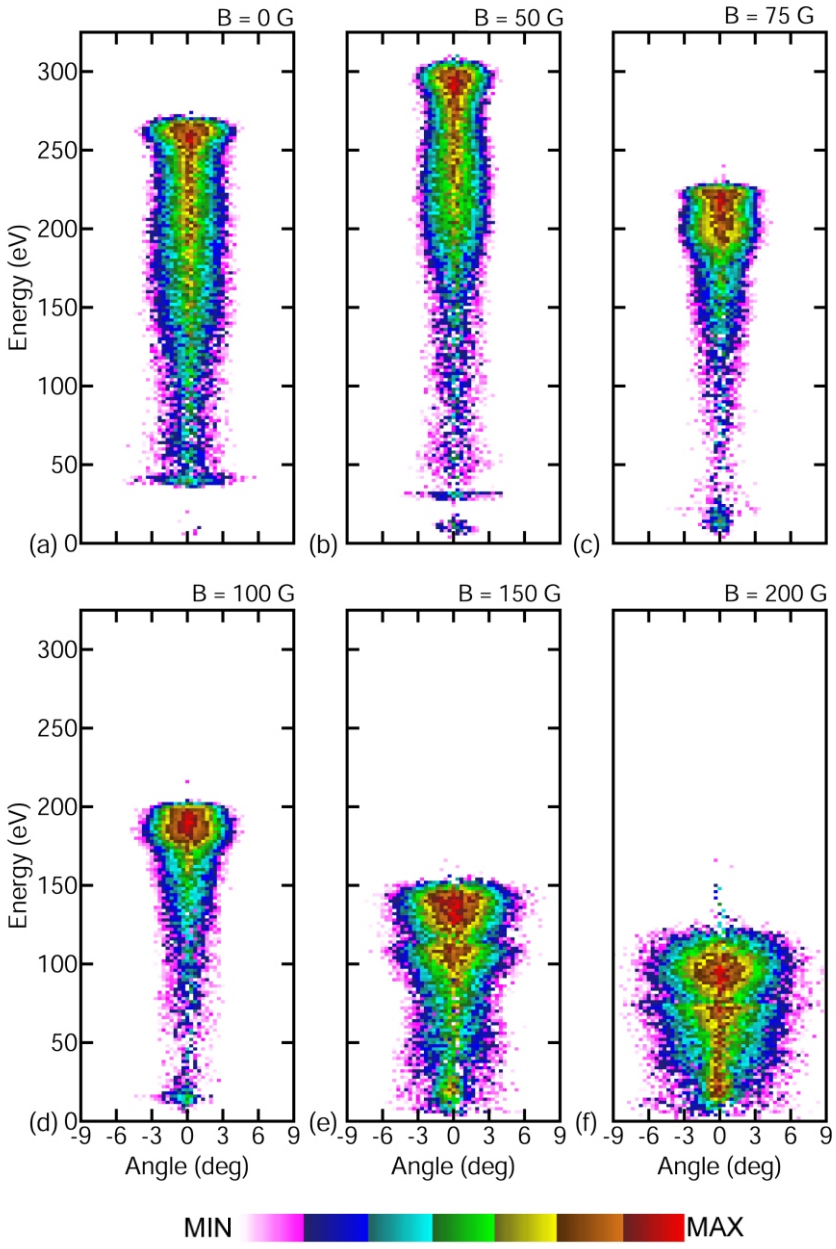

Fig. 3.13 - (Color) IEADs striking the substrate for the base case (Ar, 40 mTorr, $P_{LF} = P_{HF} = 500$ W, $\nu_{LF} = 5$ MHz, $\nu_{HF} = 40$ MHz) while varying magnetic field from 0 – 200 G. The IEADs have units of $eV^{-1}sr^{-1}$. The contours span 2 decades using a log scale. For moderate and high magnetic fields, the decrease in V_S with increasing magnetic field and the sheath reversal during the anodic part of the rf cycle result in the downshift in energy and spread in angle of IEADs.

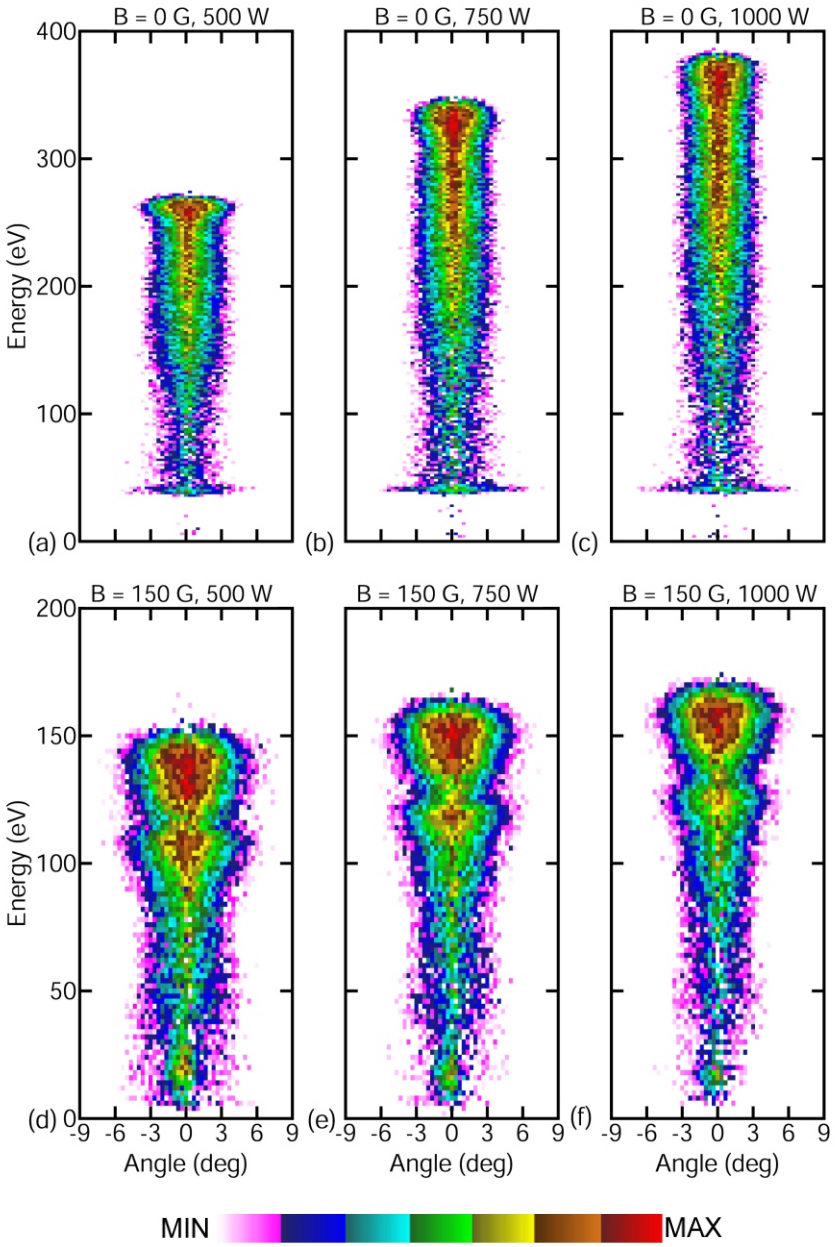

Fig. 3.14 - (Color) IEADs striking the substrate for the base case for P_{HF} = 500 W while varying P_{LF} from 500 – 1000 W. (a)-(c) B = 0 and (d)-(f) B = 150 G. The IEADs have units of $eV^{-1}sr^{-1}$. The contours span 2 decades using a log scale. When P_{LF} increases about P_{HF}, the plasma density increases and the LF voltage does not increase linearly with power.

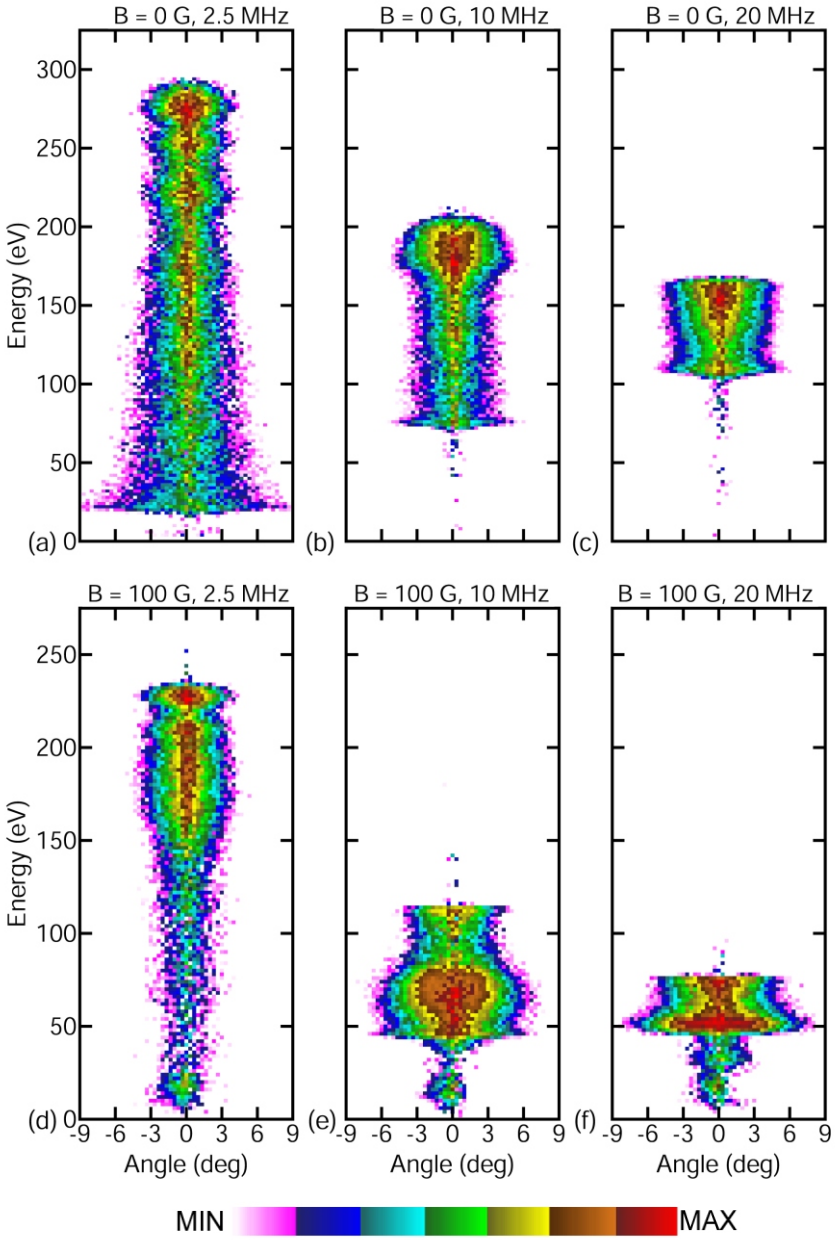

Fig. 3.15 - (Color) IEADs incident onto the substrate for ν_{LF} of 2.5, 10, 20 MHz with (a)-(c) B = 0 and (d)-(f) B = 100 G. The IEADs narrow in energy as ν_{LF} increases. For B = 100 G, the reversal of the sheath during the anodic part of the rf cycle result in the persistence of low energy peaks in IEADs.

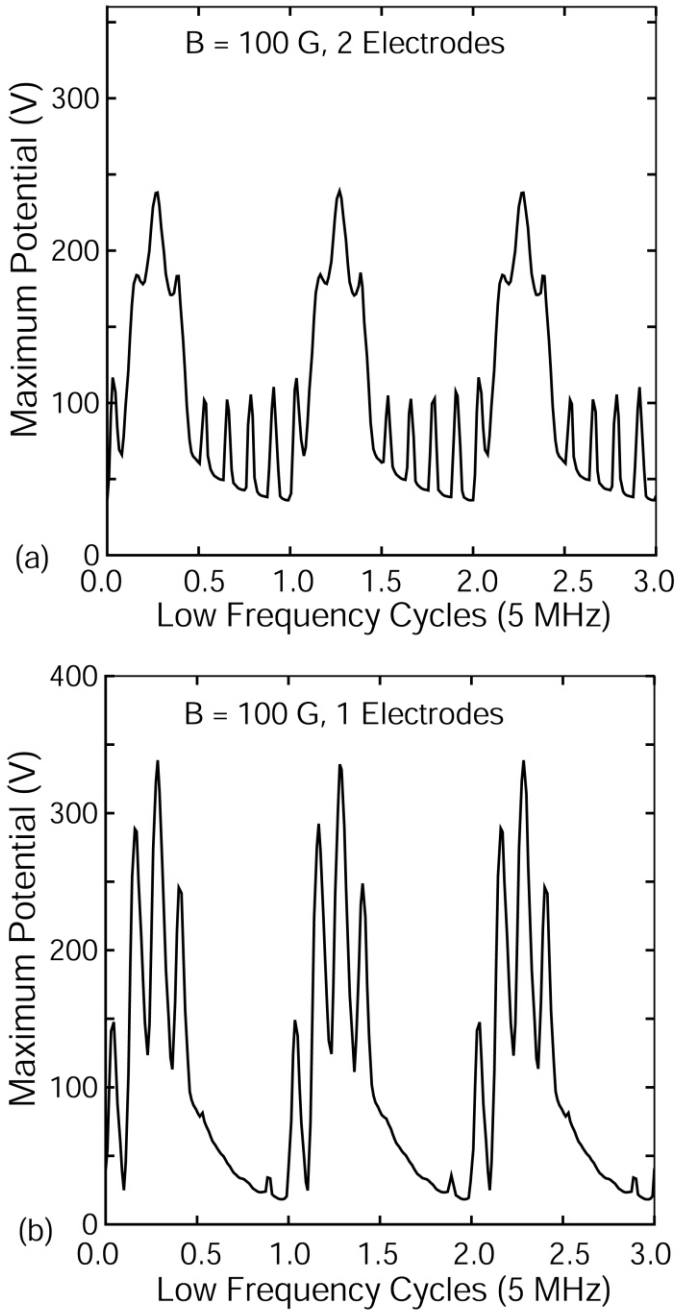

Fig. 3.16 - The maximum plasma potential during 3 *LF* rf cycles for constant applied voltage (V_{LF} = 250 V, V_{HF} = 150 V) with B = 100 G. (a) The *LF* and *HF* sources applied to separate electrodes and (b) both sources are applied to the same electrode. The conditions are otherwise the same as the base case (Ar, 40 mTorr, ν_{LF} = 5 MHz, ν_{HF} = 40 MHz). By switching to the same electrode the large negative V_{LF} nearly eliminates the contribution of the V_{HF} to the plasma potential during the *LF* cathodic cycle.

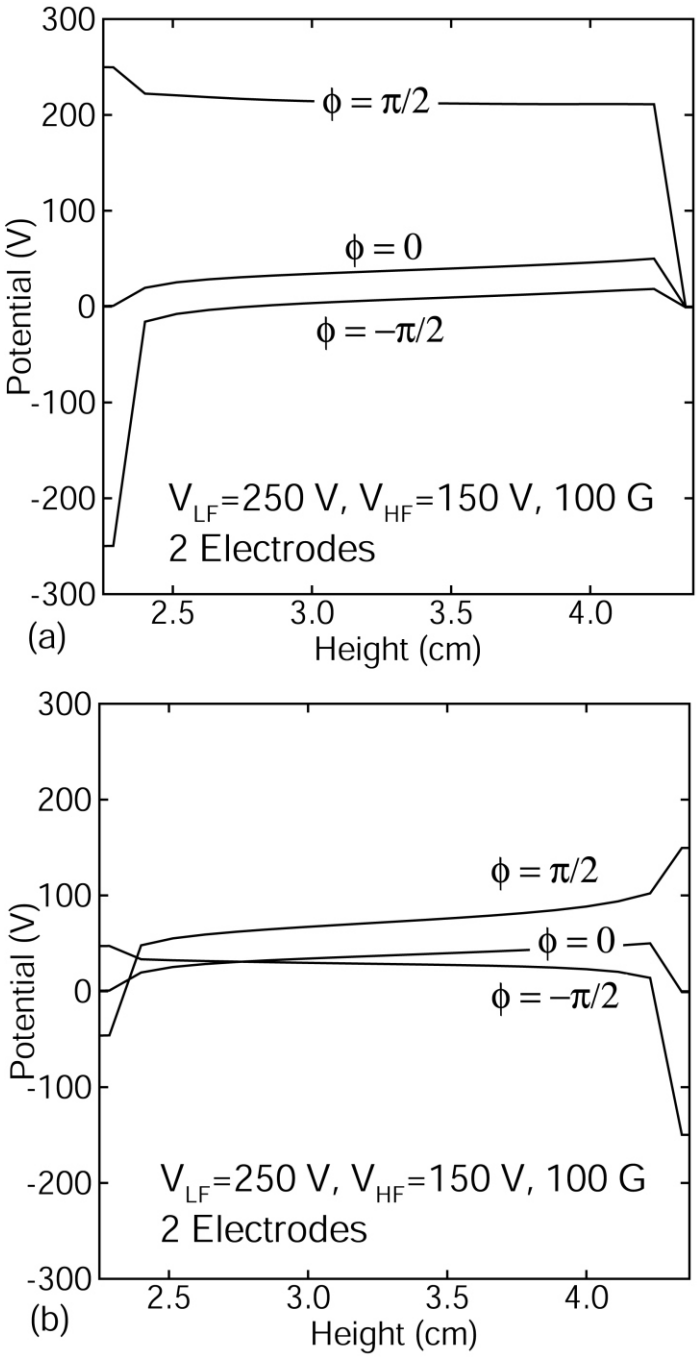

Fig. 3.17 - The plasma potential when the *HF* and *LF* sources are applied to separate electrodes at different times during the rf cycle for constant applied voltage (V_{LF} = 250 V, V_{HF} = 150 V) with B = 100 G. (a) Plasma potential as a function of height at radius r = 5 cm at different fractional phases during the *LF* cycle and (b) for different fractional phases during the *HF* cycle.

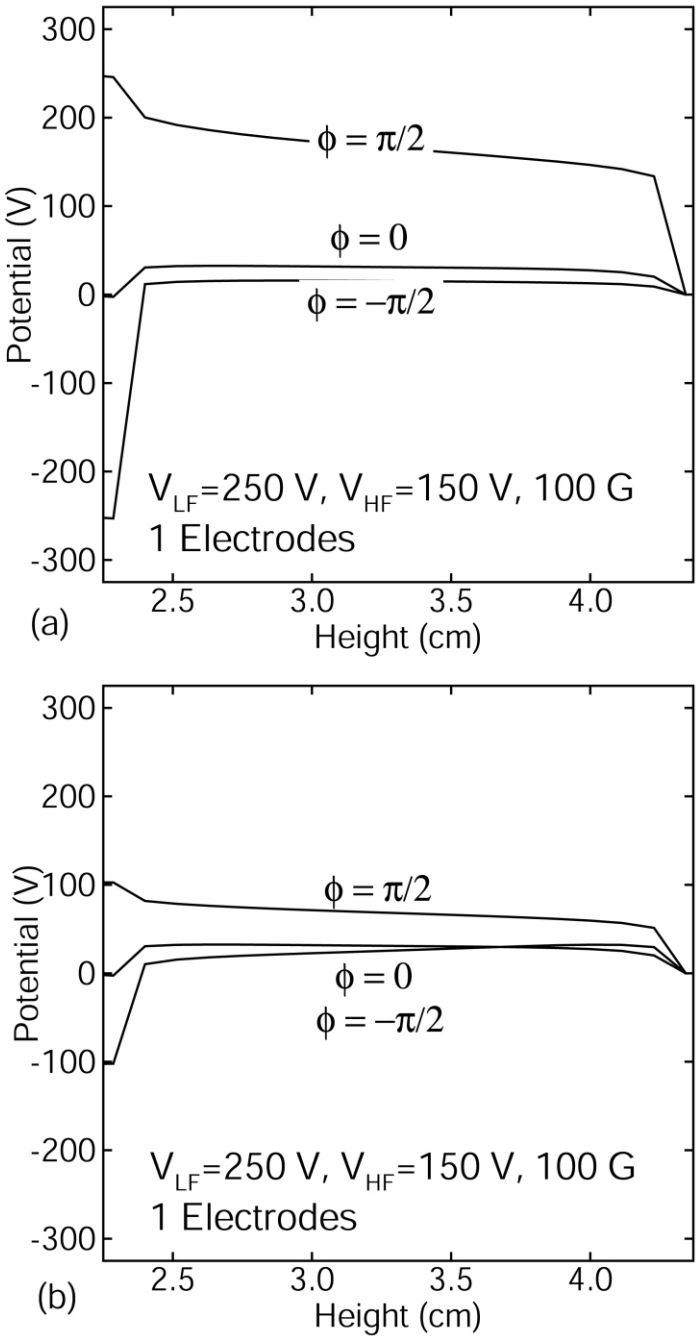

Fig. 3.18 - The plasma potential when the *HF* and *LF* sources are applied to the lower electrode at different times during the rf cycle for constant applied voltage (V_{LF} = 250 V, V_{HF} = 150 V) with B = 100 G. (a) Plasma potential as a function of height at radius r = 5 cm at different fractional phases during the *LF* cycle and (b) for different fractional phases during the *HF* cycle.

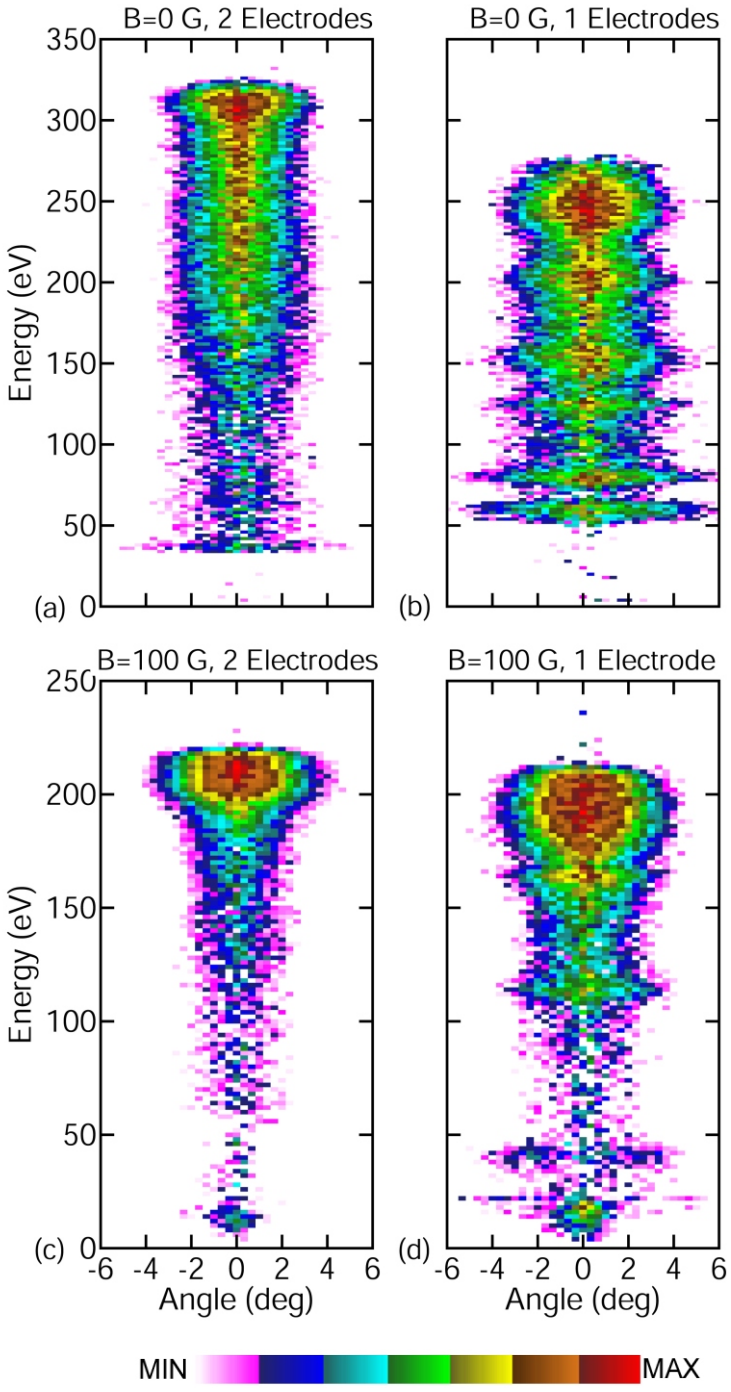

Fig. 3.19 - The comparison of IEADs for applying the *HF* and *LF* sources to separate electrodes and the same electrode. (a) 2-electrodes and (b) 1-electrode for B = 0; and (c) 2-electrodes and (d) 1-electrode for B = 100 G. For B = 0, the narrowing in energy of the IEAD when using the same electrode results from the increase of the frequency at which the sheath oscillates. The low energy tail of the IEAD at B = 100 G persists due to sheath reversal during the *LF* anodic cycle.

3.6 References

1. R. A. Lindley, C. H. Bjorkman, H. Shan, K.-H. Ke, K. Doan, R. R. Mett and M. Welch, J. Vac. Sci. Technol. A **16**, 1600 (1998).
2. K. E. Davies, M. Gross and C. M. Horwitz, J. Vac. Sci. Technol. A **11**, 2752 (1993).
3. M. J. Buie, J. T. P. Pender and P. L. G. Ventzek, Jpn. J. Appl. Phys. **36**, 4838 (1997).
4. P. Berruyer, F. Vinet, H. Feldis, R. Blanc, M. Lerme, Y. Morand and T. Poiroux, J. Vac. Sci. Technol. A **16**, 1604 (1998).
5. G. A. Hebner, E. V. Barnat, P. A. Miller, A. M. Paterson and J. P. Holland, Plasma Sources Sci. Technol. **15**, 879 (2006).
6. V. Georgieva and A. Bogaerts, J. Appl. Phys. **98**, 023308 (2005).
7. T. Kitajima, Y. Takeo, Z. Lj. Petrovic and T. Makabe, Appl. Phys. Lett. **77**, 489 (2000).
8. W. Tsai, G. Mueller, R. Lindquist, B. Frazier and V. Vahedi, J. Vac. Sci. Technol. B **14**, 3276 (1996).
9. P. C. Boyle, A. R. Ellingboe and M. M. Turner, J. Phys. D: Appl. Phys. **37**, 697 (2004).
10. P. A. Miller, E. V. Barnat, G. A. Hebner, A. M. Paterson and J. P. Holland, Plasma Sources Sci. Technol. **15**, 889 (2006).
11. E. V. Barnat, P. A. Miller, G. A. Hebner, A. M. Paterson, T. Panagopoulos, E. Hammond and J. Holland, Plasma Sources Sci. Technol. **16**, 330(2007).
12. Z. Donko and Z. Lj. Petrovic, Jpn. J. Appl. Phys. **45**, 8151 (2006).
13. L. Z. Tong and K. Nanbu, Europhys. Lett. **75**, 63 (2006).
14. H. H. Goto, H. Lowe and T. Ohmi, J. Vac. Sci. Technol. A **10**, 3048 (1992).
15. S. Rauf, IEEE Trans. Plasma Sci. **31**, 471 (2003).
16. P. Subramonium and M. J. Kushner, J. Vac. Sci. Technol. A **20**, 313 (2002).

17. A. V. Vasenkov and M. J. Kushner, J. Appl. Phys. **95**, 834 (2004).

18. A.V. Phelps and Z. Lj Petrović, Plasma Sources Sci. Technol. **8**, R21 (1999).

4. MODELING OF DUAL FREQUENCY CAPACITIVELY COUPLED PLASMA SOURCES UTILIZING A FULL-WAVE MAXWELL SOLVER

4.1 Introduction

Parallel plate capacitively coupled plasma (CCP) sources are widely used for dry-etching and deposition of materials for microelectronics fabrication. One method of improving the performance of CCP sources is applying multi-frequency radiofrequency (rf) sources with the goal of separately controlling ion and radical fluxes, and ion energy distributions to the substrate.[1-4] Typically in a dual frequency CCP reactor (DF-CCP), power is applied at a lower frequency to the bottom electrode (a few MHz to 10 MHz) holding the wafer; and higher frequency power is applied to the upper electrode (tens of MHz to hundreds of MHz) often also serving as the shower head. Power at the lower frequency is intended to control the shape of the ion energy and angular distributions (IEADs) to the wafer. Power at the higher frequency is intended to control the production of ions and radicals. (In some variants of DF-CCPs, both frequencies are applied to the lower electrode.[4]) Decoupling the two rf sources is desirable to achieve this separate control. With the low frequency (*LF*) kept at a few MHz, increasing the high frequency (*HF*) to tens to hundreds of MHz is necessary to functionally separate the two rf sources.[5]

DF-CCP reactors were first developed at a time when the wafer size was transitioning from 200 mm to 300 mm. With increases in the *HF* and wafer size, and reductions in the effective plasma shortened wavelength, finite wavelength effects became increasingly important in determining the uniformity of the plasma.[6] These effects include constructive and destructive interference and skin effects. For example, the applied voltage at the rear of the electrode must propagate around the edges of the electrode to enter the plasma. At this point, the

resulting electric field is wave-guided in the sheath at the surface of the electrode. At sufficiently low frequency (large wavelength), the electric field uniformly appears across the sheath. For sufficiently short wavelengths, constructive interference of counter-propagating waves from opposite sides of the electrode increases the amplitude of the electric field in the sheath at the center of the electrode. This results in a center-high plasma density.

Perret *et al.* investigated the uniformity of ion fluxes in a large-area square (40 cm × 40 cm) capacitive discharge sustained in argon at 150 mTorr driven at frequencies between 13.56 MHz and 81.36 MHz.[7] Center peaked ion fluxes were observed above 60 MHz with a power deposition of 50 W, an affect attributed to the finite wavelength of the counter-propagating applied electric fields constructively interfering at the center of the reactor. At higher rf power (170-265 W) and higher plasma densities, the conductivity of the plasma increased sufficiently that the skin depth for electric field penetration became commensurate with the electrode gap. At that point, edge peaked ion fluxes were observed due to the skin effect with likely a contribution from electrostatic edge effects that concentrated power there.

Hebner *et al.* performed diagnostics of single frequency and DF-CCP reactors operating in argon and driven at frequencies between 10 and 190 MHz.[8-9] They found that with grounded lower electrode the spatial distribution of argon ions transitioned from uniform to center peaked as the excitation frequency was increased on the upper electrode. At 50 mTorr and 60 MHz, they found that electron density transitioned from being uniform as a function of radius to center peaked with increasing power deposition (from 300 W to 1000 W). These trends may be explained by finite wavelength effects due to plasma shortened wavelength with increasing electron density.

Based on an analytic model, Lieberman *et al.* developed scaling laws to describe these

finite wavelength effects.[6] They found that for a discharge radius of 50 cm, an electrode separation of 4 cm, and a sheath width of 2 mm, there is a substantial skin effect for plasma densities higher than 10^{10} cm^{-3}, and there is a substantial standing wave effect for frequencies higher than 70 MHz. Lee *et al.* simulated single frequency CCP discharges using the finite element method.[10] Their two-dimensional continuum model coupled Maxwell's equations (in the frequency domain), fluid plasma equations (in the time domain) and a sheath model. At 80 MHz and 150 mTorr, they found the plasma density transitioned from center high to edge high with an increase in power from 40 to 190 W. While at 150 MHz, their results showed that the plasma density transitioned from edge-high at 40 W to center-and-edge high at 160 W.

Rauf *et al.* numerically investigated the effects of the rf source power, inter-electrode gap and gas mixture (Ar, Ar/SF_6, Ar/CF_4) on CCPs driven at 180 MHz.[11] Their two-dimensional continuum model included Maxwell's equations in the form of scalar and vector potentials. They found that electrostatic effects dominated in electronegative plasmas because the applied rf potential is considerably larger for the same applied power compared to an electropositive plasma; and that the electron density and the rf current flowing through the discharge are smaller.

In this chapter, we build upon these prior works by discussing results from a computational investigation of a DF-CCP reactor with plasmas sustained in Ar and Ar/CF_4. Systematic trends for plasma properties, electron energy distributions (EEDs), ion fluxes and ion energy and angular distributions (IEADs) are discussed for a reactor resembling an industrial design. We found that for discharges sustained in Ar, similar to the trends in a single frequency CCP, the electron density transitions from edge high to center high with increasing *HF* (from 10 to 150 MHz).[7,8] These transitions result from a radial change in the amplitude of the electric field in the sheaths. The shapes of the EEDs near the sheath and in the bulk plasma respond to

these changes in electric field as well. Since the sheath thickness (through the change in plasma density) and time variation of the electric field are sensitive to frequency, the IEADs incident onto the wafer become functions of radius. For discharges sustained in Ar/CF_4 = 90/10, the electron density also transitions from edge high to middle high with increasing *HF* (from 10 to 150 MHz). These trends are due to the coupling of electrostatic edge, skin and finite wavelength effects. The coupling of these affects become spatially dependent as the electronegativity, and so plasma conductivity, also have spatial dependence.

The effects of pressure, *HF* and *LF* power deposition (P_{HF}, P_{LF}), and gas mixtures on plasma properties are also examined with an emphasis on the effects on plasma uniformity. We found that when increasing pressure from 25 to 150 mTorr in Ar/CF_4 = 90/10 mixtures, the electron density transitions from middle high (meaning the maximum is at a middle radius of the wafer) to center high (meaning the maximum is at the center of the reactor) as the energy relaxation distance decreases and more power deposition occurs along the *HF* sheath. The radial profile of electron impact ionization sources begins to mirrors that of the electric field in the *HF* sheath at higher pressures. The *HF* field is center peaked due to the constructive interference of counter-propagating waves, a phenomenon we term the finite wavelength effect.[7] At 50 mTorr, increasing P_{HF} (from 300 W to 1000 W) or P_{LF} (from 300 W to 1500 W) decreases the uniformity of the plasma in Ar/CF_4 mixtures due to dissociative attachment processes and non-uniform power deposition along the *HF* sheath. With increasing CF_4 fraction, the decreasing plasma conductivity increases the effective wavelength of the incident wave in the plasma. The manner of power deposition then transitions from electromagnetic to electrostatic, and the maximum electron density shifts towards being edge high (meaning the maximum electron density is near the edge of electrode). The uniformity of the plasma is improved for CF_4

fractions larger than 0.2, which translates to improve radial uniformity of the ion fluxes and ion energy and angular distributions incident on the wafer.

4.2 Description of the Model and Reaction Mechanisms

The 2-dimensiona (2d) Hybrid Plasma Equipment Model (HPEM) used in this investigation is described in detail in Chapter 2. To capture the high frequency heating, excitation rates are provided by spatially dependent electron energy distributions generated by a Monte Carlo simulation (the EMCS module). As an improvement to the previously described model, a solution of Maxwell's equations is integrated into the plasma hydrodynamics modules of the HPEM. This enables the simulation of the inductive effects that result from wave penetration at high frequency into plasmas and finite wavelength effects, in addition to the electrostatic effects generally accounted for when solving Poisson's equation. This solution was implemented in the time domain so that coupling between frequencies could be explicitly addressed as well as enabling intra-rf period feedback between plasma transport and the wave.

The reaction mechanisms for the Ar and Ar/CF_4 mixtures used in this study are discussed in Ref. [12]. For Ar, the species included in the model are Ar(3s), Ar(4s), and Ar^+. The Ar(4s) is an effective state having a finite lifetime to account for the partial trapping of resonant levels in that manifold. With CF_4, the additional species included in the model are CF_4, CF_3, CF_2, CF, F, F_2, C_2F_3, C_2F_4, C_2F_6, CF_3^+, CF_2^+, CF^+, F^+, CF_3^-, and F^-. For operating conditions in this work, dominant ions and neutral radicals are Ar^+, CF_3^+, F^-, CF_2 and CF.

4.3 Plasma Properties of DF-CCP Reactors Sustained in Ar

The model reactor used in this study is schematically shown in Fig. 4.1. A metal substrate powered at the *LF* (10 MHz) through a blocking capacitor is the lower electrode. A conductive Si wafer (σ = 0.01/Ω-cm), 30 cm in diameter, sits in electrical contact with the substrate which is surrounded by a Si ring (focus ring 1, $\varepsilon/\varepsilon_0$ = 12.5, $\sigma = 10^{-6}$/Ω-cm), a dielectric focus ring (focus ring 2, $\varepsilon/\varepsilon_0$ = 8.5, $\sigma = 10^{-8}$/Ω-cm). The substrate is also encased in a dielectric having $\varepsilon/\varepsilon_0$ = 4.0. Gas is injected through a shower head 34 cm in diameter that also serves as the *HF* electrode. The *HF* electrode is surrounded by a dielectric having $\varepsilon/\varepsilon_0$ = 4.0. All other surfaces in the reactor are grounded metal including the annular pump port.

The base case operating conditions are 50 mTorr of Ar with the *LF* held constant at 10 MHz, delivering an rf power of 300 W. The *HF* is varied from 10 to 150 MHz with a constant power of 300 W. The *HF* and *LF* rf powers are fed into the reactor on the axis at the top and bottom of the reactor, respectively. So the electromagnetic waves are launched where the power cables are connected to the reactor, propagate through the surrounding dielectrics around the metal electrodes and into the plasma. Operating in this high frequency regime is particularly sensitive to the details of the design of the reactor, such as where the rf power is applied and the path the electromagnetic wave follows from the power cable to the plasma. We acknowledge the details of our observations and conclusions may change in a different reactor, though we believe the trends are general to this class of reactor.

The propagation of the *HF* electromagnetic wave in the reactor is partly illustrated in Fig. 4.2, where the EM field is plotted in the time domain (during 3 *HF* rf cycles at 150 MHz) at different radial locations along the *HF* sheath. As the *HF* wave propagates from the edge of the electrode towards the center of the reactor along the *HF* sheath, there is a phase change

corresponding to the propagation delay. The magnitude of the electric field increases due to the constructive interference towards the center of the reactor. Note the electric field becomes increasingly positively biased because the time plotted is during the first half of the *LF* anodic cycle.

4.3.1 Electron Density and Electromagnetic Fields

The electron density ([e]) is shown in Fig. 4.3 for *LF* = 10 MHz (300W) and *HF* = 10-150 MHz (300 W). These quantities have been averaged over the longer *LF* cycle. (The plasma is fairly well confined between the electrodes and does not appreciably extend into the volume of the reactor above the pump port. Therefore only the region of the reactor directly above the substrate is shown in this and following figures.) The reactor averaged electron density increases with increasing *HF* (1.4×10^{10} cm^{-3} at 10 MHz to 2.9×10^{11} cm^{-3} at 150 MHz), a consequence of the increased fraction of power dissipated in electron heating as the *HF* increases. The radial profile of [e] also varies with the *HF*. The electron density transitions from being nearly flat as a function of radius at *HF* =10 MHz, to edge peaked at 50 MHz (with a small peak in the center), to center peaked at 100 and 150 MHz. This general trend agrees with the experimental results reported in Ref. [8], albeit in a different geometry and absent the *LF* power.

With the increasing *HF* from 10 MHz to 150 MHz, the electric field launched by the *HF* rf source transitions from being largely electrostatic to largely electromagnetic. (For brevity, if not otherwise noted, references to the wave amplitude, phase, skin depth and wavelength are for the *HF* rf source.) This transition is partly indicated by the increasing phase change of the axial EM field in the *HF* sheath with increasing *HF*, as shown in Fig. 4.4a. Note that our model computes the EM field in the time domain. A Fourier transform is performed at the *HF* to obtain

the spatially dependent phase and magnitude of the first harmonic. At all *HF*, the phase change per cm diminishes towards the center of the reactor, which indicates a transition from a traveling wave to a standing wave due to constructive interference. Standing waves are formed when two waves having the same frequency propagate in the opposite direction. So even at 10 MHz, a standing wave is formed at the center of the reactor. This standing wave does not, however, produce significant non-uniformities in the plasma as its wavelength is much longer than the radius of the electrode.

The wave propagating inwards along the *HF* sheath is basically a surface wave and a simple analytical solution of its effective wavelength does not exist. Its wavelength was estimated by

$$\lambda_{eff} = \frac{2\pi}{(\partial\phi/\partial r)} \tag{1}$$

where λ_{eff} is the plasma effective wavelength and $\partial\phi/\partial r$ is the derivative of the phase change in the radial direction. The estimated wavelengths in the *HF* sheath as a function of radius (from 10 to 15 cm) are shown in Fig. 4.4b for *HF* = 10-150 MHz. The wavelength decreases with increasing *HF* and the half-wavelength becomes commensurate to the electrode diameter for *HF* > 100 MHz. The increase in the wavelength with decreasing radius is somewhat artificial as the phase change diminishes towards the center of the reactor. So the estimated wavelength near the periphery of the upper electrode is most indicative.

As the wavelength decreases with increasing *HF*, the EM field in the *HF* sheath becomes increasingly center peaked due to constructive interference. This trend is shown in Fig. 4.4c, where the magnitude of the *HF* electric field in the sheath is plotted as a function of radius for

HF = 10-150MHz. The fields are normalized by their values at r = 0 to emphasize their radial variations. At 10 MHz, the EM field is largely uniform with larger values near the periphery of the *HF* electrode resulting from electrostatic edge enhancement. As the *HF* increases, the wavelength decreases and the magnitude of the electric field near the edge of the electrode decreases as the location is near the zero node at a quarter wavelength. When exceeding 100 MHz the finite wavelength effect dominates over edges effect and the field becomes center peaked. At 150 MHz, the amplitude of the EM field is larger by a factor of 1.7 from the edge to the center of the electrode. This radial increase, responsible for the center peaked electron density at 150 MHz, originates from the shortening of the wavelength. As such, it may be more accurate to refer to a center high plasma density at high frequency being produced by a finite wavelength effect instead of a standing wave effect, as standing waves are produced even at 10 MHz.

The skin depth also decreases with increasing *HF*. The skin depth as a function of height at r = 5 cm for *HF* =10-150 MHz is shown in Fig. 4.5a. We calculated the skin depth according to [13]

$$\delta = \frac{1}{\omega\sqrt{\mu\varepsilon}\left\{\frac{1}{2}\left[\sqrt{1+(\sigma/\omega\varepsilon)^2}-1\right]\right\}^{1/2}}, \qquad (2)$$

where $\omega = 2\pi f$ is the angular frequency, and σ the plasma conductivity. Note that this skin depth corresponds to the evanescent wave that propagates into the bulk plasma, not to the surface wave that propagates along the *HF* sheath. Exceeding 100 MHz, the skin depth in the bulk plasma is less than 1 cm, which is shorter than half the electrode separation. Note that the skin

depth is calculated at r = 5 cm where the electron density is relatively high for *HF* of 100 MHz and 150 MHz. The skin depth in the low electron density region (for example, near the edge of the *HF* electrode) is commensurate with the electrode separation. Therefore, even at 150 MHz the *HF* wave can penetrate across the gap and propagate into the *LF* sheath at the edge of the reactor. The wave then propagates along the *LF* sheath towards the center of the reactor and so modulates the electric field in the *LF* sheath. This modulation is shown in Fig. 4.5b, where the axial electromagnetic field in the *LF* sheath at r = 1 cm is plotted in the time domain.

4.3.2 Inductive Electric Fields and Power Deposition

The *HF* wave propagates into the bulk plasma from the edge of the *HF* electrode, and so the absorption of the wave by the plasma is usually strongest near the edge of the *HF* electrode in the axial direction (into the bulk plasma). The axial gradient of the magnetic field therefore peaks near the edge of the *HF* electrode, which in turn, produces a peak in the radial *HF* field. This radial *HF* field tends to enhance the power deposition near the edge of the electrode thereby increasing the local plasma density. This radial field and its electron heating effects are usually referred to as the inductive field and inductive heating. [6, 8-11]

The magnitude of the radial *HF* field (first harmonic amplitude, E_{mr}) is shown in Fig. 4.6 for *HF* = 10-150 MHz. (To resolve E_{mr} in the bulk plasma, the dynamic range of the color bar in Fig. 4.6 does not resolve the large electric field in the dielectrics near the electrode edges and at the *HF* power cable.) As expected, E_{mr} peaks near the *HF* electrode edge at all *HF*. The magnitude of E_{mr} is not a linear function of *HF*, as the electron density profiles change with the *HF* and so do the absorption, reflection and diffraction patterns of the *HF* wave. The axial profile of E_{mr} is flat in the bulk plasma at the edge of the upper electrode for *HF* of 10 and 50

MHz owing to the large skin depth at those frequencies. As the *HF* increases, E_{mr} tends to flow along the plasma-sheath edge, producing a minimum in the bulk plasma.[6] However, even at 150 MHz, E_{mr} is relatively flat as a function of height near the edge of the *HF* electrode where the electron density is low and the local skin depth is commensurate with the electrode separation. In the bulk plasma near the edge of the *HF* electrode, the magnitudes of E_{mr} (1-4 V/cm from 10 to 150 MHz in Fig. 4.6) are much larger than those of the axial *HF* field (0.06-0.3 V/cm from 10 to 150 MHz). This results from the radial gradient of the *HF* magnetic field being much smaller than the axial gradient due to the radially traveling surface wave.

The contribution of E_{mr} to the bulk power deposition near the electrode edges is partly shown in Fig. 4.7, where the total power deposition is plotted for *HF* = 10-150 MHz. The total power deposition is obtained by a *LF* cycle average of the instantaneous power, $P_{tot} = (1/\Delta t)\int \vec{E} \cdot \vec{J} \Delta t$, where Δt is the *LF* period. With increasing *HF*, the power deposition in the middle of the electrode gap near the edge increases, indicating an increasing skin effect. The maximum in the power deposition is, however, in the sheath and this maximum moves towards the center of the reactor with increasing frequency as a result of the surface wave effect (Fig. 4.7c).[6] The skin effect, which increases power deposition in the bulk plasma, does not produce a maximum in [e] at the edge of the electrode at *HF* ≥ 100 MHz due to power deposition being dominated by the surface wave.

The *HF* and *LF* voltage amplitudes were adjusted to maintain constant power at their respective frequencies as the *HF* is increased. Due to the increase in plasma density, these voltage amplitudes generally decrease with increasing *HF*. For example, to maintain 300 W, at *HF* = 10 MHz, the rf amplitude at the *HF* cable is 125 V, whereas at *HF* = 150 MHz, the

amplitude is 78 V. However, the rf voltage amplitudes are not linear function of *HF* and depend on the details of the reactor geometry. For this particular geometry, at 50 and 100 MHz, the reactor behaves like a resonator and lower *HF* voltage amplitudes are required to deposit 300 W (45 V at 50 MHz and 30 V at 100 MHz). The *LF* rf voltage amplitude is not a linear function of the *HF* irrespective of the linearly increasing plasma density. For example, the *LF* rf voltage amplitude increases from 148 V at *HF* = 10 MHz to 193 V at *HF* = 100 MHz, and then decreases to 169 V at *HF* = 150 MHz. The DC bias generally decreases with increasing *HF*, (from -100 V at *HF* = 10 MHz to - 46 V at *HF* = 150 MHz), in agreement with previous studies.[14]

4.3.3 Electron Energy Distributions and Ionization Sources

Successful application of DF-CCP tools in semiconductor processing depends on selectively promoting desired plasma chemical reactions and preventing undesirable reactions through tailoring of the reactive fluxes to the substrate. The production of these fluxes in turn ultimately depends on electron impact reactions with feedstock gases and their fragments. As such, the ability to tailor EEDs is key to this selectivity as EEDs control the generation of radical and ions through electron impact reactions.

The tailoring of EEDs by varying the *HF* is shown in Fig. 4.8-4.9 where EEDs near the center (r = 2 cm), middle (r = 8 cm) and the edge of the electrodes (r = 15 cm) are plotted for *HF* = 50 MHz and 150 MHz. EEDs are shown at the edge of the *HF* sheath (z = 4.6 cm), mid gap (z = 3.5 cm) and at the edge of the *LF* sheath (z = 2.3 cm). (See Fig. 4.1 for these locations.) At *HF* = 50 MHz, the response of the EEDs to electric fields penetrating into the plasma is a small enhancement of the tail of the EED at large radius. This enhancement in the tail of the EED is most prominent near the *LF* sheath due to the stronger electrostatic edge effect at *LF*. The EEDs

are nearly uniform as a function of radius across the *HF* sheath. Regardless of the locations, the EEDs are typically single-temperature distributions.

With increasing *HF*, there is a transition from a single-temperature to a two-temperature EED. This transition likely results from the more efficient sheath heating at higher *HF*, which populates the high energy tail.[15] At 150 MHz, the tails of EEDs in the *HF* sheath are lifted in the center and middle of the reactor compared to the edge. This lifting results from the finite wavelength effect which produces a larger electric filed in the center of the reactor compared to the edge. With the skin depth being shorter than the electrode separation at 150 MHz, the penetration of *HF* wave into the bulk plasma is weakened and the tails of EEDs at mid-gap in the center of the plasma are not enhanced. In fact, the EEDs in the bulk plasma near the edge of the *HF* electrode are lifted in the range of 0-20 eV, an effect most likely resulting from enhanced Ohmic heating in the low electron density region. The electric field in the *LF* sheath is modulated at the *HF*. The end result of this modulation by the *HF* fields, which are center peaked, and *LF* fields, which are edge peaked, is a fairly uniform EED along the *LF* sheath.

The electron impact ionization sources by bulk electrons (S_b) are shown in Fig. 4.10 and the ionization sources by beam electrons (S_{eb}) are shown in Fig. 4.11 for *HF* = 10-150 MHz. (Beam electrons refer to electrons produced by secondary emission from the *HF* and *LF* electrodes by ion bombardment and which are accelerated in the sheaths.) As the *HF* increases, there is a systematic shift in the maximum of both S_b and S_{eb} towards the *HF* electrode and towards the center of the reactor. The shift towards the center of the reactor results from the constructive interference of the finite wavelength effect which increases the magnitude of the electric fields in the *HF* sheath and so populates the tails of the EEDs which are most responsible for ionization. The shift upwards towards the *HF* electrode can be attributed to at least two

effects – the transition from bulk Ohmic heating to sheath heating as being the dominant source of power and a decrease in the skin depth. At *HF* = 10 and 50 MHz, Ohmic heating dominates and S_b is maximum in the bulk plasma. With increasing *HF*, stochastic sheath heating begins to dominate and S_b becomes more localized towards the sheath. This shift in power deposition tends to be self-reinforcing. As the electron density shifts towards the center of the reactor a larger fraction of the power deposition occurs there which, for a fixed total power deposition, reduces the proportion at larger radius. Also, as the tail of the EED is populated at *HF* and the energy relaxation distances decreases, a larger fraction of the power deposition occurs near the *HF* electrode.

The radial dependence of the ionization sources from beam electrons, S_{eb}, largely mirrors that of the ion density. The ion fluxes into the electrodes produce the secondary electrons. The secondary electrons are launched into the bulk plasma with nearly the instantaneous sheath potential, which is modulated by both the *HF* and *LF* fields. The maximum energies of the secondary electrons usually exceed hundreds of eV. This produces a mean free path commensurate with the electrode separation. Since the amplitude of the *HF* sheath is typically lower than the *LF* sheath, the secondary electrons from the *HF* electrode have lower energies and so are more collisional. They are also more likely to be reflected back into the bulk plasma by the more negative *LF* sheath, a phenomenon termed *trapping*. Secondary electrons from the *LF* electrode are more energetic and more likely to be collected by the *HF* electrode as they are able to climb the negative potential of the smaller *HF* sheath. The end result is that, the secondary electrons produce less than 10% of the total ionization.

4.4 Plasma Properties in Ar/CF_4

4.4.1 Electron and Negative Ion Densities and Electromagnetic Fields

Discharges sustained in Ar/CF_4 mixtures behave fundamentally differently from those sustained in pure Ar owing to the electronegativity of CF_4. Dissociative attachment of CF_4 and its fragments mainly generates F^- and CF_3^-. The dominant attachment processes have resonant cross sections which are non-zero between 4.4 and 12 eV and have a peak at about 8 eV of 0.025 $Å^2$.[16] Although the rates of attachment are low compared to thermal attaching molecules such as Cl_2, these processes nevertheless decrease the electron density as they require lower electron energies compared with ionization (having a threshold energy of 16.5 eV). Perhaps more important, the products of these processes, negative ions, can also affect the spatial distribution of electrons by reshaping electrostatic potential, which in turn shapes the plasma conductivity. The final outcome is that the effective plasma wavelength and skin depth change in a non-monotonic manner as a function of both frequency and radial position, all of which induce different electromagnetic effects.

The electron density ([e]) and total negative ion density ($[M^-] = [CF_3^-]+[F^-]$) are shown in Figs. 4.12 and 4.13 for *LF* = 10 MHz (300 W) and *HF* = 10-150 MHz (300 W) for Ar/CF_4 = 90/10 at 50 mTorr. Both the electron density and negative ion density increase with increasing *HF* due to more efficient electron heating and less power dissipation by ion acceleration. The electronegativity, defined by a reactor average $[M^-]/[e]$, increases from 0.64 at 10 MHz, to 1.1 at 100 MHz, and then decreases to 0.94 at 150 MHz. The total negative ion density transitions from edge high between 10-50 MHz, to flat at 100 MHz, and to center high at 150 MHz. With increasing *HF*, the electron density transitions from edge high between 10-50 MHz, to center-and-edge high at 100 MHz, and finally to having a maximum at mid-radius at 150 MHz. In comparison, [e] is center peaked in pure Ar discharges at *HF* = 150 MHz. This outwards shift of

the peak electron density with increasing fraction of electronegative gases was also observed by Rauf et al.[11] For example, they found that the electron density transitions from center high in pure Ar discharges to being maximum at mid-radius for discharges sustained in Ar/SF_6 = 95/5 (160 MHz, 500 W, 50 mTorr).

Negative ions are heavy and relatively cool, and so cannot climb the ambipolar potential barrier or sheath potential to reach the electrodes. As a result, negative ions are confined to the electropositive core of the plasma. As the electronegativity of the core of the plasma increases, the plasma potential flattens.[17] This flattening of the potential allows for a more uniform axial distribution of the electron density. Although the maximum values of electron density with increasing *HF* are smaller than those in discharges in pure argon, the effective plasma quarter wavelengths are still commensurate with the electrode diameter, as shown in Fig. 4.14. Correspondingly the *HF* electric field transitions from edge peaked at 10-50 MHz to center peaked exceeding 100 MHz, also shown in Fig. 4.14.

4.4.2 Electron Energy Distributions

EEDs for Ar/CF_4=90/10 are shown at the edge of the *HF* sheath, mid-gap and the edge of the *LF* sheath at different radii in Fig. 4.15 for 50 MHz and Fig. 4.16 for 150 MHz. Similar to the trends in pure Ar, the EEDs transition from single-temperature distributions at 50 MHz to two-temperature distributions at 150 MHz. This is due, in part, to the similarity in the radial profiles of the electric field in the *HF* sheath in pure Ar and Ar/CF_4=90/10. The EEDs at 50 MHz near the *HF* sheath and mid-gap are essentially the same as a function of radius, with the tail of the EED raised towards the center of the reactor. This occurs even though the electric field in the sheath is not yet peaked at the center of the reactor. From the edge to the center of

the plasma, the electron density decreases by a factor of 4 along the *HF* sheath. So the lifting of the tails of the EED likely results from enhanced Ohmic heating in the center of the reactor where the electron density is relatively low.

At 50 MHz, in the bulk plasma, the electron density decreases by about a factor of 2 from the edge to the center of the reactor. The relative role of Ohmic heating in the center compared to the edge of the electrodes is therefore less pronounced in the bulk plasma compared to along the *HF* sheath. The compromise between less Ohmic heating in the center and larger sheath electric fields near the edge of the electrode produces nearly uniform EEDs in the bulk plasma. In the *LF* sheath, the compromise is such that the tails of EEDs are most prominent in the middle of the reactor (Fig. 4.15c).

The EEDs for *HF* = 150 MHz in Ar/CF_4=90/10 have 2-temperature distributions. As the electric field in the *HF* sheath is center peaked, the tails of EEDs near the *HF* sheath are lifted in the center and middle of the reactor relative to the edge. This enhancement in the tail of the EEDs extends to the bulk-plasma and to the *LF* sheath. This likely indicates a more efficient coupling of the *HF* wave through the bulk plasma to the *LF* sheath due to the lower plasma density than obtained in pure argon. The *HF* wave can either couple to the *LF* sheath through the low conductivity region of the bulk plasma near the periphery of the electrodes, or propagate around the reactor as a surface wave and then couple to the *LF* sheath. For this particular reactor, we found that the coupling through the bulk plasma is more important.

4.4.3 Electronegative Effects

Although the trends of the electromagnetic fields in Ar/CF_4 mixtures are qualitatively the same as in pure Ar, the response of the plasma and the distribution of plasma density are

different. This results from a correlation between the electron and negative ion densities which change with *HF*. For example, S_b, and [M^-] are shown in Fig. 4.17 for *HF* = 10-150 MHz in the axial and radial directions. For *HF* ≤ 50 MHz, S_b is positive throughout the reactor and [M^-] is fairly uniform, which reflects the nearly uniform EEDs. Exceeding 100 MHz, sheath heating begins to dominate, lifting the tail of the EEDs and so electrons are produced primarily closer to the oscillating *HF* sheath. Electrons are also produced to a lesser extent closer to the *LF* sheath due to more efficient coupling of the *HF* to the lower sheath. (S_b near the *LF* sheath is typically 3-5 times smaller than near the *HF* sheath). Concurrently, there is an increase in the epi-thermal portion of the EED which overlaps the dissociative attachment cross sections in the bulk plasma in the center of the reactor due to the transition to a two-temperature distribution. This increases the rate of attachment sufficiently that the net source by bulk electrons is negative in the center of the plasma. The [M^-] therefore shifts towards the center of the reactor. The flatter plasma potential also reduces the magnitude of the bulk electric field and so the amount of Ohmic heating decreases.

The compromise between the positive S_b near the *HF* and *LF* sheath and the negative S_b in the bulk plasma (all in the center of the reactor) is partly responsible for the electron density being peaked at mid-electrode at 150 MHz. This shift in electron density is also partly facilitated by the confinement of negative ions in the center of the reactor, which flattens the local plasma potential and enables electrons to diffuse or drift to the periphery of the reactor.

Beam electrons emitted from the powered electrodes are launched into the bulk plasma with essentially the instantaneous sheath potential. So these beam electrons are not particularly efficient at producing dissociative attachment having low energy resonant cross sections. As such, the ionization source by beam electrons (S_{eb}) is positive throughout the reactor for all

frequencies. The ionization by beam electrons accounts for 10-15% of the total ionization. The radial profile of S_{eb} largely mirrors that of the total ion fluxes onto the wafer and transitions from edge high for *HF* ≤ 50 MHz to uniform at *HF* = 100 MHz, to middle high at *HF* = 150 MHz.

4.4.4 Ion Density, Flux and IEADs Incident on the Wafer

The spatial distributions of ions and their fluxes to the wafer ultimately depend on their sources due to electron impact ionization (or excitation, indirectly) and their subsequent transport and reactions. Since plasma processes such as etching and deposition depend on the relative fluxes of ions, changes in these values as a function of frequency may have an impact on the robustness of the process. For example, the Ar^+ density is shown in Fig. 4.18 for *HF* = 10-150 MHz and Ar/CF_4 = 90/10. With increasing *HF*, $[Ar^+]$ transitions from being largely uniform at 10 MHz, to being edge peaked between 50-100 MHz, and to being middle peaked at 150 MHz. Since CF_n^+ ions do not charge exchange to Ar, the distribution of Ar^+ in large part reflects its ionization sources, subsequent losses and transport but not additional sources. The volumetric loss of Ar^+ is largely due to charge exchange reactions with CF_4 having a mean free path of 2 cm at 50 mTorr.[18] The edge peak in Ar^+ at 50 MHz corresponds to higher ionization sources due to the extended tails of EEDs near the edge of the *LF* electrode. The Ar(4s) density largely mirrors the electron density from 10 to 150 MHz and so multistep ionization also contributes to the edge peak of Ar^+. Exceeding 50 MHz, the maximum of $[Ar^+]$ shifts towards the *HF* electrode and the center of the reactor where sheathing heating and the finite wavelength effect produces energetic electrons that both ionize Ar and produce Ar(4s) which is then ionized. At 150 MHz, $[Ar^+]$ is peaked in the middle of the reactor due in large part to multistep ionization. The Ar^+ flux incident on the wafer closely mirrors $[Ar^+]$ at all *HFs*, as shown in Fig. 4.18.

The CF_3^+ density ($[CF_3^+]$) is shown in Fig. 4.19 for *HF* = 10-150 MHz and Ar/CF_4 = 90/10. Ionization of CF_4 to generate CF_3^+ has a threshold energy of 16.5 eV which is nearly equal to that for Ar^+. As a result, the electron impact sources for Ar^+ and CF_3^+ should be similar. In spite of its higher mass, the mobility of CF_3^+ is larger than Ar^+ in this mixture due to the lack of symmetric (or asymmetric) charge exchange with a neutral species having a large density. As a result, the spatial distribution of CF_3^+ is generally more uniform than for Ar^+, which is reflected in the fluxes to the wafer, also shown in Fig. 4.19.

The plasma density at the edge of the pre-sheath and magnitudes of the *LF* and *HF* components in the lower sheath ultimately determine the radial uniformity of IEADs onto the wafer. To demonstrate these dependencies, we separately collected the IEADs over the center of the wafer (from r = 0 to 7.5 cm) and over the outer portion of the wafer (from r = 7.5 to 15 cm). The IEADs for Ar^+ and CF_3^+ are shown in Fig. 4.20 for *HF* = 50, 100 and 150 MHz. At 50 MHz, the IEADs for CF_3^+ are more extended in energy on the outer portion of the wafer than at the center. The IEADs for Ar^+ have an opposite trend. This is particularly the case for the energy of the peak in the IEAD. These differences likely result from the plasma density being larger near the edge of the electrode producing a thinner sheath, coupled with subtleties of the responses of ions having different masses and charge exchange cross sections. So not only is there a center-to-edge variation in the IEADs but these trends are different for different ions. At 100 MHz, the IEADs are essentially uniform from center-to-edge for a given ion though there are still significant differences between Ar^+ and CF_3^+, the former having a broader distribution in energy in part due to its smaller mass.

At 150 MHz, ions bombard the wafer with higher energies compared with 50 and 100 MHz, an effect that can be attributed to two factors. First, at 50 and 100 MHz the chamber

behaves like a resonator and a lower *HF* rf voltage is required to deposit 300 W. Though the DC bias decreases from 50 to 150 MHz (less negative, from -100 to -46 V) due to the increasing electronegativity, the maximum allowable ion energy, $V_{HF} + V_{LF} - V_{DC}$, largely remains the same from 50 to 150 MHz (about 310 eV). Second, the higher plasma density at 150 MHz reduces the *LF* sheath thickness, thereby reducing the ion transit time across the sheath and extending the maximum extent of the IEAD. The likelihood for charge exchange in the sheath also diminishes. The end result is an increase in the ion energies bombarding the wafer at 150 MHz. As the plasma density and the *HF* field decrease over the outer half of the wafer, the electrostatic component of the *LF* sheath field decreases and the sheath thickness increases. The IEADs of Ar^+ and CF_3^+ are therefore shifted down in energy and have a larger center-to-edge deviation compared to 100 MHz.

4.5 Scaling with Pressure

Increasing pressure increases electron-neutral collision frequencies, reduces the mean free path for energy relaxation, and reduces diffusion losses, thereby increasing the plasma density for a constant power deposition. This increase in plasma density has been experimentally observed over a wide range of operating conditions in high frequency CCP discharges.[8-9] The increase in the electron density above the increase in pressure emphasizes skin depth effects by shortening the absorption length, thereby increasing the relative power deposition near the edges of the electrodes where the electromagnetic field enters the plasma. The energy relaxation distance also decreases with increasing pressure, thereby localizing power deposition by electrostatic field enhancement. So transitioning to an edge-high distribution of plasma is expected with increasing pressure. Volynets *et al.* performed diagnostics in a single

frequency CCP reactor driven at 100 MHz in pure argon and argon/fluorocarbon gas mixtures.[19] With increasing pressure and holding power constant at 750 W, they found that the spatial distribution of the plasma transitioned from center high at 10 mTorr to center-and-edge high at 80 mTorr (with a higher peak at the edge).

In pure Ar discharges, our computational results qualitatively agree with the experimental results in Ref. [19]. To match the experiment conditions in Ref. [19], a 100 MHz rf source is applied on the upper electrode delivering a power of 750 W to sustain a pure Ar discharge (no *LF* power). At 100 MHz, the sheath field is center peaked due to the prevalence of the finite wavelength effect. The electron density at the mid gap as a function of radius is shown in Fig. 4.21 at 10, 50 and 80 mTorr. With increasing pressure, the electron density transitions from center high at 10 and 50 mTorr to edge high at 80 mTorr. The center high to edge high transition with increasing pressure results from the dominance of the skin effects associated with the evanescent wave propagating into the bulk plasma and the surface wave propagating along the *HF* sheath.

To investigate the consequences of pressure at a high excitation frequency on plasma uniformity in electronegative gas mixtures, the *LF* and *HF* were held constant at 10 and 150 MHz respectively, each delivering 300 W. The gas mixture is Ar/CF_4 = 90/10. The electron density ([e]) is shown in Fig. 4.22 while varying pressure from 25 to 150 mTorr. The electron density has been averaged over the longer *LF* cycle. With increasing pressure, the electron density moderately increases from a maximum of 9.8×10^{10} cm^{-3} at 25 mTorr to 1.4×10^{11} cm^{-3} at 150 mTorr. Exceeding 50 mTorr, the maximum in electron density shifts towards the center of the reactor and towards the *HF* electrode. This inward shift with increasing pressure is

different from what is observed in pure Ar discharges (an outward shift) and largely results from electronegative effects, as will be explained later.

The magnitude of the *HF* electric field (first harmonic amplitude, E_m) in the *HF* sheath is shown in Fig. 4.23a as a function of radius for pressures from 25 to 150 mTorr. The electric fields are normalized by their values at r = 0 to emphasize their radial variations. From 25 to 150 mTorr, the radial profile of the EM field largely remains the same as the electron density is only increased by about a factor of only 1.4. Given the increase in electron collision frequency with increasing pressure, the small change in electron density is not sufficient to produce dramatic changes in the plasma-shorted wavelength. As such, the finite wavelength effect alone is not responsible for the transition from middle high to center high electron density.

Concurrent to the increase in the electron density with increasing pressure, the electron-neutral collision frequencies also increase. So the plasma conductivity and consequently, the skin depth, are not linear functions of pressure, as shown in Fig. 4.23b. The magnitude of the radial *HF* field (first harmonic amplitude, E_{mr}) as a function of radius in the middle of the gap is shown in Fig. 4.23c for pressures from 25 to 150 mTorr. Exceeding 75 mTorr, E_{mr} decreases with pressure at small radii, an indication of the plasma overall being less conductive. Near the edge of the *HF* electrode (r = 17 cm), the magnitude of the radial *HF* field does not change systematically with pressure. The peak values of E_{mr} near the edge of the electrode at 100 mTorr and 150 mTorr are still less than that at 25 mTorr. As such, the inductive heating from the radial *HF* field and skin effects are not particularly enhanced with increasing pressure under our operating conditions.

The consequences of the shortening of the energy relaxation distance with increasing pressure on the spatial distribution of EEDs are partly shown in Fig. 4.24, where EEDs at

different distances from the *HF* electrode are plotted at r = 5 cm for 25 and 150 mTorr. At 25 mTorr, the EEDs in the bulk plasma (d = 1.7-0.3 cm where d is the distance from the *HF* electrode) are largely indistinguishable due to the large energy relaxation distance and uniform Ohmic heating in the bulk plasma. The energy relaxation distance can be estimated by $\lambda_\varepsilon \approx (\lambda_m \lambda_{in}/3)^{1/2}$, where λ_m is the total mean free path for momentum transfer and λ_{in} is the mean free path accounting for all collisional energy loss processes.[20] λ_ε decreases from 2.1 to 0.36 cm from 25 mTorr to 150 mTorr. The tails of EEDs near the *HF* sheath (d = 0.1 and 0.2 cm) are lifted due to the stochastic sheath heating that dominates at 150 MHz. At 150 mTorr, there is a systematic depression of the EEDs from the *HF* electrode into the bulk plasma due to the shortening of the energy relaxation distance. At the lower pressure, the tail remains high to mid-gap.

The shortening of the energy relaxation distance with increasing pressure also results in increasing power deposition along the *HF* sheath, as shown in Fig. 4.25a-b. The total power deposition is obtained by an average over the *LF* cycle of the instantaneous power, $P_{tot} = (1/\Delta t)\int \vec{E} \cdot \vec{J}\, dt$, where Δt is the *LF* period. As more power is dissipated closer to the *HF* electrode with increasing pressure, the bulk electron impact source function (S_b) becomes increasingly peaked in the *HF* sheath, as shown in Fig. 4.25c. In turn, in the radial direction, S_b increasingly mirrors the electric field in the *HF* sheath (Fig. 4.25d), which is center peaked from due to the finite wavelength effect. The close correleation of S_b with power deposition and the decrease in energy relaxation distance is ultimately responsible for the shift of the peak electron density towards the center of the reactor with increasing pressure. With increasing pressure, attachment progressively dominates over ionization processes in the bulk plasma adjacent to the *HF* sheath and so net electron losses result, as shown in Fig. 4.25c. Further into the bulk plasma,

the attachment losses decrease as the epi-thermal portion of the EED that overlaps the dissociative attachment cross sections is also depressed. This effect is most pronounced at higher pressures due to the more distinct separation of the EEDs between the sheath and bulk regions.

The shift in the maximum electron density towards the center of the reactor with increasing pressure observed at a *HF* of 150 MHz is a function of the value of the high frequency. For example, at *HF* = 50 MHz (for otherwise same operating conditions), the electron density remains edge peaked from 25 mTorr to 150 mTorr. The shortening of the energy relaxation distance with increasing pressure does results in increasing power deposition along the *HF* sheath. However, different from 150 MHz, the *HF* electric field is edge peaked at *HF* = 50 Hz and so is the ionization source. Since the [e] is already edge peaked at 25 mTorr, further increasing the pressure only reinforces this spatial nonuniformity since the power deposition becomes more localized.

The spatial distributions of ions and their fluxes to the wafer ultimately depend on their sources due to electron impact ionization, and their subsequent transport and reactions. The ionization cross sections of Ar and CF_4 (branching to CF_3^+ and F) have similar thresholds and magnitudes (within a factor of 1.5). However, unlike CF_3^+, Ar^+ has large cross sections for symmetric charge exchange for charge exchange reactions with CF_4 and its fragments.[18] In spite of the larger mass of CF_3, it has a larger effective mobility than Ar^+ due to the latter's large rate of momentum transfer and depleting reactions. As such, even though their source functions are similar, differences between the spatial distributions of Ar^+ and CF_3^+ develop with increasing pressure.

For example, the Ar^+ density and Ar^+ flux incident on the wafer are shown in Fig. 4.26

for pressures of 25, 50, 75 and 100 mTorr for an Ar/CF_4 = 90/10 mixture. With increasing pressure, the maximum $[Ar^+]$ increases from 1.0×10^{11} cm^{-3} at 25 mTorr to 2.1×10^{11} cm^{-3} at 100 mTorr. The spatial distribution of $[Ar^+]$ follows that of the electron density, shifting towards the center of the reactor and towards the *HF* electrode. The mean free path for loss of Ar^+ from charge exchange reactions with CF_4 and its fragments decreases with increasing pressure and so its distribution appears less diffusion dominated and more like its source function. The mean free path for Ar^+ charge exchanging with CF_4 decreases from about 4 cm at 25 mTorr to 0.8 cm at 150 mTorr.[18] As the source of Ar^+ moves away from the wafer with increasing pressure and Ar^+ is depleted by charge exchange reactions while diffusing to the wafer, the Ar^+ flux decreases with increasing pressure.

The CF_3^+ density and flux incident on the wafer are shown in Fig. 4.27. The maximum $[CF_3^+]$ increases from 4.6×10^{10} cm^{-3} at 25 mTorr to 2.1×10^{11} cm^{-3} at 100 mTorr. Although the source of CF_3^+ undergoes the same transition as that of Ar^+ with increasing pressure (increasingly center peaked along the *HF* sheath), the profile of CF_3^+ is more diffusion dominated. In the absence of significant identity changing charge exchange reactions, volumetric losses are dominated by positive-negative ion recombination. As such, the CF_3^+ flux incident on the wafer linearly increases with pressure, which reflects the increase in the ionization sources of both Ar^+ and CF_3^+.

The plasma density at the edge of the lower sheath, and the magnitudes of the *LF* and *HF* components in the lower sheath, ultimately determine the radial uniformity of IEADs onto the wafer. To show these dependencies, we separately collected IEADs over the center of the wafer (from r = 0 to 7.5 cm) and over the edge of the wafer (from r = 7.5 to 15 cm). The IEADs for Ar^+ and CF_3^+ are shown in Fig. 4.28 for pressures of 25 and 150 mTorr. The IEADs for CF_3^+ are

less extended in energy than those for Ar^+ as CF_3^+ is heavier and experiences more rf cycles (both *HF* and *LF*) when traversing the *LF* sheath. As the overall uniformity of the plasma is not significantly improved from 25 to 150 mTorr, large center-to-edge ratios of the sheath thickness and the electric field at the lower sheath persist with increasing pressure. Consequently, there is a large center-to-edge variation of IEADs across the wafer from 25 to 150 mTorr.

4.6 Scaling with *HF* Power Deposition

In an ideal DF-CCP reactor, varying the *HF* power while keeping other operating conditions unchanged should only modulate the magnitude of the plasma density and leave the spatial distribution of the plasma and the IEADs incident on the wafer unchanged. Booth *et al*. experimentally investigated the dependence of electron density and ion flux on rf power in a DF-CCP reactor (*LF* = 2 MHz and *HF* = 27 MHz).[21] They found that both the 27 and 2 MHz rf powers have significant effects on the plasma density and the ion flux, likely due to the relative small separation between the *LF* and the *HF*. The goal of separately controlling the radical fluxes and the ion energies onto the wafer is achieved to some degree in our model reactor when keeping the *LF* power constant at 300 W in an Ar/CF_4 = 90/10 mixture at 50 mTorr. For example, the total negative ion density remains center peaked while varying *HF* power deposition (P_{HF}) from 300 W to 1000 W, as shown in Fig. 4.29a. The magnitude of the negative ion density increases (and perhaps becomes slightly more center peaked) with power deposition. This is due to the decrease in the plasma wavelength with increase in conductivity at higher powers which intensifies the constructive interference at the center of the reactor, though this is a small effect.

The electron density is shown in Fig. 4.29b while varying *HF* power from 300 to 1000 W.

The maximum electron density linearly increases with P_{HF}, from 1.1×10^{11} cm^{-3} at 300 W to 3.0×10^{11} cm^{-3} at 1000 W. As P_{HF} increases, the electron density profile becomes increasingly middle peaked. This trend results from the combination of at least two factors. First, as P_{HF} increases and the excited state densities increase, multi-step ionization processes account for a larger fraction of the total ionization. Since this contribution scales with the square of the electron density, there is a larger fractional change at higher plasma densities. Second, increasing P_{HF} is most efficient at lifting the tails of EEDs near the *HF* sheath. In the bulk plasma, the EEDs are less affected due to the decreasing skin depth of the *HF* with increasing electron density, as shown in Fig. 4.30a-b. In fact, the bulk Ohmic heating decreases as a fraction of the total power with increasing P_{HF} due to the increasing electron density. With increasing P_{HF}, the electron temperature T_e ($\langle \varepsilon \rangle = \frac{3}{2} kT_e$) near the *HF* sheath increases while T_e in the bulk plasma decreases, as shown in Fig. 4.30c. The end result is that in the center of the reactor, the electron losses from dissociative attachment processes dominate over the gains from ionization processes (at least, over the range of P_{HF} studied). This trend prevents the maximum of the electron density from moving towards the center of the reactor.

Although the electron density is middle peaked for P_{HF} = 300-1000 W, the tails of EEDs are most lifted in the center of the reactor. This is a consequence of the maximum in the electric field in the sheath produced by the constructive interference in the finite wavelength effect. The end result is that the [Ar^+] and [CF_3^+] profiles are also middle peaked but to a less degree compared to the electron density (Fig. 4.29 c-d). Due to the lack of charge exchange losses, the [CF_3^+] profile is more axially uniform and diffusion dominated compared to that of [Ar^+].

The radial profiles of ion fluxes incident on the wafer largely mirror the radial profiles of their densities – the center-to-edge ratios increase with increasing P_{HF}, as shown in Fig. 4.31. As

the plasma becomes increasingly non-uniform with increasing P_{HF}, so do the thickness and electric field of the *LF* sheath. The IEADs therefore become increasingly more non-uniform (center-to-edge) with increasing P_{HF}, as shown in Fig. 4.32. The IEADs incident on the wafer are not independent of P_{HF} for our operating conditions. As the electron and ion densities increase with increasing P_{HF} from 300 W to 1000 W, the *LF* voltage decreases to keep the *LF* power deposition constant. The decrease in *LF* rf amplitude over this range in *HF* power is 160 V to 90 V and the change in dc bias is -41V to -5 V. The IEADs therefore degrade in energy. In doing so, the radial variation of the IEADs is somewhat diminished at 1000 W.

4.7 Scaling with *LF* Power Deposition

In a DF-CCP rector, the role of the *LF* power deposition (P_{LF}) is to control the IEADs incident onto the wafer without, ideally, affecting the magnitude of the fluxes nor their spatial dependencies. T_e as a function of height is shown in Fig. 4.33 at r = 2 cm while varying *LF* power deposition from 300 W to 1500 W. The increase in *LF* rf amplitude for P_{LF} from 300 W to 1500 W is 160 V to 376 V and the change in dc bias is -41 V to -110 V. The *HF* power is kept constant at 300 W and the gas mixture is Ar/CF_4 = 90/10 at 50 mTorr. Increasing P_{LF} mainly increases Ohmic heating in the bulk plasma with only a small contribution to stochastic heating due to the increase in sheath speed with increasing amplitude. The bulk T_e therefore increases with P_{LF}, by only about 0.5 eV (from 0.8 eV to 1.3 eV at mid gap in the center of the reactor) for P_{LF} of 300 to 1500 W, though there is a measurable effect.

As a consequence of the small increase in T_e in the bulk plasma with increasing P_{LF}, the rates of attachment decrease while those for ionization increase. For example, at P_{LF} = 300 W, there are net losses of electrons in the bulk plasma over the inner two thirds of the wafer due to

dissociative attachment. Increasing P_{LF} increases the rate of bulk ionization and the region and the net electron losses shrinks. This trend is shown in Fig. 4.34, where the electron impact ionization sources by bulk electrons (S_b) and beam electrons (S_{eb}) are shown for P_{LF} of 300 W and 1500 W. The region of net negative S_b decreases in volume with increasing P_{LF}, particularly near the center of the reactor. S_{eb} also generally increases with increasing P_{LF} due to the increase in ion fluxes to the wafer which increases the rate of secondary electron emission. Since these secondary electrons are launched into the bulk plasma with nearly the instantaneous *LF* sheath potential with energies usually exceeding hundreds of eV, they do not directly contribute to the resonant attachment processes as there is little overlap with the cross sections.

Following the transition in S_b at the center of the reactor from net negative to net positive with increasing P_{LF}, the maximum of electron density also shifts inwards, as shown in Fig. 4.35a. The maximum electron density increases with P_{LF} (from 1.1×10^{11} cm^{-3} for P_{LF} = 300 W to 2.4×10^{11} cm^{-3} at 1500 W), though not in direct proportion to the increase in P_{LF}. This is a consequence of the majority of the *LF* power still being dissipated by ion acceleration. These trends are essentially the same as those measured experimentally, albeit with different operating conditions.[21] The maximum positive ion densities also increases with P_{LF}, though not in direct proportion. The maximum [Ar^+] at mid-gap increases from 1.0×10^{11} cm^{-3} at P_{LF} = 300 W to 1.7×10^{11} cm^{-3} at 1500 W. The positive ion densities also transition from being middle peaked to center peaked as P_{LF} increases, as shown in Fig. 4.35b-d. The maximum negative ion density at the mid-gap decreases from 1.1×10^{11} cm^{-3} at P_{LF} = 300 W to 8.8×10^{10} cm^{-3} at 1500 W. This small decrease in negative ion density likely results from the increasing T_e in the bulk plasma which is not favorable to attachment processes. With the increase in electron density, the shift towards the center of the reactor is exacerbated by the finite-wavelength effect. The higher

plasma density produces a shorter wavelength which contributes to more intense constructive interference in the center of the reactor.

In the model reactor, the magnitude of the ion fluxes, the ion energies onto the wafer and their spatial dependencies are functions of P_{LF}. The fluxes of positive ions largely mirror their respective ion densities, transitioning from being middle peaked to being center peaked with increasing P_{LF}, as shown in Fig. 4.36. As the *LF* rf amplitude increases with P_{LF} to deposit more power, the IEADs incident on the wafer shift up in energy and also narrow in angle with increasing P_{LF}. For example, the IEADs incident onto the wafer for P_{LF} = 1500 W is shown in Fig. 4.37. (See Fig. 4.32a for IEADs with P_{LF} = 300 W.) This is, to some degree, the desired result – controlling the shape of the IEAD with *LF* power if other plasma properties, such as magnitude and uniformity of fluxes, are not affected. As the plasma remains non-uniform with increasing P_{LF}, so do the *LF* sheath thickness and the electric field at the lower electrode. Hence a large center-to-edge variation of IEADs across the wafer persist with increasing P_{LF} from 300 W to 1500 W.

4.8 Scaling with Gas Chemistry

In high frequency CCPs, the relative importance of electromagnetic and electrostatic effects are functions of the gas mixture, particularly electronegative mixtures, through its influence on the conductivity of the plasma. This in turn impacts the uniformity of the plasma. For example, Rauf *et al.* investigated the consequences fractional substitution of CF_4 and SF_6 to 100 mTorr of argon in a 100 W CCP operating at 180 MHz.[11] They found that the maximum of the electron density shifted towards the edges of the electrodes with increasing SF_6 and CF_4 fraction, effects attributed to the change in spatial dependence of conductivity with addition of

the electronegative gas. The outward shift in electron density in Ar/CF_4 was less intense due to the lower electronegativity of CF_4 compared to SF_6.

Our results for scaling of plasma properties with CF_4 fraction in Ar/CF_4 mixtures generally agree with those of , Rauf *et al.*[11]. For example, the electron density is shown in Fig. 4.38 for CF_4 fractions of 0 to 0.3 for a pressure of 50 mTorr and $P_{LF} = P_{HF} = 300$ W. With increasing CF_4 fraction there is a systematic shift of the peak electron density towards the edge of the electrodes and a decrease in the peak electron density (from 3.8×10^{11} cm^{-3} for pure Ar to 4.4×10^{10} cm^{-3} for Ar/CF_4=70/30). As the electron density decreases, so does the conductivity of the plasma. The effective plasma wavelength therefore increases which weakens the finite wavelength effect by reducing constructive interference at the center of the electrode. This weakening is shown in Fig. 4.39a, where the electric field along the *HF* sheath is plotted as a function of radius. With increasing CF_4 fraction, the *HF* sheath field becomes less center peaked and the plasma becomes more electrostatic in nature.[11] Another consequence of the decreasing electron density is an increase in the skin depth, as shown in Fig. 4.39b, which contributes to more bulk electron heating and so improves the overall uniformity of the plasma.

As the uniformity of the electron density improves with increasing CF_4 fraction, the radial uniformities of ion densities, and their fluxes incident on the wafer also improve, as shown in Fig. 4.40 and Fig. 4.41. The axial gradient for $[Ar^+]$ is more severe compared to $[CF_3^+]$ due to the large rate of charge exchange reactions which deplete Ar^+.[18] The density and flux of Ar^+ decrease, while those of CF_3^+ increase, with increasing CF_4 fraction. The uniformities of the plasma and fluxes to the wafer optimize at a CF_4 fraction of about 0.2.

As the uniformity of the thickness and the magnitude of the electric field in the *LF* sheath track that of the plasma, the uniformity of the IEADs to the wafer are also functions of the CF_4

fraction. For example, IEADs incident to the wafer for Ar^+ and CF_3^+ are shown in Fig. 4.42 for $Ar/CF_4 = 0.8/0.2$. Due to the improved uniformity of the plasmas, the center-to-edge uniformity of IEADs also improves compared to lower CF_4 fractions. (See Fig. 4.32a for IEADs with $Ar/CF_4 = 90/10$.)

4.9 Concluding Remarks

The properties of dual frequency capacitively coupled plasma sources sustained in Ar and Ar/CF_4 have been computationally investigated using results from a two-dimensional plasma transport model having a time-domain solution of the full-wave, Maxwell equations to resolve electromagnetic and electrostatic effects. Similar to the single frequency CCP, in pure Ar DF-CCPs show the trend of a shift in the peak electron density towards the center of the reactor as the *HF* increases. With increasing *HF*, the length of the wave decreases and the phase change along the *HF* sheath increases. From 10-150 MHz, the phase change diminishes toward the center of the reactor, indicating the formation of standing wave. The radial non-uniformity of the *HF* field is therefore increased and center peaked for *HF* exceeding 100 MHz due to constructive interference from this finite wavelength effect. The larger electric field in the *HF* sheath lifts the tails of EEDs in the center of the reactor, thereby increasing ionization rates and producing a center peaked electron density. The maximum of the ionization source, corresponding to the spatial variations of EEDs, shifts towards the center of the reactor and towards the *HF* electrode due to the enhanced sheath heating and decreasing energy relaxation distance with increasing *HF*.

For discharges sustained in $Ar/CF_4 = 90/10$, the electron density transitions from edge high between 10-50 MHz, to center-and-edge high at 100 MHz, to mid-radius high at 150 MHz.

This trend likely results from the increasing electronegative nature of the plasma which flattens the time averaged plasma potential. As in the pure Ar discharge, the EEDs in Ar/CF_4 transition from single-temperature at 50 MHz to a two-temperature distribution at 150 MHz, with tails of EEDs being most prominent near the *HF* sheath in the center of the reactor. This lifting of the tail of the EED also produces increases in the densities of negative ions and CF_3^+ in the center of the reactor. The peak in electron density at mid-radius partly results from the enhanced attachment losses in the center of the reactor. The Ar^+ density is peaked in the middle of the reactor from the multi-step ionization as the Ar(4s) density mirrors the electron density. The plasma non-uniformity at 50 and 150 MHz translates to the non-uniformity of ion fluxes and IEADs incident on the wafer.

With increasing pressure, while keeping other operating conditions unchanged (P_{HF} = P_{LF} = 300 W, 50 mTorr, Ar/CF_4 = 90/10), the maximum of the electron density shifts towards the center of the reactor and towards the *HF* electrode. The shift towards the *HF* electrode is due to the decreasing energy relaxation distance with increasing pressure. As more power is dissipated closer to the *HF* sheath, the bulk electron ionization source increasingly mirrors the electric field in the *HF* sheath which is center peaked due to the finite wavelength effect. Changes in power deposition due to changes in skin depth and inductive heating are not major effects for our operating conditions.

With increasing P_{HF} (P_{LF} = 300 W, 50 mTorr, Ar/CF_4 = 90/10), the uniformity of the plasma decreases and the electron density becomes increasingly mid-peaked. Though the ionization sources are center peaked along the *HF* sheath, the large rates of attachment in the bulk plasma at the center of the reactor prevent the peak electron density from moving inwards. Increasing P_{HF} also results in a degradation in the energy of the IEADs incident on the wafer.

The *LF* voltage decreases with increasing plasma density to maintain a constant *LF* power deposition.

Increasing P_{LF} (P_{HF} = 300 W, 50 mTorr, Ar/CF_4 = 90/10) increases bulk and beam ionization and while reducing net electron losses from dissociative attachment processes in the center of the reactor. As a result, the electron density becomes increasingly center peaked. Exceeding P_{LF} = 1000 W, the plasmas become highly non-uniform and with large center to edge variations of ion fluxes and IEADs incident on the wafer.

Increasing the CF_4 fraction (P_{HF} = P_{LF} = 300 W, 50 mTorr) in argon decreases the electron density thereby increasing the effective plasma wavelength. The uniformity of the electric field along the *HF* sheath consequently improves thereby improving the uniformity of the plasma. For our conditions, the uniformity of ion fluxes and IEADs incident onto the wafer optimize with CF_4 fractions of about 0.2.

Due to the coupling of finite wavelength, electromagnetic skin, electrostatic edge and electronegative effects, there are no simple scaling laws for plasma uniformity when varying gas mixture, power and pressure. The plasma uniformity is a function of conductivity and energy relaxation distance with a strong second order effects due to feedback of EEDs on ionization sources. The consequences of the operating parameters on the plasma properties in DF-CCP reactors can be better understood by analyzing the correlation of finite wavelength, electromagnetic skin, electrostatic edge and electronegative effects, and their impact on the spatial distributions of EEDs.

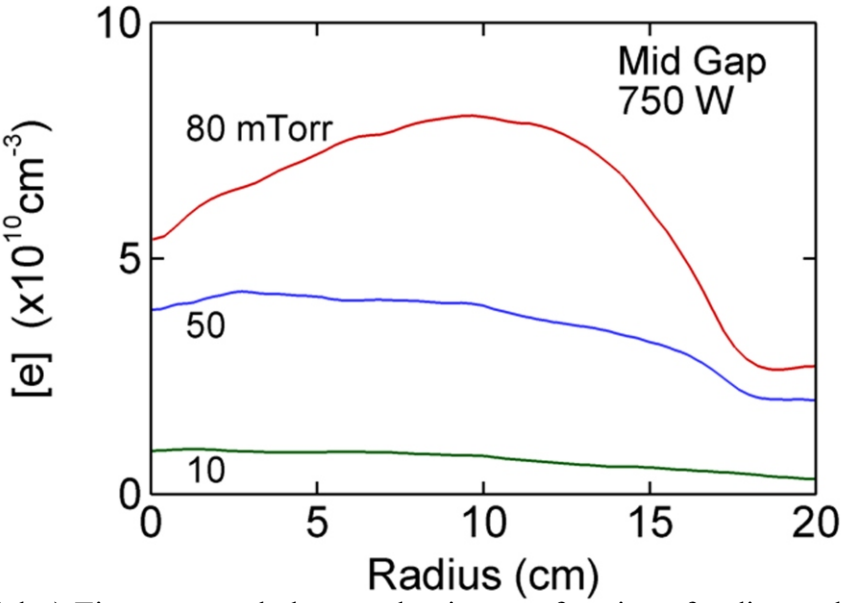

Fig. 4.21 - (Color) Time averaged electron density as a function of radius at the mid gap with a single frequency excitation (100 MHz from the upper electrode) in pure Ar discharges. Note in this paper, results in pure Ar discharges are only presented in Fig. 2. All other figures are for results in Ar/CF_4 mixtures.

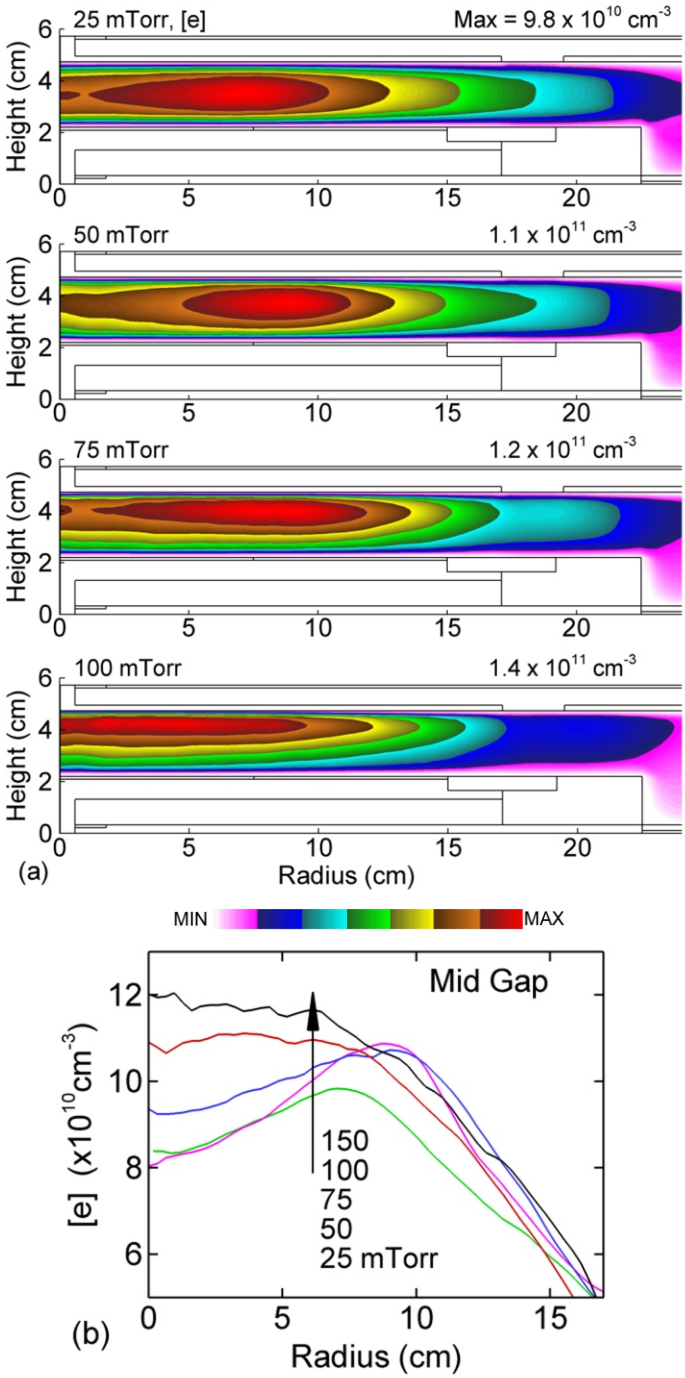

Fig. 4.22 - (Color) Time averaged electron density ([e]) for increasing pressure (Ar/CF_4 = 90/10, $P_{HF} = P_{LF}$ = 300 W, *HF* = 150 MHz, *LF* = 10 MHz). (a) Electron density for pressures of 25, 50, 75 and 100 mTorr, (b) radial [e] profile at mid gap. The maximum value or range of values in each frame is noted. The electron density is on a linear scale. The maximum of the electron density shifts towards the center of the reactor, and towards the *HF* electrode. The finite wavelength effect is not responsible for this shift.

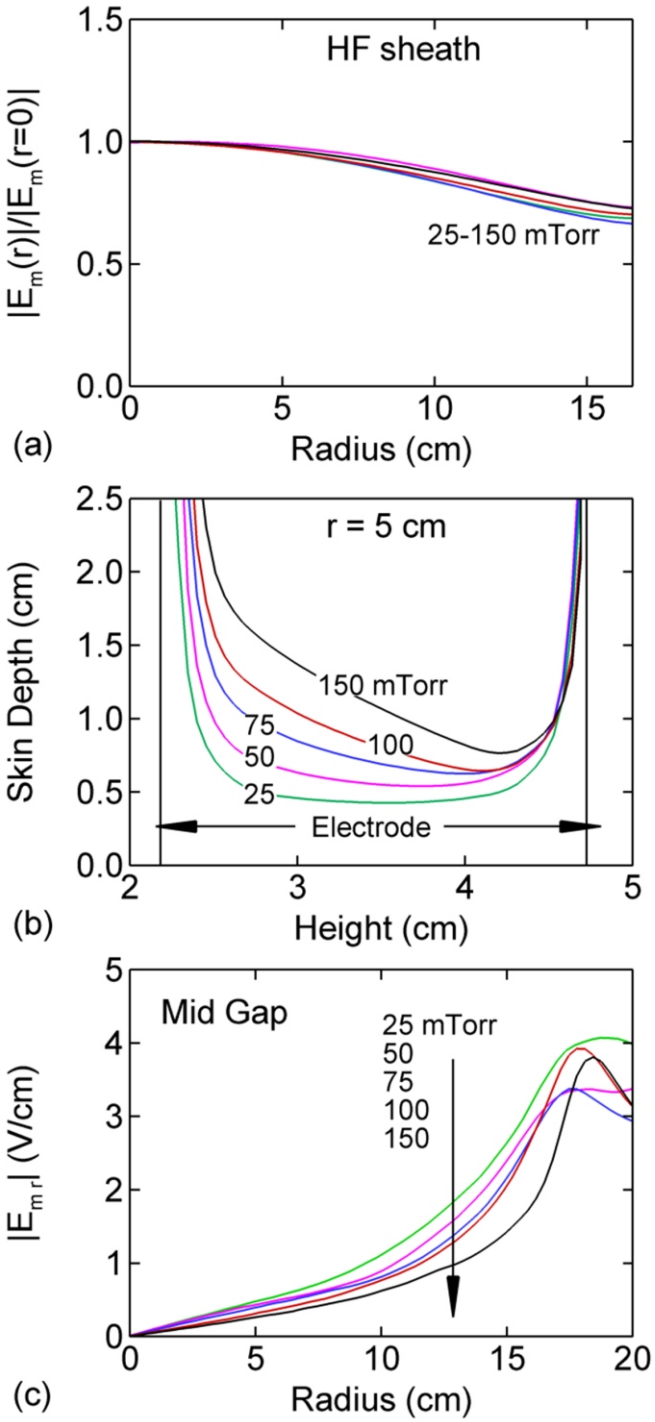

Fig. 4.23 - (Color) Electromagnetic properties for pressures of 25, 50, 75, 100 and 150 mTorr (Ar/CF_4 = 90/10, $P_{HF} = P_{LF}$ = 300 W, *HF* = 150 MHz, *LF* = 10 MHz). (a) Magnitude of the *HF* field (first harmonic amplitude, E_m) along the *HF* sheath (Normalized by the magnitude of the field at the center of the reactor), (b) skin depth as a function of height at r = 5 cm and (c) magnitude of the radial *HF* field (first harmonic amplitude, $|E_{mr}|$). The skin depth and the maximum of $|E_{mr}|$ are not linear function of pressure due to the nonlinear changes in the plasma conductivity.

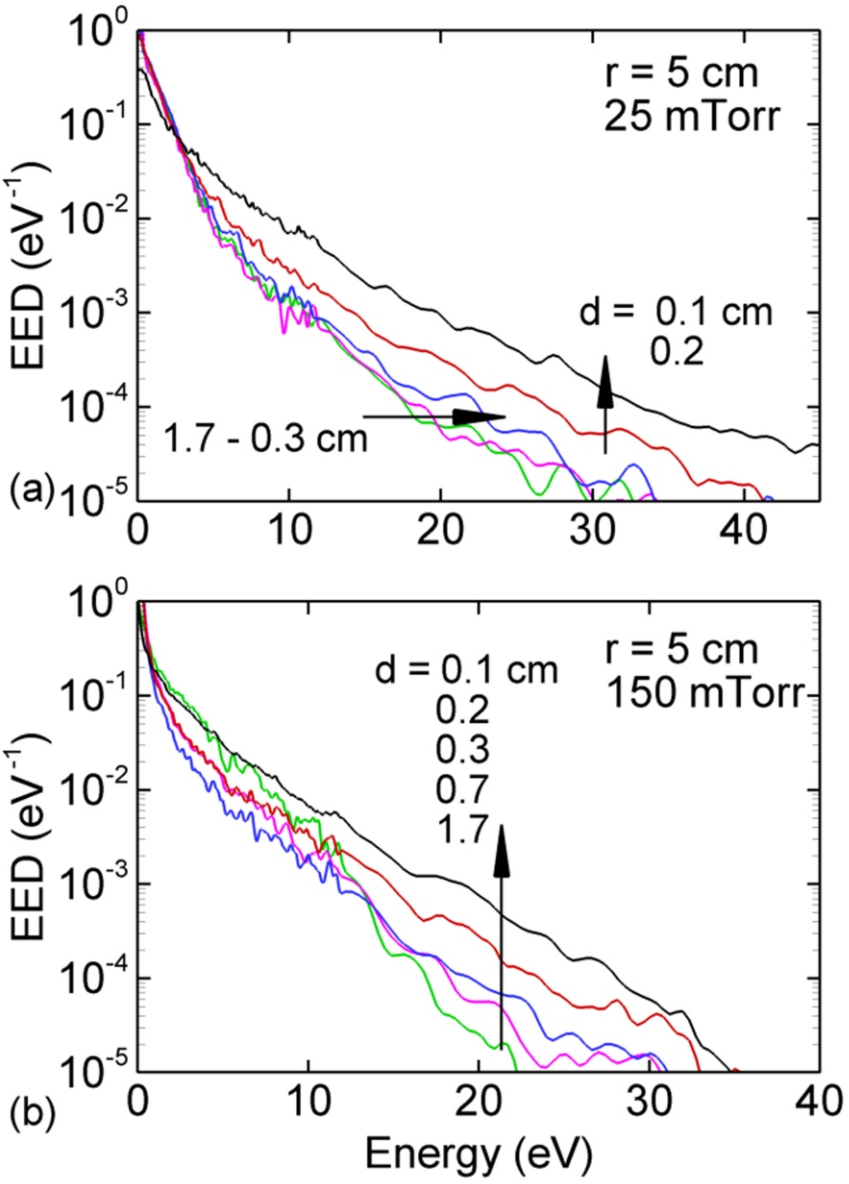

Fig. 4.24 - (Color) EEDs at different axial locations at r = 5 cm (Ar/CF_4 = 90/10, $P_{HF} = P_{LF}$ = 300 W, *HF* = 150 MHz, *LF* = 10 MHz). (a) 25 mTorr, (b) 150 mTorr. The distances to the *HF* electrode are noted in each frame. At 150 mTorr, the electron energies are systematically degraded from the *HF* electrode into the bulk plasma due to the shortening of energy relaxation distance.

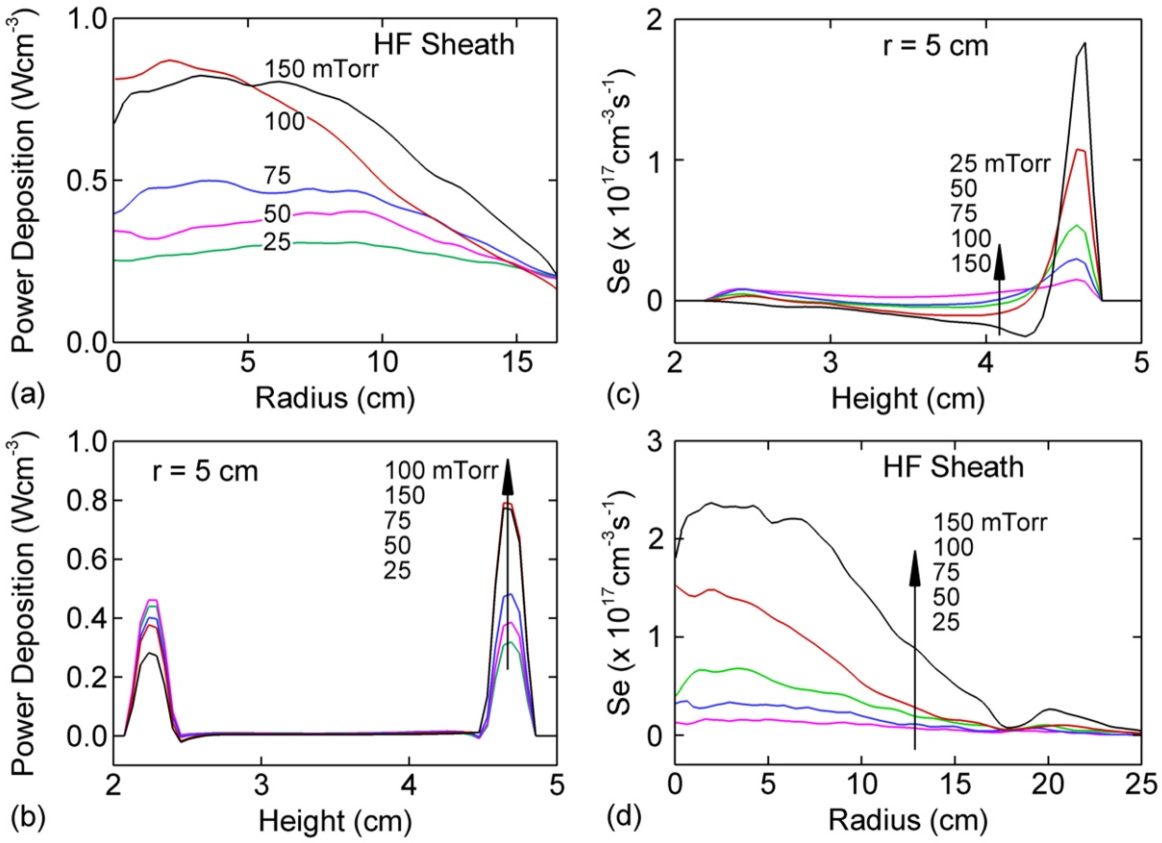

Fig. 4.25 - (Color) Time averaged total power deposition ($P_{tot} = (1/\Delta t)\int \bar{E} \cdot \bar{J} \Delta t$) and bulk electron impact ionization source (S_b) for pressures of 25, 50, 75, 100 and 150 mTorr (Ar/CF_4 = 90/10, $P_{HF} = P_{LF}$ = 300 W, *HF* = 150 MHz, *LF* = 10 MHz). (a) Total power deposition as a function of radius in the *HF* sheath, (b) total power deposition as a function of height at r = 5 cm, (c) S_b as a function of height at r = 5 cm and (d) S_b as a function of radius in the *HF* sheath. The total power deposition and S_b increasingly peak in the *HF* sheath and in the center of the reactor with increasing pressure.

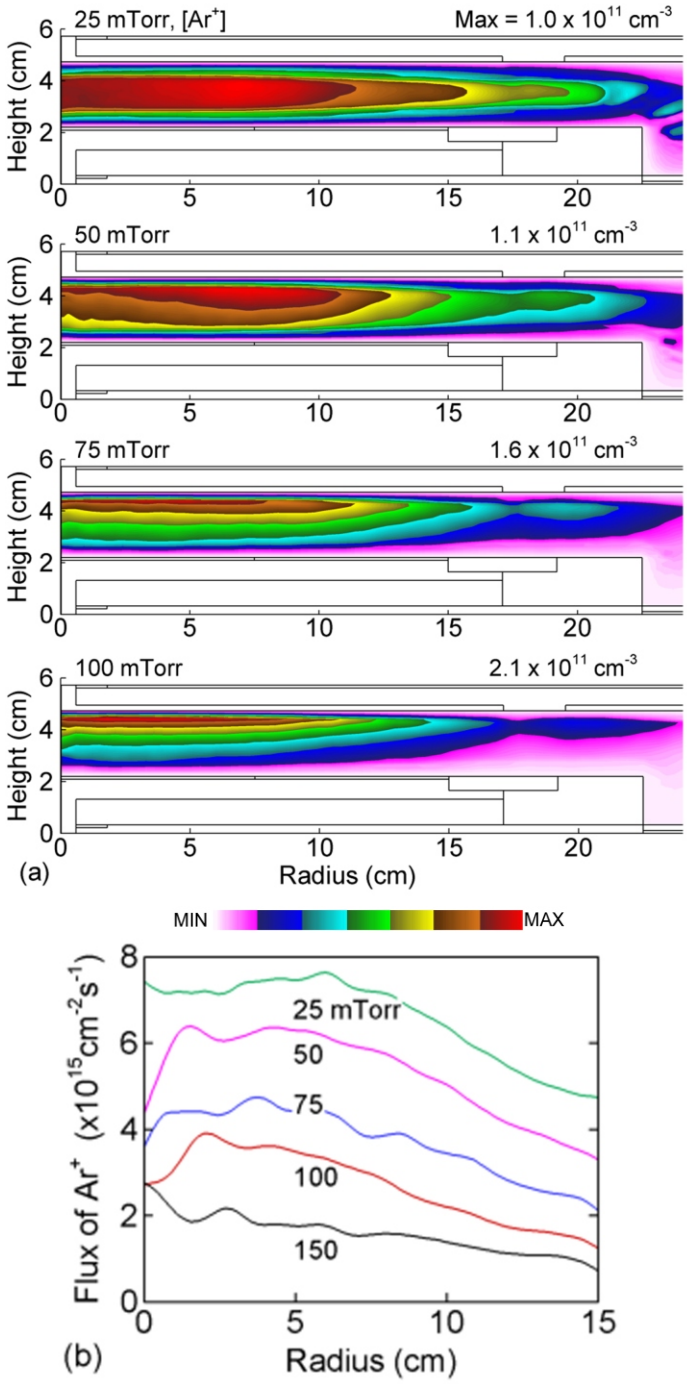

Fig. 4.26 - (Color) Time averaged Ar^+ density and flux incident on the wafer for increasing pressure (Ar/CF_4 = 90/10, $P_{HF} = P_{LF}$ = 300 W, HF = 150 MHz, LF = 10 MHz). (a) Ar^+ density for pressures of 10, 50, 75 and 100 mTorr, (b) Ar^+ flux onto the wafer. The maximum value or range of values in each frame is noted. The Ar^+ density is a linear scale over two decades.

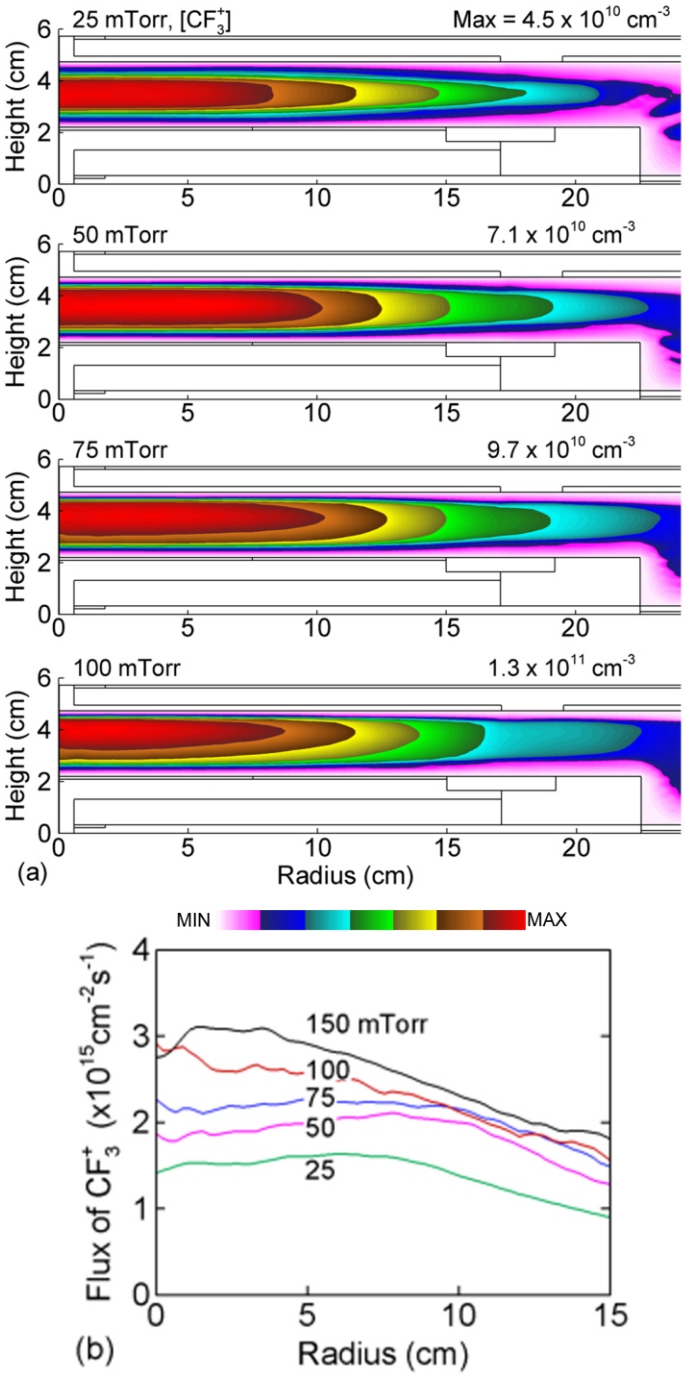

Fig. 4.27 - (Color) Time averaged CF_3^+ density and flux incident on the wafer for increasing pressure ($Ar/CF_4 = 90/10$, $P_{HF} = P_{LF} = 300$ W, $HF = 150$ MHz, $LF = 10$ MHz). (a) CF_3^+ density for pressures of 10, 50, 75 and 100 mTorr, (b) CF_3^+ flux onto the wafer. The maximum value or range of values in each frame is noted. The CF_3^+ density is a linear scale over two decades.

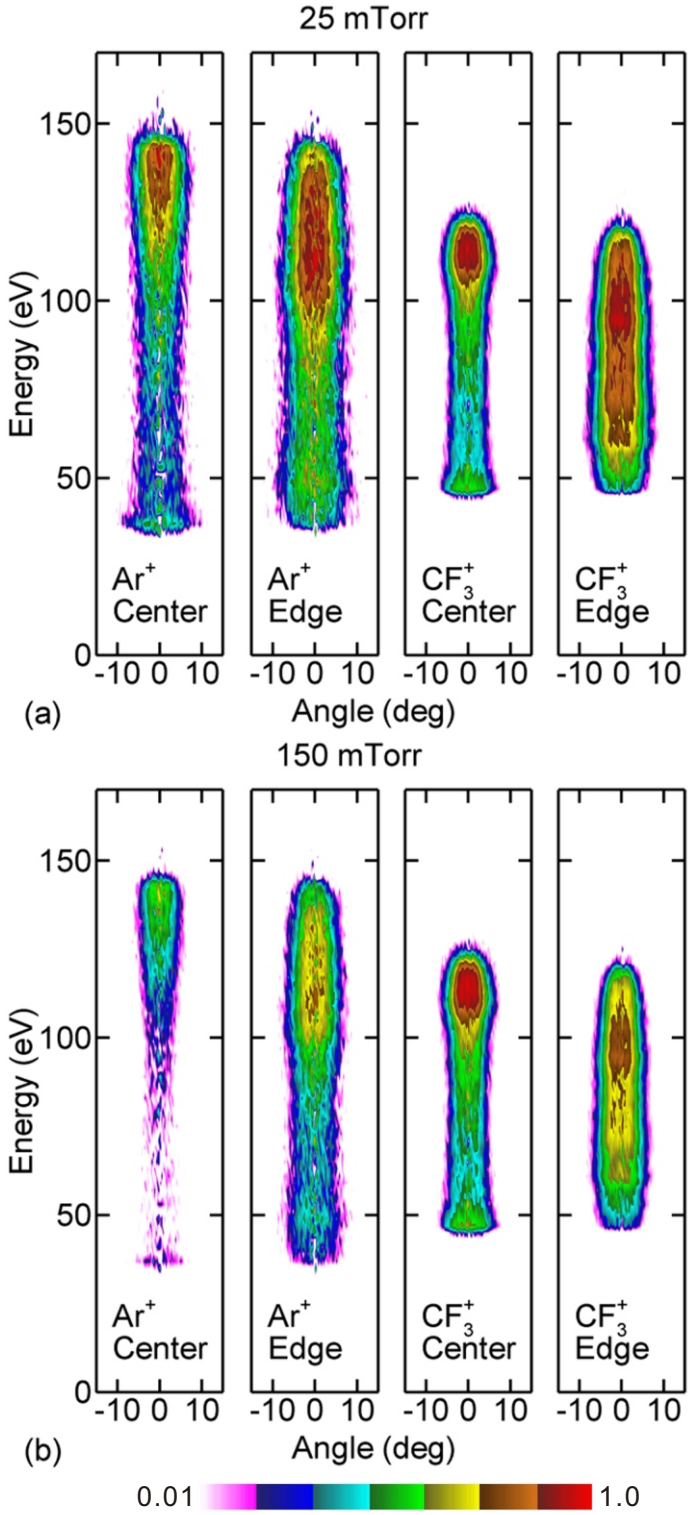

Fig. 4.28 - (Color) IEADs of Ar^+ and CF_3^+ incident onto the wafer (Ar/CF_4 = 90/10, $P_{HF} = P_{LF}$ = 300 W, *HF* = 150 MHz, *LF* = 10 MHz). (a) 25 mTorr and (b) 100 mTorr. The IEADs are separately collected over the center of the wafer (from r = 0 to r = 7.5 cm) and over the edge of the wafer (from r = 7.5 to r = 15 cm). The IEADs have units of $eV^{-1}sr^{-1}$. The contours span 2 decades using a log scale.

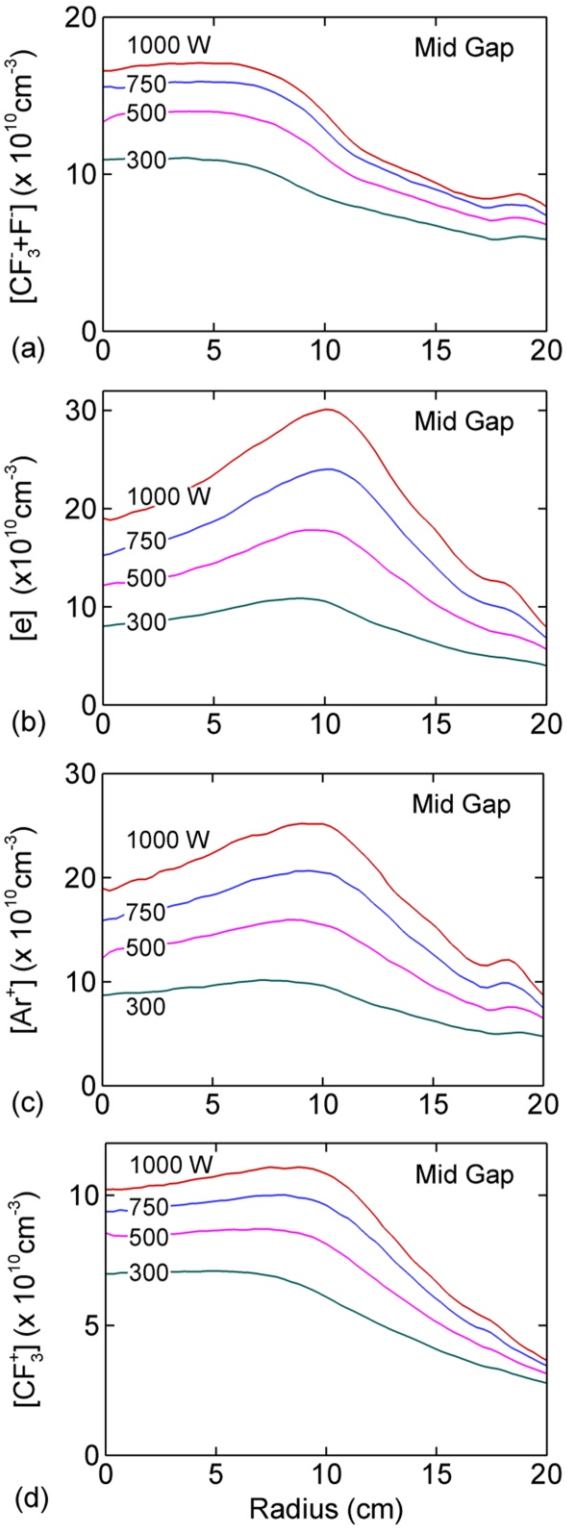

Fig. 4.29 - (Color) Time averaged plasma densities as a function of radius at the mid gap for *HF* power depositions of 300, 500, 750 and 1000 W (Ar/CF_4 = 90/10, P_{LF} = 300 W, *HF* = 150 MHz, *LF* = 10 MHz, 50 mTorr). (a) Total negative ion density ($[CF_3^- + F^-]$), (b) electron density, (c) Ar^+ density and (d) CF_3^+ density. The plasma non-uniformity increases with increasing *HF* power deposition.

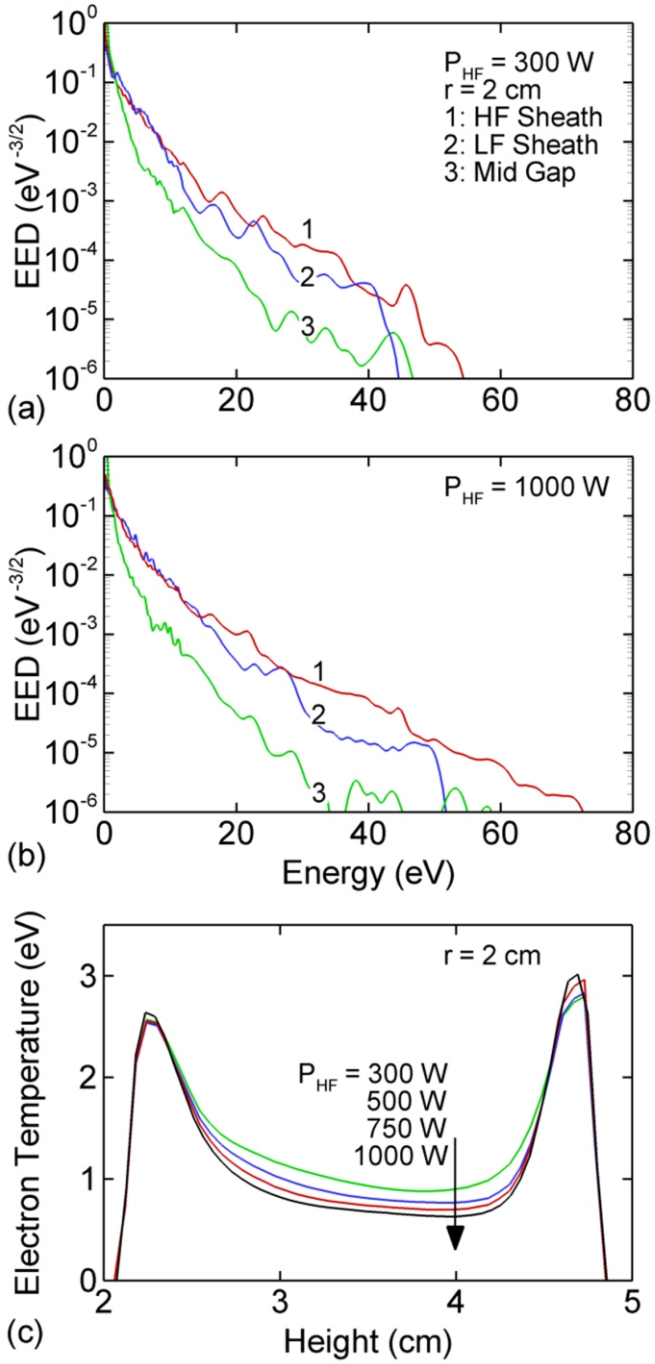

Fig. 4.30 - (Color) Heating of electrons with increasing P_{HF} (Ar/CF_4 = 90/10, P_{LF} = 300 W, HF = 150 MHz, LF = 10 MHz, 50 mTorr). (a) EEDs at different axial locations at r = 2cm for P_{HF} = 300 W and (b) P_{HF} = 1000 W, (c) electron temperature as a function height at at r = 2cm. Bulk Ohmic electron heating reduces with increasing P_{HF} due to the increasing electron density.

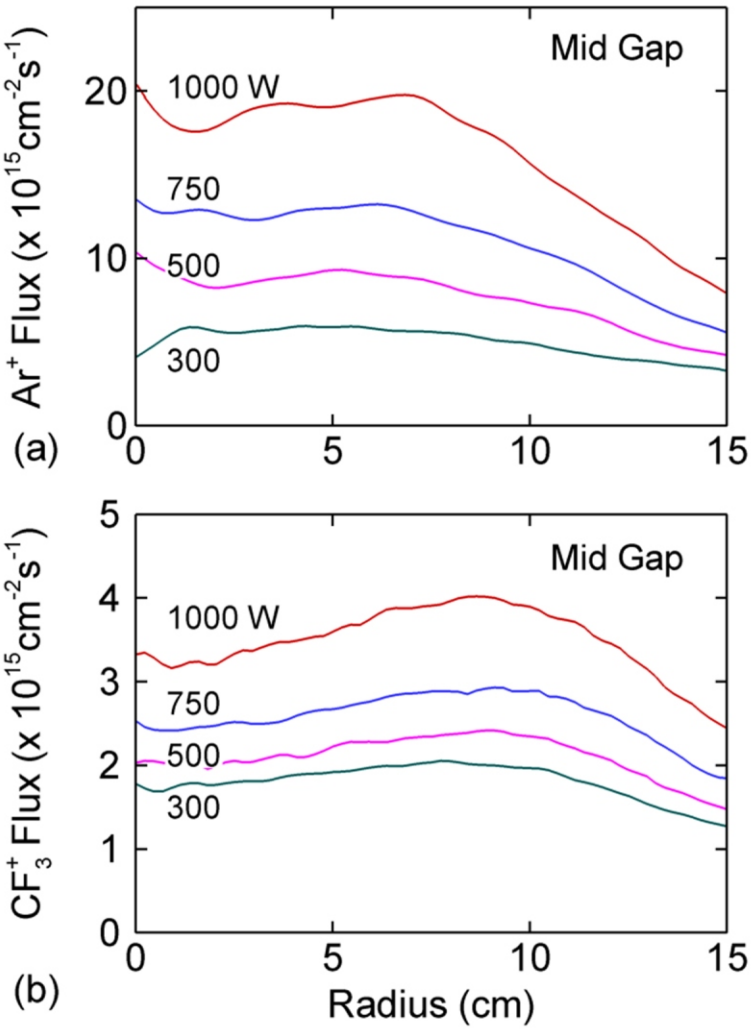

Fig. 4.31 - (Color) Time averaged ion fluxes incident on the wafer for P_{HF} of 300, 500, 750 and 1000 W (Ar/CF_4 = 90/10, P_{LF} = 300 W, HF = 150 MHz, LF = 10 MHz, 50 mTorr). (a) Ar^+ flux and (b) CF_3^+ flux.

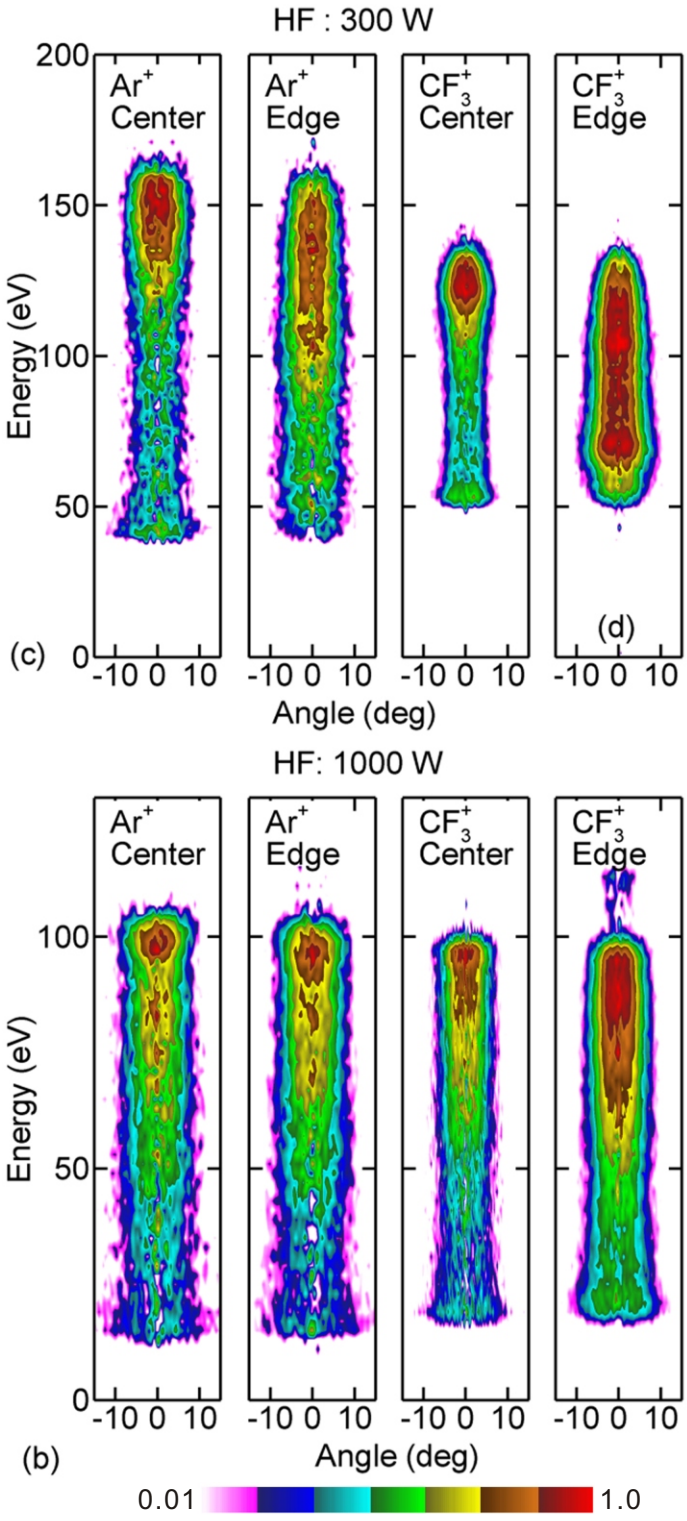

Fig. 4.32 - (Color) IEADs of Ar^+ and CF_3^+ incident onto the wafer (Ar/CF_4 = 90/10, P_{LF} = 300 W, *HF* = 150 MHz, *LF* = 10 MHz, 50 mTorr). (a) P_{HF} = 300 W and (b) P_{HF} = 1000 W. The IEADs are separately collected over the center of the wafer (from r = 0 to r = 7.5 cm) and over the edge of the wafer (from r = 7.5 to r = 15 cm). The IEADs have units of $eV^{-1}sr^{-1}$. The contours span 2 decades using a log scale.

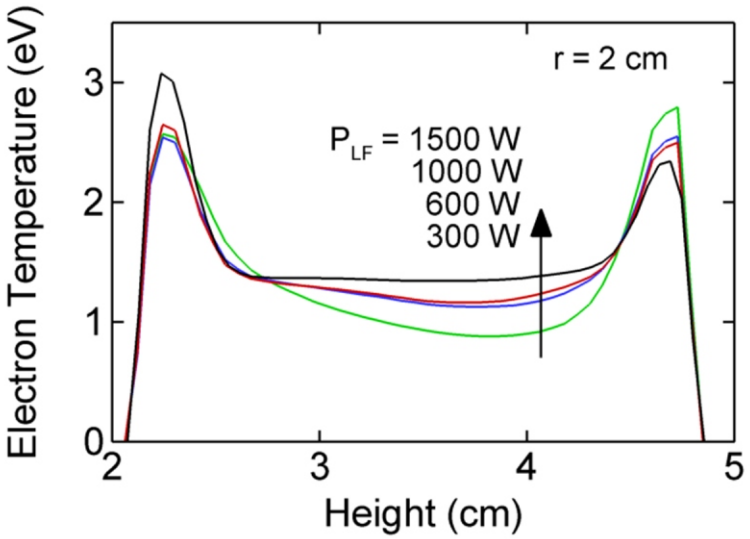

Fig. 4.33 - (Color) Electron temperature (T_e) as a function of height at r = 2cm for P_{LF} of 300, 600, 1000 and 1500 W (Ar/CF_4 = 90/10, P_{HF} = 300 W, HF = 150 MHz, LF = 10 MHz, 50 mTorr). Increasing P_{LF} powers mainly increases bulk T_e.

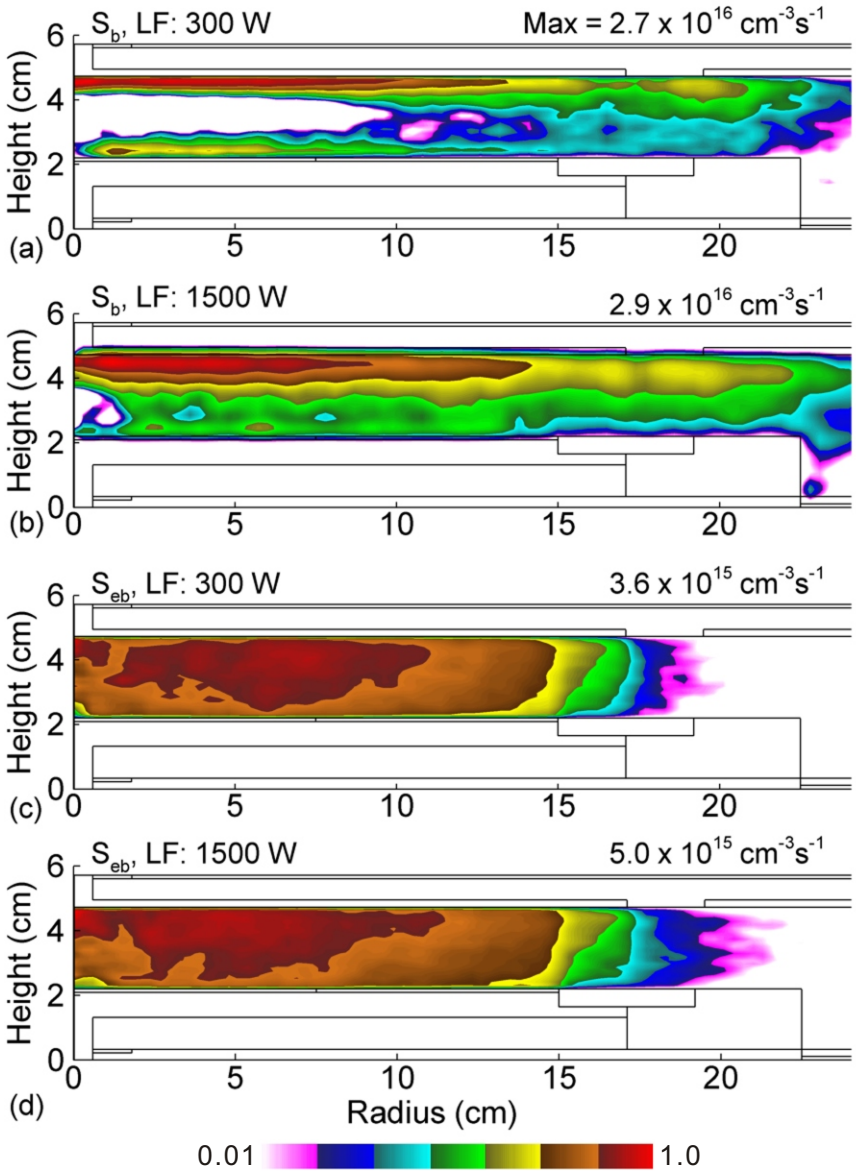

Fig. 4.34 - (Color) Time averaged ionization source (Ar/CF_4 = 90/10, P_{HF} = 300 W, HF = 150 MHz, LF = 10 MHz, 50 mTorr). (a) Ionization from bulk electrons (S_b) for P_{LF} = 300 W and (b) P_{LF} = 1500 W, (c) beam electron ionization source (S_{eb}) for P_{LF} = 300 W and (d) P_{LF} = 1500 W. The maximum value in each frame is noted. S_b and S_{eb} are plotted on log scales over two decades. In the white region in the center of the reactor the S_b is negative and could not be resolved using a log scale.

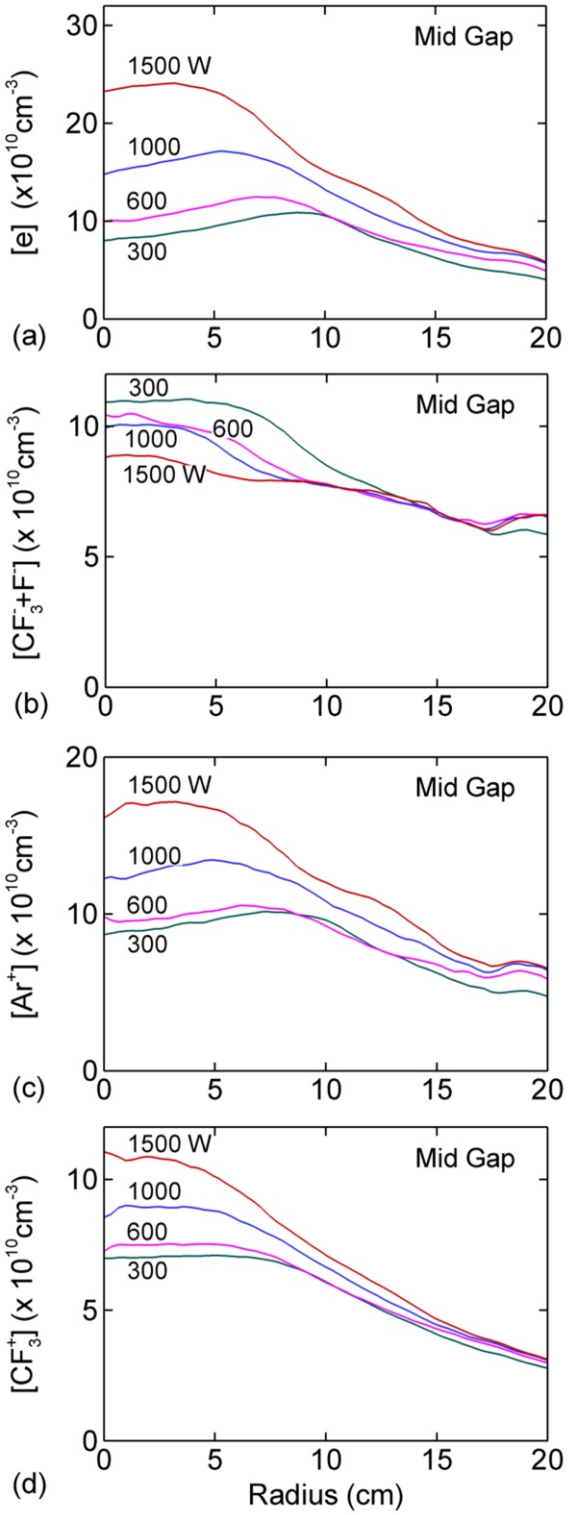

Fig. 4.35 - (Color) Time averaged plasma densities as a function of radius at the mid gap for *LF* power of 300, 600, 1000 and 1500 W (Ar/CF_4 = 90/10, P_{HF} = 300 W, *HF* = 150 MHz, *LF* = 10 MHz, 50 mTorr). (a) Electron density, (b) total negative ion density ($[CF_3^- + F^-]$), (c) Ar^+ density and (d) CF_3^+ density. The plasma non-uniformity increases with increasing *LF* power deposition.

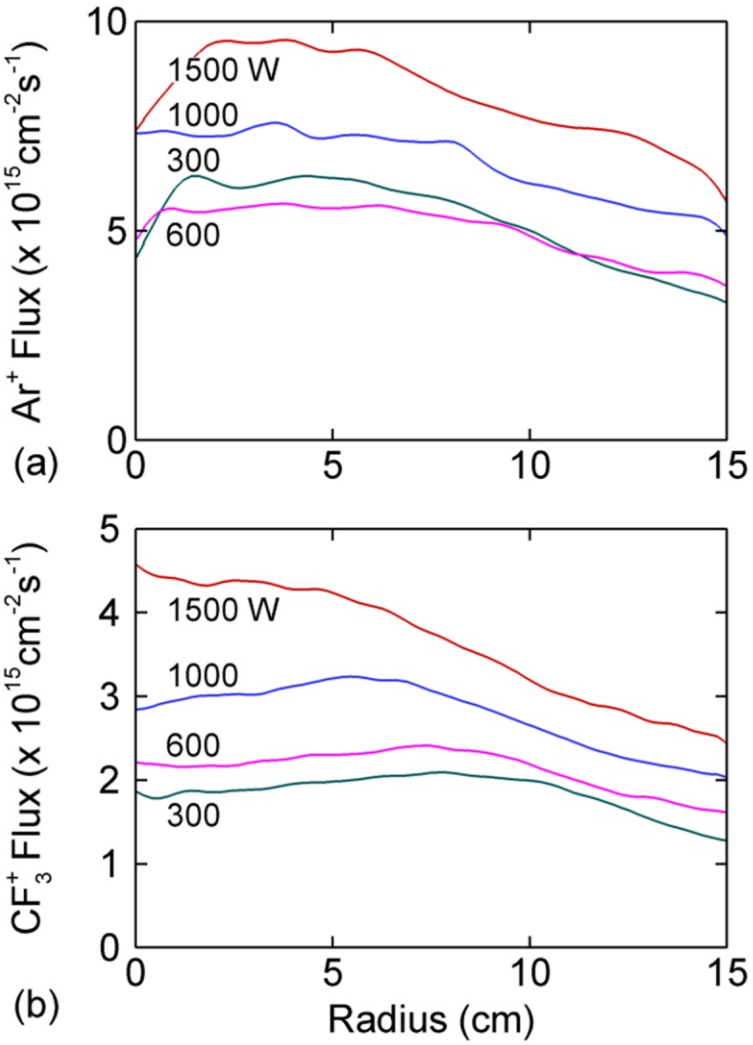

Fig. 4.36 - (Color) Ion fluxes incident on the wafer for *LF* power of 300, 600, 1000 and 1500 W (Ar/CF_4 = 90/10, P_{HF} = 300 W, *HF* = 150 MHz, *LF* = 10 MHz, 50 mTorr). (a) Ar^+ flux and (b) CF_3^+ flux.

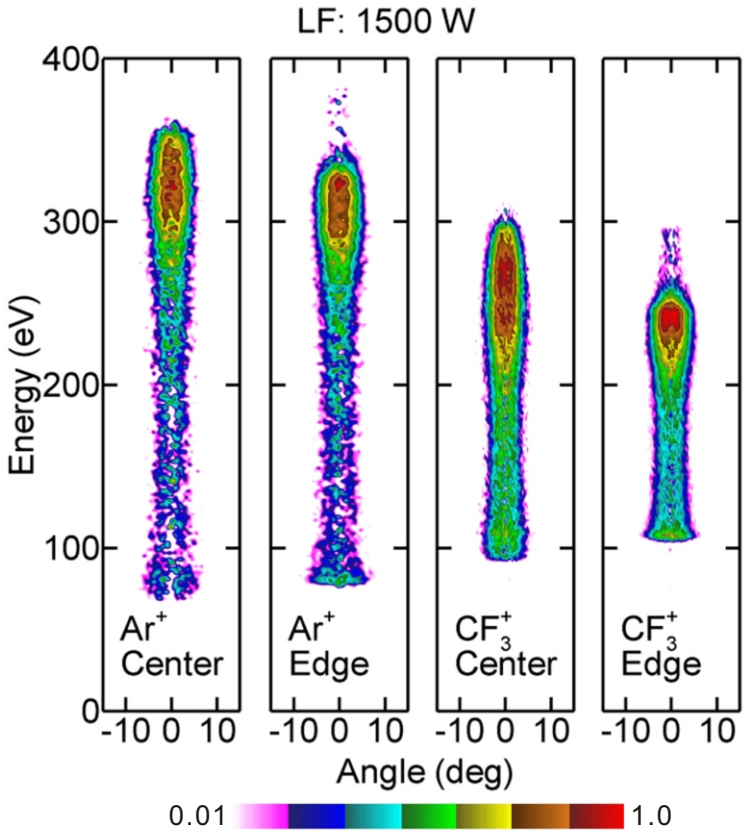

Fig. 4.37 - (Color) IEADs of Ar^+ and CF_3^+ incident onto the wafer for a *LF* power of 1500 W (Ar/CF_4 = 90/10, P_{HF} = 300 W, *HF* = 150 MHz, *LF* = 10 MHz, 50mTorr). The IEADs are separately collected over the center of the wafer (from r = 0 to r = 7.5 cm) and over the edge of the wafer (from r = 7.5 to r = 15 cm). The IEADs have units of $eV^{-1}sr^{-1}$. The contours span 2 decades using a log scale.

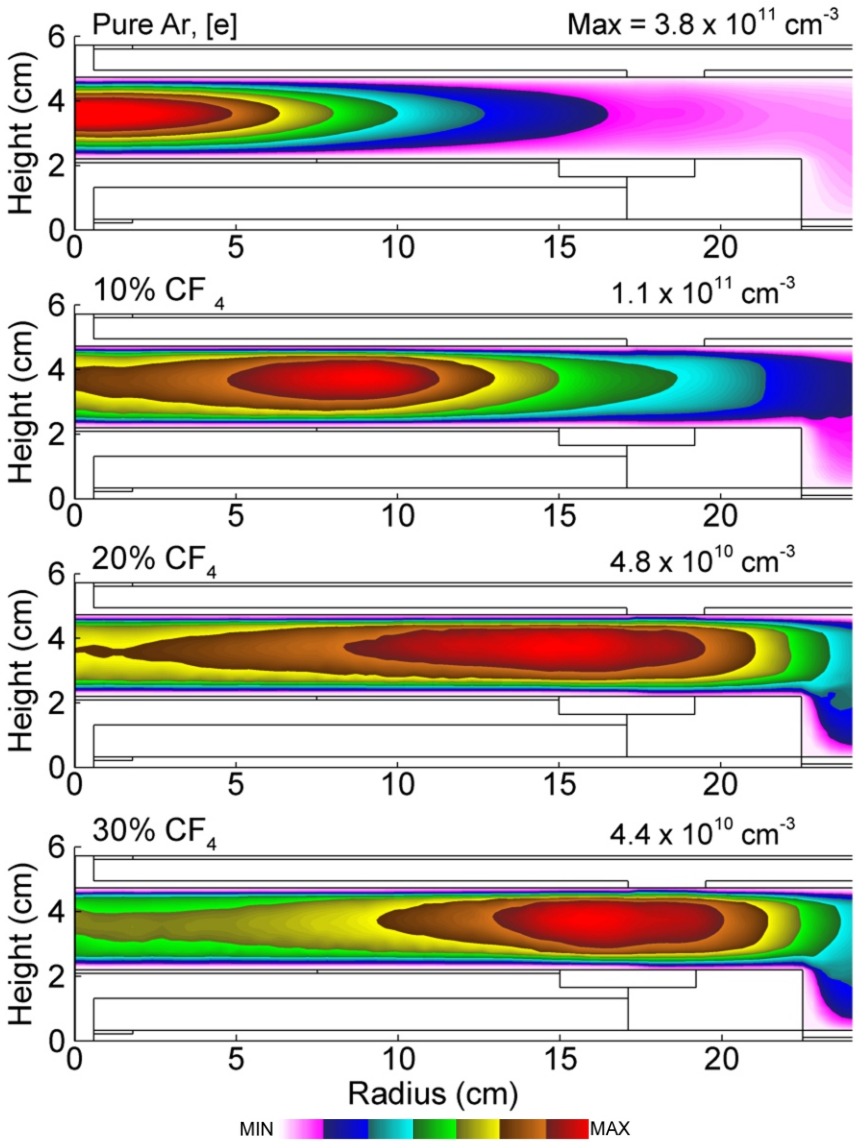

Fig. 4.38 - (Color) Time averaged electron density ([e]) for CF_4 fractions of 0, 0.1, 0.2 and 0.3 ($P_{HF} = P_{LF} = 300$ W, $HF = 150$ MHz, $LF = 10$ MHz, 50 mTorr). The maximum value in each frame is noted. [e] is plotted on a linear scale. The maximum of the electron density shifts towards the edge of the electrode with increasing CF_4 fraction due to the increasing effective plasma wavelength.

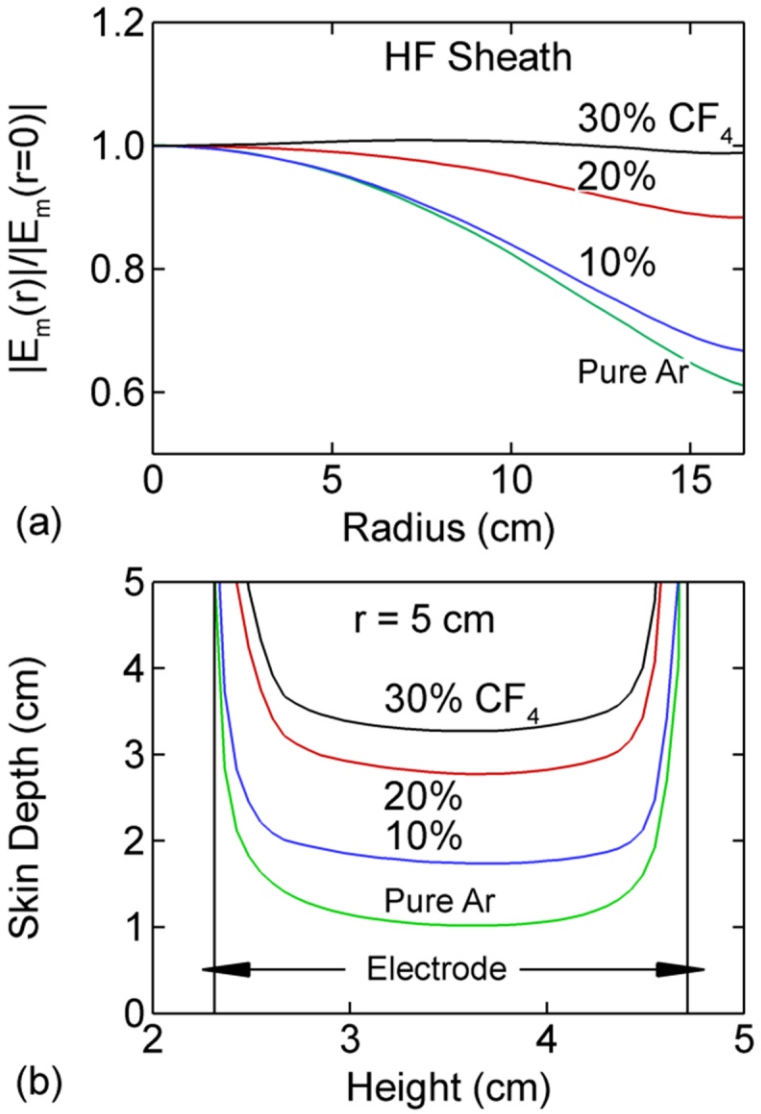

Fig. 4.39 - (Color) Electromagnetic properties for CF_4 fractions of 0, 0.1, 0.2 and 0.3 ($P_{HF} = P_{LF}$ = 300 W, *HF* = 150 MHz, *LF* = 10 MHz, 50 mTorr). (a) Magnitude of the *HF* electric field (first harmonic amplitude, $|E_m|$) along the *HF* sheath (Normalized by the magnitude of the field at the center of the reactor), (b) skin depth as a function of height at r = 5 cm.

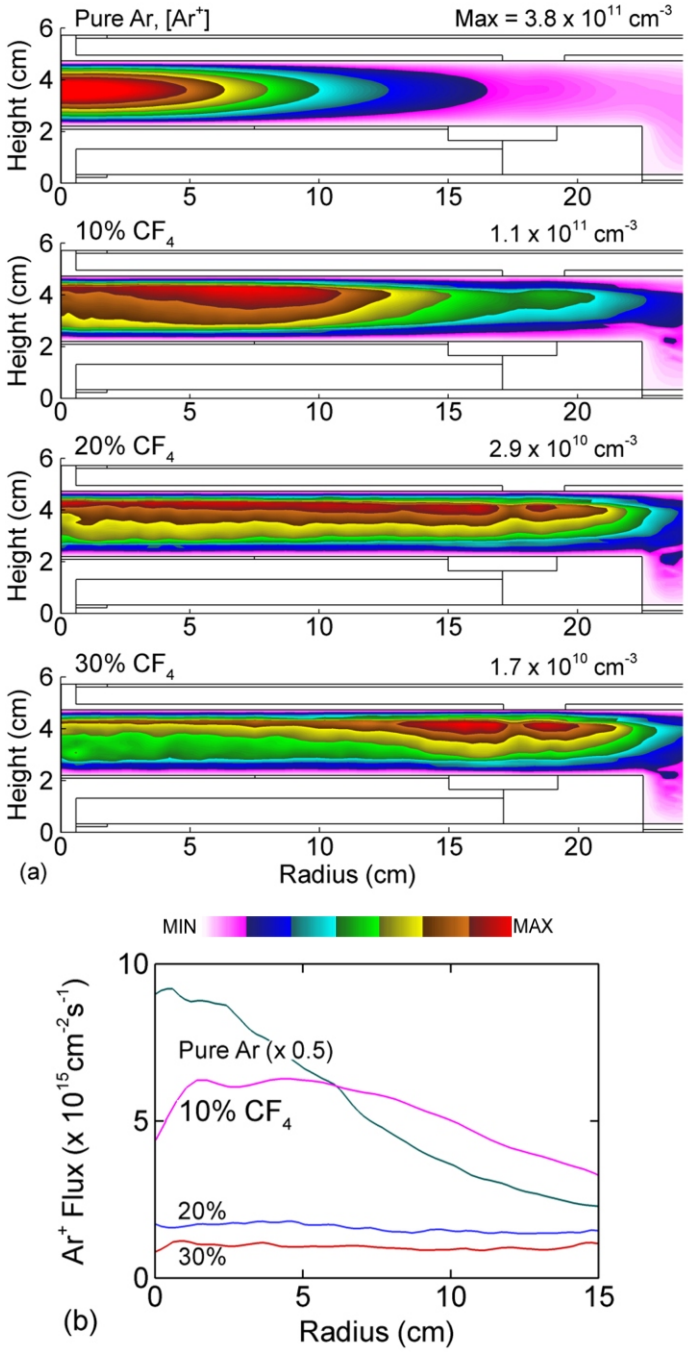

Fig. 4.40 - (Color) Time averaged Ar^+ density and flux incident on the wafer for CF_4 fractions of 0, 0.1, 0.2 and 0.3 ($P_{HF} = P_{LF} = 300$ W, $HF = 150$ MHz, $LF = 10$ MHz, 50 mTorr). (a) Ar^+ density and (b) Ar^+ flux onto the wafer. The maximum value or range of values in each frame is noted. The Ar^+ density is plotted on a linear scale.

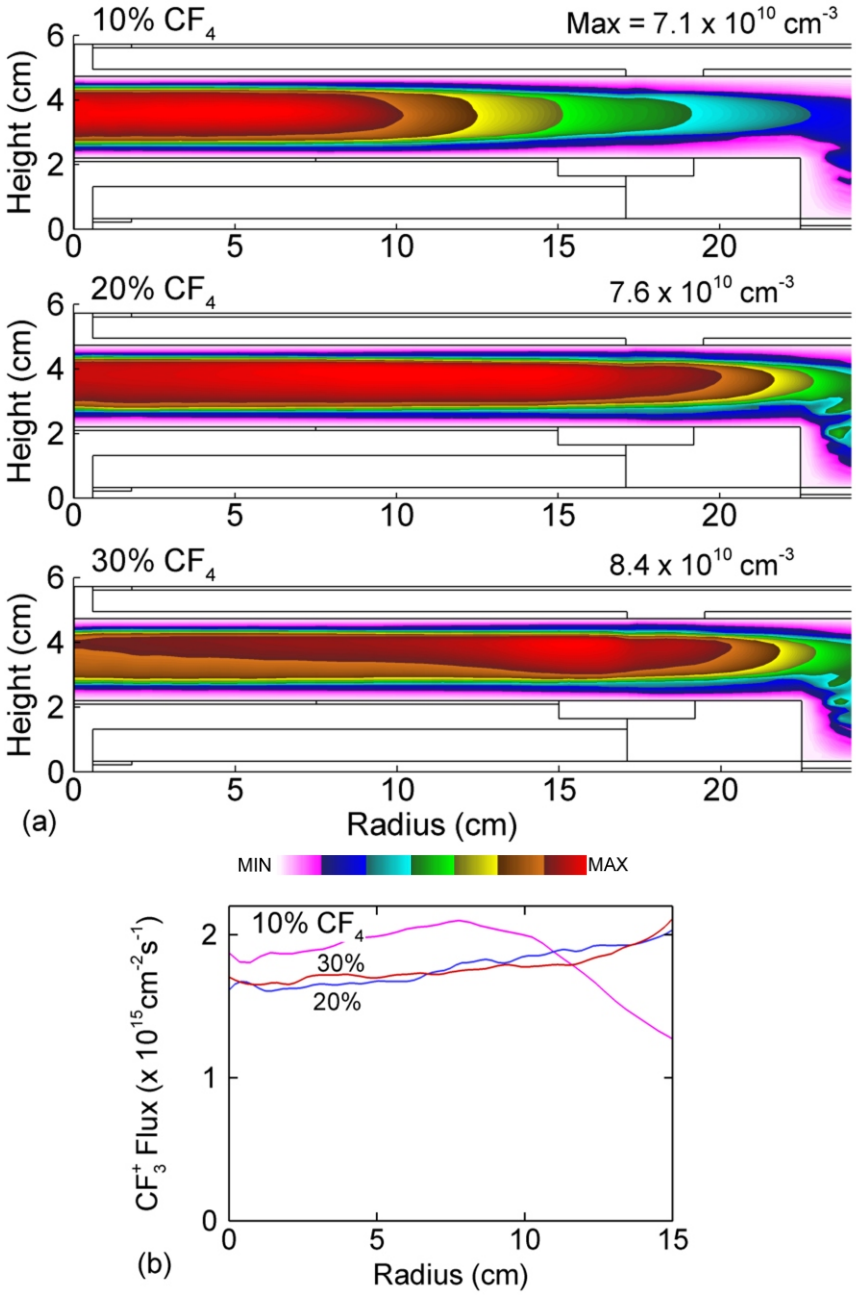

Fig. 4.41 - (Color) Time averaged CF_3^+ density and flux incident on the wafer for CF_4 fractions of 0, 0.1, 0.2 and 0.3 ($P_{HF} = P_{LF} = 300$ W, $HF = 150$ MHz, $LF = 10$ MHz, 50 mTorr). (a) CF_3^+ density and (b) CF_3^+ flux onto the wafer. The maximum value or range of values in each frame is noted. The CF_3^+ density is plotted on a linear scale

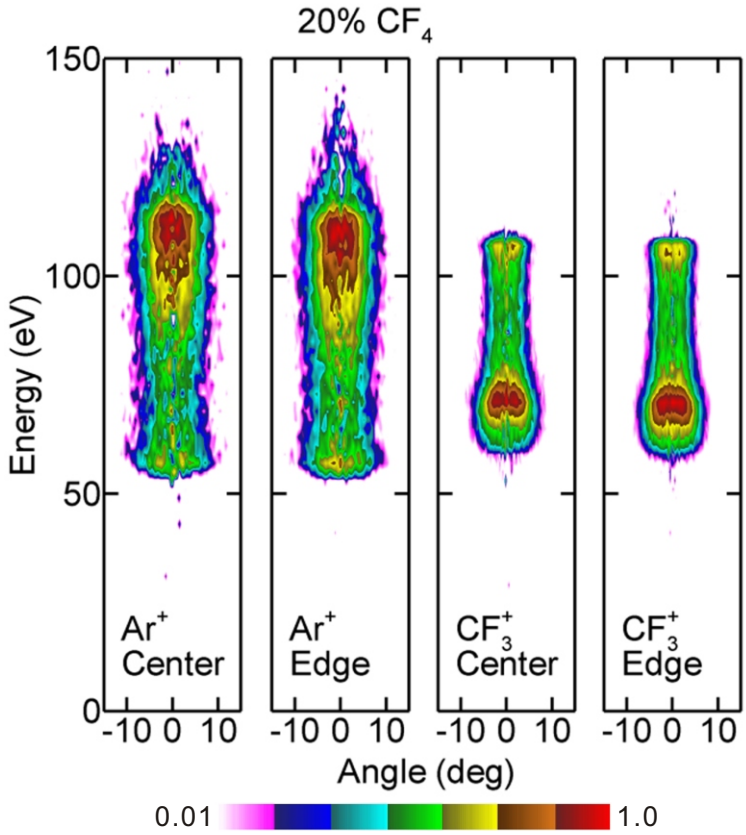

Fig. 4.42 - (Color) IEADs of Ar^+ and CF_3^+ incident onto the wafer for a CF_4 fraction of 0.2 (P_{HF} = P_{LF} = 300 W, *HF* = 150 MHz, *LF* = 10 MHz, 50 mTorr). The IEADs are separately collected over the center of the wafer (from r = 0 to r = 7.5 cm) and over the edge of the wafer (from r = 7.5 to r = 15 cm). The IEADs have units of $eV^{-1}sr^{-1}$. The contours span 2 decades using a log scale.

4.10 Figures

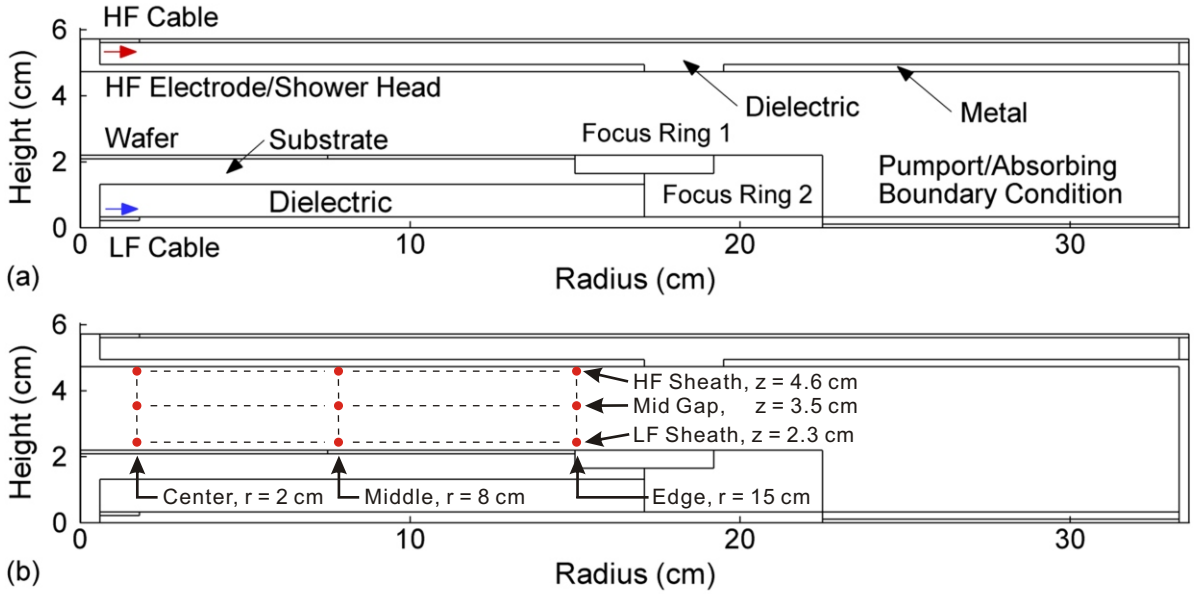

Fig. 4.1 - Properties of the DF-CCP reactor. (a) Schematic showing the wafer on a substrate powered at low frequency surrounded by dielectric focus rings. The showerhead is powered at high frequency and is also surrounded by a dielectric. The *HF* and *LF* electric fields are launched into the reactor at the cable connections. (b) The radial and axial positions where EEDs will be plotted.

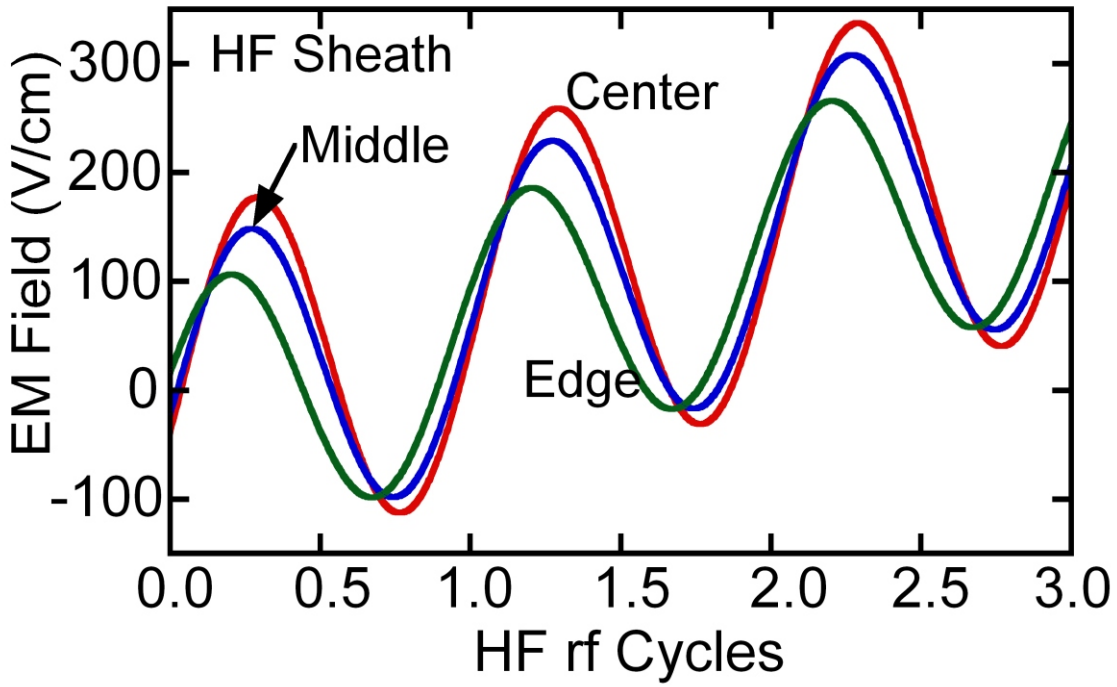

Fig. 4.2 - (Color) The amplitude of the electromagnetic field in the *HF* sheath at different radial locations over three *HF* rf cycles (center, r = 1 cm; middle, r = 8 cm; edge, r = 16 cm).

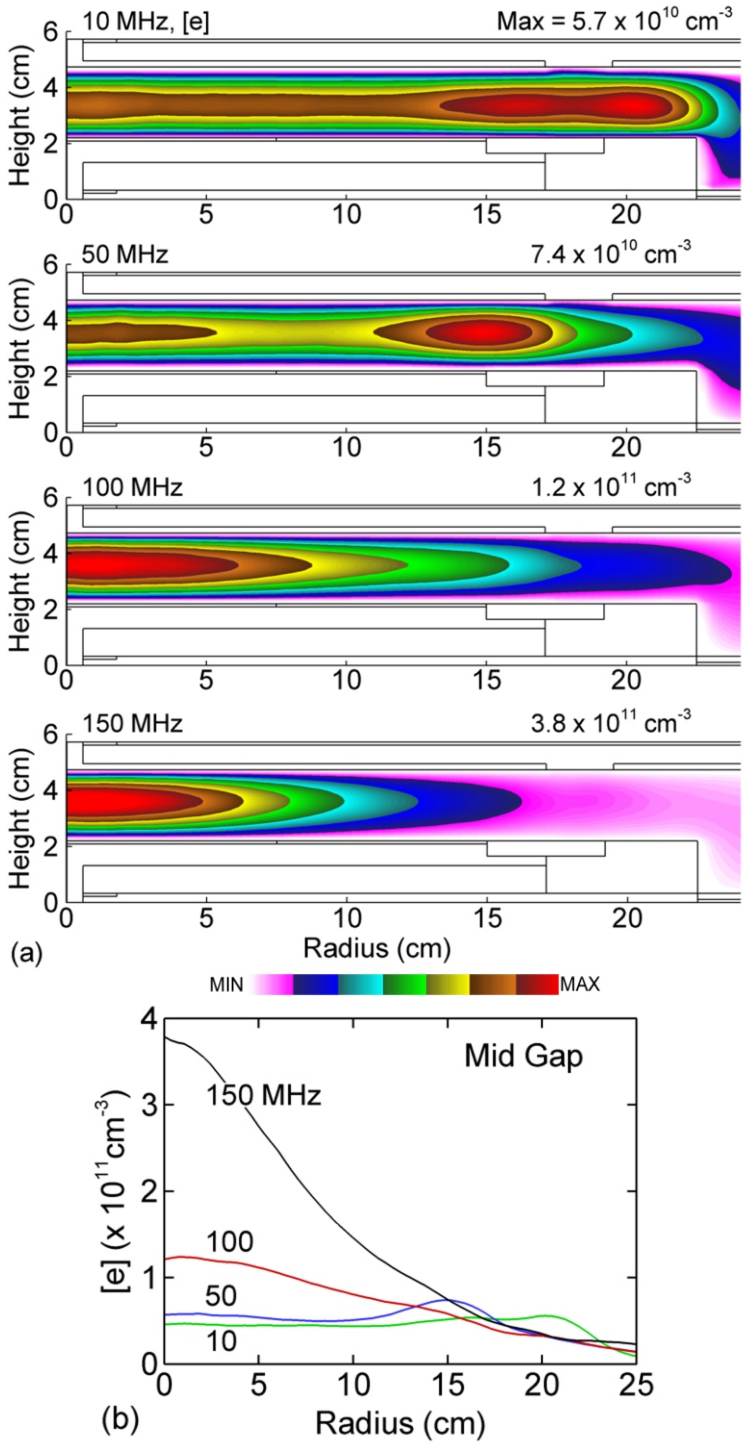

Fig. 4.3 - (Color) Time averaged electron density ([e]) for the base case conditions (Ar, 50 mTorr, $P_{HF} = P_{LF} = 300$ W, $LF = 10$ MHz). (a) $HF = 10$, 50, 100, 150 MHz and (b) radial [e] profile at the mid gap (z = 3.5 cm). The maximum value or range of values in each frame is noted. The electron density is plotted on a linear scale. The electron density transitions from being flat at HF =10 MHz, to edge peaked at 50 MHz, to center peaked at 100 and 150 MHz.

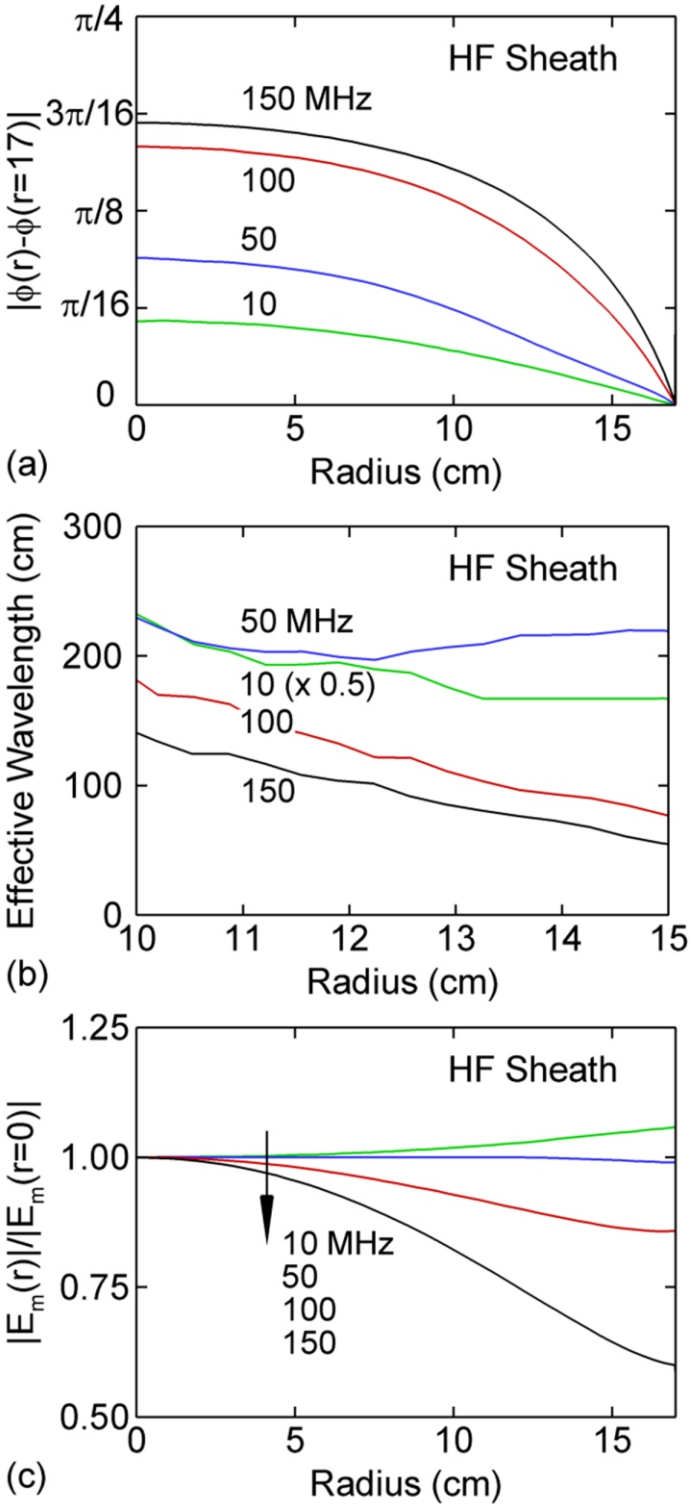

Fig. 4.4 - (Color) Electromagnetic properties for the base case conditions (Ar, 50 mTorr, P_{HF} = P_{LF} = 300 W, *LF* = 10 MHz) and *HF* = 10-150 MHz. (a) Relative phase (with respect to the edge of the *HF* electrode) along the *HF* sheath, (b) plasma effective wavelength along the *HF* sheath and (c) magnitude of the *HF* field along the *HF* sheath (normalized by the magnitude at the center of the reactor). The *HF* field is highly peaked in the center at 150 MHz due to constructive interference.

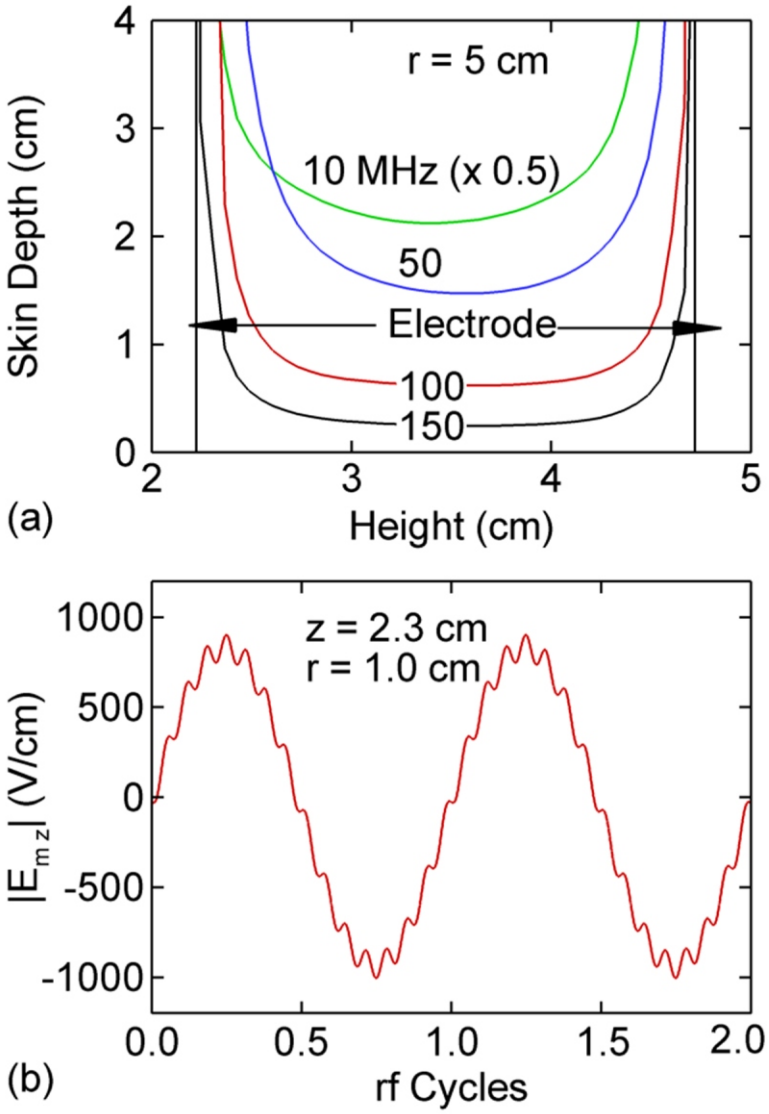

Fig. 4.5 - (Color) Electromagnetic properties for the base case conditions (Ar, 50 mTorr, P_{HF} = P_{LF} = 300 W, *LF* = 10 MHz) and *HF* = 10-150 MHz. (a) Skin depth as a function of height at r = 5 cm and (b) the axial electromagnetic field in the *LF* sheath at r = 1 cm (in the time domain).

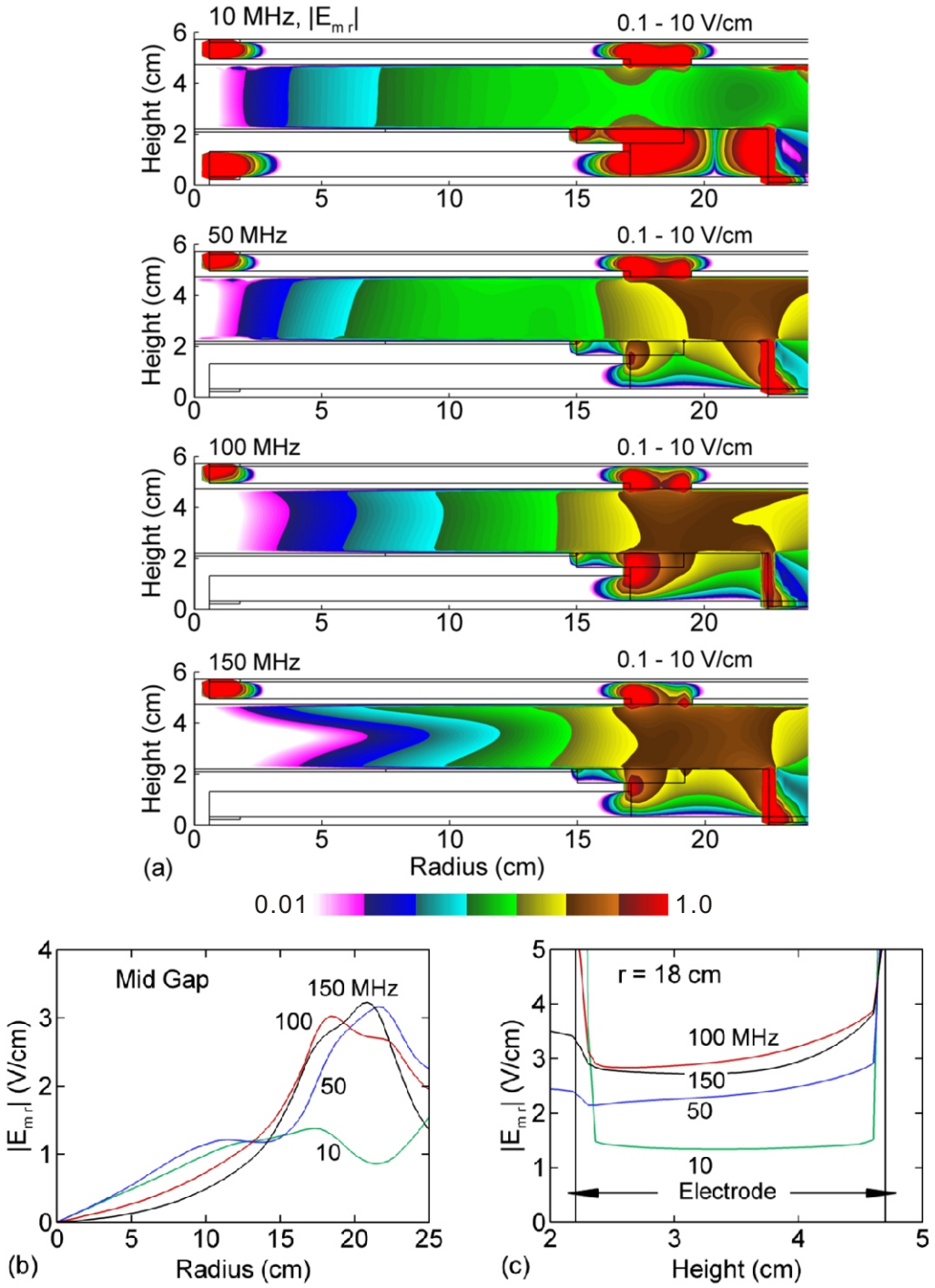

Fig. 4.6 - (Color) Magnitude of the radial *HF* field ($|E_{mr}|$) for the base case conditions (Ar, 50 mTorr, P_{HF} = P_{LF} = 300 W, *LF* = 10 MHz). (a) *HF* = 10, 50, 100, 150 MHz; (b) $|E_{mr}|$ as a function of radius at the middle of the gap, and (c) $|E_{mr}|$ as a function of height at r = 18 cm. The range of values in each frame is noted. The $|E_{mr}|$ is a log scale over two decades.

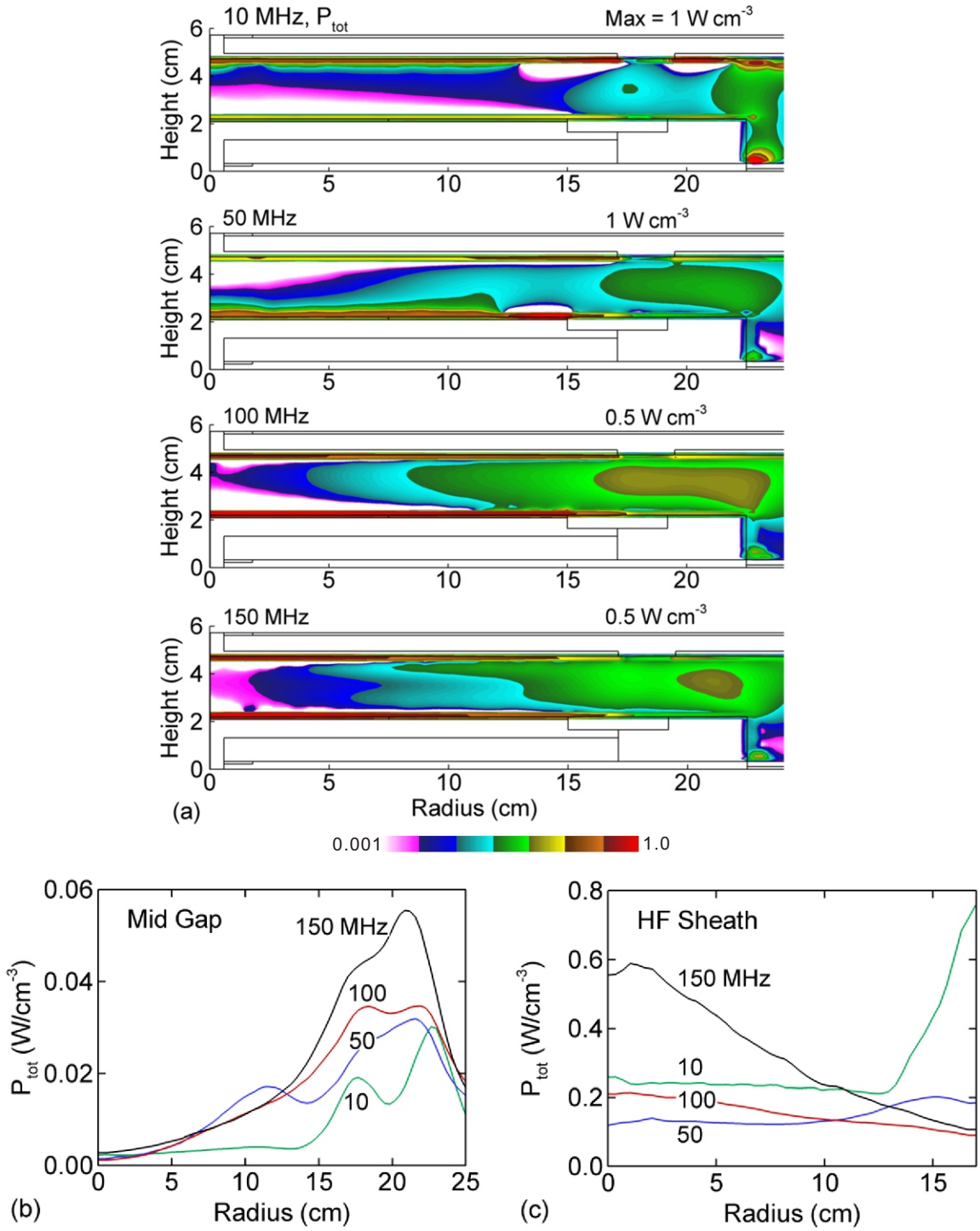

Fig. 4.7 - (Color) Time averaged total power deposition ($P_{tot} = (1/\Delta t)\int \vec{E} \cdot \vec{J}\, dt$) for the base case conditions (Ar, 50 mTorr, $P_{HF} = P_{LF} = 300$ W, $LF = 10$ MHz). (a) $HF = 10$, 50, 100, 150 MHz; (b) P_{tot} as a function of radius at the middle of the gap (z = 3.5 cm), and (c) P_{tot} as a function of radius at the edge of the HF sheath (z = 4.56 cm). The maximum value or range of values in each frame of the contour plots is noted where P_{tot} is on a log scale over three decades.

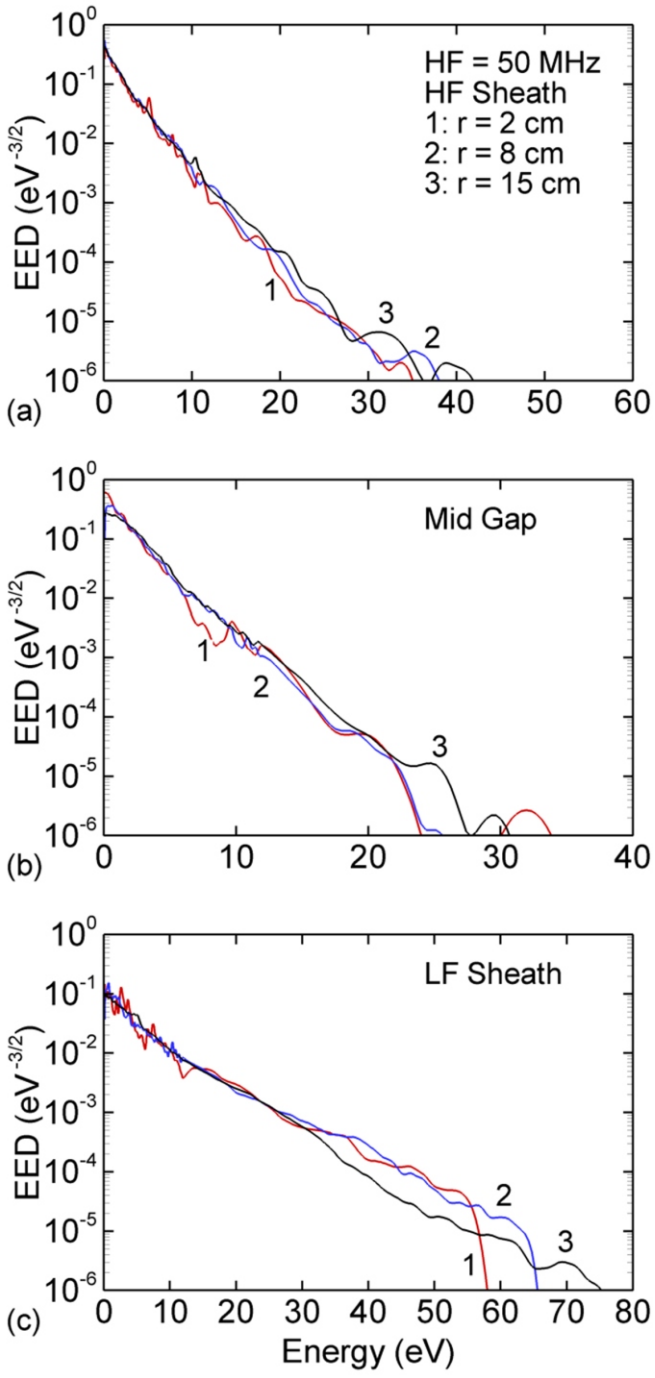

Fig. 4.8 - (Color) EEDs at different locations in the reactor for the base case conditions (Ar, 50 mTorr, $P_{HF} = P_{LF} = 300$ W, $LF = 10$ MHz) with $HF = 50$ MHz. (a) In the *HF* sheath, (b) at mid-gap and (c) in the *LF* sheath. (These locations are shown in Fig. 1b.) Near the edge of the *LF* electrode, the EEDs in the *LF* sheath have more prominent tails due to the electrostatic edge enhancement.

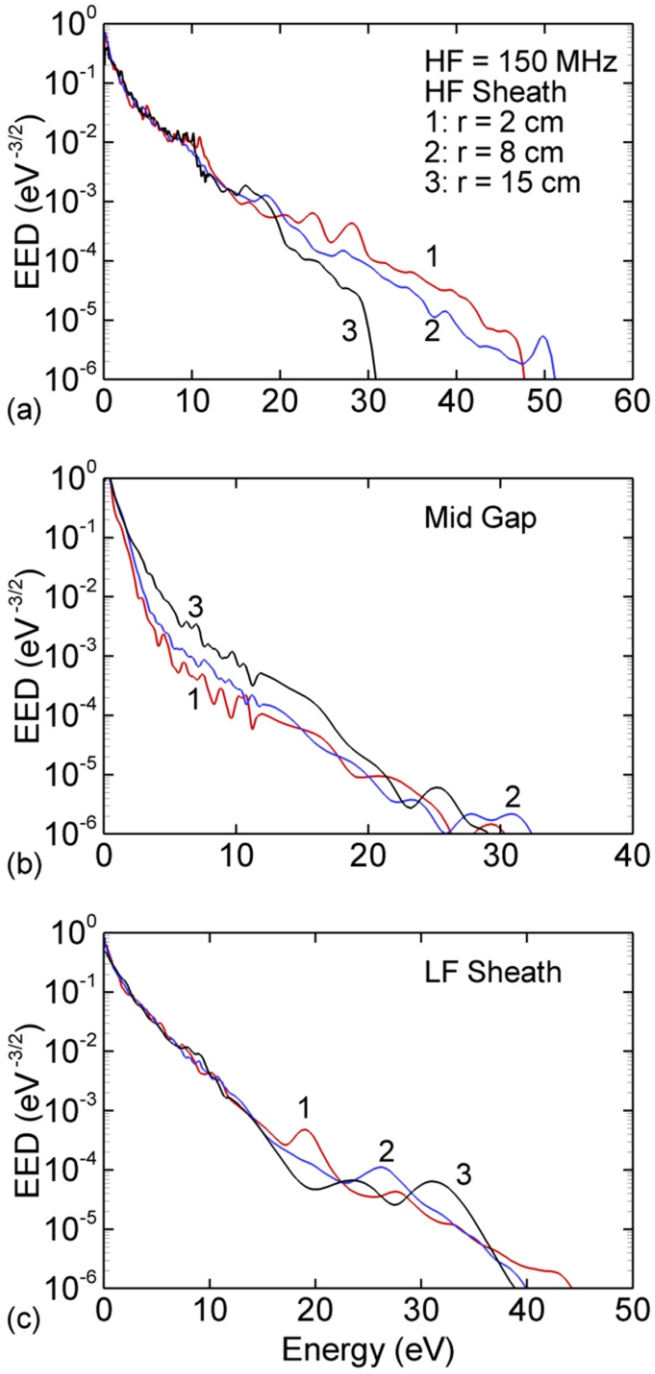

Fig. 4.9 - (Color) EEDs at different locations in the reactor for the base case conditions (Ar, 50 mTorr, $P_{HF} = P_{LF} = 300$ W, $LF = 10$ MHz) with $HF = 150$ MHz. (a) In the *HF* sheath, (b) at mid- gap and (c) in the *LF* sheath. (These locations are shown in Fig. 1b.) Near the center of the reactor, EEDs in the *HF* sheath have more prominent tails due to the finite wavelength effect which increases sheath heating.

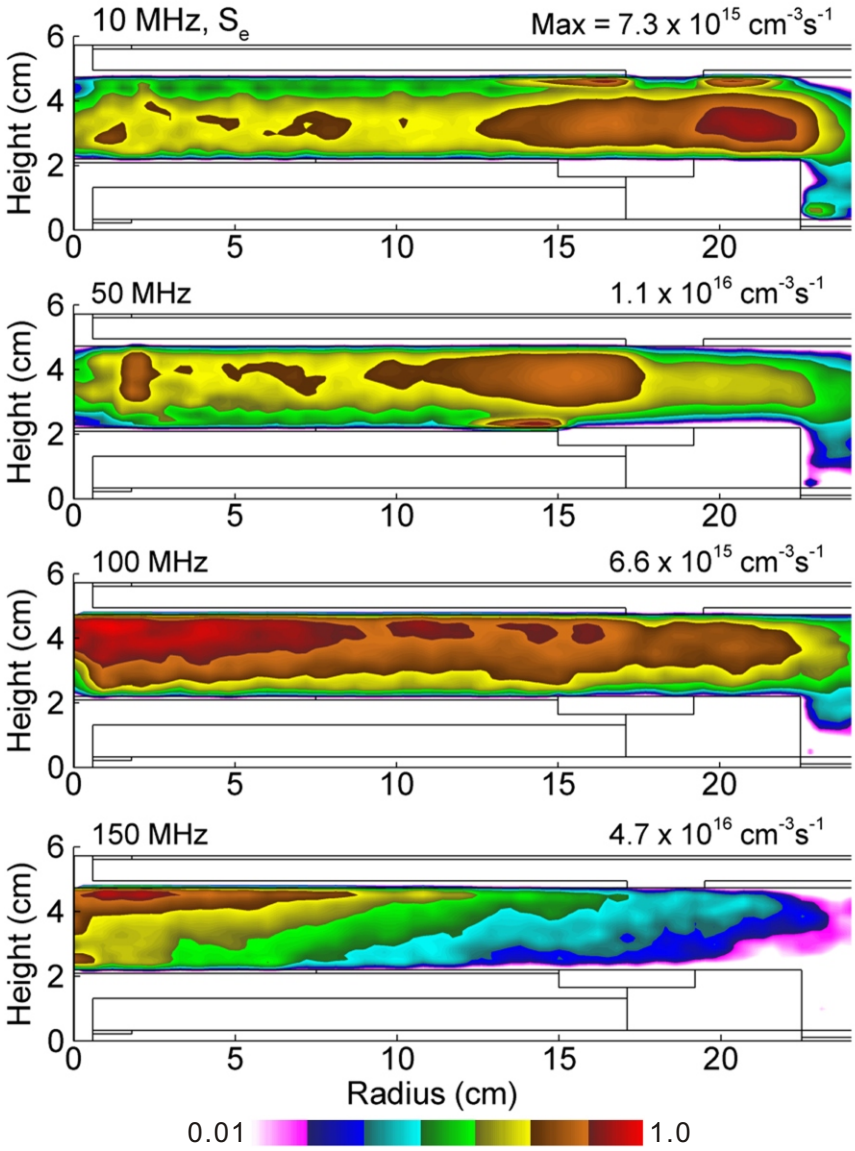

Fig. 4.10 - (Color) Time averaged electron impact ionization source (S_b) by bulk electrons for the base case conditions (Ar, 50 mTorr, $P_{HF} = P_{LF} = 300$ W, $LF = 10$ MHz) and HF of 10, 50, 100 and 150 MHz. The maximum value in each frame is noted. S_b is a log scale over two decades. With increasing HF, the maximum of S_b shifts towards the HF electrode due to enhanced sheath heating, and towards the center of the due to the finite wavelength effect.

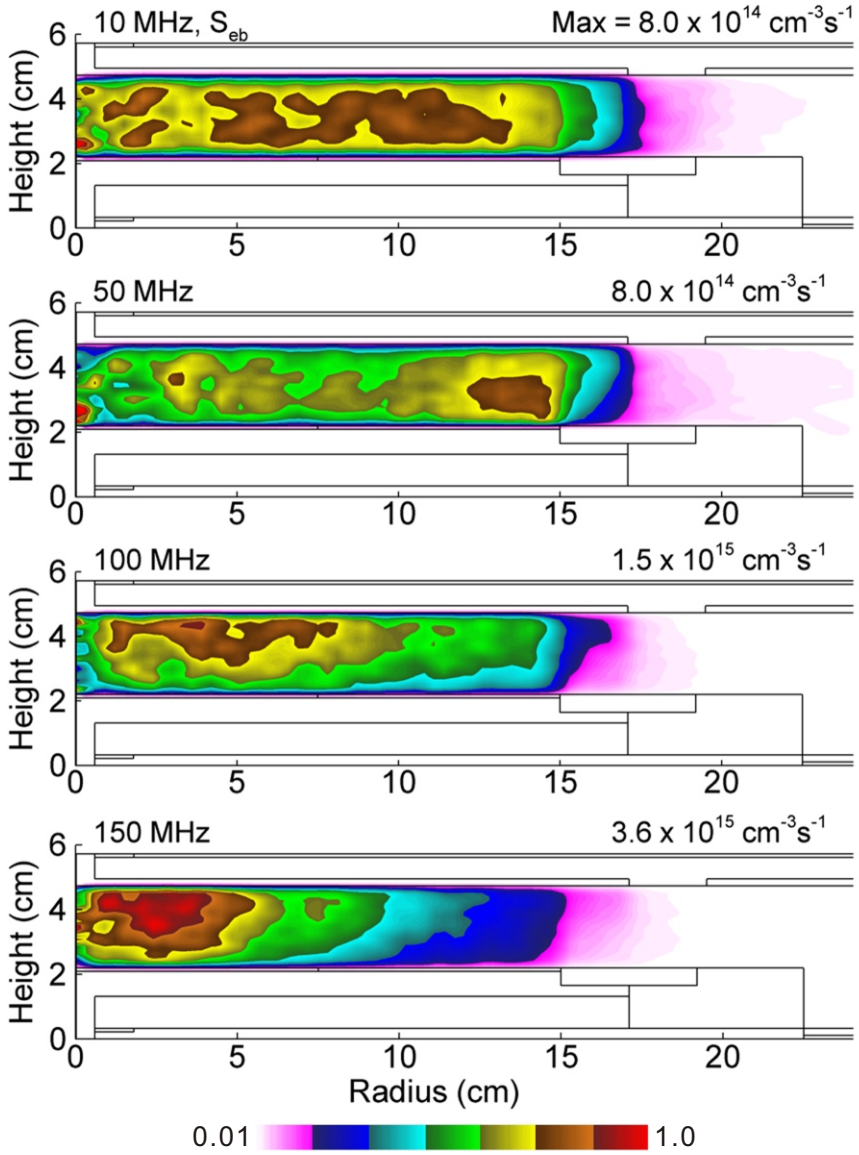

Fig. 4.11 - (Color) Time averaged ionization source (S_{eb}) by secondary electrons for the base case conditions (Ar, 50 mTorr, $P_{HF} = P_{LF} = 300$ W, $LF = 10$ MHz) and HF of 10, 50, 100 and 150 MHz. The maximum value in each frame is noted. S_{eb} is a log scale over two decades. The distribution of S_{eb} follows the ion fluxes which produce the secondary electrons. S_{eb} accounts for less than 10% of the total ionization.

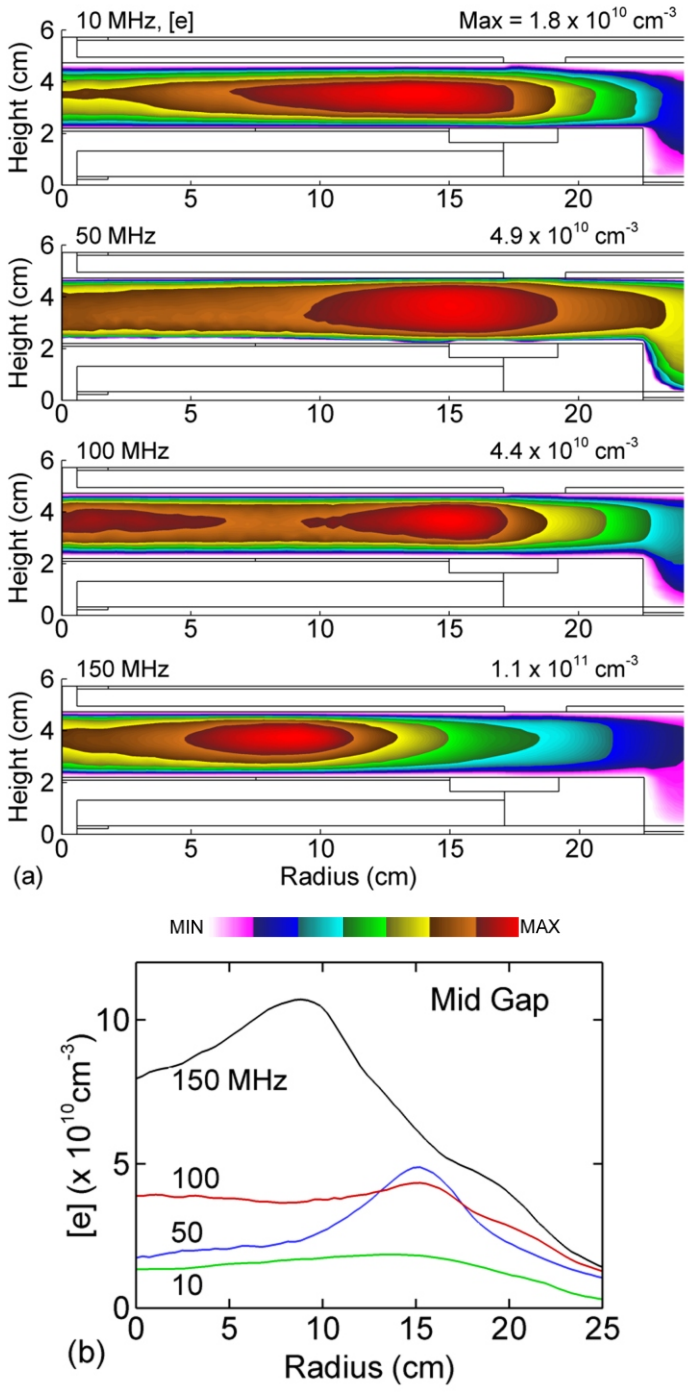

Fig. 4.12 - (Color) Time averaged electron density ([e]) for Ar/CF_4 = 90/10. (a) *HF* = 10, 50, 100, 150 MHz and (b) [e] as a function of radius at mid-gap. The conditions are otherwise the same as the base case (50 mTorr, $P_{HF} = P_{LF}$ = 300 W, *LF* = 10 MHz). The maximum value or range of values in each frame is noted. [e] is on a linear scale. With increasing *HF*, the [e] transitions from edge high between 10-50 MHz, to center-and-edge high at 100 MHz, and to mid-radius high at 150 MHz.

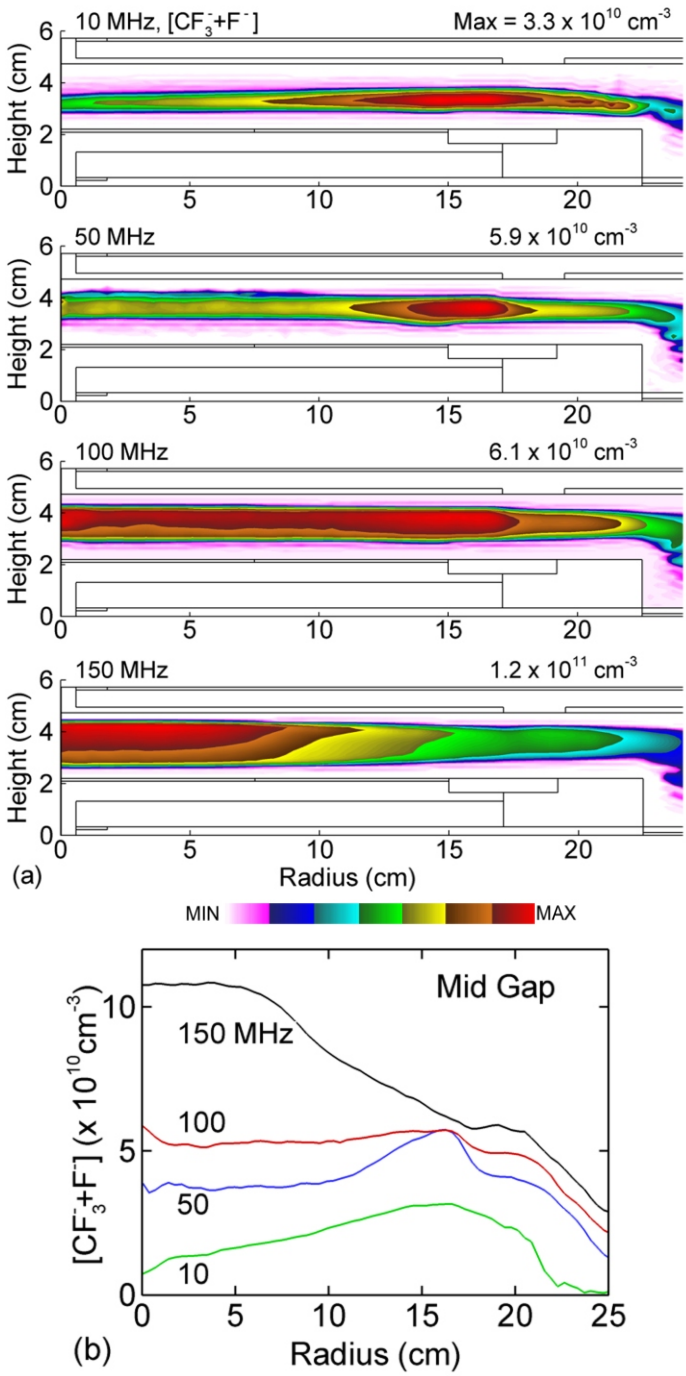

Fig. 4.13 - (Color) Time averaged total negative ion density ($[CF_3^-]+[F^-]$) for Ar/CF_4 = 90/10. (a) *HF* = 10, 50, 100, 150 MHz and (b) ($[CF_3^-]+[F^-]$) as a function of radius at mid-gap. The maximum value or range of values in each frame is noted. ($[CF_3^-]+[F^-]$) is on a linear scale. With increasing *HF*, the maximum of the total negative ion density shifts towards the center of the reactor due to a shift in the EEDs which favor attachment.

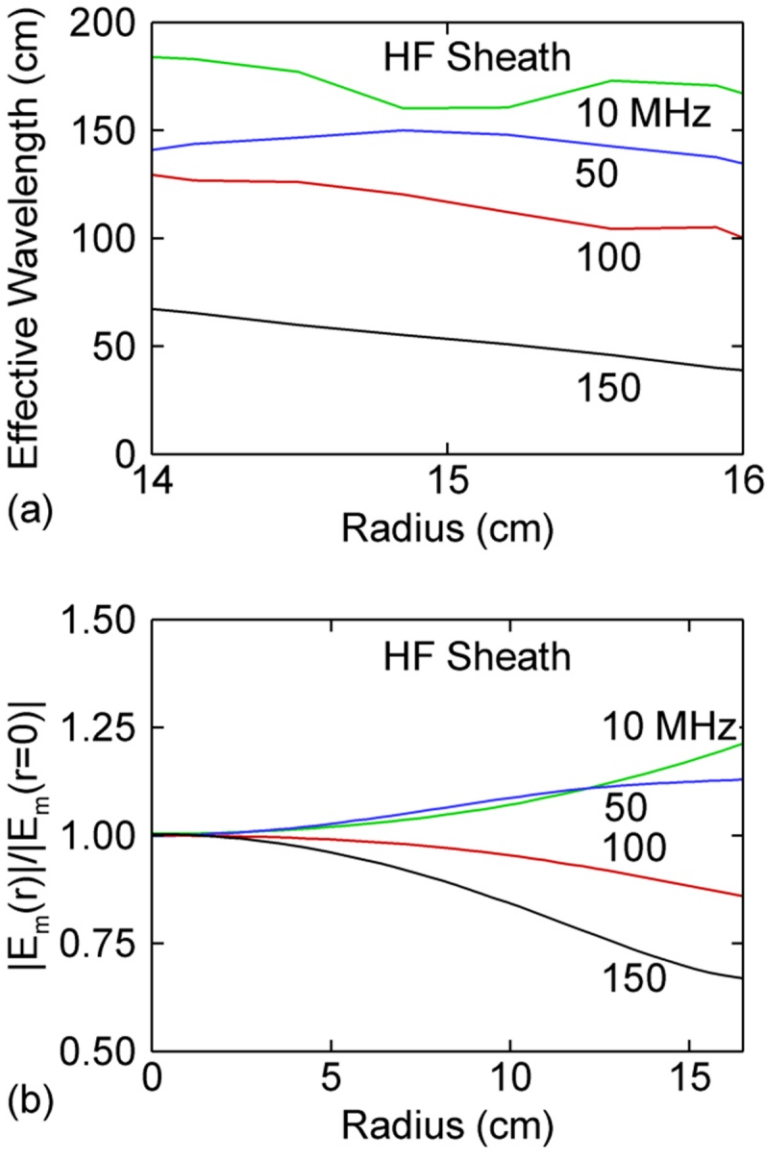

Fig. 4.14 - (Color) Electromagnetic properties for Ar/CF_4 = 90/10 and *HF* = 10-150 MHz. (a) Plasma effective wavelength in the *HF* sheath, (b) magnitude of the *HF* electric field in the *HF* sheath (normalized by the magnitude of the field at the center of the reactor). The changes in the plasma wavelength and electric field as a function of radius are not as dramatic as in pure Ar as the local electron density largely remains the same or even increases with *HF*.

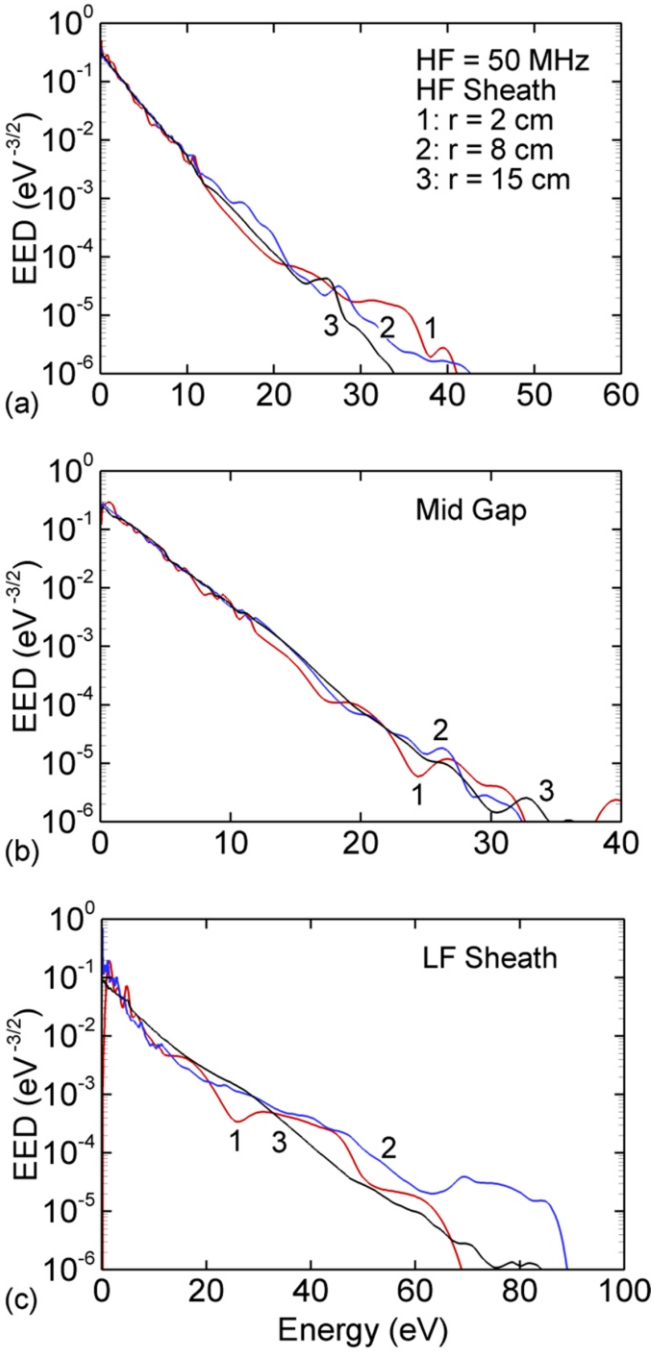

Fig. 4.15 - (Color) EEDs at different locations in the reactor for Ar/CF_4 = 90/10 and *HF* = 50 MHz. (a) In the *HF* sheath, (b) at mid-gap and (c) in the *LF* sheath. (These locations are shown in Fig. 1b.)

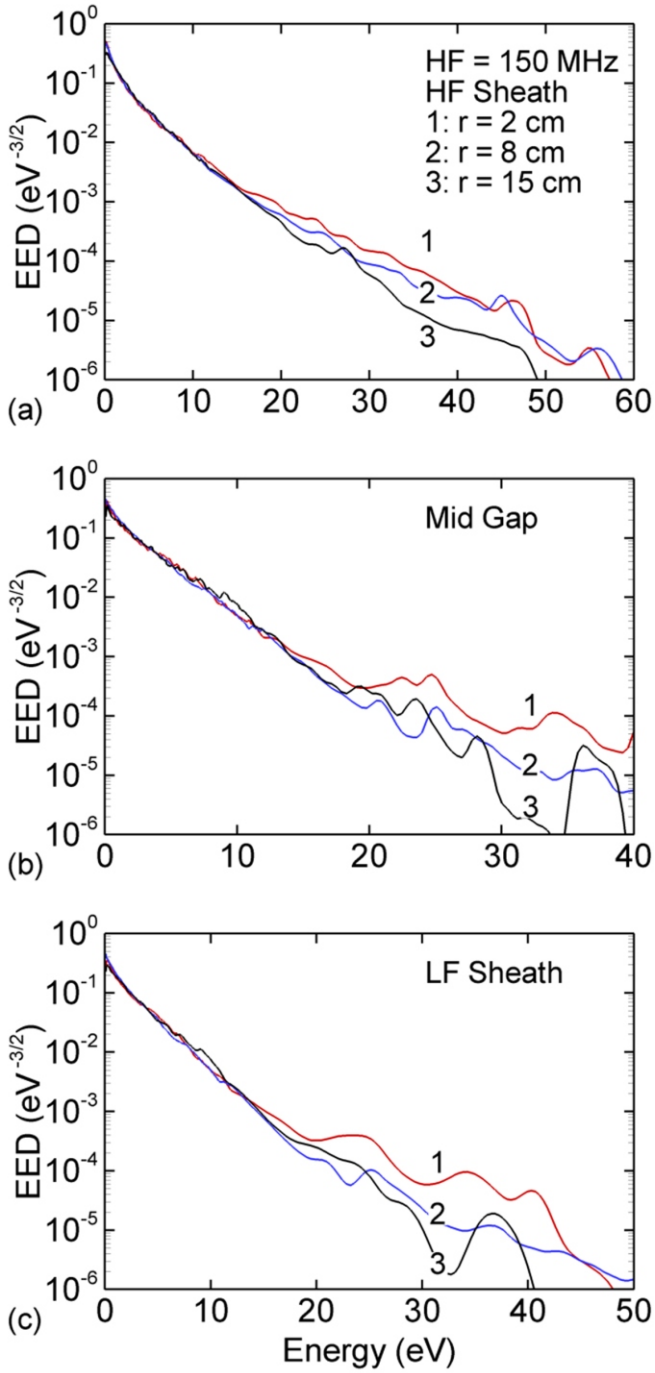

Fig. 4.16 - (Color) EEDs at different locations in the reactor for Ar/CF_4 = 90/10 and *HF* = 150 MHz. (a) In the *HF* sheath, (b) at mid-gap and (c) in the *LF* sheath. (These locations are shown in Fig. 1b.)

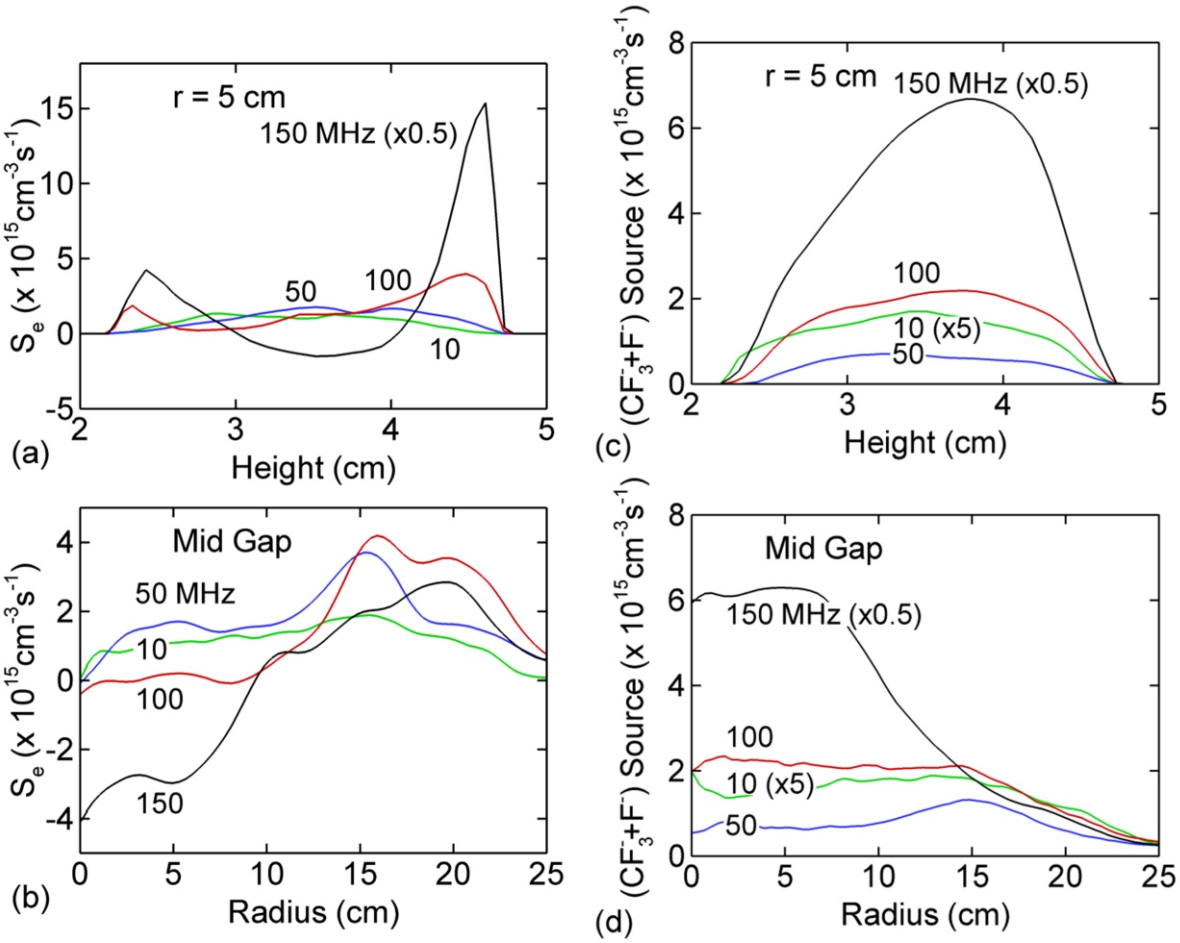

Fig. 4.17 - (Color) Source functions for $Ar/CF_4 = 90/10$ and *HF* = 10-150 MHz. The conditions are otherwise same as the base case (50 mTorr, $P_{HF} = P_{LF} = 300$ W, *LF* = 10 MHz). (a) Electron impact ionization source by bulk electrons as a function of height at r = 5 cm and (b) as a function of radius at mid-gap. (c) Source function for total negative ion production a function of height at r = 5 cm and (d) as a function of radius at mid-gap. Exceeding 100 MHz, sheath heating begins to dominate and electrons are produced closer to the oscillating *HF* sheath. There are net electron losses in the bulk plasma from attachment.

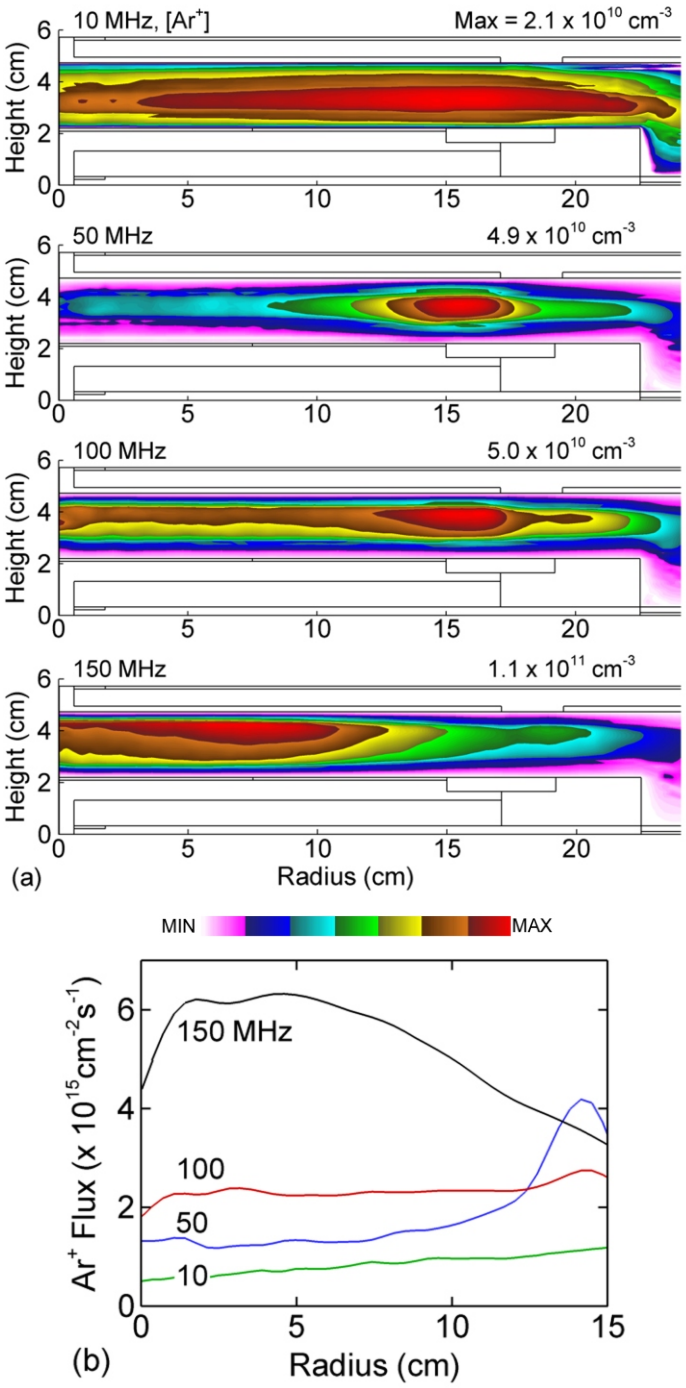

Fig. 4.18 - (Color) Time averaged Ar^+ density ($[Ar^+]$) for $Ar/CF_4 = 90/10$. (a) *HF* = 10, 50, 100, 150 MHz and (b) Ar^+ flux incident onto the wafer. The conditions are otherwise the same as the base case (50 mTorr, $P_{HF} = P_{LF} = 300$ W, *LF* = 10 MHz). The maximum value or range of values in each frame is noted. $[Ar^+]$ is on a linear scale. $[Ar^+]$ is peaked in the middle of the reactor at 150 MHz with significant contributions from multistep ionization.

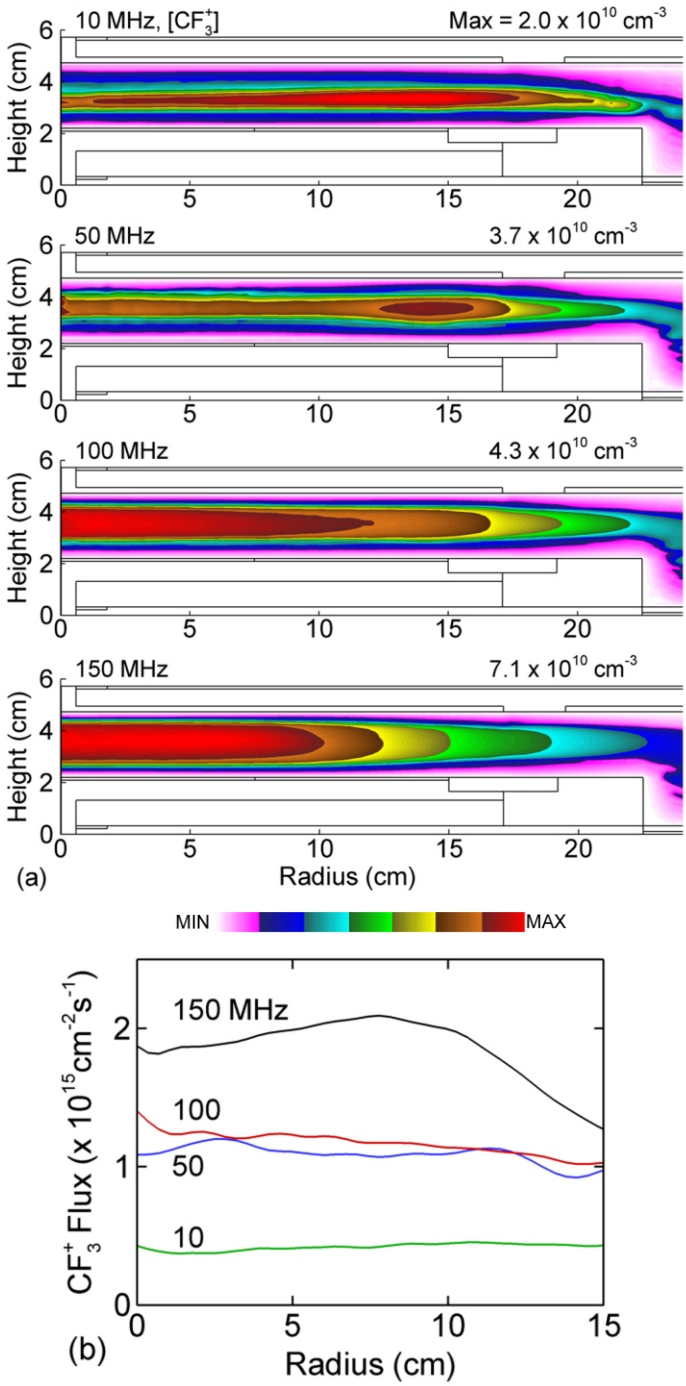

Fig. 4.19 - (Color) Time averaged CF_3^+ density ($[CF_3^+]$) for Ar/CF_4 = 90/10. (a) *HF* = 10, 50, 100, 150 MHz and (b) CF_3^+ flux incident onto the wafer. The conditions are otherwise same as the base case (50 mTorr, $P_{HF} = P_{LF} = 300$ W, *LF* = 10 MHz). The maximum value or range of values in each frame is noted. $[CF_3^+]$ is on a linear scale. $[CF_3^+]$ and flux are relatively uniform up to 150 MHz when there is a shift towards the center of the reactor.

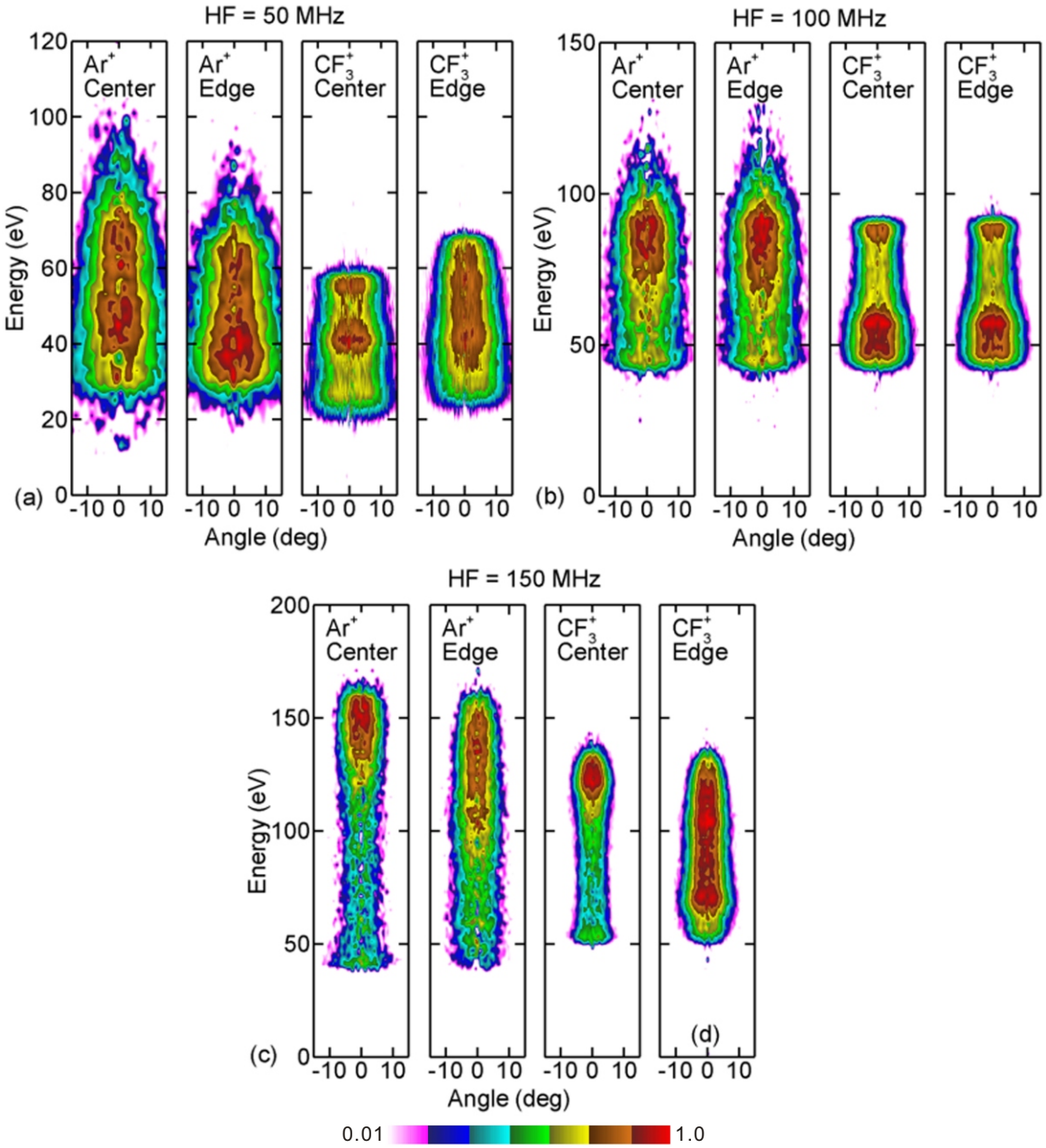

Fig. 4.20 - (Color) IEADs of Ar^+ and CF_3^+ incident onto the wafer for Ar/CF_4 = 90/10 and *HF* of (a) 50 MHz, (b) 100 MHz and (c) 150 MHz. The conditions are otherwise same as the base case (50 mTorr, $P_{HF} = P_{LF}$ = 300 W, *LF* = 10 MHz). The IEADs are separately collected over the center of the wafer (from r = 0 to 7.5 cm) and over the outer portion of the wafer (from r = 7.5 to 15 cm). The IEADs have units of $eV^{-1}sr^{-1}$. The contours span 2 decades using a log scale. Non-uniform plasma distributions at 50 and 150 MHz result in center to edge variations in the IEADs.

4.11 References

1. W. Tsai, G. Mueller, R. Lindquist, B. Frazier and V. Vahedi, J. Vac. Sci. Technol. B **14**, 3276 (1996).
2. V. Georgieva and A. Bogaerts, J. Appl. Phys. **98**, 023308 (2005).
3. T. Kitajima, Y. Takeo, Z. Lj. Petrovic and T. Makabe, Appl. Phys. Lett. **77**, 489 (2000).
4. L. Z. Tong and K. Nanbu, Europhys. Lett. **75**, 63 (2006).
5. P. Chabert, J. Phys. D: Appl. Phys. **40**, R63 (2007).
6. M. A. Lieberman, J. P. Booth, P. Chabert, J. M. Rax and M. M. Turner, Plasma Sources Sci. Technol. **11**, 283 (2002).
7. A. Perret, P. Chabert, J. P. Booth, J. Jolly, J. Guillon and Ph. Auvray, Appl. Phys. Lett. **83**, 243 (2003).
8. G. A. Hebner, E. V. Barnat, P. A. Miller, A. M. Paterson and J. P. Holland, Plasma Sources Sci. Technol. **15**, 879 (2006).
9. P. A. Miller, E. V. Barnat, G. A. Hebner, A. M. Paterson and J. P. Holland, Plasma Sources Sci. Technol. **15**, 889 (2006).
10. I. Lee, D. B. Graves, and M. A. Lieberman, Plasma Sources Sci. Technol. **17**, 015018 (2008).
11. S. Rauf, K. Bera and K. Collins, Plasma Sources Sci. Technol. **17**, 035003 (2008).
12. C. A. Balannis, *Advanced Engineering Electromagnetics*, (Wiley, New York), 1989, p. 149.
13. S. Rauf and M. J. Kushner, J. Appl. Phys. **82**, 2805 (1997).
14. S. Rauf and M. J. Kushner, IEEE Trans. Plasma Sci. **27**, 1329 (1999).
15. E. Abdel-Fattah and H. Sugai, Appl. Phys. Lett. **83**, 1533 (2006).

16. R. A. Bonham, Jpn. J. Appl. Phys., Part 1 **33**, 4157 (1994).

17. A. J. Lichtenberg, V. Vahedi, M. A. Lieberman, and T. Rognlien, J. Appl. Phys. **75**, 2339 (1994).

18. E. R. Fisher, M. E. Weber and P. B. Armentrout, J. Chem. Phys. **92**, 2296 (1990).

19. V. N. Volynets, A. G. Ushakov, D. Sung, Y. N. Tolmachev, V. G. Pashkovsky, J. B. Lee, T. Y. Kwon and K. S. Jeong, J. Vac. Sci. Technol. A **26**, 406 (2008).

20. M. A. Lieberman and A. J. Lichtenberg, *Principles of Plasma Discharges and Materials Processing*, (Wiley, New York, 2005) p 706.

21. J. P. Booth, G. Curley, D. Maric and P. Chabert, Plasma Sources Sci. Technol. **19**, 015005 (2010).

5. MODELING OF FLUORINE PLASMA TREATMENTS OF POLYPROPYLENE

5.1 Introduction

The fluorination of the surface layers of hydrocarbon polymers modifies the wetting properties of the polymer by decreasing the surface energy and increasing hydrophobicity.[1-3] The fluorination process usually entails the removal of hydrogen from the hydrocarbon polymer backbone, forming an alkyl site, and the passivation of the alkyl site with a fluorine atom.[4] As most hydrocarbon polymers are heat sensitive, it is desirable for the fluorination to take place at low temperatures. As such, low-pressure, non-equilibrium plasmas are attractive options for this surface treatment.

In low-pressure plasmas sustained in fluorine-containing feedstock gases, electron-impact reactions (mainly by dissociative excitation or attachment) produce fluorine-containing radicals at low ambient gas and surface temperatures. These radicals can both abstract hydrogen from the polymer surface layers, producing alkyl sites, and passivate those sites with fluorine atoms. Compared to fluorination by exposure to elemental fluorine gas at atmospheric pressure, low-pressure plasma fluorination proceeds more rapidly and more controllably. Significant fluorination of hydrocarbon polymers can occur in only a few seconds in low-pressure plasmas.[5-6] This fluorination typically occurs to a depth of at most 10 nm thereby leaving the bulk properties largely unchanged.[7] An added feature of plasma fluorination is that surface properties evolve under the simultaneous influence of fluorine-containing radicals, vacuum ultraviolet (VUV) radiation, and ion bombardment.[8]

A measure of the fluorination of a hydrocarbon polymer is the F/C atomic ratio of the surface layers, as determined by x-ray photoelectron spectroscopy (XPS or ESCA). Corbin et al.

[9] showed that in an inductively coupled Ar/F_2 =95/5 discharge at 50 W and 2 Torr, fluorination of polyethylene (PE) to an F/C of 1.8 (the maximum F/C is 2.0) was achievable in less than 1 min. Exposure to elemental fluorine gas resulted in an F/C of 0.2 over 3 min. Anand et al. [10] performed XPS to probe the surface layer and depth of fluorination after treatment of PE in an inductively coupled He/F_2 = 95/5 plasma. For a 3 mTorr discharge at 50 W, the fluorination depth was about 4 nm with there being competition between ion-assisted etching and fluorination. The fluorination depth increased with increasing pressure or flow rates and the fluorinated surface was cross-linked. Hopkins et al. [11] treated a variety of polymers (including PE, polypropylene, polyisoprene, polystyrene, polycarbonate) in 150 mTorr, 50 W inductively coupled CF_4 plasmas. They concluded that hydrogen abstraction from the polymer by fluorine to form HF is the initiating step to plasma fluorination. This is thermodynamically favored since C–H bond strengths are 3-4 eV as compared with 5.9 eV for H–F and 5.0 eV for C–F bonds. They found that, compared with saturated polymers, unsaturated polymers are more susceptible to plasma fluorination. A reaction pathway comprising fluorine addition at C=C double bonds was suggested.

Bond energies in hydrocarbon polymers are 3-4 eV while ions can gain tens to hundreds eV in traversing the plasma sheath at the polymer surface in a low-pressure plasma. These ions are capable of breaking bonds, sputtering and affecting surface composition through bond scission, and subsequent cross-linking. The sputtering yields of ions are functions of incident ion energy, polymer surface bonding energy, and mass difference between the ions and the atom or molecular fragments on the polymer backbone. Stelmashuk et al. [12] and Biederman et al. [13] performed radio-frequency (rf) magnetron sputtering of polypropylene (PP) in Ar plasmas over pressures of 5-67 mTorr and powers of 25-100 W. Ion bombardment and subsequent heating of

the PP caused changes in the molecular structure of the target including melting and cross-linking. They found that sputtering preferentially lowered the proportion of CH_3 groups in the PP, transforming them into CH and CH_2 groups, which promoted cross-linking. They also found that the rates of sputtering of PP and PE are less than one-third that for polytetrafluorethylene (PTFE). This is likely a result of the more favorable mass ratio of the incident Ar ions to the C–F bond in PTFE as compared with the C–H bond in PE. Biederman et al. modeled bombardment of PE by Ar ions using molecular dynamics and proposed that the ions cause chain scission, cross-linking, and carbonization of the target.[14] The ejected species were dominated by atomic and molecular hydrogen, but also included large chain fragments containing up to 20 CH_2 units.

VUV radiation is typically produced in low-pressure plasmas. In particular, in Ar/F_2 plasmas, excited states of F, F_2 and Ar produce radiation in the range of 95-157 nm. Impurities (e.g., H_2O, O_2, and CO_2) also emit in this region (115-360 nm). The C–C or C–H bonds of hydrocarbon polymers absorb radiation below 160 nm producing hemolytic bond scission and giving rise to either polymer ablation or to the formation of functional groups and reactive sites (e.g., double bonds and radicals).[15-20] Corbin et al. investigated the enhancement of fluorination of PE under VUV irradiation originating from a He/F_2 discharge.[21] The PE was immersed in a He/F_2 mixture and isolated from the plasma by a VUV-transmitting window. They found that radiation below 180 nm increased the rate of fluorination. Dorofeev and Skurat performed photolysis of PP in vacuum with 147 nm radiation from a Xe lamp and subsequent UV absorption spectroscopy on the irradiated sample.[22-24] They found that PP photolysis at 147 nm primarily liberates H_2 along with the formation of a C=C bond with a quantum yield of about 0.25. The scission of the C–C bond produces two radicals that undergo disproportionation form-

ing a methyl group and a chain-end double bond. They also observed scission of C–H and C–C bonds, which splits the atomic hydrogen and methyl groups, respectively, with a quantum yield about 0.025.

Ono et al. [25] studied VUV photo-degradation of PTFE by ultraviolet photoelectron spectroscopy (UPS) and quadruple mass spectrometry. They found that, unlike the photolysis of PP and PE, C=C bond generation is not a major process. They found CF_n (n=1-3) in the ejecta, indicating that the polymer C–C backbone undergoes scission, a process also observed by Skurat et al.[26] Ono et al. estimated the quantum yield for atomic fluorine photolysis at 147 nm to be 0.0025.

In this chapter, results are presented from a computational investigation of the gas-phase and surface kinetics during the fluorination of PP in a low-pressure capacitively coupled Ar/F_2 plasma (CCP) while accounting for both ion bombardment and VUV illumination. A surface reaction mechanism for the fluorination of PP films was developed, incorporated into a 2-dimensional model for gas and surface processes, and applied to a CCP reactor patterned after an industrial prototype.[27] It is found that the degree of fluorination, as expressed by the F/C ratio, affects the rate of additional fluorination due to a deactivation effect and steric hindrance by adjacent F atoms. For films electrically floating in the plasma (and not in contact with an electrode) and with moderate exposure times (< tens of s), ion bombardment is not particularly important to the final F/C ratio. However, given longer exposure time or placement of the film on an electrode, ion sputtering produces significant changes in surface composition. In general, photon-induced reactions have little affect on film properties for moderate exposure times (< tens of seconds) largely due to the lower magnitudes of photon fluxes as compared with radical and ion fluxes. It is found that fluorination generally increases monotonically with power, pressure, and

F_2 concentration. Good agreement for fluorination rates and surface compositions between model and experimental results was achieved.

5.2 Description of the Model and Gas Phase Reaction Mechanism

Following every iteration of the HPEM, the electric fields and source functions for ions are recorded as a function of position and phase in the rf cycle. With these values, the energy and angular distributions of ions (IEADs) incident on the PP film are obtained using the PCMCM described in detail in Ref. 28 and Ref. 29. The IEADs are used to compute probabilities of energy-dependent surface processes such as sputtering. The MCRTM, described in Ref. 30, is also called after every iteration to provide photon fluxes incident on the PP film. The VUV radiation tracked in the model originates from resonance transitions from F(3s) and Ar(4s) and from $F_2(C^1\Sigma_u, H^1\Pi_u)$. An outcome of the MCRTM is trapping factors for resonance radiation and these factors are used to update the radiative lifetimes of the radiating states in the reaction mechanism.

With the surface reaction mechanism described in Sec. 5.3, the SKM is called after each iteration to integrate the coupled rate equations for the coverage of surface species using site-balance techniques. Input to the SKM include fluxes of electrons, ions (and energy distributions), neutrals and VUV radiation from the other modules of the HPEM. The SKM is described in detail in Ref. 31.

A schematic of the CCP reactor used in this study is shown in Fig. 3.1.[27] The modeled parallel-plate reactor has electrodes 46 cm × 46 cm separated by 2.54 cm. One electrode is grounded and the opposite is powered at 10 MHz through a blocking capacitor. The feedstock gases are injected through nozzles in both electrodes and pumped out at the right side of the reac-

tor. The reactor is integrated into a web-processing line where a polymer film enters from the left side of the reactor and translates to the right where, in an actual device, the collector roll might be located. Typical web speeds are up to several to tens of cm-s^{-1} and the film spends from seconds to tens of seconds in the discharge. The thickness of the PP film is 2.5×10^{-3} cm, which is smaller than our mesh resolution. In principle, this discrepancy should only affect the electrical properties of the film. Accordingly, the permittivity (dielectric constant) of the film was scaled so that the area capacitance (F-cm^{-2}) is the same as the actual film. The model is 2-dimensional, and so only the plane perpendicular to the film and parallel to the web direction is resolved.

The movement of the polymer film through the plasma was also modeled. The speed and direction of the web are specified. Assuming that the film is moving from left-to-right as shown in Fig. 3.1, during execution of the SKM, at every $\Delta t = \Delta x/v$ (Δx is the numerical mesh spacing of the polymer film and v is the web speed), the surface properties of the mesh point to the left on the surface are translated to the mesh point to the right. The surface properties of the leftmost film mesh point are set to the initial conditions (untreated PP in this case) whereas the surface properties of the rightmost mesh point are translated outside the computational domain. These latter surface compositions are referred to as the exit properties of the film.

The gas-phase reaction mechanism for Ar/F_2 plasma is summarized in Table 5.1. With mole fractions of F_2 greater than a few percent, the production of F atoms mainly comes from electron dissociative attachment of F_2, producing highly electronegative plasmas. Direct dissociation of F_2, due to excitation to the dissociative electronic states $F_2(a^3\Pi)$ and $F_2(A^1\Pi)$ (minimum threshold energy 3.16 eV), is not a major contributor at our conditions in comparison with dissociative attachment. The density of F atoms is generally five orders of magnitude larger than

that of F^+ for our conditions. Therefore, the majority of loss of F^- results from associative detachment between F^- and F as opposed to ion-ion neutralization processes. The gas phase reaction mechanism includes Ar(4s) metastable (Ar^* in Table 5.1), radiative states of Ar(4s) (Ar^{***} in Table 5.1), and Ar(4p) radiative states (Ar^{**} in Table 5.1). Resolving these states in the reaction mechanism is necessary to characterize the photon transport in Ar/F_2 plasmas.

5.3 Surface Reaction Mechanism for Polypropylene Fluorination

Isotactic PP is a saturated hydrocarbon polymer with a carbon backbone containing hydrogen and methyl ($–CH_3$) groups arranged in an alternating fashion. (See Fig. 3.2.) The reactivities of the hydrogen atoms in PP depend on the position of the C atom to which they are attached: primary C atoms (C_P) are bonded to one other carbon atom, secondary C atoms (C_S) are bonded to two other C atoms, and tertiary C atoms (C_T) are bonded to three other C atoms. Therefore, a PP repeating unit consists of two secondary H atoms (H_S), a tertiary H atom (H_T), and three primary H atoms (H_P) in the methyl ($–CH_3$) group. The reactivities of H atoms bound to C atoms generally scale as $H_T > H_S > H_P$.

The general surface reaction mechanism for PP fluorination is given in Table 5.2. The initial total density of surface sites, as reported for virgin PP, is $\approx 10^{15}$ cm^{-2}.[32] The total number of surface sites may vary with treatment time as, for example, methyl groups are removed from the PP chain by ions or photons, or gaps are made in the PP chain by ion bombardment. When a gap is made in the PP chain, reactions occur with the newly formed free radicals in the broken chain as well as with the exposed PP chain in the underlying layer.

The basic fluorination process is represented by the sequence of reactions of abstraction and passivation;

$$–(CH_2)(CH)(CH_3)– + \bullet F_g \rightarrow –(CH_2)(CH)(CH_2\bullet)– + HF_g\,, \quad (1)$$

$$–(CH_2)(CH)(CH_2\bullet)– + \bullet F_g \rightarrow –(CH_2)(CH)(CH_2F)–, \quad (2)$$

$$–(CH_2)(CH)(CH_2\bullet)– + F_{2g} \rightarrow –(CH_2)(CH)(CH_2F)– + \bullet F_g\,. \quad (3)$$

The subscript *g* denotes a gas phase species. $–(CH_2)(CH)(CH_3)–$ represents the repeating unit of the saturated hydrocarbon, represented here as having a linear arrangement of C_S, C_T, and C_P. As such, $–(CH_2)(CH)(CH_2\bullet)–$ represents a polymer free radical on the C_P. $–(CH_2)(CH)(CH_2F)–$ represents a fluorinated site on the C_P. In this sequence, an F atom extracts an H atom from the PP chain at the C_P site to form gas phase HF and an alkyl site (e.g., a free radical on a carbon atom). That radical is then passivated by either an F atom to form C–F surface bonding, or an F atom is abstracted from a gas-phase F_2 to form the C–F. For clarity, a specific reaction sequence has been shown for the C_P site. The modeled reaction mechanism contains all possible combinations and permutations of partially and fully fluorinated PP sites. For example,

$$–(CHF)(CH)(CH_2F)– + \bullet F_g \rightarrow –(CF\bullet)(CH)(CH_2F)– + HF_g\,, \quad (4)$$

$$–(CF\bullet)(CH)(CH_2F)– + \bullet F_g \rightarrow –(CF_2)(CH)(CH_2F)–\,. \quad (5)$$

represent the abstraction of H from a partially fluorinated C_S site and the subsequent passivation to form a fully fluorinated C_S. As discussed below, the probability of abstraction and fluorination depends on the location on the PP chain (e.g., primary, secondary, or tertiary) and the state of local fluorination (e.g., is there a fluorinated site adjacent to the H atom to be abstracted). The latter dependence results from both steric factors (i.e., physical blocking) from the larger F atoms

and deactivation effects. To account for all permutations of abstraction and fluorination from all combinations of partially fluorinated sites, alkyl sites, and chain fragments, the mechanism has 4,540 reactions. The successive reactions of H abstraction, followed by passivation by F or F_2 progresses until, ideally, all H atoms are replaced by F atoms. For PP, this would result in an F/C = 2.

In general, surface reactions with plasma-delivered species can be classified as: fluorine abstraction of hydrogen, fluorine addition, ion sputtering, and photon induced. With the exception of fluorine addition, these reactions create free radical sites, thereby introducing the probability of cross-linking, that is the formation of a C–C bond between different PP molecules or between different portions of the same PP molecule. As any functional group can further react with neutrals, ions, or photons, many dozens of different configurations of the PP backbone can be produced. To adequately characterize such a complex mechanism using a reasonable number of parameters, we implemented a reaction hierarchy that addresses the major pathways in a systematic way while also accounting for secondary pathways.

5.3.1 F-abstraction Reactions

The fluorination process starts with the abstraction of H from the PP backbone creating alkyl sites for subsequent fluorination. H can be abstracted from any of the primary, secondary or tertiary sites in PP. The probability of abstraction generally scales as $H_T > H_S > H_P$. For example, the reactivity for abstraction of H from PP by O atoms, scales as $H_T = 10 \cdot H_S = 100 \cdot H_P$ [33]. H-abstraction probabilities by F atoms should be greater than those by O atoms due to the larger electron affinity of F atoms. To calibrate these probabilities, analogies were made to gas-phase reactions. One example is the abstraction of H by F from iso-butane,

$$\text{iso-}C_4H_{10} + \bullet F \rightarrow \text{iso-}C_4H_9\bullet + HF \qquad k = 6.8 \times 10^{-11}\ cm^3s^{-1}, [34] \qquad (6)$$

$$\text{iso-}C_4H_{10} + \bullet F \rightarrow \text{tert-}C_4H_9\bullet + HF \qquad k = 9.6 \times 10^{-11}\ cm^3s^{-1}. [34] \qquad (7)$$

where k is the room temperature rate coefficient. From these reactions, we estimated that the rate of H_T abstraction is about 1.4 times larger than that of H_P. For this work, we used probabilities that scale as $H_T = H_S = 1.5 \cdot H_P$. To determine absolute surface reaction probabilities, we compared H abstraction by F atoms to H abstraction by O atoms in the gas phase,

$$\text{iso-}C_4H_{10} + \bullet O \rightarrow \text{tert-}C_4H_9\bullet + \bullet OH \qquad k = 3.0 \times 10^{-13}\ cm^3s^{-1}. [33] \qquad (8)$$

The rate of H_T abstraction by O atoms is about 100 times slower than by F atoms. With the probability for H_T abstraction being 10^{-3} for O atoms [33], we assigned the reaction probability for abstraction by F atoms to be on the order of 10^{-1}.

This initial estimate for H abstraction by F atoms is for the fully hydrogenated PP site. It is known that H-atom abstraction and fluorination become progressively more difficult as F atoms are added to the PP backbone because of a deactivation effect and steric hindrance by those F atoms.[9, 34] To reduce the number of adjustable probabilities in the surface reaction mechanism to account for these dependencies, a hierarchy of reaction probabilities was developed based on the following considerations. Reaction probabilities will first depend on the reactivity of primary, secondary, and tertiary sites. Second, reactivities will depend on the local F/C ratio, thereby accounting for steric factors and electrophilic effects. To enable setting of relative rates of reactions of different fluorination states, reference was made to reactions of gas-phase analogs.

For example, the rate of H atom abstraction by F from a long-chain alkane differs depending on the number of fluorinated bonds,

$$C_3H_8 + \bullet F \rightarrow n\text{-}C_3H_7 + HF \qquad k = 5.8 \times 10^{-11}\ cm^3s^{-1},\ [35] \qquad (9)$$

$$C_2F_5CF_2H + \bullet F \rightarrow n\text{-}C_3F_7 + HF \qquad k = 3.2 \times 10^{-13}\ cm^3s^{-1}.\ [36] \qquad (10)$$

The rate of abstraction for $C_2F_5CF_2H$ is 100 times smaller than that for propane, C_3H_8. To some degree this scaling should translate to the difference in probability of abstraction of H from PP between initial and final fluorination states. Having said that, we need to take into account the intrinsic difference in access by F atoms to bonded H atoms on the surface of a polymer as compared with the gas phase. In gas-surface reactions, F atoms must diffuse into the surface to react with H atoms that are oriented away from the PP surface. Sites underlying the PP backbone thereby get fluorinated more slowly as compared with sites on top of the PP backbone. The effect is more pronounced for a PP chain underlying the chain on the top surface. As such, if we average the abstraction probabilities over the fluorination depth, the resulting probabilities are smaller than the gas-phase analogs. In our site-balance model, we decreased the abstraction probabilities from the gas-phase analogs to account for F diffusion to underlying sites and hindrance by previously fluorinated sties. For the fully hydrogenated PP backbone, we set the abstraction probabilities of hydrogen from tertiary, secondary, and primary sites as $P_T = 3 \times 10^{-5}$ and $P_S = P_P = 5 \times 10^{-5}$. These values are maximum values for P_S, P_P, and P_T in the hierarchy of H abstraction probabilities.

As the transport of fluorine into the film is diffusion-limited, steric hindrance does not play a major role in fluorination of the underlying PP backbone. After F atoms diffuse into the

PP network, they are confined between the PP chains thereby having a greater probability to react with adjacent C–H bonds. Therefore, the decrease of abstraction probabilities with increasing degree of fluorination is less severe for the underlying PP backbone. The abstraction probability for the last H_T in a PP unit [–$(CF_2)(CH)(CF_3)$–] was set to $P_T = 10^{-5}$. The abstractions probabilities for the last H_S [–$(CHF)(CF)(CF_3)$–] and last H_P [–$(CF_2)(CF)(CHF_2)$–] were set to $P_S = P_P = 3 \times 10^{-5}$. As compared with the fully hydrogenated PP, these probabilities are 1.7 times smaller for P_S and P_P; and 3 times smaller for P_T. The hierarchy of F abstraction probabilities is listed in Table 5.3.

The surface species in our model in different fluorination states, such as [–$(CH_2)(CF)(CH_3)$–], are grouped into PP repeating units. In this example, C_S and C_P and C_T are in the same PP unit and are bonded to each other. To account for the change in fluorination rates with fluorination depth due to diffusion effects, we allowed that C_S and C_P can represent segments on different layers of the PP backbone. Though some surface species are still expressed in the form of a PP unit, the C atoms in them might be on different layers and not bonded to each other in the polymer backbone. As such, some surface species become virtual two-layer species.

Starting with untreated PP, we assigned the first fluorinated C atom to represent a segment on the topmost layer. The remaining fully hydrogenated C atoms represent segments on the underlying PP backbone. For example, starting with [–$(CH_2)(CH)(CH_3)$–], if C_S is first fluorinated, then we assigned that site to the top layer and assigned the fully hydrogenated C_P and C_T to be on the underlying backbone. So in [–$(CHF)(CH)(CH_3)$–], (–CHF) represents a C_S segment on the top backbone and the corresponding P_S was set to 5×10^{-5} (P_S in Fig. 3). (CH_3) and (CH)are on the underlying PP backbone and the corresponding P_P and P_T (shown in Fig. 3)

were set to 2×10^{-5} and 10^{-5}, respectively. Note that the assignment to an underlying-layer was only applied to fully hydrogenated sites.

In general the rate-limiting step in the fluorination process is the initial abstraction of H to create an alkyl site. The probability of fluorine addition to an alkyl site should be large compared to that for H abstraction because of the more negative change in enthalpy of the addition process. Although probabilities for F addition by F_2 reactions are smaller than that by F atoms, and as will be shown below, the flux of F_2 incident onto the surface is usually larger than that of F. The end result is that the lifetime for surface radical species is short because of passivation by both F and F_2. The fluorination process then follows the sequence of creating one free radical, passivating that radical by F or F_2, followed by creating another free radical.

The likelihood of creating multiple radicals on the same PP repeat unit before passivation occurs is small. Even in the absence of the rapid fluorination of free radicals, the probability for abstracting the second H in the vicinity of another radical is smaller than abstracting the first H atom. By analogy to related work the rate coefficients for creating second and third radicals in the same gas-phase alkane molecule are usually significantly smaller than for creating the first radical. One such example is the abstraction of H from methane by Cl atoms,

$$CH_4 + \bullet Cl \rightarrow CH_3 + HCl \qquad k = 9.2 \times 10^{-14}\ cm^3s^{-1},\ [37] \qquad (11)$$

$$\bullet CH_3 + \bullet Cl \rightarrow HCl + \bullet\bullet CH_2 \qquad k = 3.0 \times 10^{-17}\ cm^3s^{-1}.\ [38] \qquad (12)$$

Based on analogies to these and other reactions, and considering that F is typically more reactive than Cl, we set surface reaction probabilities for creating the second free radical as being five times smaller than that for the first radical. This applies to reactions that create the second radi-

cal on the same C and to reactions that create the second radical in the same PP unit (radicals on different C atoms). We acknowledge that this estimate may exaggerate the decreased propensity for additional radical formation and so provides an upper bound to the reaction probability.

5.3.2 Cross-linking

Creating adjacent free radicals on the PP backbone enables the possibility of cross-linking reactions. For example, a surface species [–$(CH_2)(CF)(CH_2\bullet)$–] (D_1) containing a free radical is produced by F abstraction. Prior to the passivation of D_1, a second free radical (D_2) can be produced on an adjacent PP repeating unit [–$(CF\bullet)(CH)(CH_3)$–]. If D_1 and D_2 are physically close to each other, they can react and cross-link prior to being passivated by F atoms,

$$-(CH_2)(CF)(CH_2\bullet)- + -(CF\bullet)(CH)(CH_3)- \rightarrow -(CH_2)(CF)[(CH_2)-(CF)](CH)(CH_3)-. \quad (13)$$

Here, two different PP units are cross-linked by the formation of a C–C bond [(CH_2)–(CF)]. Because of the large number of surface species containing radicals and the correspondingly large variety of potential cross-linking products, we generalized the cross-linking reaction of –$(CH_2)(CF)(CH_2\bullet)$– as

$$-(CH_2)(CF)(CH_2\bullet)- + M \rightarrow -(CH_2)(CF)(CRH_2)- + M. \quad (14)$$

where M represents the density of all surface species containing free radicals. The R in [–$(CH_2)(CF)(CRH_2)$–] denotes cross-linking on the corresponding C_P site. Note that Eq. (14) does not indicate to which PP segment the C_P is cross-linked. The rate of Eq. (14) is determined

by

$$Rate = \left[-(CH_2)(CF)(CH_2\bullet)-\right][M][N_{PP}]P_{cr}\,f_{cr} \qquad (15)$$

where [–(CH$_2$)(CF)(CH$_2$•)–] and [M] are the fractional coverages of –(CH$_2$)(CF)(CH$_2$•)– and M respectively, [N_{PP}] is the surface density of PP units (10^{15} cm^{-2}), and f_{cr} is the cross-linking frequency for unity coverage of M. As any radical site could potentially cross-link with M, P_{cr} is the probability that a specific site [–(CH$_2$)(CF)(CH$_2$•)– in this example] will cross-link with M. We set f_{cr} as 10^3 s^{-1} for all cross-linking reactions and established a hierarchy for P_{cr} based on the location on the PP chain and the state of local fluorination.

Free radicals created before F addition are most likely to be cross-linked since the unfluorinated PP chain has the smallest steric hindrance. The cross-linking probabilities of the fully hydrogenated PP chain (except for the radicals) are P_{cr} = 10^{-2}, 5 × 10^{-3}, 5 × 10^{-3}, for cross-linking on C_P, C_S, and C_T sites respectively. These values are the largest in the hierarchy of cross-linking probabilities. With addition of F, the site-specific probabilities have the same dependence on the local bonding as the F abstraction probabilities. For example, P_{cr} for C_P is decreased by a factor of 1.7 to 6 × 10^{-3} for [–(CF$_2$)(CF)(CF$_2$•)–].

5.3.3 F Addition

In the gas phase, the addition of an F atom to an alkyl radical is a three-body process and typically has a small effective two-body rate coefficient at low pressure. On the polymer surface, phonons act as the third body so that the reaction probability of F addition can have a high effective two-body rate. To estimate the surface probability, comparisons were made between rates of

gas-phase F addition in the high-pressure limit and rates of abstraction by F atoms. For example,

$$\bullet CH_3 + \bullet F \rightarrow CH_3F \qquad k = 9.3 \times 10^{-11}\ cm^3s^{-1}, [39] \qquad (16)$$

$$CH_4 + \bullet F \rightarrow \bullet CH_3 + HF \qquad k = 4.7 \times 10^{-11}\ cm^3s^{-1}, [40] \qquad (17)$$

$$\bullet CF_3 + \bullet F \rightarrow CF_4 \qquad k = 2.0\times 10^{-11}\ cm^3s^{-1}, [41] \qquad (18)$$

$$CHF_3 + \bullet F \rightarrow \bullet CF_3 + HF \qquad k = 3.2 \times 10^{-13}\ cm^3s^{-1}. [42] \qquad (19)$$

In general, the rate coefficients for F addition are larger than the corresponding H-abstraction reactions by F atoms. There is also less reduction in the rate coefficients for F addition with increasing F/C ratio as compared with H abstraction. Based on these reference reactions, we set the probability for F addition at the first alkyl site on any of C_P, C_S, and C_T for otherwise fully hydrogenated PP as 10^{-4}. The hierarchy of F addition probabilities is shown in Table 5.4.

Similar techniques were used to determine reaction probabilities for F addition by F_2 at an alkyl radical. For example, gas-phase analogues are,

$$C_2H_6 + \bullet F \rightarrow \bullet C_2H_5 + HF \qquad k = 1 \times 10^{-10}\ cm^3s^{-1}, [43] \qquad (20)$$

$$\bullet C_2H_5 + F_2 \rightarrow C_2H_5F + \bullet F \qquad k = 1.3 \times 10^{-11}\ cm^3s^{-1}, [43] \qquad (21)$$

$$\bullet CF_3 + F_2 \rightarrow CF_4 + \bullet F \qquad k = 1.5 \times 10^{-14}\ cm^3s^{-1}. [41] \qquad (22)$$

Comparing these reactions, F addition by F_2 should have smaller probabilities than the abstraction reaction by F. Based on these and other reactions, we scaled probabilities for F addition by F_2 to be five times smaller than those for addition by F atoms.

5.3.4 Ion Sputtering of Polypropylene

In Ar/F_2 plasmas, the ions incident on the PP film include Ar^+, F^+, and F_2^+. Sputtering differs from abstraction or addition reactions in the ability to ablate C atoms from the PP, thereby changing the structure of the PP surface. Apart from this physical sputtering, F^+ and F_2^+ are also capable of inducing abstraction or addition reactions. Having said that, for our conditions, the fluxes of F and F_2 neutrals exceed those of the ion fluxes by several orders of magnitude and so we neglected the additional abstraction or addition that might be produced by F^+ and F_2^+ in addition to their physical sputtering reactions. Sputtering of individual H atoms by F^+ and F_2^+ was also neglected as H abstraction by F proceeds at rates that are also orders of magnitude higher.

The sputtering yields of C from the PP backbone as a function of energy for Ar^+ and F^+ were estimated using *SRIM*.[44] The SKM uses a general form of ion-energy-dependent reaction probability,

$$Y(E) = p_o \cdot \frac{E^n - E_{th}^n}{E_r^n - E_{th}^n}, \tag{23}$$

where $Y(E)$ is the sputtering yield at ion energy E, p_o is the yield at reference energy E_r, and E_{th} is the threshold energy. Results from *SRIM* were fitted to the form of Eq. (23). For the same ion energy, the sputtering yields of C atoms by Ar^+ or F^+ incident on PTFE were typically higher than the yields for PP, as PTFE has a more favorable mass ratio with the incident ion. To simplify the mechanism, we used sputtering yields for PTFE as an approximation for sputtering of C_T and C_S in all fluorination states. When a C atom is sputtered, we assumed that the F and H atoms initially bonded to that C atom remain bonded and thus also leave the PP surface. We also assumed that sputtering of C_T also removes the CH_3 bonded to it. Although this simplification

exaggerates sputtering at low F/C ratios, it captures the removal of the top surface layer by ion bombardment and the subsequent exposure of the fresh underlying hydrocarbons. The sputtering parameters used in Eq. (23) are shown in Table 5.5. Because of lack of fundamental data, we assumed that F_2^+ has the same sputtering yields as Ar^+ because the molecular weights of the two ions are similar.

For example, a typical sputtering reaction of a nearly fully fluorinated PP segment is,

$$–(CF_2)(CF)(CHF_2)– + \bullet F^+_g \rightarrow –(CH_2)(\bullet CF)(CHF_2)– + \bullet CF_{2g} + \bullet F_g\,, \quad (24)$$

$$–(CH_2)(\bullet CF)(CHF_2)– + \bullet F_g \rightarrow –(CH_2)(CF_2)(CHF_2)–. \quad (25)$$

where C_S (with two F atoms attached) is ablated and the underlying C_S (with two H atoms attached) is exposed to the plasma. Since the CH_2 functional group actually lies on the layer underneath $–(\bullet CF)(CHF_2)–$, the latter species contains a chain-end on the first layer having a free radical. Since the PP polymer is likely to be randomly oriented at the surface with respect to the alignment of the PP backbones, sputtering of, for example, C_S may in fact expose, C_P, C_S, or C_T in the underlying chain. For simplicity and consistency we assumed that removal of C_T (together with attached methyl group) or C_S will expose the same type of site in the underlying layer. For surface species that contain segments on different layers, we expect that the C atoms on the underlying layer are less likely to be sputtered because of shielding from the top layer. As a result, we only considered sputtering of C atoms on the top layer.

Because of the expected large neutral fluxes compared to ion fluxes, the free radicals produced by ion bombardment will likely be quickly passivated by F or F_2. We represented the passivation process in Eq. (25) by adding an additional F atom to the initial C_T to terminate the

chain. Although this is an approximation for our conditions, it facilitated the elimination of many hundreds of reactions in our mechanism with little loss of accuracy. This rapid passivation of free radicals also hinders the plasma from reaching the exposed hydrocarbon on the underlying layer. As a result, we assumed that the abstraction and additions rates on the second underlying layer are 100 times slower than the rates on the surface layer given the same state of fluorination. The rapid passivation, producing short lifetimes for surface free radical sites, enables us to ignore the sputtering of free radicals thereby eliminating an additional set of reactions with little loss of accuracy.

Ion bombardment can also ablate short-chain molecules from the polymer surface. For example, short-chain fragments containing up to 20 CH_2 units have been observed following bombardment of PE by Ar^+.[13] In our reaction mechanism, short-chain ablation is represented by the removal of a length of the backbone cleaved at the bonds between the C_S and C_T atoms. Removal of this chain then exposes fresh PP backbone on the underlying layer. The exposed PP backbone, as an untreated PP surface, continues to react with the gas-phase species.

5.3.5 Photon-induced Reactions

In Ar/F_2 discharges, VUV photons incident onto the PP primarily result from the resonance states of Ar (105 nm) and F (95 nm) and by electronic transitions in F_2 (157 nm). Quantum yields for photon-induced reactions on PP are available for the resonance transition in Xe at 147 nm.[22-24] For example, VUV irradiation abstracts H_2 from a PP backbone and forms a double bond,

$$-(CH_2)(CH)(CH_3)- + h\nu(147\text{ nm}) \rightarrow H_{2g} + -(CH)=(C)(CH_3) -. \; p = 0.25 \qquad (26)$$

where p is the quantum yield.[22] For partially fluorinated PP, we assumed that H_2 will be extracted if both tertiary and secondary H atoms are available on a PP unit; F_2 will be extracted if all tertiary and secondary H atoms have been substituted by F atoms; and HF will be extracted for other cases.

VUV irradiation can also sever C–C bonds and allow for disproportionation reactions. Dorofeev et al. [22] determined that a representative process is,

$$2[-(CH_2)(CH)(CH_3)-] + h\nu\,(147\text{ nm}) \rightarrow -(CH_2)(CH_2)(CH_3) + (CH_2)=(C)(CH_3)-.\quad p = 0.25 \quad (27)$$

where two chain-ending units are produced. The quantum yield for this process is about 0.25 at 147 nm.

The ablation of methyl radicals can also occur under VUV irradiation,[22]

$$-(CH_2)(CH)(CH_3)- + h\nu\,(147\text{ nm}) \rightarrow -(CH_2)(CH)\bullet- + CH_{3g}.\quad p = 0.025 \qquad (28)$$

where the yield is smaller than ablation of H_2 by an order of magnitude.

With increasing fluorination, the quantum yields for these photon-surface reactions decrease due to the stronger C-F bonds and the steric hindrance of the F atoms. For example, the quantum yield for F abstraction from PTFE at 147 nm is only about 0.0025. The hierarchy for photon-surface reaction probabilities used in the model is shown in Table 5.6. We used the measured yields at 147 nm as approximations for those at 157 nm. To obtain the quantum yields at 95 nm and 105 nm, we further assumed that quantum yields are linearly proportional to photon

energy. In the Ar/F_2 discharges considered here, the fluxes of photons onto the film are usually several orders of magnitude lower than the fluxes of F atoms. Consequently, the ablation of single H or F atoms by VUV photons was neglected because H abstraction by F atoms and passivation of free radicals by F and F_2 proceed at rates that are expected to be orders of magnitude larger. Photon induced cross-linking was also neglected for the same reason.

Double bonds resulting from the VUV illumination are likely to be rapidly passivated by F atoms and F_2 molecules. To estimate this probability, comparisons were made between rates of gas-phase double bond passivation reactions in the high-pressure limit and rates of passivation of free radicals [Eq.(16)],

$$C_2H_4 + F\bullet \rightarrow C_2H_4F\bullet \qquad k = 1.7 \times 10^{-10}\ cm^3s^{-1}.\ [45] \qquad (29)$$

In general, the rates of double bond passivation by F atoms are similar to the rates of F passivation of free radicals. Consequently, we set the probability for passivation of double bonds by F atoms to 10^{-4} regardless of fluorination state.

5.4 Plasma Properties of Ar/F_2 Plasma

A representation of the reactor implemented in the model is shown in Fig. 4. This is a two-dimensional simulation in Cartesian coordinates. The square electrodes are 46 cm on a side (and so the depth perpendicular to the plane of the simulation is 46 cm). The upper electrode is powered at 10 MHz through a blocking capacitor and the lower electrode is grounded. Both electrodes serve as shower-heads with discrete nozzles for gas introduction and are surrounded by dielectric having $\varepsilon/\varepsilon_0 = 8.0$. All other surfaces in the reactor are grounded metal including the

pump port at the right boundary of the reactor. The gap between the electrodes is 2.54 cm. The PP film is placed in the middle of the reactor. Unprocessed PP film is fed from the left side of the reactor and the film moves from left to right through the reactor, thereby achieving continuous treatment. The film is treated as an electrically floating dielectric. The base conditions are Ar/F_2 = 60/40 (by volume) at 500 mTorr, a flow rate of 600 sccm, and a power deposition of 600 W (0.28 W/cm^2 of electrode area or 0.11 W/cm^3 of inter-electrode volume). The applied voltage is adjusted to yield this power. The web moves at 9 cm-s^{-1}, which produces a 6 s residence time in the reactor.

The resulting rf cycle-averaged electron temperature (T_e), ionization by bulk electrons (S_b), and ionization by secondary beam electrons (S_{eb}) for these conditions are shown in Figs. 4b-d. For 600 W, the applied rf potential is 296 V in amplitude, producing a dc bias of 11 V. This slightly positive dc bias is developed as the area of the powered electrode is equal to that of grounded surface and the plasma is highly electronegative. The T_e in the bulk plasma is 3 eV. The intervening dielectric produces a layered structure in the T_e, higher above the dielectric adjacent to the sheath at the upper electrode, as a result of the dc bias and larger sheath potential. Because of the large capacitance of the thin PP film, it acquires a floating potential, though not instantaneously during the rf cycle. This allows for some sheath oscillation at the sheath boundary and a higher T_e of 3.5 eV. The distribution of T_e in the bulk plasma is more uniform as a result of Ohmic heating and a large thermal conductivity. Local maxima in T_e occur near the edges of the electrodes because of electric field enhancement.

With T_e nearly uniform in the bulk plasma, the rate of ionization by bulk electrons largely follows the electron density and has a maximum value of 9.8×10^{17} cm^{-3}s^{-1}. Ionization sources peak near the electrode edges because of the elevated T_e resulting from the electric field en-

hancement. With the sheath 1-2 mm thick, and the mean free path for electron collisions being longer than the sheath width, secondary electrons are launched into the bulk plasma from the upper electrode with essentially the instantaneous sheath potential. The sheath potential on the upper electrode has a maximum value of approximately V_{rf} -V_{dc} or 285 V. The mean free path for electrons at this energy is about 1.0 cm, close to electrode-film spacing of 1.3 cm. As a result, the secondary electrons undergo at most one or two collisions and produce little ionization (maximum value 2.6 × 1015 cm-3s-1) before intersecting and charging the film.

The cycle-averaged electron density [e], negative ion density [F-], total positive ion density [Total Ions], and plasma potential are shown in Figs. 5a-d. [e] with a peak value of 1.3 × 1010 cm-3 closely mirrors the bulk ionization source and has a maximum near the edge of the electrode. F2 rapidly attaches electrons and the mean free path of electrons for attachment is about 2 cm, commensurate to the electrode-film gap. Electrons are therefore as likely to be lost by attachment as by diffusion to surfaces. Negative ions cannot climb the ambipolar potential barrier and so are restricted to the core of the plasma. As a result, the loss of negative ions is dominated by volumetric processes (ion-ion neutralization and associative detachment) and there are time-averaged electrostatic traps for negative ions in the bulk plasma. The end result is that the peak value of [F-] is 2.0 × 1011 cm-3 and the reactor-averaged electronegativity ([F-]/[e]) is about 15. Note that the spatial locations at which the electron, negative ion and positive ion densities have their peak values are different. As a result, their maximum values may differ even-while quasi-neutrality is being maintained.

The cycle-averaged densities of F_2 and F are shown in Figs. 5e-f. The reactor averaged [F_2] and [F] are 3.9 × 10^{15} cm^{-3} and 2.0 × 10^{15} cm^{-3}, respectively, representing a dissociation fraction of 0.2. The distribution of F atoms is fairly uniform because of the low reactivity of F

atoms on previously passivated surfaces. Injection of the Ar/F_2 mixture through discrete nozzles produces local minima in [F], where the feedstock gases jet into the reactor, and corresponding peaks in the feedstock density. $[F_2]$ also has a rather uniform distribution with a slightly lower value in the center of the plasma where the dissociation rates are higher. The higher value of $[F_2]$ near the electrodes or the PP results from associative desorption.

As discussed above, surface reactions of the PP sheet with the Ar/F2 plasma produce gas species such as HF (from F abstraction reactions) and fragments of the PP chain (CnHm from ion and photon bombardment). HF is relatively stable – all chemical reactions of HF with the gas phase species in this system are highly endothermic. On a reactor averaged basis, the HF density is 1.8×1012 cm-3, sufficiently small to neglect the consequences of electron impact reactions with HF on electron transport. Hydrocarbon fragments of the PP chain from ion and photon bombardment were neglected in the gas phase reaction mechanism due to their low rates of production. The most likely reactions they would undergo are the same as on the surface, H atom abstraction by F atoms, which would not significantly affect the fluxes to the substrate.

5.5 Plasma Fluorination of Polypropylene

5.5.1 Surface Characteristics for the Base Case

With the PP immersed in the plasma, both sides of the film are fluorinated. For purposes of presentation, the path followed when plotting surface quantities starts at the left end of the reactor on the bottom side of the PP film, then turns the corner on the right end, and finally continues on the same side of the PP film, back to the left end of the reactor (see Fig. 4a). Following this path, fluxes of neutrals, ions, and photons incident on the PP film for the base case are shown in Fig. 6. The fluxes of F and F_2 are essentially uniform on both sides of the film. As the

dissociation fraction of F_2 was found to be 0.2, the flux of F_2, 4.3×10^{19} $cm^{-2}s^{-1}$, is about 1.5 times that of F. These fluxes of neutrals are four orders of magnitude larger than those of the ions (Ar^+, F^+, F_2^+). As such, the influence of ions will be dominantly through processes that have threshold energies (such as sputtering) as opposed to the competing contributions to abstraction or passivation. The flux of Ar^+ (1.5×10^{15} $cm^{-2}s^{-1}$) exceeds that of F_2^+ (by 3 times) and F^+ (by 6 times), resulting in part from the higher mole fraction of Ar in the feedstock and the lower ionization potential of Ar (15.8 eV) relative to F (17.4 eV), while being commensurate to F_2 (15.7 eV).

In addition to direct ionization, multistep ionization from excited states is an appreciable source of Ar^+ and provides for the more uniform distribution of Ar^+. The top of the film (in Fig. 4a) faces the powered electrode and so has line-of-sight to the electric-field-enhanced corners of the electrodes. The peaks in the flux of F_2^+ on the top of the film, resulting dominantly from single-step electron-impact ionization, reflects the higher ionization sources at the edge of the electrodes. The flux of Ar^+, having more distributed sources due to multi-step ionization, has smaller peaks.

The fluxes of VUV photons are a few times 10^{13} $cm^{-2}s^{-1}$ and thus are 10^6 times smaller than that of the F flux and 10^2 times smaller than that of the ion flux. As such, photons are of secondary importance in determining the composition of the surface with the exception of processes unique to photons, such as initiating double-bond formation. The edge effect on the top of the film is more severe for the photon fluxes. Although there is some trapping of the VUV radiation (a trapping factor of 5.8 for resonance radiation from F and 5.0 for Ar), much of the VUV flux arrives at the substrate following line-of-sight transport from its source, and so mirrors the larger source functions at the edges.

The energy and angular distributions (IEADs) summed for all ions incident on the top and bottom PP surfaces are shown in Fig. 7. The corresponding plasma potential at 30 cm is also shown in Fig. 7 at approximately the peak of the anodic cycle (phase $\varphi = \pi/2$), peak of the cathodic cycle ($\varphi = 3\pi/2$), and the zero crossings in the rf voltage displaced by V_{dc}. The rf amplitude is 296 V to deliver a power of 600 W. The top side of the film faces the powered electrode. In spite of being a floating dielectric, the capacitance of the PP film is large enough that a significant rf drift current is collected with an accompanying cathodic sheath on the top side when the top electrode is the anode. During the cathodic part of the cycle for the top electrode, the film discharges and there is virtually no sheath. As the pressure is relatively high (500 mTorr), charge-exchange collisions (with collision frequencies on the order of 10^7 s^{-1}) effectively degrade IEADs in energy. With the exception of the increased energy due to the positive dc bias, the IEAD incident on the bottom side of the PP is similar to that on the top side.

If the film were stationary in the discharge, film surface properties would be a function of position in the discharge reflecting the spatial distribution of reactants. With a moving web, each site on the film averages the spatial distribution of fluxes as that site moves under the fluxes from entry to exit points. The film is ultimately uniformly processed with a surface composition given by those sites exiting the reactor. Exceptions include differences in fluxes incident on the top and bottom sides of the film. This is not to say that the spatial distributions of the fluxes are not important. As the surface composition of the film changes, so does the reactivity of the film. For example, a given ratio of radical-to-ion fluxes at the entry of the film to the reactor may elicit a different response than that at the exit of the reactor since the surface composition will have changed. Having said that, the trends in surface coverages on the top and bottom sides of the film are largely the same due to the magnitudes of the neutral fluxes and IEADs being similar.

Typically, the PP film surface compositions at the exit of the reactor differ by less than 10% between the top and bottom surfaces. As such, surface properties will be discussed for only the bottom side.

The coverage of surface species (PP units in various fluorination states) on the bottom side of the film are shown in Figs. 8a-b for the first 10 cm of the film travel into the reactor. This corresponds to a treatment time of 1.1 s. The sequential nature of the fluorination is shown by the change in fractional surface coverages as a function of distance (which corresponds to time). In the first two centimeters, the surface species [aside from the untreated PP, $(CH_2)(CH)(CH_3)$] having the largest coverages are those containing a single free radical on C_P [$(CH_2)(CH)(CH_2\bullet)$], C_S [$(CH\bullet)(CH)(CH_3)$], and C_T [$(CH_2)(C\bullet)(CH_3)$]. These correspond to products of the first H-abstraction reactions. The sum of the fractional coverage of PP units that have unreacted alkyl sites reaches a maximum of about 0.27 between 1-2 cm (0.11-0.22 s residence time). This represents approximately 0.09 of all carbon atoms. Alkyl sites with a dangling bond on C_S or C_P have larger coverages than that of C_T as a result of the fact that the first abstraction of H by F atoms does not discriminate by site. Since there are larger numbers of secondary and primary H atoms, C_S or C_P will have more alkyl sites.

Following these first abstractions, cross-linking and F-atom addition reactions passivate the alkyl sites and the fractional coverages of alkyl sites monotonically decrease beyond 2 cm (0.22 s). This decrease correlates with an increase in the fractional coverages of sites having a single F atom and where C_P, C_S or C_T are cross-linked [$(CH_2)(CR)(CH_3)$, $(CRH)(CH)(CH_3)$, $(CH_2)(CH)(CRH_2)$]. The sum of the coverages of these cross-linked sites peaks at about 0.15 between 4-6 cm (0.44-0.67 s). Further fluorination, and ion and photon activated processes, monotonically decrease these fully hydrogenated cross-linked sites beyond 6 cm (0.67 s).

The decrease in fully hydrogenated alkyl sites also maps onto an increase in the fractional coverages of sites in which a single F atom has been substituted for H in the starting PP [$(CH_2)(CH)(CH_2F)$, $(CHF)(CH)(CH_3)$, $(CH_2)(CF)(CH_3)$]. The sum of these singly fluorinated sites peaks at about 0.26 between 4-6 cm (0.44-0.67 s). The fluorination of these alkyl sites by F and F_2 compete with ion bombardment or photolysis, which potentially removes the F atom, and abstraction, which produces new free radicals. The abstraction and addition reactions also replace H atoms with F atoms on fully hydrogenated cross-linked sites and so that surface species such as $(CH_2)(CH)(CRHF)$ and $(CRF)(CH)(CH_3)$ are produced. The fractional coverage of these species is less than that of the singly fluorinated sites without cross-linking and peak at about 0.03 between 10-15 cm (1.1-1.7 s), as shown in Figs. 8b and 8d. (Note that the parenthetical times following distances into the reactor represent the residence time of the film in the reactor at those points.)

The abstraction of the second H atom, which produces a free radical in a singly fluorinated backbone, potentially generates a large number of species. For example, the second H abstraction after a first fluorination on C_P can result in three species: $(CH_2)(CH)(CHF\bullet)$, $(CH_2)(C\bullet)(CH_2F)$, and $(CH\bullet)(CH)(CH_2F)$. These radicals are quickly passivated, producing doubly fluorinated sites that increase to fractional coverages of 0.01-0.1 by 10 cm (1.1 s) [$(CH_2)(CH)(CHF_2)$ and $(CF_2)(CH)(CH_3)$ in Fig. 8b]. Concurrent to the increase in the coverages of sites having radicals or F atoms, the coverage of pure hydrocarbon sites [$(CH_2)(CH)(CH_3)$] undergoes an exponential decrease. Within the first 10 cm (1.1 s) the fractional coverage of the untreated PP decreases to 0.03.

Due to the steric hindrance and the decrease in reaction rates with increasing fluorination, the fluorination to higher F/C ratios proceeds at a slower rate. This is shown in Figs. 8c-d for

surface coverages between 10 (1.1 s) and 54 cm (the exit of the reactor, corresponding to a residence time of 6 s). The doubly fluorinated sites on the C_P and C_S sites, [$(CF_2)(CH)(CH_3)$, $(CH_2)(CH)(CRF_2)$], have maximum coverage between 10-20 cm (1.1-2.2 s). As additional abstraction and passivation reactions take place, a large variety of species are produced. For example, the triply fluorinated sites having the earliest and largest fractional coverage is $(CF_2)(CF)(CH_3)$, peaking at 30 cm (3.3 s). Following this sequence of abstraction and fluorination, the fully fluorinated PP unit [$(CF_2)(CF)(CF_3)$] achieves a fractional coverage of 0.07 at the exit. The precursors for the fully fluorinated sites are dominantly $(CF_2)(CF)(CHF_2)$ and $(CF_2)(CH)(CF_3)$. As the fully fluorinated sites do not significantly react with neutral gas-phase species, they lose C and F atoms dominantly by ion or photon bombardment.

Cross-linking consumes two adjacent alkyl groups and so eliminates the possibility of passivation by F or F_2. Cross-linking is therefore in competition to the fluorination process. This role cross linking in this competition is indicated by the large coverage of $(CF_2)(CF)(CRF_2)$ at the exit of the reactor (0.15 at 54 cm or 6 s). Other cross-linked PP sites having relatively large coverages at 54 cm are $(CF_2)(CH)(CRF_2)$, $(CRF)(CF)(CF_3)$, and $(CF_2)(CR)(CF_3)$, with fraction coverages ranging from 0.05 to 0.12. At the exit of the reactor, the modeled F/C ratio of the PP surface is 1.39.

The more slowly fluorinated sites [e.g., $(CF_2)(CH)(CF_3)$, $(CF_2)(CH)(CRF_2)$] take longer to fully fluorinate because of the reduction in rates of both H abstraction and passivation accounting for diffusion of gas-phase radicals into the film. As discussed earlier, the CH groups in $(CF_2)(CH)(CF_3)$ and $(CF_2)(CH)(CRF_2)$ are located on the underlying PP backbones, thereby having more resistance to H abstraction. The dominant surface species having H that is left on the top PP surface after 6 s is $(CF_2)(CF)(CHF_2)$. The last H_P is the most difficult to be abstracted

because of deactivation effects and steric hindrance. At the exit of the film, only about 0.04 of the original inventory of H atoms are left on the top surface. All other H atoms were abstracted by F atoms with the resulting radical sites either passivated by an F atom or cross-linked.

The consequences of ion and photon bombardment, though small as a fraction of the total reactivity, tend to produce more stable species that integrate in density as the film moves through the plasma. The end result is that those species have non-negligible densities at the exit of the reactor. As with the neutral channels, reactions of ions and photons are capable of producing many hundreds of other types of sites. Although any single site has a small density, cumulative densities can be non-negligible. The cumulative contributions of reactions initiated by ions and photons to fluorination are shown in Fig. 9a. The separate contributions from ions and photons are shown in Figs. 9b-c. The total coverage of surface species resulting from both ions and photons having only 1 F atom peaks at 10^{-3} at 12 cm (1.3 s) and decreases monotonically thereafter. The total coverages of surface species containing 3-6 F atoms increase monotonically in the first 48 cm while the total coverages of species containing 2 F atoms largely remain constant at 2×10^{-3}.

Beyond 48 cm (5.3 s), the fluxes of ions and photons incident on the PP film quickly decrease as the PP film translates out of the discharge. Due to the rapid neutral diffusion out of the discharge, the fluxes of F and F_2 remain largely unchanged while the plasma density decreases. Reactions initiated by ions and photons thereby decrease whereas those by F and F_2 do not significantly diminish. As a result, the total coverages of species resulting from ion and photon bombardment containing 1 and 2 F atoms decrease as further fluorination by neutrals promotes them to species having 3-6 F atoms. At the exit of the reactor, most surface species resulting from reactions of ions and photons contain 3 or 4 F atoms. The sum of the fractional coverages

of all these sites is 0.01 at the exit of the film.

The coverages of surface species resulting from ion bombardment, shown in Fig. 9b, is first dominated by $(CH_2)(CF_2)$, which reaches a maximum of 5×10^{-4} at 24 cm (2.7 s), and decreases thereafter because of further fluorination. At the exit of the reactor, the dominant species resulting from sputtering is $(CF_2)(CF_2)$, with a fractional coverage of 3×10^{-3}. $(CF_2)(CF_2)$ results from the ablation of methyl groups (in all fluorination states) by ion or photon bombardment. This produces a radical on C_T, which is passivated by an F atom. For example, removal of (CH_2F) from $(CF_2)(CF)(CH_2F)$ produces $(CF_2)(CF\bullet)$, which forms $(CF_2)(CF_2)$ following passivation. Ablation of the methyl group can also produce precursors to $(CF_2)(CF_2)$. For example, ablation of (CHF_2) from $(CH_2)(CF)(CHF_2)$ forms $(CH_2)(CF\bullet)$. The subsequent passivation results in the formation of $(CH_2)(CF_2)$. Further fluorination sequentially produces $(CHF)(CF_2)$ and $(CF_2)(CF_2)$. Note that VUV irradiation also ablates methyl groups, which can lead to the same species. For our conditions the amount of $(CF_2)(CF_2)$ resulting from VUV irradiation is no more than half that from ions.

Unlike ablation of the C_P methyl groups, ablation of C_S or C_T, with the attached H, F, or C atoms, exposes fresh underlying PP backbone. In our site-balance model, this is represented by a species (nominally a PP unit) that contains segments on the top and underlying layers. A likely sequence of events is the following: Consider the initial PP unit $(CF_2)(CH)(CH_3)$ where the C_T and the accompanying C_P methyl group, $(CH)(CH_3)$, are sputtered. This leaves the C_S chain end, $-(CF_2\bullet)$, on the top layer that, following passivation, becomes $-(CF_3)$. The removal of C_T and C_P exposes the same groups on the lower layer, producing, as viewed from the plasma, $(CF_3)(CH)(CH_3)$. The F-atom passivation that terminates the chain on the top layer is a steric hindrance to the fresh $(CH)(CH_3)$ exposed on the lower level thereby reducing the rate of fluori-

nation of the $(CH)(CH_3)$. Since the top layer tends to be highly fluorinated because of the high reactivity of the chain-end free radical, it is also less likely to further react. The end result is that $(CF_3)(CH)(CH_3)$ and $(CH_2)(CF_2)(CHF_2)$, another two-layer species, have surface coverages at the exit of the reactor, 6×10^{-4} and 2×10^{-4}, respectively, as shown in Fig. 9b. Cross-linking $[(CRF_2)(CH)(CH_3)$ and $(CH_2)(CF_2)(CRF_2)]$ can occur prior to or after sputtering. Ion-induced cross-linking has a surface coverage below 6×10^{-4} at the exit of the reactor.

The coverage of surface species produced by VUV irradiation is shown in Fig. 9c. In the first 6 cm of the reactor, the major photon-activated process is the extraction of H_2 from the fully hydrogenated PP backbone with the generation of double-bonded carbon $(CH)=(C)(CH_3)$ and $(CH_2)=(C)(CH_3)$ (a chain end species), whose coverages peak at 2.0×10^{-4} and 1.0×10^{-4}, respectively, at about 6 cm. Unsaturated sites resulting from the extraction of HF or F_2 have even lower coverages due to the slower extraction rates. The photon-activated disproportionation reaction breaks the PP backbone into short chains with the generation of chain-ending species (all species except $(CH)=(C)(CH_3)$ in Fig. 9c). The sum of the coverages of these chain-ending species is about 0.003 at the exit. These relatively low coverages are caused by the low magnitudes of photon fluxes as compared with that of neutrals and ions. A secondary contributing cause to these low coverages is that these chain-ending species are more rapidly removed by ion and photon bombardment because of lower surface binding energies. (To ablate these species, only one C–C bond needs to be broken.)

The coverages of cross-linked species are shown in Fig. 10a. The free radicals on C_P have larger cross-linking probabilities as C_P protrudes from the PP chain and so the majority of cross-linking occurs on C_p. At the exit of the reactor, the fully fluorinated cross-linked C_p $[(CF_2)(CF)(CRF_2)]$ has the largest (and still increasing) coverage at 0.15. This increase largely

results from the fluorination of the precursors of $(CF_2)(CF)(CRF_2)$ [$(CF_2)(CH)(CRF_2)$, $(CHF)(CF)(CRF_2)$ and $(CF_2)(CF)(CRHF)$] after cross-linking. The coverage of fully fluorinated cross-linked C_S sites [$(CRF)(CF)(CF_3)$] and C_T sites [$(CF_2)(CR)(CF_3)$] are 0.06 and 0.05 at 54 cm (6 s), respectively.

The coverages of the sum of cross-linked C_P, C_S, and C_T sites are shown in Fig. 10b. As number of sites with free radicals decreases with increasing degree of fluorination, most of cross-linking occurs in the first 30 cm (3.3 s). The exit coverage of cross-linked C_P sites (0.4) is about twice that of the C_S sites and four times that of the C_T sites. The sum of coverages of all cross-linked sites is about 0.73 at 54 cm (6 s), which is about 70 times larger than the sum of all sites formed due to ion and photon bombardment. Note that, within our modeled system, cross-linked C_P is bonded to two C atoms whereas C_S and C_T are bonded to 3 and 4 C atoms, respectively. Cross-linking, which connects free radicals to adjacent C atoms, eliminates those bonds from being fluorinated. Cross-linking therefore competes with the F addition process, reducing the maximum possible F/C ratio from that of a fully fluorinated backbone. At the same time, cross-linked sites are also more resistive to ion sputtering and VUV photolysis, processes that potentially remove C–F bonds from the surface. So depending on operating conditions, cross-linking could also be beneficial to the fluorination process. For the process conditions investigated in this work, the C/F ratio is generally decreased by cross-linking.

The fractional coverages of CH and CF_n functional groups as a function of position are shown in Fig. 11a. β–C refers to C atoms that do not have C–F bonds but have neighboring C atoms that do have C–F bonds. (This type of species is discernable by XPS.) For example, (CH_2) and (CH_3) are β–C species in $(CH_2)(CF)(CH_3)$. The coverage of singly fluorinated sites (CF) saturates in the first 10 cm (residence time of 1.1 s) because of the rapid fluorination of fully hy-

drogenated PP on the top layer. The fluorination of exposed PP on the underlying layers (producing CF) and the fluorination of CF to higher states (consuming CF) proceed at slower rates and are at a near equilibrium from 10 to 54 cm (1.1 - 6 s).

The fluorination first produces a peak coverage of 0.33 for β–C sites at about 15 cm (1.6 s), decreasing thereafter. As a result of steric hindrance, and electrophilic and diffusion effects, the fractions of doubly and triply fluorinated sites (CF_2 and CF_3) increase at slower rates. The fraction of CF_2 sites begins to saturate at the exit with a coverage of 0.37, mainly consisting of perfluorinated C_S and doubly fluorinated C_P sites. The general scaling for the F/C ratio, shown in Fig. 11b, is for a more rapid fluorination during the first 15 cm (1.7 s), here to a value of 0.5, caused by the single fluorination of fully hydrogenated PP. This relatively rapid fluorination is followed by a slower approach towards 1.39 over the rest of the treatment. This latter, and slower, fluorination results from the double and triple fluorination of C_S and C_P sites and from the reactions with the lower-layer PP chains.

A comparison of computed and experimental results [27] for functional group surface coverages after 6 seconds of treatment is given in Table 5.7. The prediction for F/C ratio agrees well with the experiment. The discrimination between CH and β–C in our model is somewhat arbitrary because of the finite number of configurations that we are able to model. If we instead compare the sum of CH and β–C with experiment, the agreement is better. The overestimation of CF and underestimation of CF_3 most likely originate from the approximate manner in which F atom diffusion into the surface layers is addressed. Another source of discrepancy is that the F/C ratios obtained from the experimental ESCA measurements arise from analysis of the outermost 6-8 nm of the surface, which does not directly correspond to the effective depth addressed in the simulation.

5.5.2 Exposure Time

To investigate the effects of longer exposure time on the surface composition while minimizing the changing of other parameters, the web speed was reduced to about 2 cm-s^{-1} to enable a residence time of 26 s to match experiments [27]. Surface coverages for the major surface species are shown in Fig. 12a. At the exit of the reactor, 54 cm (26 s), the dominant surface species is $(CF_2)(CF)(CRF_2)$, the fully fluorinated PP unit with cross-linking on C_P (0.41 coverage). The coverage of the fully fluorinated PP backbone $(CF_2)(CF)(CF_3)$ reaches saturation at about 0.2 after 30 cm (14.3 s). Other dominant surface species include fully fluorinated PP units with cross-linking on C_S $[(CRF)(CF)(CF_3)]$ and C_T $[(CF_2)(CR)(CF_3)]$. So with a longer exposure time, apart from fluorination, the dominant changes in surface composition still result from cross-linking.

As the hydrogenated PP becomes fluorinated, the rates of fluorine addition decrease while the effects of ion and photon bombardment continue to integrate. This integration is demonstrated by the nearly linear increase of coverage of $(CF_2)(CF_2)$ from 0 to 48 cm (0-23 s). Recall that $(CF_2)(CF_2)$ is formed by the ablation of the methyl group (for all fluorination states). Beyond 48 cm (23 s), the film translates out of the discharge and the fluxes of ions and photons decrease rapidly so that the surface coverage of $(CF_2)(CF_2)$ remains nearly constant beyond 48 cm (23 s).

The fractional coverages of functional groups and the F/C ratio are shown in Figs. 12b-c. The persistence of small fractions of CH (0.005) results from the ablation of C_S and C_T groups by ion bombardment and the slow rates of fluorination of the fresh underlying PP backbone. In the absence of sputtering, photolysis, and cross-linking, we would expect CF, CF_2 and CF_3 to each

have 1/3 of the fractional coverage at the exit. The dominance of CF_2 (0.42 coverage) is largely attributed to the cross-linking of C_P sites, which eliminates the possibility of CF_3 groups. The cross-linking of C_T converts it to a β–C site by eliminating the possibility of F attachment and this conversion contributes to the high coverage β–C (0.04) at the exit of the reactor. The cross-linked C_T sites have no F or H bonding and are bonded to only other C atoms.

The F/C ratio first undergoes a rapid increase in the first 20 cm (9.5 s), then stabilizes at about 1.7 between 20-54 cm (9.5-26 s). This stabilization can be attributed to two effects. First, the top PP surface is highly fluorinated and cross-linked after the first 20 cm (9.5 s), as discussed in Part I.[27] Second, ion bombardment and the slow fluorination of exposed fresh backbone also reach a balance beyond 20 cm (9.5 s). As such, considering economic issues such as the utilization of feedstock gases and power consumption, under the base case conditions the optimal exposure time should be around 10 s.

The model results for fractional surface coverages are compared to experiments [27] for 26 s of treatment in Table 5.7. The general agreement is good, though the model underestimates the fraction of CH and β–C groups. Again, these discrepancies likely originate from the approximate means of addressing F atom diffusion to the under-layer and from the differences in the depths addressed between the ESCA and the model.

5.5.3 F_2 Fraction

In order to investigate process parameters that are not easily or inexpensively addressed experimentally, we varied the F_2 fraction, pressure (Section V.D) and power (Section V.E) in the model. Reactant fluxes incident on the bottom side of the PP film as a function of position are shown in Figs. 13a-c while varying the F_2 fraction from 0.1 to 0.6 for a web speed of 9 cm-s^{-1} at

500 mTorr. The F-atom flux increases with increasing F_2 fraction. Since the power is held constant at 600 W, the increases in fluxes are sub-linear with F_2 fraction and begin to saturate for F_2 fractions greater than 0.5. With increasing F_2 fraction, the reactor averaged $[F^-]$ increases from 1.2×10^{10} cm^{-3} to 3.0×10^{10} cm^{-3} and the total positive ion density also increases to maintain charge neutrality. The end result is that the total ion flux incident on the film also increases and saturates. Ar(4s), $F_2(C^1\Sigma_u, H^1\Pi_u)$, and F(3s) are the sources of VUV photons illuminating the PP film. With increasing F_2 fraction, the Ar inventory decreases and the F and F_2 inventory increases so that the total photon flux is not a linear function of F_2 fraction. The scaling of the F/C ratio with F_2 fraction is shown in Fig. 13d. The F/C ratio increases with F_2 fraction commensurate with the increase in F atom fluxes and therefore also begins to saturate for F_2 fractions exceeding 0.5.

Surface compositions of the PP film at the exit of the reactor as a function of increasing F_2 fraction are shown in Fig. 14a. The coverages of CF_2 and CF_3 groups increase with increasing F_2 fraction while coverages of CH and β–C groups decrease. These trends reflect the increase in the F atom flux. The surface coverage of CF remains largely unchanged. The fluorination of purely hydrocarbon sites to singly fluorinated sites producing CF and the fluorination of CF to CF_2 (consuming CF) are not particularly sensitive to the increase of F flux. The effect of the F_2 fraction is largely on the rates of reaction and not to produce a fundamental change in the dominant reactions in the mechanism.

The fractional coverages of the sum of PP unit sites modified by ion and photon bombardment and the sum of cross-linked unit sites are shown in Fig. 14b as a function of F_2 fraction. Ion fluxes increase with F_2 fraction, but the fraction of PP unit sites modified by ions and photons does not monotonically increase with F_2 fraction as there are concurrent nonlinear changes

in the incident ion energies. For example, the ion energy distributions (IEDs) are shown in Fig. 14d. The increasing F_2 flux with increasing F_2 fraction reduces the average lifetime of sites with free radicals by increasing the rate of passivation, thereby decreasing radical densities. At the same time, the rate of abstraction increases with increasing F atom flux, which increases the density of sites with free radicals. So increasing the F and F_2 fluxes could either increase or decrease the density of polymer radicals depending on the state of fluorination of the surface. Since the rate of formation of cross-linked sites scales with the square of the density of radicals, the density of cross-linked sites could either increase or decrease with increasing F_2 fraction. For our conditions, at the same fluorination state, the probabilities for F-atom addition are generally larger than those for F abstraction. Adding the passivation caused by F_2, the total free radical inventory decreases with increasing F_2 fraction and so the fraction of cross-linked sites decreases slightly with F_2 fraction, as shown in Fig. 14b.

To provide a relative estimate of the efficiency of the fluorination process, we define the fluorination efficiency as

$$\eta = \frac{(F/C)_0}{(F/C)_m} \times \frac{2[N_S]}{\phi_F \tau} \tag{30}$$

where $(F/C)_0$ is the ratio at the exit of the reactor and $(F/C)_m$ is the maximum ratio, which for PP is 2. $[N_S] = 6 \times 10^{15}$ cm^{-2} is the density of H sites (six H atoms per PP unit and 10^{15} cm^{-2} units), ϕ_F is the F atom flux, and τ is the exposure time to the plasma. The factor of two accounts for one F atom being required to abstract an H atom and one being required to passivate the resulting alkyl site. If the PP were exposed to a total fluence of $2[N_S]$ F atoms and each atom either abstracted or passivated, the F/C would be equal to 2. (Note that this approach over-

estimates η since some passivation of radicals is performed by F_2.) η and the F/C ratio at the exit from the reactor are shown in Fig. 14c as a function of F_2 fraction. The efficiencies are small, of the order of 10^{-5}-10^{-4}, perhaps because of the non-unity reaction probabilities, values which decrease with increasing F/C. The decrease in η with increasing F_2 fraction is caused by this less-efficient fluorination as the F/C ratio increases. So the increase in F atom flux that is obtained by increasing the F_2 fraction is used somewhat less efficiently.

5.5.4 Pressure

Reactant fluxes as a function of position on the bottom side of the PP film are shown in Fig. 15 while varying the reactor pressure from 100 to 700 mTorr for Ar/F_2 = 60/40 and a web speed of 9 cm-s^{-1}. With increasing pressure, the fraction of the power deposition expended in bulk plasma processes (e.g., dissociation of F_2) increases while the fraction of power dissipated by ion acceleration in the sheath decreases. Coupled with the increase in the total inventory of F_2, the reactant fluxes increase. With a constant power of 600 W, the increase in reactant fluxes begins to saturate between 500-700 mTorr. Though ion and photon fluxes both increase with pressure, which could potentially remove C-F bonding and so be detrimental to fluorination, the increase in the F-atom flux dominates. The end result is that the F/C increases with increasing pressure, though sub-linearly, as shown in Fig. 15d.

The surface composition at the exit of the film is shown in Fig. 16a as a function of pressure. The increase in F atom flux with increasing pressure increases the surface coverages of CF_n (n = 1-3) while decreasing the coverages of CH and β–C groups because of the more rapid fluorination. The increase in coverages of CF_n groups slows above 500 mTorr, commensurate with the saturation in the F atom flux.

The IEDs incident on the bottom side of the PP film are shown in Fig. 16d for pressures from 100 to 700 mTorr. The IED at 700 mTorr loses the high-energy tail and is downshifted in energy compared to the IED at 100 mTorr. This downshift in energy results from the more frequent charge-exchange collisions in the sheath with increasing pressure, thereby producing a decrease in the probability of ion ablation. This decrease in probability partially offsets the increase in ion fluxes. The end result is that the sum of the total sites modified by ion and photon bombardment increases with pressure up to 500 mTorr, and then decreases at higher pressures, as shown in Fig. 16b. The sum of coverages of cross-linked sites decreases with increasing pressure as the increase in F and F_2 fluxes passivate free radical sites before they can cross-link, as shown in Fig. 16b. Again, at higher pressures there is a slowing in the rate of fluorination with increasing F/C, which decreases the utilization of the larger fluxes and decreases η, as shown in Fig. 16c.

5.5.5 Power

Reactant fluxes are shown in Fig. 17 while varying the plasma power from 200 W to 1500 W for a web speed of 9 cm-s^{-1}. While keeping Ar/F_2 = 60/40, the dissociation fraction of F_2 increases from 0.14 at 200 W (0.09 W/cm^2 of electrode area or 0.037 W/cm^3 of inter-electrode volume) to 0.35 at 1500 W (0.71 W/cm^2 of electrode area or 0.28 W/cm^3 of inter-electrode volume). The increase in F flux is less than linear with power as a consequence of an increasing proportion of the power being dissipated by ion acceleration. Commensurate with the increase in F atom flux (which increases F/C) with increasing power, the ion and photon fluxes (which decrease or slow the rate of increase of F/C) also increase.

With the increase in rf voltage with increasing power, the ion energies bombarding the

PP film also increase, as shown in Fig. 18d. The resulting increase in the probability for ion ablation together with the increase in ion fluxes compete with the increase in fluorination produced by the higher F atom flux. This competition contributes to the saturation of the F/C ratio with increasing power above 1000 W, as shown in Fig. 17d.

Surface coverages of functional groups at the exit are shown in Fig. 18a as a function of power. The sum of coverages of CH and β–C decreases from 0.3 at 200 W to 0.17 at 1500 W, in response to the increase in F flux, which more rapidly abstracts and passivates the -CH sites. As the F flux increases by only a factor of 1.7 from 200 W to 1500 W while the ion flux increases by a factor of 3.5, the coverages of CF_2 and CF_3 groups increase only moderately with increasing power.

With increasing power, more sites are modified by ion and photon bombardment (primarily above 1000 W), while the fraction of sites that are cross-linked only moderately decreases, as shown in Fig. 18b. The increase in ion and photon modified sites is largely caused by the increase in ion fluxes and energy, which alone should increase the proportion of cross-linked sites. However, the increase in F-atom fluxes is sufficient to offset the increased rate of free radical site production and cross-linking decreases. Above 1000 W, the coverages of ion-ablated sites increases rapidly as a result of the increase in ion energy. These effects partly contribute to the decrease in fluorination efficiency, as also shown in Fig. 18c. The less efficient fluorination at higher F/C ratios with increasing power also contributes to the decrease in η.

5.6 Concluding Remarks

The low-pressure plasma fluorination of PP in CCPs sustained in Ar/F_2 mixtures was computationally investigated. The surface reaction mechanism includes a hierarchy of fluorina-

tion reactions (abstraction and addition), ion sputtering, photon activated process, and cross-linking. Good agreement was obtained between the model and experimental results for the F/C ratio and the fraction of functional groups.

The sequence of hydrogen abstraction and passivation by F and F_2 with rates slowed by steric hindrance and deactivation with increasing F/C generally explains the experimentally observed trends. Concurrent to the passivation of free radical sites (produced by H abstraction) by F and F_2 fluxes, which creates fluorine-containing functionalities, adjacent free radicals will also cross-link. This cross-linking of up to 10% of the carbon atoms partially accounts for the lack of full fluorination, that is, an F/C < 2, even after long plasma exposure. Cross-linking is most likely on C_P sites as they protrude from the PP chain and contain more C-H bonding that can potentially lead to cross-links. The elimination of these sites, which potentially could become CF_3 sites, and the effective conversion of C_P sites to C_S sites, increases the proportion of CF_2 functionalitiy. As the PP film is electrically floating in the plasma and charge-exchange collisions further degrade the IEADs in energy, ablation of fluorinated segments by ion sputtering is not appreciable for exposure time less than 30 s for powers of < 0.7 W/cm^2. The ablation is most efficient at removing CH_3 groups (including fluorinated states) because of lower surface binding energy. VUV illumination does not produce major changes in surface composition for exposure times less than 30 s for powers < 0.7 W/cm^2 because of the relatively low magnitude of photon fluxes. However, the cumulative effects of decreasing rates of fluorination as F/C increases, coupled with ion sputtering and VUV photolysis, reduces the efficiency of fluorination for long exposure times or high powers.

This modeling study and the companion experimental investigation [27] have provided opportunities to quantify complex plasma functionalization processes. Although the numerical

values mentioned below are particular to the conditions investigated, they nevertheless do provide some insights to these processes.

- For the base case conditions, at one point during the functionalization 9% of the PP carbon atoms in the surface layers are in the form of free radicals. The presence of so many radicals that have not yet reacted with F atoms and F_2 molecules is likely the reason why cross-linking is so prevalent.
- After only 1.1 s of processing, 97% of the PP units have at least one F atom added. By the end of the reactor, 96% of the surface H atoms have been removed.
- Excluding PP units involved in some type of cross-linking, at the exit of the reactor in the base case only 7% of the surface is fully fluorinated. At the same time, about 70% of the PP units are involved with cross-linking at the exit of the reactor. About 10% of all of the PP units are cross-linked through the tertiary C, which leads to the large β-shift C in the final ESCA spectra.
- Only about 1% of the PP units left on the surface at the exit of the reactor have been involved in an ion-impact reaction. As such, much of the cross-linking results from radical reactions leading to cross linking early during plasma exposure.

5.7 Tables

Table 5.1. Ar/F_2 Gas-phase Reaction Mechanism

Species:

F_2	F_2,	Ar
$F_2^*(C^1\Sigma_u, H^1\Pi_u)$	$F^*(3s)$	$Ar^*(4s\text{-}^3P_0, {}^3P_2)$
F_2^+	F^+	$Ar^{**}(4p)$
	F^-	$Ar^{***}(4s\text{-}^3P_1, {}^1P_1)$
		E

Reaction[a]	Rate Coefficient[b]	Reference
Electron Impact		
$e + F_2 \rightarrow F + F + e$	c	46
$e + F_2 \rightarrow F^- + F$	c	46
$e + F_2 \rightarrow F_2^* + e$	c	46
$e + F_2 \rightarrow F_2^+ + e + e$	c	46
$e + F_2^+ \rightarrow F + F$	$8 \times 10^{-8}\ T_e^{-0.5}$	46
$e + F \rightarrow F^* + e$	c	47
$e + F^* \rightarrow F + e$	c	47
$e + F^* \rightarrow F^+ + e$	c	47
$F^* \rightarrow F$	$5 \times 10^7\ s^{-1}$	E
$e + F \rightarrow F^+ + e + e$	c	47
$e + Ar \rightarrow Ar^* + e$	c	48
$e + Ar \rightarrow Ar^{**} + e$	c	48
$e + Ar \rightarrow Ar^+ + e + e$	c	49
$e + Ar^* \rightarrow Ar^+ + e + e$	c	50
$e + Ar^* \rightarrow Ar + e$	c	48, d
$e + Ar^* \rightarrow Ar^{**} + e$	c	51

$e + Ar^{**} \rightarrow Ar^{+} + e + e$	c	52
$e + Ar^{**} \rightarrow Ar + e$	c	48, d
$e + Ar^{**} \rightarrow Ar^{*} + e$	c	51, d
$Ar^{**} \rightarrow Ar^{*}$	$1 \times 10^{5}\ s^{-1}$	E
$e + Ar^{*} \rightarrow Ar^{***} + e$	$10^{-8} \exp(-0.075/T_e)$	h, f
$e + Ar^{***} \rightarrow Ar^{*} + e$	1×10^{-8}	H
$e + Ar^{**} \rightarrow Ar^{***} + e$	$8.87 \times 10^{-7}\ T_e^{0.5}$	h, f
$e + Ar^{***} \rightarrow Ar^{**} + e$	$8.87 \times 10^{-7}\ T_e^{0.5} \exp(-1.52/T_e)$	h, f
$e + Ar^{***} \rightarrow Ar^{+} + e + e$	$10^{-7}\ T_e^{0.6} \exp(-3.8/T_e)$	h, f
Radiative Transitions		
$F_2^{*} \rightarrow F_2$	$2 \times 10^{8}\ s^{-1}$	53, e
$F^{*} \rightarrow F$	$5 \times 10^{7}\ s^{-1}$	54, e
$Ar^{***} \rightarrow Ar$	$1 \times 10^{8}\ s^{-1}$	55, e
Heavy Particle Reactions		
$Ar^{*} + Ar^{*} \rightarrow Ar^{+} + Ar + e$	1.2×10^{-9}	56
$Ar^{**} + Ar^{**} \rightarrow Ar^{+} + Ar + e$	1.2×10^{-9}	56
$Ar^{*} + Ar^{**} \rightarrow Ar^{+} + Ar + e$	1.2×10^{-9}	57
$Ar^{*} + Ar^{***} \rightarrow Ar^{+} + Ar + e$	1.2×10^{-9}	56
$Ar^{**} + Ar^{***} \rightarrow Ar^{+} + Ar + e$	1.2×10^{-9}	56
$Ar^{***} + Ar^{***} \rightarrow Ar^{+} + Ar + e$	1.2×10^{-9}	56
$Ar^{*} + Ar \rightarrow Ar^{***} + Ar + e$	$10^{-10}\ T_g^{0.5} \exp(-875/T_g)$	56, g
$Ar^{***} + Ar \rightarrow Ar^{*} + Ar + e$	1×10^{-10}	56

$Ar^+ + Ar \rightarrow Ar^+ + Ar$	5.7×10^{-10}	57
$Ar^+ + F_2 \rightarrow F_2^+ + Ar$	1×10^{-11}	H
$F^+ + F \rightarrow F^+ + F$	1×10^{-9}	58
$F_2^+ + F_2 \rightarrow F_2^+ + F_2$	1×10^{-9}	H
$F_2^+ + F \rightarrow F^+ + F_2$	7.9×10^{-10}	58
$F^- + Ar^+ \rightarrow F + Ar$	5×10^{-7}	59
$F^- + F_2^+ \rightarrow F_2 + F$	1×10^{-7}	58
$F^- + F^+ \rightarrow F + F$	7×10^{-7}	58
$F^- + F \rightarrow F_2 + e$	1×10^{-10}	60
$F + F + M \rightarrow F_2 + M$	6.8×10^{-34} cm^6-s^{-1}	61

[a] Only reactions directly affecting species densities are shown here. Additional electron impact collisions (e.g. momentum transfer, vibrational excitation) are included in the solution of Boltzmann's equation.

[b] Rate coefficients have units of cm^3-s^{-1} unless noted otherwise.

[c] Rate coefficient is calculated from the electron energy distribution obtained in the EETM using the cross section from the cited reference.

[d] Cross section was obtained by detailed balance.

[e] Natural lifetime. Lifetime used in the model is the trapped value obtained from the MCRTM.

[f] T_e is the electron temperature (eV).

[g] T_g is the gas temperature (K).

[h] Estimated.

Table 5.2. Surface Reaction Mechanism for PP in Ar/F_2 Plasmas

	Reaction[a]	Probability	Comment
	H Abstraction and F addition		
(1)	$-(CH_2)(CH)(CH_3)- + \bullet F_g \rightarrow -(CH_2)(CH)(CH_2\bullet)- + HF_g$	Table 5.3	b
(2)	$-(CH_2)(C\bullet)(CH_3)- + \bullet F_g \rightarrow -(CH_2)(CF)(CH_3)-$	Table 5.4	
(3)	$-(CH_2)(C\bullet)(CH_3)- + F_{2g} \rightarrow -(CH_2)(CF)(CH_3)- + F_g$	Table 5.4	
	Cross-linking		
(4)	$-(CH_2)(CH)(CH_2\bullet)- + M \rightarrow -(CH_2)(CH)(CRH_2)-$	C	
	Ion sputtering of C_S		
(5)	$-PP-(CH_2)(CH)(CH_3)-PP- + I^+_g \rightarrow -PP\bullet + \bullet(CH)(CH_3)-PP- + \bullet\bullet CH_{2g} + I_g$	Table 5.5	d
	Ion sputtering of C_T (with C_P)		
(6)	$-PP-(CH_2)(CH)(CH_3)-PP- + I^+_g \rightarrow -PP\bullet + \bullet(CH_2)-PP- + \bullet CH(CH_3)_g + I_g$	Table 5.5	d
	Ion sputtering of C_P		
(7)	$-PP-(CH_2)(CH)(CH_3)-PP- + I^+_g \rightarrow -PP-(CH_2)(CH\bullet)-PP- + \bullet CH_{3g} + I_g$	Table 5.5	d
	Ion-induced short-chain desorption		
(8)	$-PP-PP-PP- + I^+_g \rightarrow -PP\bullet + \bullet PP- + \bullet\bullet PP_g + I_g$	Table 5.5	d
	Photon extraction of H_2, HF and F_2		
(9)	$-(CHF)(CH)(CH_2F)- + h\nu \rightarrow -(CF)=(C)(CH_2F)- + H_{2g}$	Table 5.6	e
(10)	$-(CHF)(CF)(CH_2F)- + h\nu \rightarrow -(CF)=(C)(CH_2F)- + HF_g$	Table 5.6	e
(11)	$-(CF_2)(CF)(CH_2F)- + h\nu \rightarrow -(CF)=(C)(CH_2F)- + F_{2g}$	Table 5.6	e

Photon C–C bond scission and disproportionation

(12)	$-PP-(CHF)(CH)(CH_2F)-PP- + h\nu \rightarrow -PP-(CHF)(CH_2)(CH_2F) + \bullet PP-$	Table 5.6	e
(13)	$-PP-(CHF)(CH)(CH_2F)-PP- + h\nu \rightarrow -PP\bullet + (CHF)=(C)(CH_2F)-PP-$	Table 5.6	e

Photon ablation of C_P

(14)	$-PP-(CH_2)(CH)(CH_3)-PP + h\nu \rightarrow -PP-(CH_2)(CH\bullet)-PP + \bullet CH_{3g}$	Table 5.6	e

Saturation of double bonds by F

(15)	$-(CF)=(C)(CH_2F)- + F_g \rightarrow -(CF\bullet)(CF)(CH_2F)-$	0.0001	

[a] Only representative reactions for each process are shown. Reactions for all permutations of fluorinated and cross-linked sites are included using the reaction hierarchy discussed in the text. Subscript g denotes gas phase species.

[b] "•" denotes a free radical.

[c] R denotes a cross-linked site. Cross-linking probabilities are discussed in Sec. III-A. M denotes the sum of all free radical sites on the PP surface.

[d] PP denotes a PP repeating unit in any fluorination state. I_g^+ denotes an ion and I_g is a neutralized ion.

[e] *hν* denotes a VUV photon.

Table 5.3. Hydrogen Abstraction Probabilities

Site	Local Configuration[a]	Probability	Comment
C_P	$-(CH_2)(CH)(CH_3)- + \bullet F_g \rightarrow -(CH_2)(CH)(CH_2\bullet)- + HF_g$		
	$-(CH_2)(CH)(CH_3)-$	5×10^{-5}	
	$-(CH_2)(CH)(CH_2F)-$	5×10^{-5}	
	$-(CH_2)(CH)(CHF_2)-$	3×10^{-5}	
	$-(CHF)(CF)(CHF_2)-$	3×10^{-5}	
	$-(CH_2)(CF)(CH_3)-$	2×10^{-5}	b
	$-(CHF)(CH)(CH_3)-$	2×10^{-5}	b
C_S	$-(CH_2)(CH)(CH_3)- + \bullet F_g \rightarrow -(CH\bullet)(CH)(CH_3)- + HF_g$		
	$-(CH_2)(CH)(CH_3)-$	5×10^{-5}	
	$-(CHF)(CH)(CH_2F)-$	3×10^{-5}	
	$-(CHF)(CF)(CH_3)-$	3×10^{-5}	
	$-(CH_2)(CF)(CH_3)-$	2×10^{-5}	b
	$-(CH_2)(CF)(CH_2F)-$	2×10^{-5}	b
C_T	$-(CH_2)(CH)(CH_3)- + \bullet F_g \rightarrow -(CH_2)(C\bullet)(CH_3)- + HF_g$		
	$-(CH_2)(CH)(CH_3)-$	3×10^{-5}	
	$-(CH_2)(CH)(CH_2F)-$	1×10^{-5}	b
	$-(CHF)(CH)(CH_2F)-$	1×10^{-5}	b

[a] Only representative configurations for each process are shown. All permutations and combination of surface species are included in the reaction mechanism.

[b] Special case for fully hydrogenated sites with fluorinated C neighbors. See Sec. III.

Table 5.4. Fluorine Addition Probabilities

Site	Local Configuration[a]	Addition probability by: F	Addition probability by: F_2	Comment
C_P	$-(CH_2)(CH)(CH_2\bullet)-$	1×10^{-4}	0.2×10^{-4}	
	$-(CH_2)(CH)(CHF\bullet)-$	1×10^{-4}	0.2×10^{-4}	
	$-(CH_2)(CH)(CF_2\bullet)-$	5×10^{-5}	1×10^{-5}	
	$-(CH_2)(CF)(CH_2\bullet)-$	5×10^{-5}	1×10^{-5}	B
	$-(CHF)(CH)(CH_2\bullet)-$	5×10^{-5}	1×10^{-5}	
C_S	$-(CH\bullet)(CH)(CH_3)-$	1×10^{-4}	0.2×10^{-4}	
	$-(CF\bullet)(CH)(CH_3)-$	1×10^{-4}	0.2×10^{-4}	
	$-(CH\bullet)(CF)(CH_3)-$	5×10^{-5}	1×10^{-5}	B
	$-(CH\bullet)(CF)(CH_2F)-$	5×10^{-5}	1×10^{-5}	
C_T	$-(CH_2)(C\bullet)(CH_3)-$	1×10^{-4}	0.2×10^{-5}	
	$-(CH_2)(C\bullet)(CFH_2)-$	5×10^{-5}	1×10^{-5}	
	$-(CHF)(C\bullet)(CH_3)-$	5×10^{-5}	1×10^{-5}	B
	$-(CH_2)(C\bullet)(CH_2F)-$	5×10^{-5}	1×10^{-5}	B

[a] Only representative configurations for each process are shown. All permutations and combination of surface species are included in the reaction mechanism.

[b] Special case. See Section III.

Table 5.5. Coefficients for Sputtering Yields $Y(E) = p_o\left(\left(E^n - E_{th}^n\right)/\left(E_r^n - E_{th}^n\right)\right)$

Ion	Site	p_o	E_r	E_t	N
F^+	C_P	0.12	150	30	1.2
F^+	C_S, C_T	0.05	150	40	1.2
F^+	Short-chain Desorption	0.12	150	40	1.2
Ar^+, F_2^+	C_P	0.04	150	30	2.0
Ar^+, F_2^+	C_S, C_T	0.016	150	40	2.0
Ar^+, F_2^+	Short-chain Desorption	0.04	150	40	2.0

Table 5.6. Probabilities For Photon-Surface Reactions

Process[a]	Probability 95 nm	105 nm	157 nm
Extraction and Double Bond Formation			
$-(CH_2)(CH)(CH_3)- + h\nu \rightarrow H_2 + -(CH)=(C)(CH_3)-$	0.41	0.375	0.25
$-(CH_2)(CF)(CH_3)- + h\nu \rightarrow HF + -(CH)=(C)(CH_3)-$	0.41	0.375	0.25
$-(CHF)(CF)(CH_3)- + h\nu \rightarrow F_2 + -(CH)=(C)(CH_3)-$	0.013	0.012	0.008
Scission and Disproportionation			
$-(CH_2)(CH)(CH_3)- + h\nu \rightarrow -(CH_2)(CH_2)(CH_3)$	0.21	0.19	0.125
$-(CH_2)(CH)(CH_3)- + h\nu \rightarrow (CH_2)=(C)(CH_3)-$	0.21	0.19	0.125
$-(CHF)(CF)(CH_3)- + h\nu \rightarrow -(CHF)(CF_2)(CH_3)$	0.005	0.0045	0.003
$-(CHF)(CF)(CH_3)- + h\nu \rightarrow (CHF)=(C)(CH_3)-$	0.005	0.0045	0.003
Abaltion of C_P			
$-(CH_2)(CH)(CH_3)- + h\nu \rightarrow \bullet CH_{3g} + -(CH_2)(CH\bullet)-$	0.041	0.0375	0.025

[a] Only example processes are shown here. All permutations and combination of surface species are included in the reaction mechanism.

Table 5.7. Comparison of Modeled Surface Coverage and Experimental ESCA F/C Atomic Ratios

	Surface Fractional Coverage and F/C [a]			
Bonding	6 s Treatment		26 s Treatment	
	Simulation	Experiment	Simulation	Experiment
CH	0.03	0.12	0.01	0.02
β-C	0.19	0.18	0.04	0.10
CF	0.29	0.26	0.35	0.30
CF_2	0.37	0.34	0.42	0.45
CF_3	0.12	0.10	0.18	0.13
F/C	1.38	1.41	1.73	1.57

[a] Operating conditions: Ar/F_2 = 60/40, 600 W, 500 mTorr, web speed = 9 cm-s^{-1} (6 s) and 2 cm-s^{-1} (26 s).

5.8 Figures

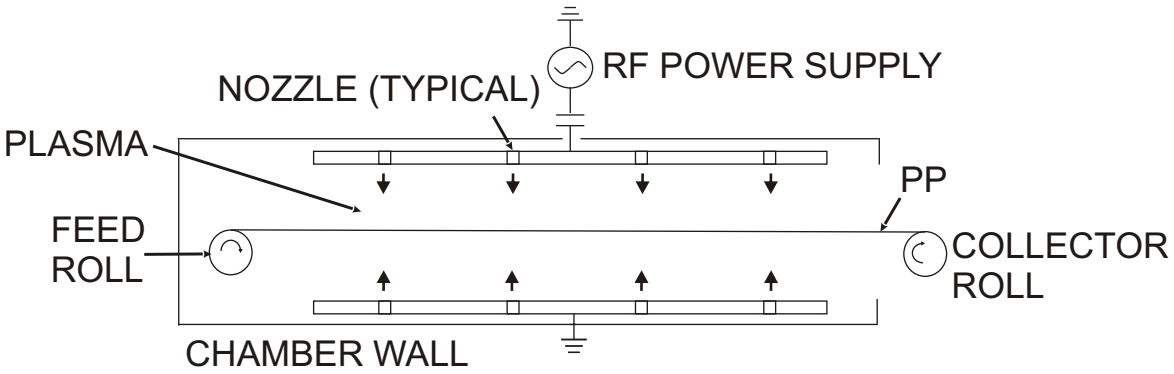

Fig. 5.1 - Schematic of the plasma fluorination reactor. The plasma is produced in a capacitively coupled discharge between two parallel electrodes. The PP web traverses the plasma region at speeds of a few to tens of cm-s^{-1} with residence times of a few to tens of seconds.

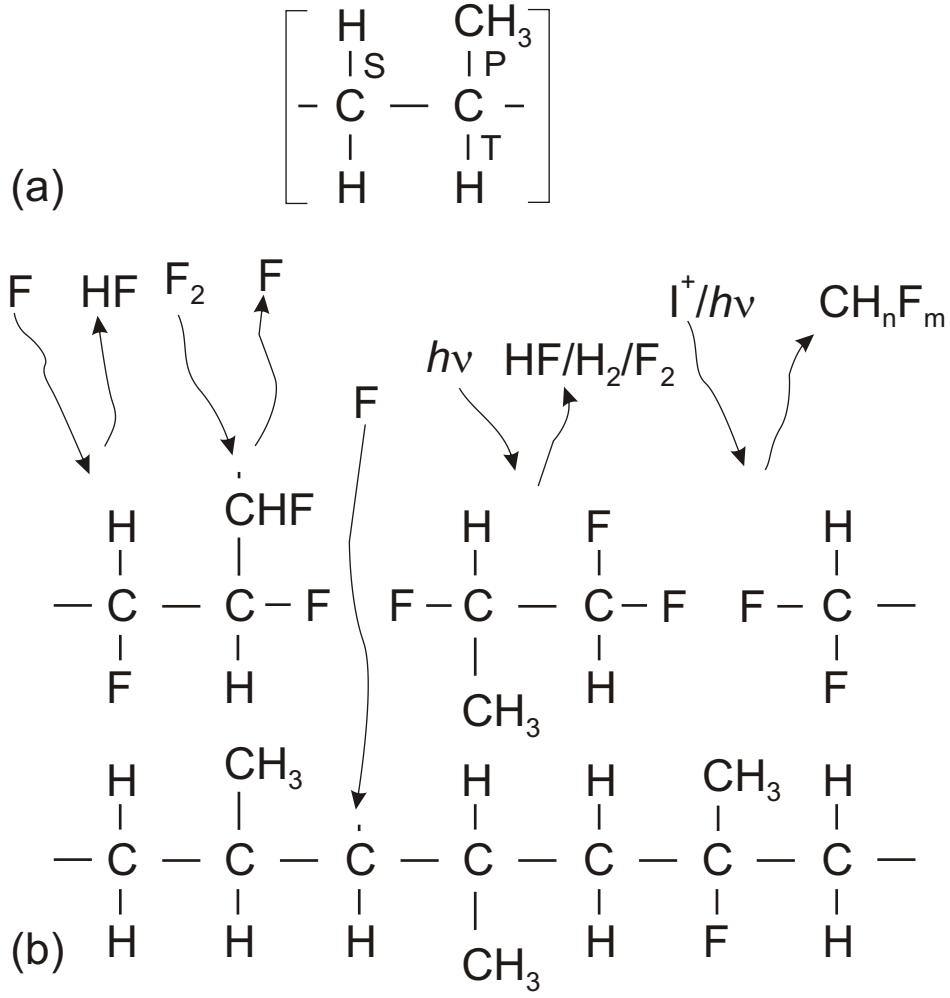

Fig. 5.2 - Schematic of surface reaction mechanism. (a) A repeating unit of PP. The P, S, and T subscripts denote the primary, secondary and tertiary carbon sites. (b) Surface site balance model. PP is a saturated hydrocarbon polymer consisting of two secondary H atoms, a tertiary H atom, and a methyl group containing 3 primary H atoms attached to the carbon backbone. The total number of surface sites is allowed to vary in the model as groups are sputtered. I^+ represent ions and $h\upsilon$ represents photons. CH_nF_m denotes fragments of the PP backbone that are ablated by ions or photons.

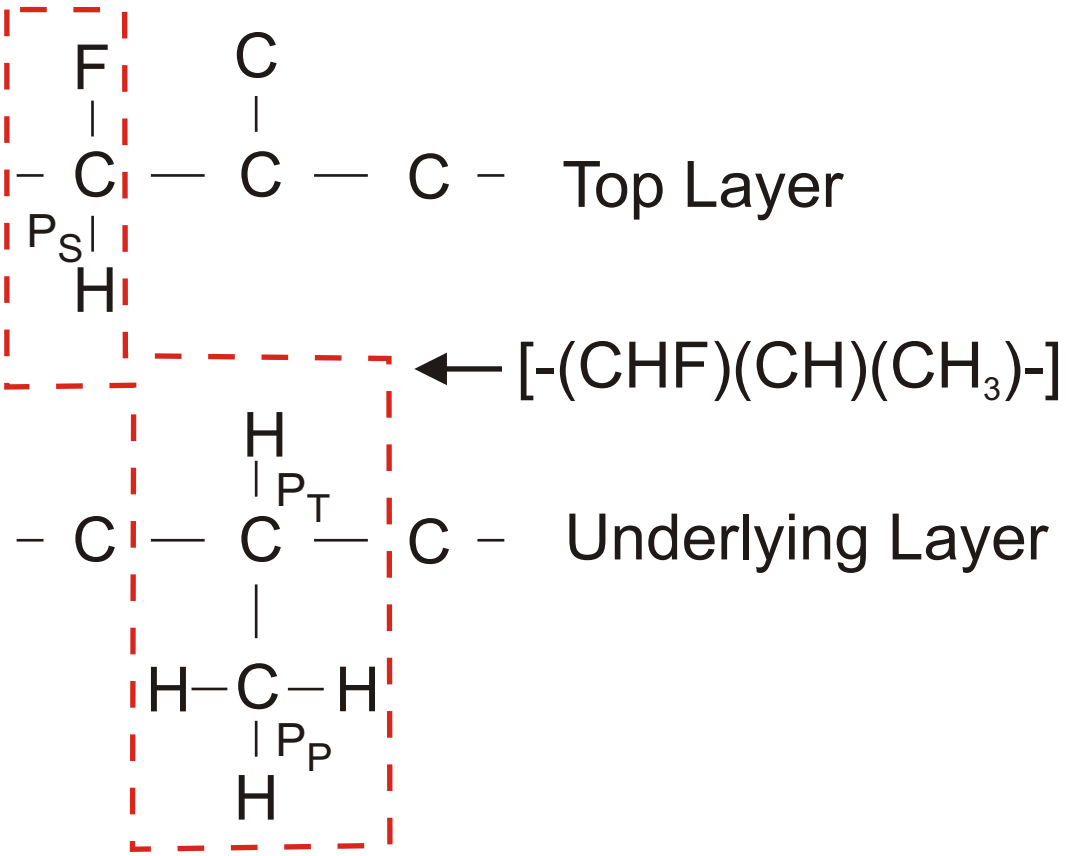

Fig. 5.3 - A virtual two-layer surface species is used to address the change in fluorination rates with fluorination depth due to diffusion effects. [CHF] represents a C_S segment on the topmost backbone. [CH_3] and [CH] are on the underlying PP backbone.

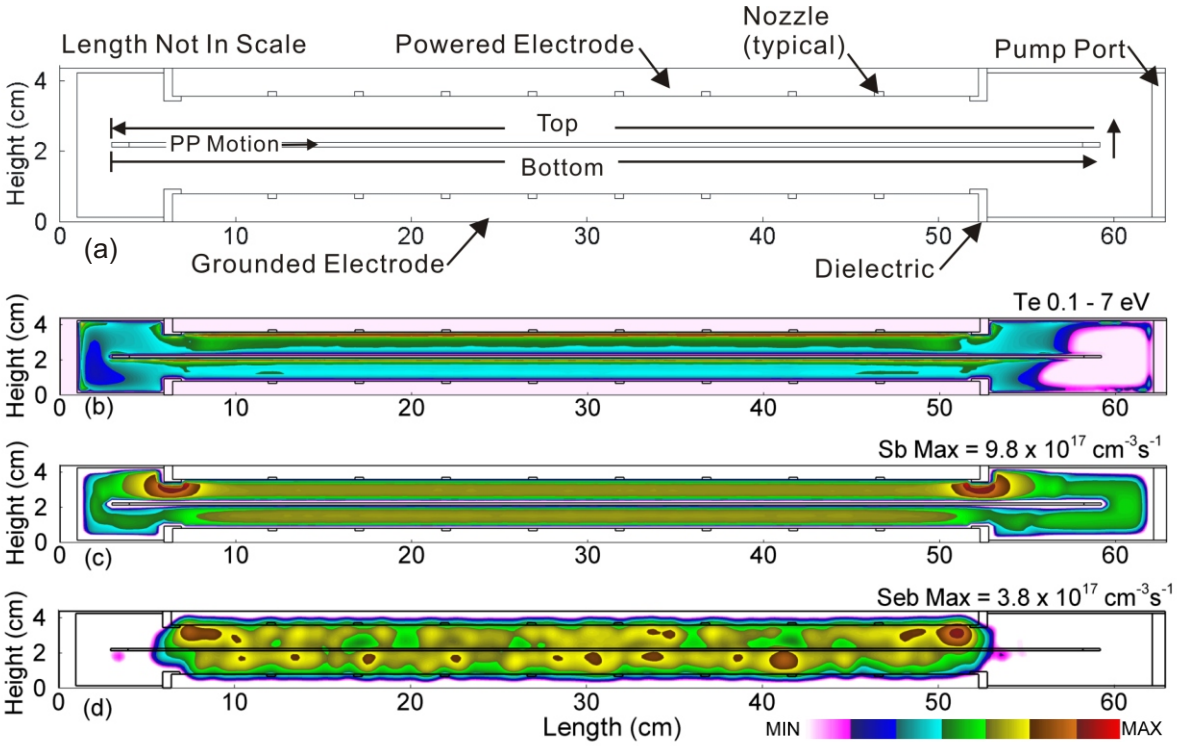

Fig. 5.4 - (Color) Geometry for the reactor used in the model and plasma properties for the base case (Ar/F_2=60/40, 500 mTorr, 600 sccm, 600 W at 10 MHz and web speed of 9 cm-s^{-1}). (a) Geometry, (b) Electron temperature, (c) Ionization by bulk electrons, S_b, (d) Ionization by sheath-accelerated beam electrons, S_{eb}. The feed and collector rolls are not included here as they are outside of the plasma volume. The PP film enters through the left side of the reactor and translates to the right. The intervening dielectric produces a layered structure in T_e. The bulk ionization source peaks near the electrode edges because of the elevated T_e from electric field enhancement. The bulk and beam ionization are plotted on log scales over two decades. The maximum value or range of values in each frame is noted.

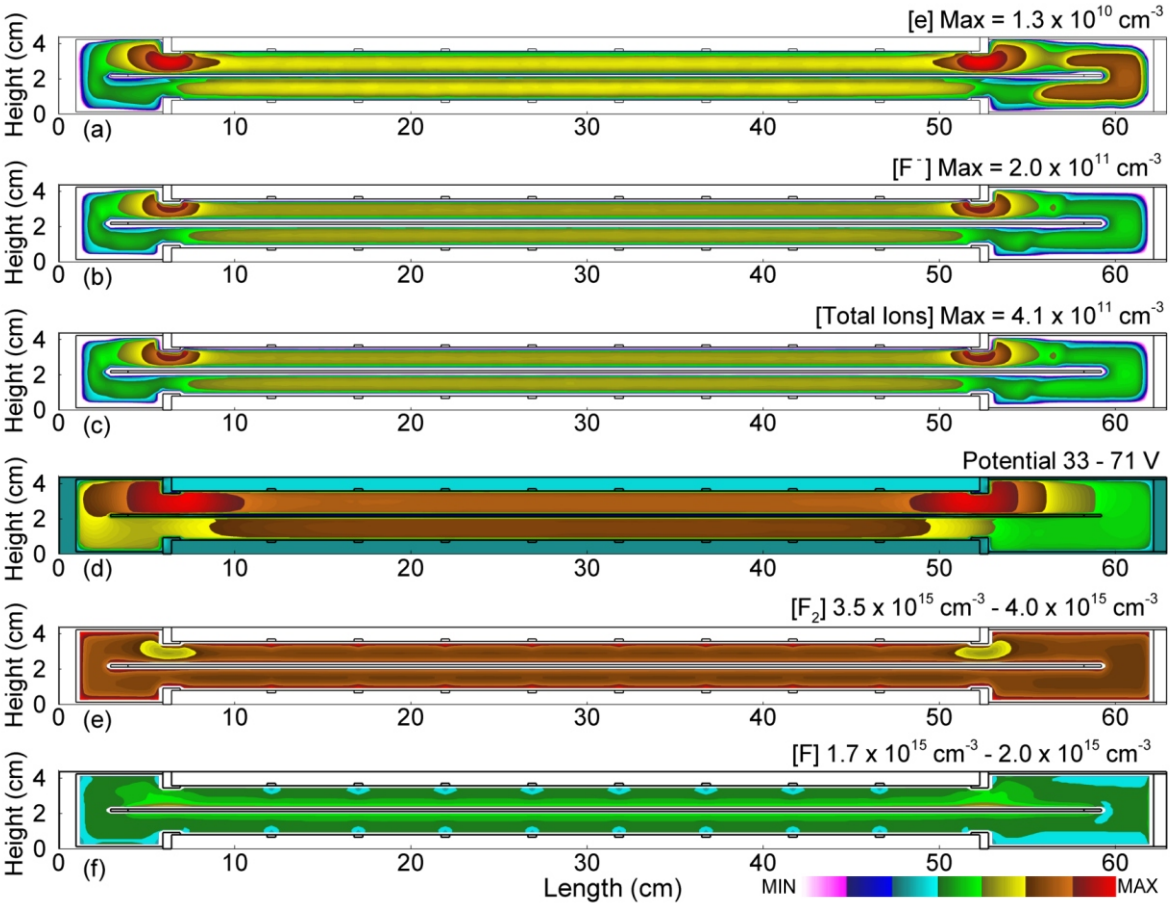

Fig. 5.5 - (Color) Plasma properties and neutral densities for the base case (Ar/F_2=60/40, 500 mTorr, 600 sccm, 600 W at 10 MHz and web speed of 9 cm-s^{-1}). (a) Electron density, (b) F^- density, (c) Cycle averaged plasma potential, (d) Total positive ion density, (e) [F_2], and (f) [F]. Loss of F^- is dominated by volumetric processes (associative detachment and ion-ion neutralization,) and there are time averaged electrostatic traps for F^-. Electron and F^- densities largely mirror the bulk ionization source. The uniform [F] is due to the uniform T_e and rapid F atom diffusion. The electron and ion densities are plotted on log scales over two decades. The maximum value or range of values in each frame is noted.

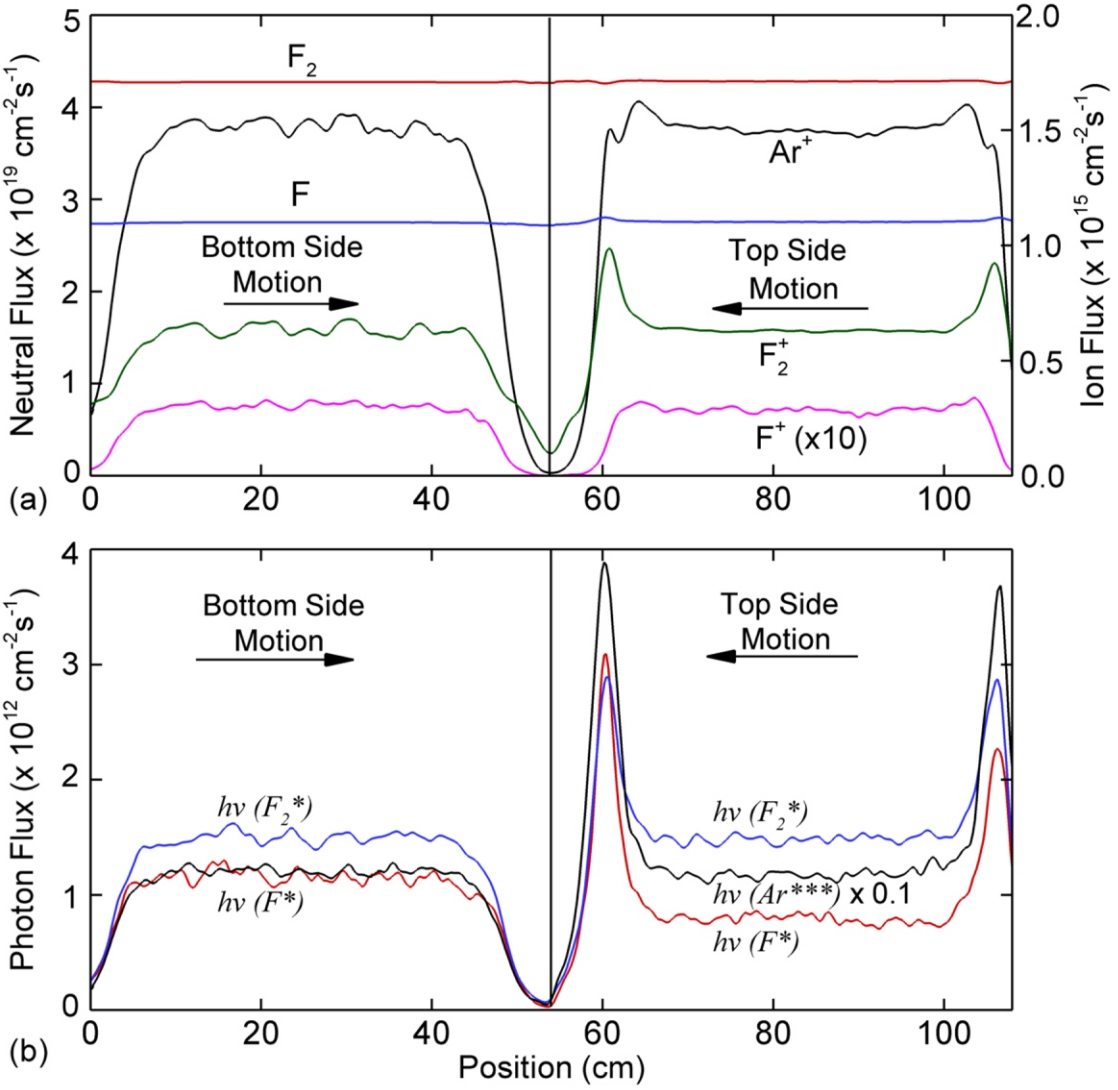

Fig. 5.6 - (Color) Fluxes incident on the PP film for the base case (Ar/F_2=60/40, 500 mTorr, 600 sccm, 600 W at 10 MHz and web speed of 9 cm-s^{-1}). (a) Neutrals and ions and (b) VUV photons. Fluxes of F and F_2 are generally four orders of magnitude larger than ion fluxes (Ar^+, F^+, F_2^+). Photon fluxes are several orders of magnitude lower than the fluxes of neutrals and ions.

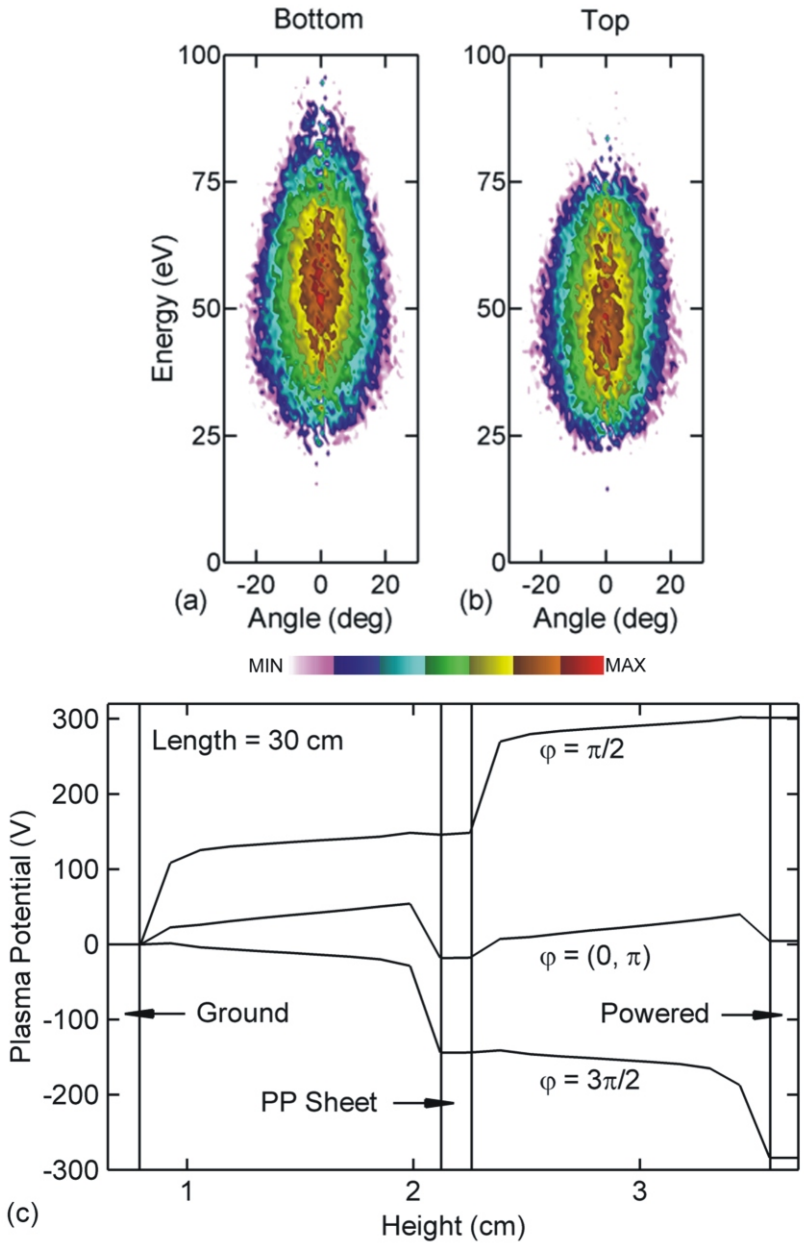

Fig. 5.7 - (Color) IEADs striking the PP surfaces for the base case and the corresponding plasma potential (Ar/F_2=60/40, 500 mTorr, 600 sccm, 600 W at 10 MHz and web speed of 9 cm-s^{-1}). (a) IEADs incident on the bottom surface, (b) IEADs incident on the top surface, and (c) Plasma potential as a function of height at different phases during an rf cycle (position = 30 cm). The contours for the IEADs span two decades using a log scale.

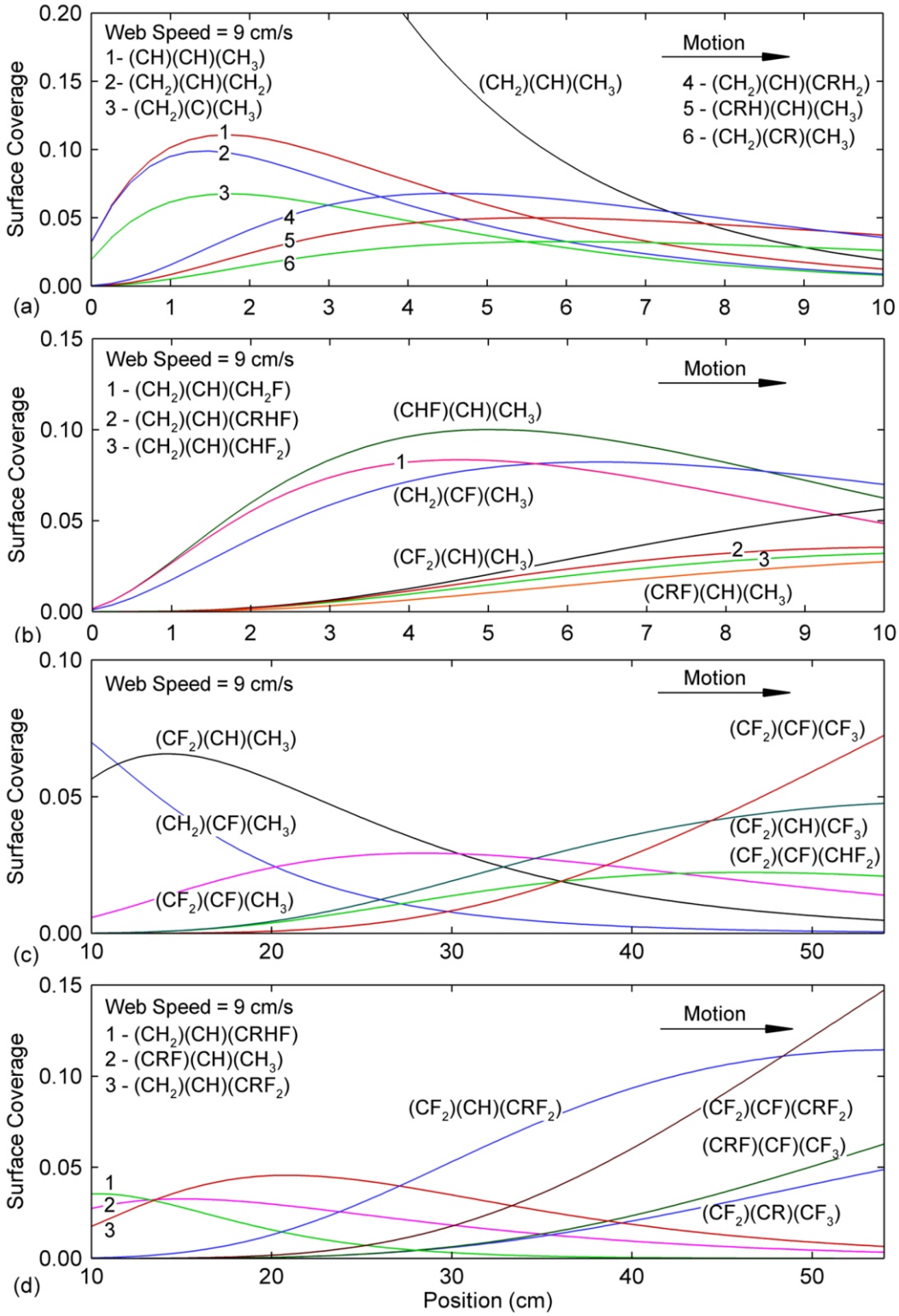

Fig. 5.8 - (Color) Coverages of sites on the bottom side of the PP film for the base case (Ar/F_2=60/40, 500 mTorr, 600 sccm, 600 W at 10 MHz and web speed of 9 cm-s^{-1}) as a function of position. (a) and (b) First 10 cm (1.1 s) of the film entry into the reactor. (c) and (d) Between 10 (1.1 s) and 54 cm (the end of the film, a residence time of 6 s) The surface species with largest fractional coverage at the exit of the film from the reactor is the perfluorinated PP unit with cross-linking on C_P [denoted by $(CF_2)(CF)(CRF_2)$].

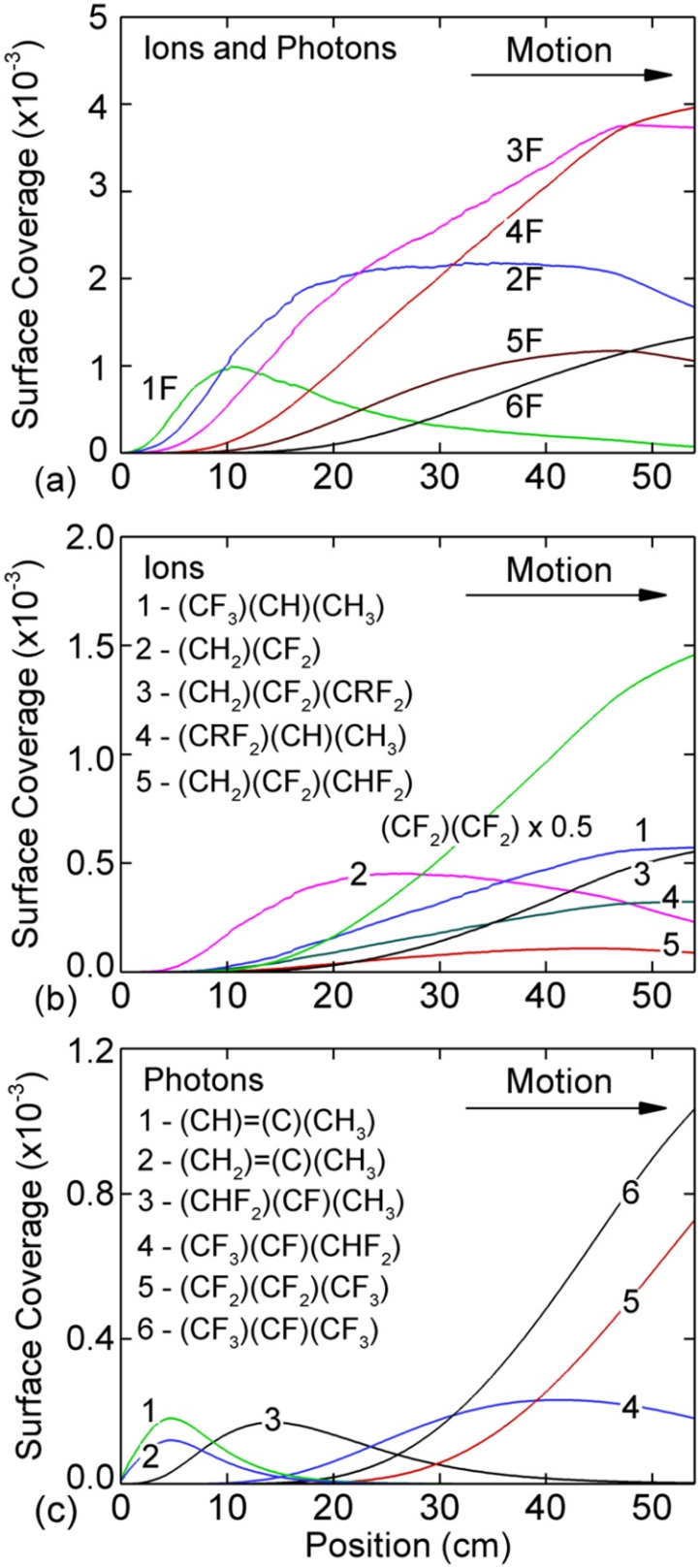

Fig. 5.9 - (Color) Effects of ion sputtering and VUV illumination for the base case (Ar/F_2=60/40, 500 mTorr, 600 sccm, 600 W at 10 MHz and web speed of 9 cm-s^{-1}) as a function of position. (a) Cumulative coverages of sites containing 1-6 F atoms resulting from ion sputtering and photon-activated processes. Major surface species resulting from (b) ion bombardment and (c) VUV irradiation.

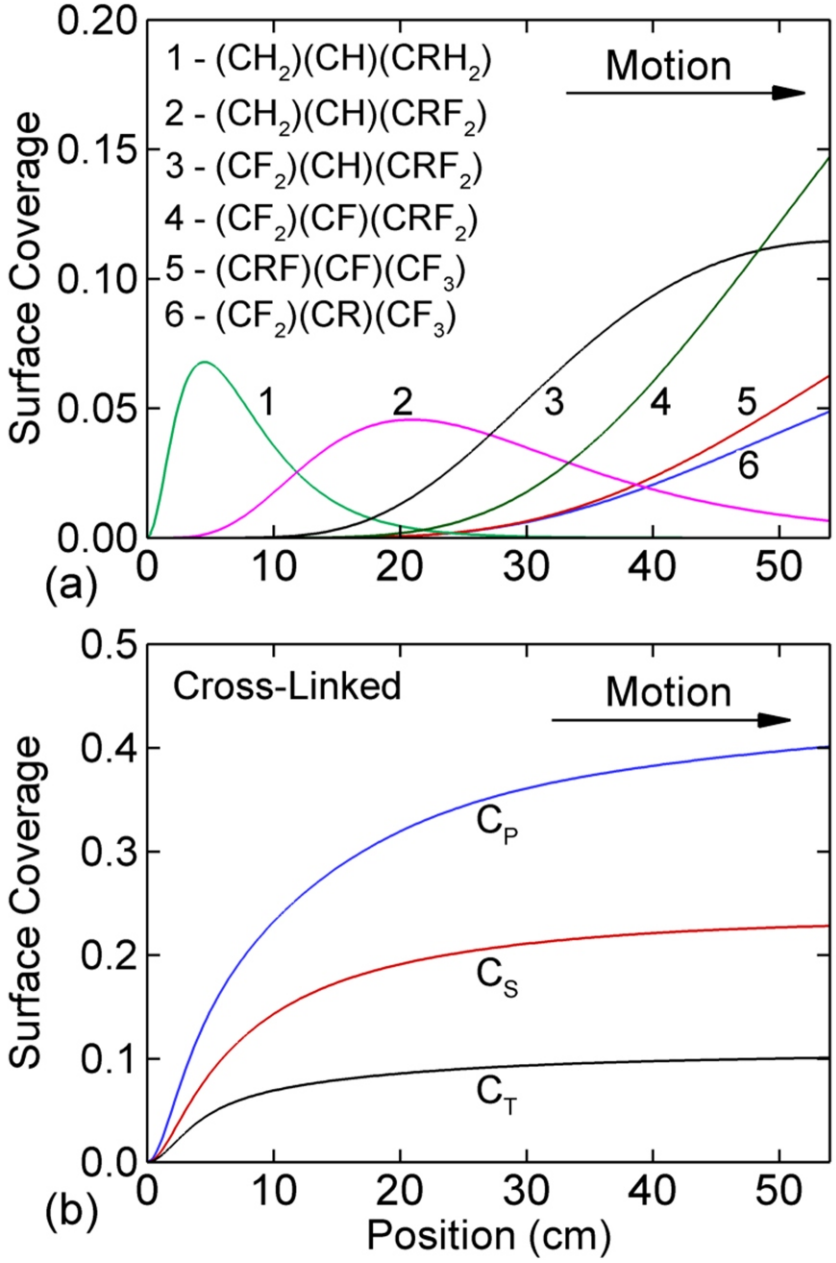

Fig. 5.10 - (Color) Consequences of cross-linking for the base case (Ar/F_2=60/40, 500 mTorr, 600 sccm, 600 W at 10 MHz and web speed of 9 cm-s^{-1}) as a function of position. (a) Major cross-linked species and (b) coverages of the sum of PP unit sites with cross-linked C_P, C_S and C_T .

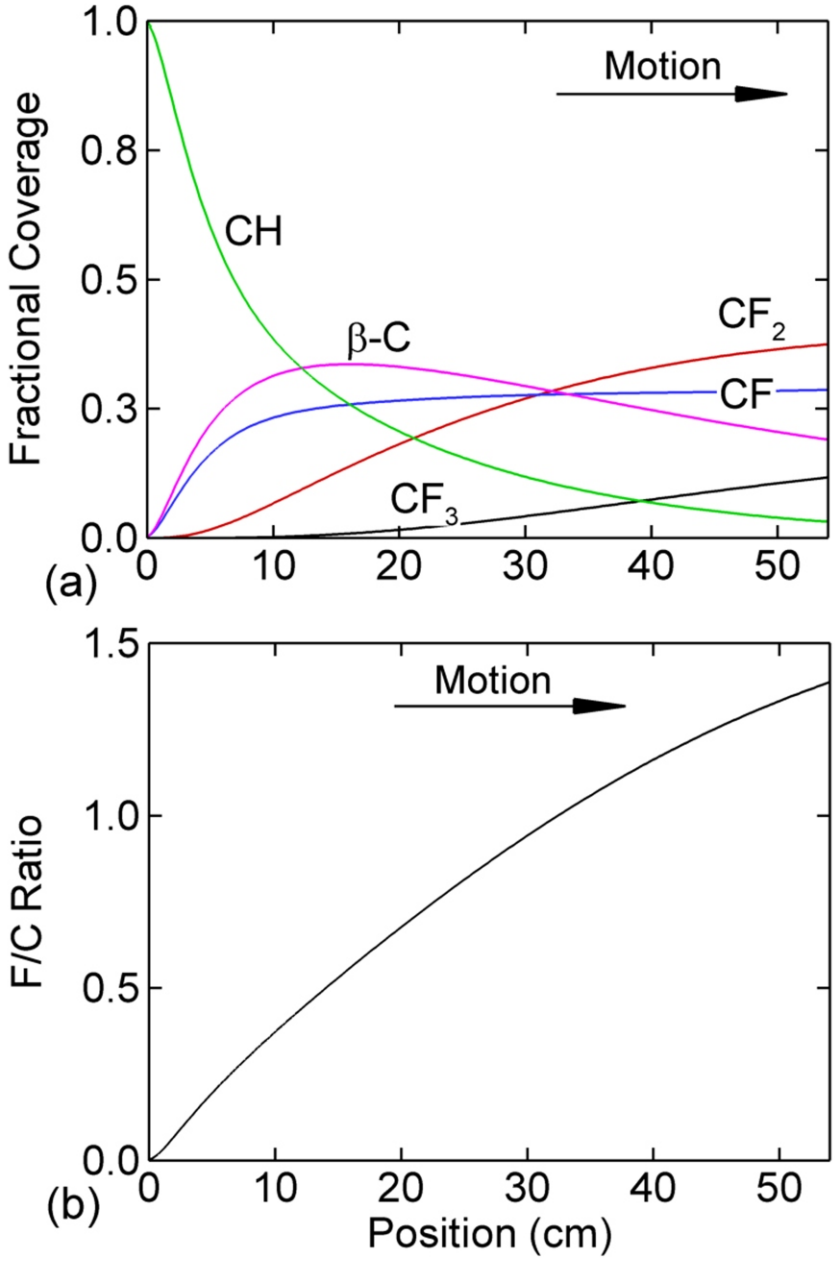

Fig. 5.11 - (Color) Functionalization of the bottom surface of the PP film for the base case (Ar/F_2=60/40, 500 mTorr, 600 sccm, 600 W at 10 MHz and web speed of 9 cm-s^{-1}) as a function of position. (a) Coverage of functional groups and (b) F/C ratio. The sequential nature of the fluorination is shown by the successive dominance of CF_n with larger n as the film translates downstream.

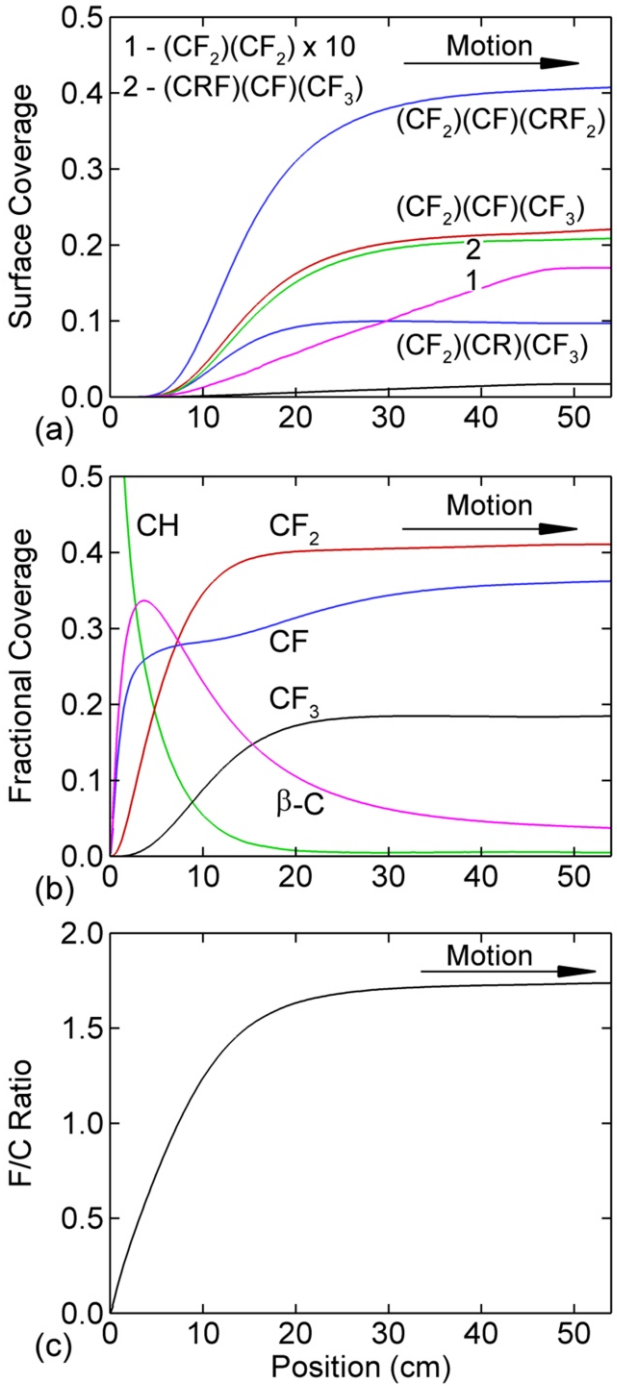

Fig. 5.12 - (Color) Functionalization of the bottom surface of the PP film as a function of position for 26 s treatment with a web speed of 2 cm-s^{-1}. The conditions are otherwise same as the base case (Ar/F_2=60/40, 500 mTorr, 600 sccm, 600 W at 10 MHz). (a) Coverage of surface species, (b) coverages of functional groups, and (c) F/C ratio.

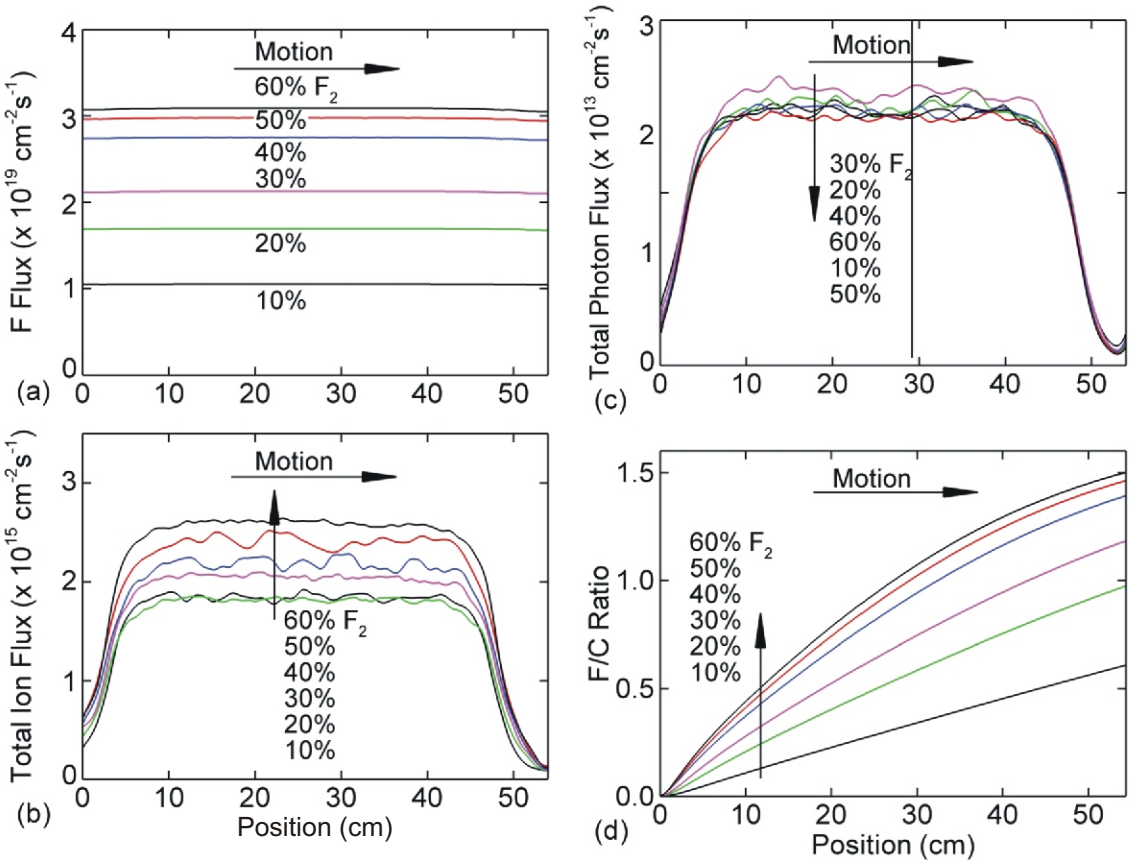

Fig. 5.13 - (Color) Fluxes incident on the bottom side of the PP film and corresponding F/C ratios for F_2 fractions of 10 – 60%. The conditions are otherwise same as the base case (500 mTorr, 600 sccm, 600 W at 10 MHz and web speed of 9 cm-s^{-1}). (a) F flux, (b) total ion flux, (c) total photon flux, and (d) F/C ratio. The F/C ratio at the exit increases with increasing F_2 fraction but does so sub-linearly with F_2 fraction.

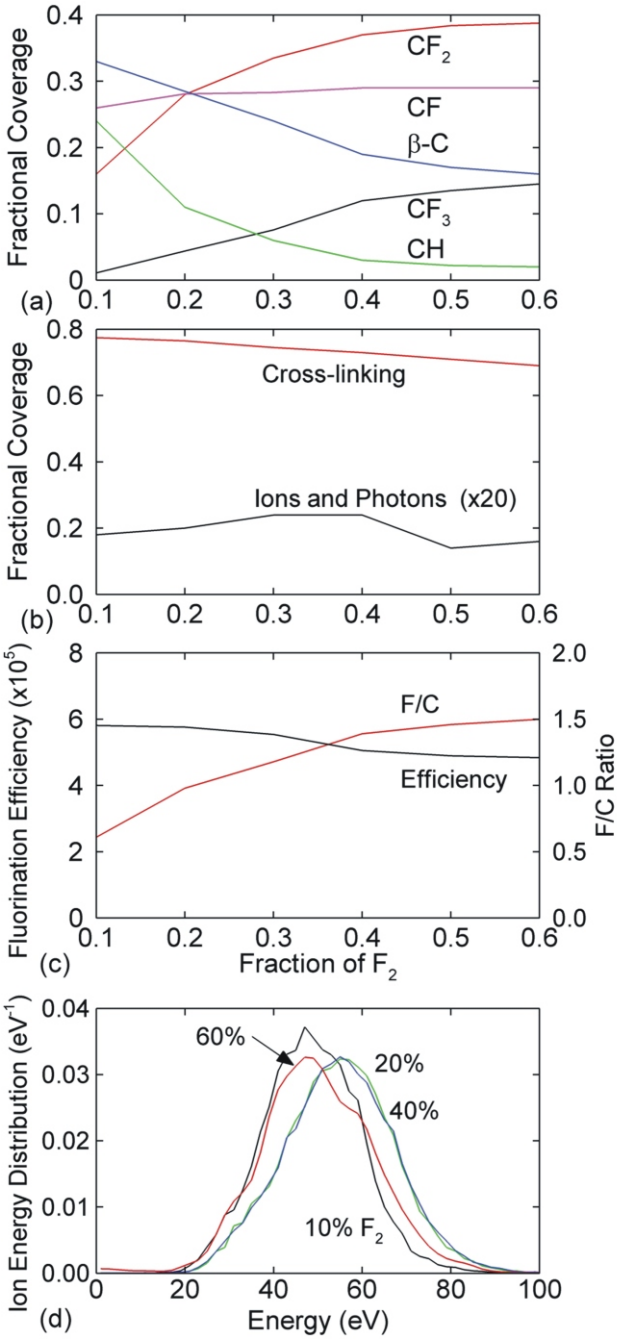

Fig. 5.14 - (Color) Surface compositions at the exit from the reactor on the bottom side of the film and fluorination efficiency as a function of F_2 fraction. The conditions are otherwise same as the base case (500 mTorr, 600 sccm, 600 W at 10 MHz and web speed of 9 cm-s^{-1}). (a) Fractional coverage of functional groups, (b) fractional coverage of total PP unit sites modified by ion and photon bombardment, (c) η, fluorination efficiency and F/C ratio, and (d) ion energy distributions. η decreases with increasing F_2 fraction because of the less efficient fluorination as F/C increases.

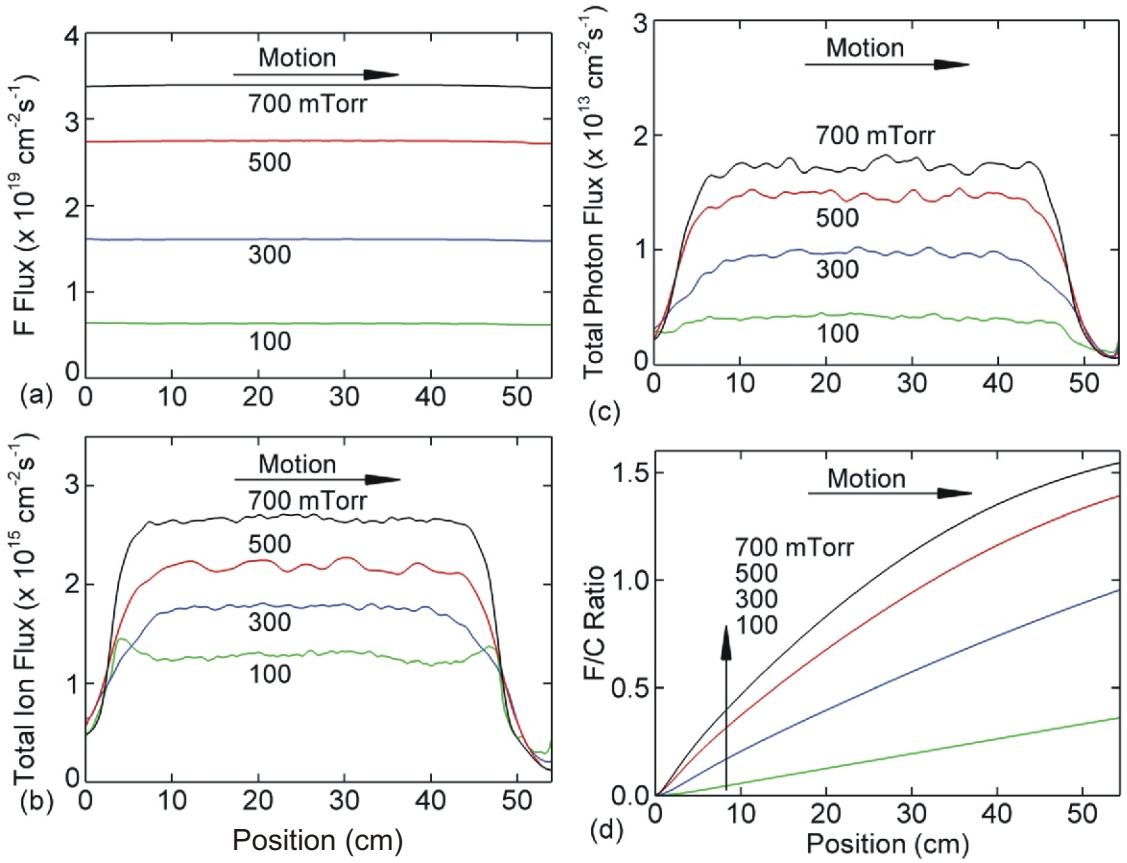

Fig. 5.15 - (Color) Fluxes incident on the bottom side of the PP film and corresponding F/C ratios for pressures of 100 – 700 mTorr. The conditions are otherwise same as the base case (Ar/F_2 = 60/40, 600 sccm, 600 W at 10 MHz and web speed of 9 cm-s^{-1}). (a) F flux, (b) total ion flux, (c) total photon flux, and (d) F/C ratio. The F/C ratio at the exit from the reactor increases with increasing pressure but begins to saturate at high pressures.

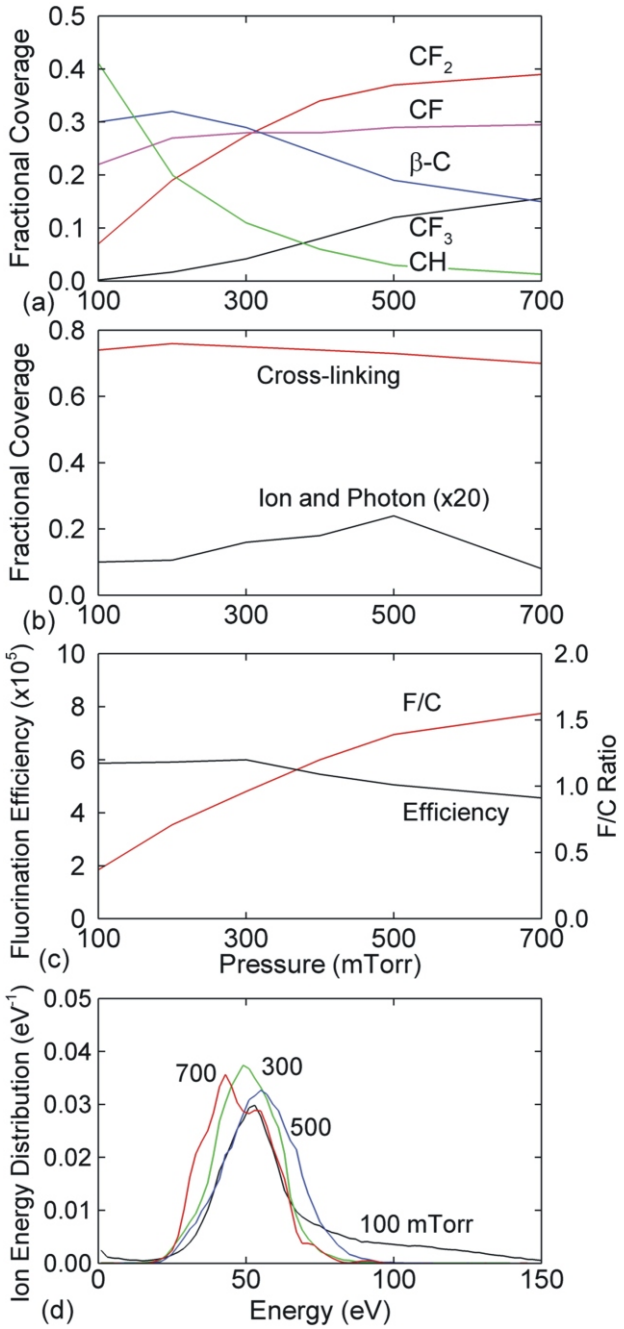

Fig. 5.16 - (Color) Surface compositions at the exit from the reactor on the bottom side of the film and fluorination efficiency as a function of pressure. The conditions are otherwise same as the base case (Ar/F_2 = 60/40, 600 sccm, 600 W at 10 MHz and web speed of 9 cm-s^{-1}). (a) Fractional coverage of functional groups, (b) fractional coverage of total PP unit sites modified by ion and photon bombardment, (c) η, fluorination efficiency and F/C ratio, and (d) ion energy distributions. For pressures > 500 mTorr, the sum of PP unit sites modified by ion and photon bombardment decreases with increasing pressure as a result of decreasing ion-ablation processes.

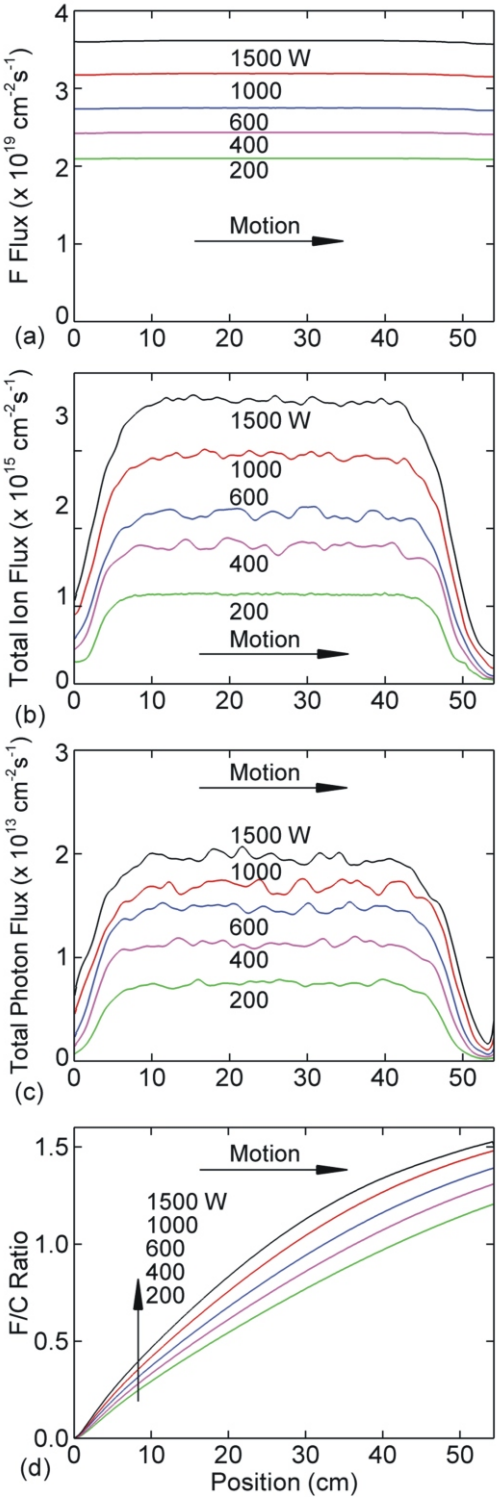

Fig. 5.17 - (Color) Fluxes incident on the bottom side of the PP film and corresponding F/C ratios for powers of 100 – 1500 W. The conditions are otherwise the same as the base case (Ar/F_2 = 60/40, 600 sccm, 500 mTorr at 10 MHz and web speed of 9 cm-s^{-1}). (a) F flux, (b) total ion flux, (c) total photon flux, and (d) F/C ratio.

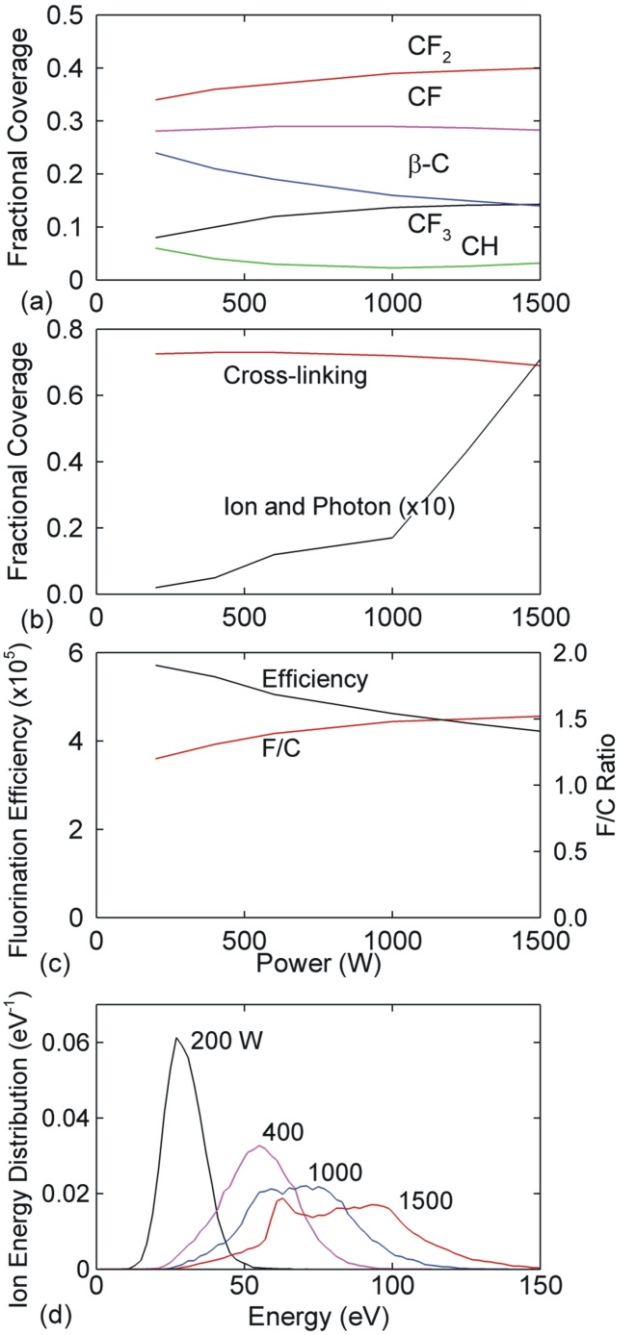

Fig. 5.18 - (Color) Surface compositions at the exit from the reactor on the bottom side of the film and fluorination efficiency as a function of power. The conditions are otherwise same as the base case (Ar/F_2 = 60/40, 600 sccm, 500 mTorr at 10 MHz and web speed of 9 cm-s^{-1}). (a) Fractional coverage of functional groups, (b) fractional coverage of total PP unit sites modified by ion and photon bombardment, (c) η, fluorination efficiency and F/C ratio, and (d) ion energy distributions.

5.9 References

1. M. Strobel, S. Corn, C. S. Lyons, and G. A. Korba, J. Polym. Sci. Part A: Polym. Chem. **23**, 1125 (1985).
2. I. H. Loh, M. Klausner, R. F. Baddour, and R. E. Cohen, Polym. Eng. Sci. **27**, 861, (1987).
3. G. Kranz, R. Luschen, T. Gesang, V. Schlett, O. D. Hennemann, and W. D. Stohrer, Int. J. Adhesion and Adhesives **14**, 243 (1994).
4. W. T. Miller, and S. D. Koch, J. Am. Chem Soc. **79**, 3084 (1957).
5. T. Yagi, and A. E. Pavlath, J. Appl. Polym. Sci. **38**, 201 (1984).
6. N. de Geyter, R. Morent, L. Gengembre, C. Leys, E. Payen, S. Van Vlierberghe, and E. Schacht, Plasma Chem. Plasma Proc.. **28**, 289 (2008).
7. M. Anand, R. E. Cohen, and R. F. Baddour, Polymer **22**, 370 (1981).
8. D. Barton, J. W. Bradley, K. J. Gibson, D. A. Steele, and R. D. Short, J. Phys. Chem. B **104**, 7150 (2000).
9. G. A. Corbin, R. E. Cohen, and R. F. Baddour, Polymer **23**, 1546 (1982).
10. M. Anand, R. E. Cohen, and R. F. Baddour, ACS Symposium Series **162**, 353 (1981).
11. J. Hopkins, and J. P. S. Badyal, J. Phys. Chem. **99**, 4261 (1995).
12. V. Stelmashuk, H. Biederman, D. Slavinska, M. Trchova, and P. Hlidek, Vacuum **75**, 207 (2004).
13. H. Biederman, V. Stelmashuk, I. Kholodkov, A. Choukourov, and D. Slavinska, Surf. Coating Technol. **174-175**, 27 (2003).
14. H. Biederman, Vacuum **59**, 594 (2000).
15. R. Wilken, A. Hollander, and J. Behnisch, Plasmas and Polymers **7**, 19 (2002).
16. A. Hollander, J. E. Klemberg-Sapieha, and M. R. Wertheimer, J. Polym. Sci. Part A **33**,

2013 (1995).

17. C. M. Chan, and T. M. Ko, Surf. Sci. Rep. **24**, 1 (1996).
18. F. D. Egitto, and L. J. Matienzo, Polymer Degradation and Stability **30**, 293 (1990).
19. F. D. Egitto, Pure Appl. Chem. **62**, 1699 (1990).
20. V. N. Vasilets, A. V. Kuznetsov, and V. I. Sevastianov, J. Biomed. Matls. Res. **69A**, 428 (2004).
21. G. A. Corbin, R. E. Cohen, and R. F. Baddour, Macromolecules **18**, 98 (1985).
22. Yu. I. Dorofeev, and V. E. Skurat, Russian Chem. Rev. **51**, 527, (1982).
23. Yu. A. Dorofeev, and V. E. Skurat, Doklady Akademii Nauk SSSR **243**, 1479 (1978).
24. V. Skurat, Nucl. Instr. Meth. Phys. Res. B **208**, 27 (2003).
25. M. Ono, H. Yamane, H. Fukagawa, S. kera, D. Yoshimura, K. K. Okudaira, E. Morikawa, K. Seki, and N. Ueno., Nucl. Instr. Meth. Phys. Res. B **236**, 377 (2005).
26. V. E. Skurat, and A. P. Nikiforov, High Perf. Polymers **16**, 339 (2004).
27. S. Kirk, M. Strobel, C.-Y. Lee, S. J. Pachuta, M. Prokosch, H. Lechuga, M. Jones, C. Lyons, S. Degner, Y. Yang and M. J. Kushner, "Fluorine Plasma Treatments of Polypropylene Films Part I: Surface Diagnostics", Submitted to Plasma Processes and Polymers.
28. M. J. Kushner, J. Appl. Phys. **94**, 1436 (2003).
29. J. Lu, and M. J. Kushner, J. Vac. Sci. Technol. A **19**, 2652 (2001).
30. K. Rajaraman, and M. J. Kushner, J. Phys. D **37**, 1780 (2004).
31. D. Zhang, and M. J. Kushner, J. Vac. Sci. Technol. A **18**, 2661 (2000).
32. D. Briggs, “Surface Analysis of Polymers by XPS and Static SIMS”, (Cambridge University Press, Cambridge, 1998), Chap. 4.

33. R. Dorai, and M. J. Kushner, J. Phys. D **36**, 666 (2003).

34. G. C. Fettis, J. H. Knox, and A. F. Trotman-Dickenson, Can. J. Chem. **38**, 1643 (1960).

35. P. S. Fredricks and J. M. Tedder, J. Chem. Soc., **144-150** (1960).

36. A. M. B. Giessing, A. Feilberg, T. E. Mogelberg, J. Sehested, M. Bilde, T. J. Wallington, and O. J. Nielsen, J. Phys. Chem. **100**, 6572 (1996).

37. Y. D. Gao, and R. G. MacDonald, J. Phys. Chem. A **110**, 977 (2006).

38. A. Goldbach, F. Temps, and H. Gg. Wagner, Ber. Bunsenges. Phys. Chem. **94**, 1367 (1990).

39. L. Wang, V. V. Kislov, A. M. Mebel, X. M. Yang, and X. Y. Wang, Chem. Phys. Lett. **406**, 60 (2005).

40. C. Moore, and I. W. M. Smith, J. Chem. Soc. Faraday Trans. **91**, 3041 (1995).

41. I. C. Plumb, and K. R. Ryan, Plasma Chemistry and Plasma Processing **6**, 11 (1986).

42. T. L. Pollock, and W. E. Jones, Can. J. Chem. **51**, 2041 (1973).

43. A. Persky, Chem. Phys. Lett. **380**, 286 (2003).

44. J. F. Ziegler, www.srim.org, accessed on 5 May 2008.

45. F. L. Nesbitt, R. P. Thorn, W. A. Payne, and D. C. Tardy, J. Phys. Chem. A **103**, 4470 (1999).

46. M. Hayashi, and T. Nimura, J. Appl. Phys. **54**, 4879 (1983).

47. W. L. Morgan (private communication), Kinema Software, http://www.kinema.com

48. K. Tachibana, Phys. Rev. A **34**, 1007 (1986).

49. D. Rapp, and P. Englander-Golden, J. Chem. Phys. **43**, 1464 (1965).

50. R. H. McFarland, and J. D. Kinney, Phys. Rev. **137**, 1058 (1965).

51. I. P. Zapesochnyi, Y. N. Semenyuk, A. I. Dashchenko, A. E. Imre, and A. I. Zapesochny, JETP Lett. **39**, 141 (1984).

52. L. Vriens, Phys. Lett. **8**, 260 (1964).

53. M. Diegelmann, K. Hohla, F.Rebentrost, and K. L. Kompa, J. Chem. Phys. **76**, 1233 (1982).

54. K. Sasaki, Y. Kawai and K. Kadota, Rev. Sci. Instrum. **70**, 76 (1999).

55. G. M. Lawrence, Phys. Rev A **175**, 40 (1968).

56. A. N. Klucharev, and V. Vujnovic, Phys. Rep. **185**, 55 (1990).

57. H. W. Ellis, R. Y. Pai, E. W. McDaniel, E. A. Mason, and L. A. Viehland, At. Data Nucl. Data Tables **17**, 177 (1976).

58. G. I. Font, W. L. Morgan, and G. Mennenga, J. Appl. Phys. **91**, 3530 (2002).

59. R. E. Olson, J. R. Peterson, and J. Moseley, J. Chem. Phys. **53**, 3391 (1970).

60. P. Ho, J. E. Johannes, R. J. Buss, and E. Meeks, J. Vac. Sci. Technol, A **19**, 2344 (2001).

61. C. J. Ultee, Chem. Phys. Lett **46**, 366 (1977).

AUTHOR'S BIOGRAPHY

Yang Yang was born in Dingxing County, Hebei Province, China, in 1977. He received his B. E. degree in Nuclear Engineering from Shanghai Jiaotong University in 1999. He obtained his M. S. in 2002 where he worked on measurements of void fractions of two-phase flow and modeling of passive circulation for pressurized water reactors under guidance of Prof. Jijun Xu at Shanghai Jiaotong University. He studied at the University of Illinois at Urbana-Champaign and worked on inertial electrostatic confinement fusion under guidance of Prof. George H. Miley between 2003 and 2005. He transferred to Iowa State University in 2005 and has been working with Prof. Mark J. Kushner on modeling of low-temperature plasmas. His work has resulted in 3 refereed journal publications, 11 conference presentations, and he received the Coburn and Winters award and a student merit award at the 56th International Symposium of the American Vacuum Society. Upon graduation in April 2010 with his Ph. D. from Iowa State University, he will work with Applied Materials, Inc. in Santa Clara, CA as a process engineer.